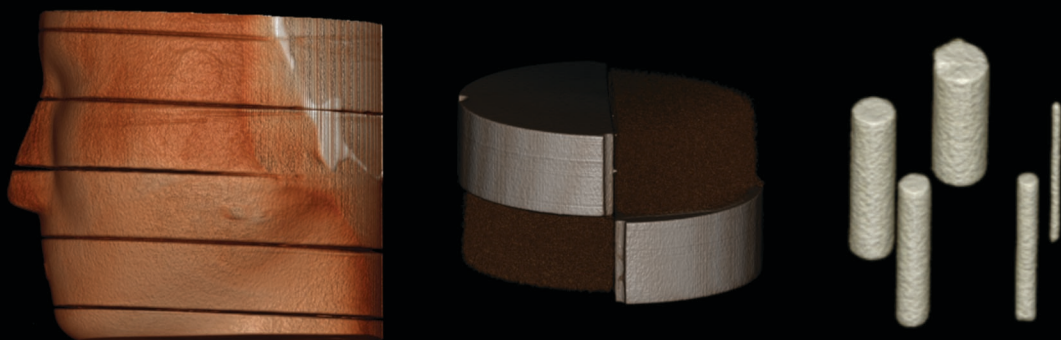**KU Leuven**
Biomedical Sciences Group
Department of Oral Health Sciences
Oral Imaging Center

OPTIMISATION OF CONE BEAM COMPUTED TOMOGRAPHY FOR DENTOMAXILLOFACIAL APPLICATIONS

Ruben PAUWELS

Doctoral thesis in Biomedical Sciences
Leuven, 2012

KU Leuven
Group Biomedical Sciences
Faculty of Medicine
Department of Oral Health Sciences
Oral Imaging Center

OPTIMISATION OF CONE BEAM COMPUTED TOMOGRAPHY FOR DENTOMAXILLOFACIAL APPLICATIONS

Ruben PAUWELS

Doctoral thesis in Biomedical Sciences

Leuven, 2012

KU Leuven
Group Biomedical Sciences
Faculty of Medicine
Department of Oral Health Sciences
Oral Imaging Center

OPTIMISATION OF CONE BEAM COMPUTED TOMOGRAPHY FOR DENTOMAXILLOFACIAL APPLICATIONS

Ruben PAUWELS

<u>Jury</u>:

Promoter: Prof. Dr. Reinhilde Jacobs
Co-promoter: Prof. Dr. Ir. Hilde Bosmans
Co-promoter: Prof. Dr. Ria Bogaerts
Chair: Prof. Dr. Dominique Declerck
Secretary: Prof. Dr. Ir. Frederik Maes
Jurymembers: Prof. Dr. Robert Hermans
              Prof. Dr. Ir. Klaus Bacher
              Prof. Dr. Gerard Sanderink
              Prof. Dr. Ralf Schulze

Leuven, 26.04.2012

Doctoral thesis in Biomedical Sciences

Acknowledgements

A first word of thanks goes to my promoter Prof. Reinhilde Jacobs for giving me the chance to follow this PhD programme. Her trust and support throughout the years has been invaluable, and her contribution to this thesis goes far beyond the scientific aspects of it. All of the time and effort she has spent on me has given me the drive to keep going.

I also wish to thank my co-promoters Prof. Ria Bogaerts and Prof. Hilde Bosmans. It has been an honour and a pleasure to have such a multi-disciplinary team guiding me through this project. I am truly grateful to all of you for helping me grow as a researcher.

My gratitude goes towards Prof. Mark Waer, Rector at the Catholic University of Leuven, Prof. Jan Goffin, Dean of the Faculty of Medicine, and Prof. Dominique Declerck, head of the Department of Oral Health Sciences, for allowing me to undertake this PhD project, and Krista Bogaert, Adiminstrative Coordinator of the Executive Committee of the Biomedical Sciences Group for helping me out with all sorts of questions.

I would like to thank all members of the Examining Committee for taking their time to review this manuscript and to provide many useful comments and topics for further discussion: Prof. Steven Dymarkowski, chair of the Examining Committee and delegate of the Thesis Advisory Committee; Prof. Frederik Maes and Prof. Robert Hermans, members of the internal jury; Prof. Klaus Bacher, Prof. Gerard Sanderink and Prof. Ralf Schulze, members of the external jury.

Special thanks to Prof. Keith Horner, coordinator of the SEDENTEXCT project, and all of our project partners for the wonderful experience. Also a big word of thanks to the other KU Leuven researchers involved in SEDENTEXCT, and various private dentists and companies who allowed us to perform scans on their CBCT devices.

Another word of thanks goes to a large, international group of people which I am honoured to call my co-workers and friends at the Oral Imaging Center. I truly could not have wished for a better work environment, and I will always cherish the moments we shared at the lab or after hours. Some of you have been working at the lab longer than me, others have started there together with me, and others joined later-on. Unfortunately, many of you were only able to stay with us for a limited period of time. But I have great memories from all of you. I am lucky to have met people from all around the world, from every continent with the

exception of Oceania and Antarctica (maybe we can set up some kind of evolutionary penguin study using CBCT?).

Next, I would like to thank my family for their continuous support throughout the years: my mother and father, Magda Dumon and Herman Pauwels, and the rest of the 'bende': Jochen, Zus (a.k.a. Evelyn), and Thao. Also thanks to Casper, Nelson and Kiki for their non-verbal support (not counting 'meow' or 'purr').

Thank you to my non-work-related friends for either helping me getting my mind off things, or for actively supporting me and getting me through occasional tough times! I owe a special (personal) thanks to many of you.

Now let's see what the future brings!

Table of Contents

PART II: IMAGE QUALITY

List of Abbreviations

1-D	One-dimensional
2-D	Two-dimensional
3-D	Three-dimensional
AEC	Automatic exposure control
Al	Aluminium
ALARA	As low as reasonably achievable
BEIR	Biological Effects of Ionizing Radiation
CBCT	Cone-beam computed tomography
CNR	Contrast-to-noise ratio
CT	Computed tomography
CTDI	Computed tomography dose index
D	Absorbed organ dose
D_i	Mean absorbed organ dose situated in slice i of anthropomorphic phantom
DICOM	Digital Imaging and Communications in Medicine
F_i	Organ fraction in slice i of anthropomorphic phantom
FOV	Field of view
FPD	Flat panel detector
FWHM	Full width at half maximum
Gy	Gray
H	Equivalent dose / radiation weighted dose
HA	Hydroxyapatite
HU	Hounsfield Unit
ICRP	International Commission on Radiation Protection
IOR	Intra-oral radiograph
kVp	Peak kilovoltage
LiF	Lithium fluoride
LNT	Linear no-threshold
LSS	Life Span Study
Lp/mm	Line pairs per millimetre
mAs	Product of tube current (mA) and exposure time (s)

MSCT	Multi-slice computed tomography
MPE	Medical physics expert
MTF	Modulation transfer function
NPS	Noise power spectrum
Pb	Lead
PMMA	Polymethyl methacrylate
PSF	Point spread function
QA	Quality assurance
QC	Quality control
QCT	Quantitative computed tomography
ROI	Region of interest
SI	International System of Units
Sr	Strontium
Sv	Sievert
Ti	Titanium
TLD	Thermoluminescent dosimeter
UNSCEAR	United Nations Scientific Committee on the Effects of Atomic Radiation
W_T	Tissue weighting factor

Introduction

Radiography in dentistry

Radiography was introduced in dentistry shortly after the initial report on the discovery of X-rays by Wilhelm Roentgen in 1895, and has become an indispensable part of dental practice. Currently, a variety of intra- and extra-oral dental radiographic techniques are applied for diagnosis, treatment planning and follow-up (Figure I.1).

Intra-oral dental radiography is performed by placing the radiographic film or sensor inside the mouth of the patient, and aiming a small circular or rectangular X-ray beam towards it. Depending on the visualized area, intra-oral radiographs are defined as periapical, bitewing or occlusal views. They are applied for a variety of dental indications, often being used as an initial radiographic examination.

Additionally, various two-dimensional (2-D) and three-dimensional (3-D) extra-oral techniques are used. Conventional 2-D extra-oral images are the lateral cephalogram and the antero-posterior radiograph. The dental panoramic radiograph is a specific image of the upper and lower jaw which is acquired by projecting a narrow beam orthogonally to the dental arch, providing an overview of the teeth, jaw bones and adjacent structures.

Although 2-D radiographs are conventionally applied in dental practice, they often fail to answer the clinical question due to the superposition of tissues on the image. The use of 3-D imaging is often indicated, and different tomographic modalities have been used in addition to 2-D radiographs. Classical (linear and spiral) tomography is nowadays replaced by computed tomography (CT). In CT imaging, a 3-D image is reconstructed using a large number of 2-D (or consecutive 1-D) projections which are acquired by rotating the X-ray tube and detector, with the scanned object as centre of rotation. An array of terminologies is used for CT devices. From a geometrical point of view, there are two types of CT scanners, using a fan-shaped or cone-shaped beam (Figure I.2). Fan-beam CT can use a single row of detectors (single-slice CT), and can be used in sequential mode or by making a continuous spiral trajectory (spiral CT). Most scanners today use multiple detector rows, up to 320, and are then referred to as multi-slice CT (MSCT) or multi-detector CT (MDCT). In cone-beam CT (CBCT), a cone- or pyramid-shaped X-ray beam is used in conjunction with a 2-D detector array (Miracle *et al.* 2009, Scarfe *et al.* 2012). It should be noted that the use of wide beams in current-generation MSCT scanners leads to a fading distinction between MSCT and CBCT

based on beam shape alone. Still, there are a number of additional differences between CBCT and MSCT. Apart from the cost and size of the devices, certain hardware and software aspects may differ between them. The type of detector and its configuration varies, with CBCT using solid-state flat panel detectors (FPD) or image intensifiers, and modern MSCT using arcs of solid-state detectors, with recent evolutions in detector materials and technology leading to higher detector efficiencies. Scan times for current-generation MSCTs have been significantly reduced and are far below those of CBCT. Furthermore, CBCT typically uses a modified backprojection algorithm (Feldkamp *et al.* 1984), with iterative reconstruction being used scarcely and in its most basic form. In MSCT, the use of iterative reconstruction has been introduced for a variety of clinical applications. A final difference is the common use of automatic exposure control (AEC) and real-time dual energy scanning in current-generation MSCT, enabling further optimisation of patient radiation dose.
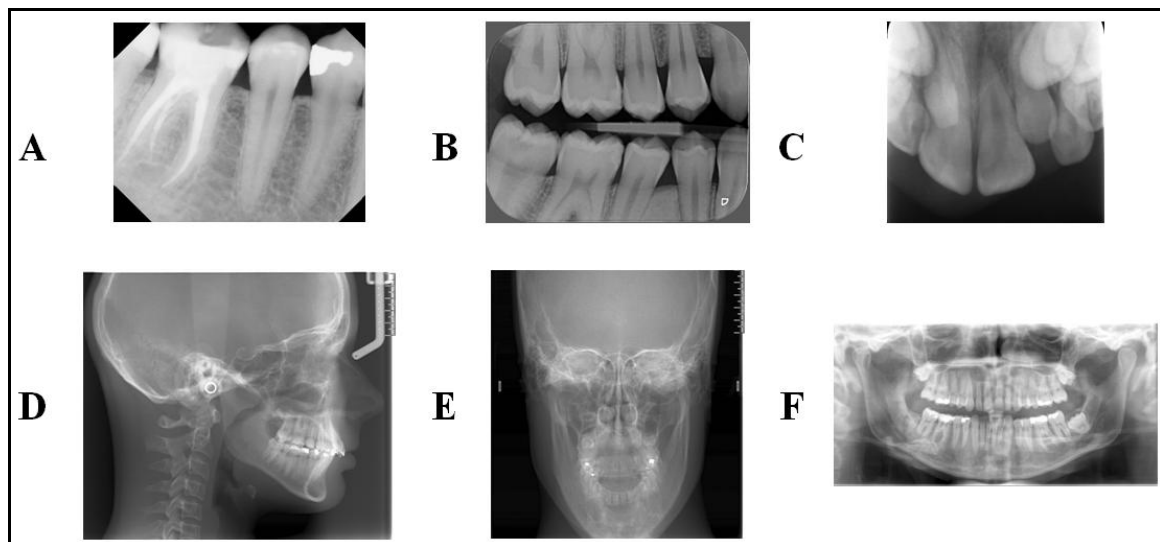
Figure I.1 Intra- and extra-oral radiographic and (non-computed) tomographic techniques. (A) periapical intra-oral radiograph (IOR), (B) bitewing IOR, (C) occlusal IOR, (D) lateral cephalogram, (E) anteroposterior cephalogram, (F) panoramic radiograph.

Cone beam computed tomography

The first commercial CBCT device was introduced in 1998. Over a decade later, a large number of manufacturers are distributing one or several types of CBCT scanners. They are used for a wide array of clinical indications, mainly in the areas of implant surgery, endodontics, orthodontics and maxillofacial surgery (Dawood *et al.* 2009). From a radiological perspective, the main advantage of CBCT is the ability to acquire 3-D images of the dentomaxillofacial region with high detail. Furthermore, as this is a volumetric imaging

modality, reconstructed datasets can be manipulated in a versatile way, and visualized and reformatted for an optimal evaluation. There are additional, more practical benefits to CBCT imaging which have supported its acceptance in dental practice: the size of the scanner, cost, and ease of use make it accessible for both private dental practices, radiology clinics as well as dental and general hospitals.
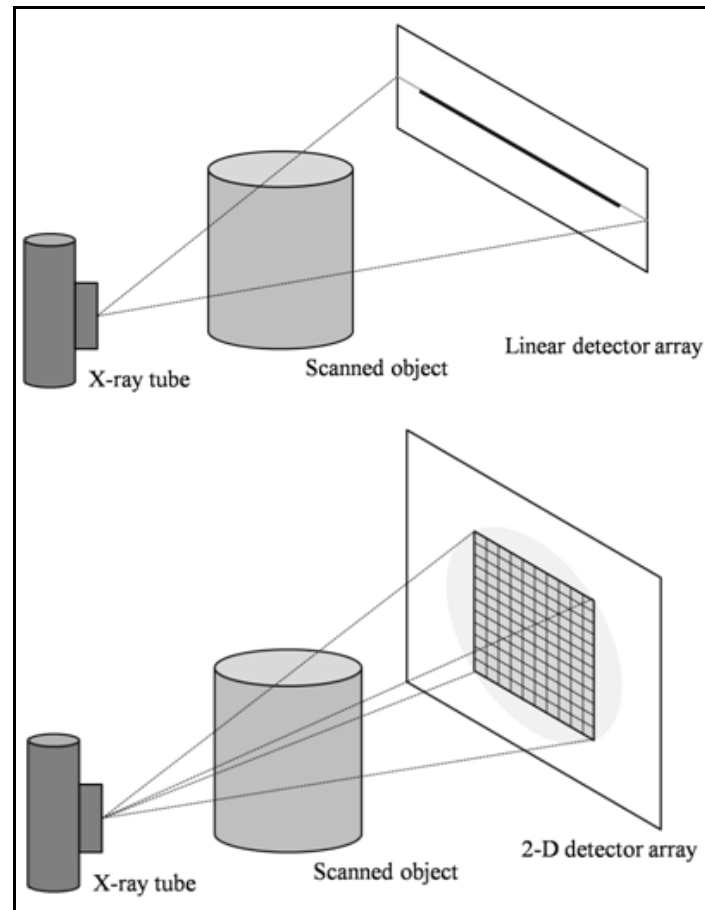
Figure I.2 Fan-beam versus cone-beam geometry in computed tomography

Radiation dose: terminology

As X-rays are a form of ionising radiation, there are different detrimental effects to cells and tissues. For low exposures, only the so-called stochastic effects have to be considered. They occur by chance with a probability related to the cumulative exposure. There are two types of stochastic effects: cancer induction and genetic effects. These effects are a result of mutations in the somatic and germ cells, respectively. At high radiation exposures, in additional to

stochastic effects, deterministic effects occur due to the excessive radiation-induced damage to tissues.

When the first undesirable effect from X-rays became apparent, radiation protection was gradually introduced. Radiation protection encompasses the protection of people (*i.e.* workers, patients and public) from all kinds of ionising radiation. It is based on the principles of justification, optimisation and limitation. Justification implies that the advantage of the use of X-rays should always outweigh the detriment. The optimisation principle is also known as the ALARA (*i.e.* as low as reasonably achievable) principle, which states that all radiation doses should be reduced to the minimum, even when they are below the permitted dose limits. Limitation is the principle of determining radiation dose limits for individuals. Dose limits typically do not apply for patients, as they can be subjected to large amounts of radiation for diagnostic and therapeutic purposes.

Application of the ALARA principle in medical exposures aims to reduce the exposure to the lowest feasible level, while attaining an image which is suitable to address each specific clinical question. In X-ray imaging practice, this reduction can be attained by reducing the tube output to the lowest acceptable level. The tube output is principally determined by a few general tube parameters: voltage peak (kVp), filtration, tube current (mA), and exposure time (s). Other developments at certain points of the imaging chain, such as improvements in detector technology or reconstruction algorithms, can be interpreted as an additional opportunity to reduce the exposure even further. A basic principle in X-ray imaging is that a minimal quality level has to be achieved, and every component in the imaging chain that influences the dose to achieve this level should be taken into consideration. In this regards, other basic methods of patient dose reduction are the collimation of the X-ray beam to the desired region of interest (ROI) and the shielding of certain areas of the patients body.

To express the amount of radiation dose received by a person and the stochastic risk corresponding to this dose, different measures have been defined. The International Commission on Radiation Protection (ICRP) and International Commission on Radiation Units and Measurements (ICRU) have reported and updated various units and factors for the measurement of radiation exposures. The absorbed dose quantifies the amount of energy which is deposited in an object divided by the mass of the object. The International System of Units (SI) has defined the gray (Gy) as the absorption of one joule per kilogram for any type of matter exposed to any type of ionising radiation. When human subjects are subjected to radiation, the absorbed dose to different tissues can be measured or calculated. However, this measure does not take the biological effect of different types of radiation into account. The

equivalent dose, also referred to as the radiation weighted dose, measures the amount of radiation absorbed by biological tissues by multiplying the absorbed dose with a radiation quality factor , which depends on the relative biological damage ('effectiveness') of different types of radiation. This quality factor equals 1 for X-rays, implying that the numerical value for absorbed dose and equivalent dose is equal for X-ray exposures. The SI unit of equivalent doses is sievert (Sv), with an X-ray dose of 1 Gy corresponding to an equivalent dose of 1 Sv. In a final step in determining the actual risk from X-ray exposures, the radiation sensitivity of different tissues is taken into account to calculate the effective dose. The term 'effective dose' (with sievert as unit) was introduced in ICRP and is defined as:

$$E = \sum_T w_T H_T$$

With w_T as the tissue weighting factor for tissue T, H_T as the equivalent dose for tissue T, and the sum of all tissue weighting factors being 1. All organ or tissues which are considered to be sensitive for the induction of stochastic effects are included in this weighted sum. The ICRP has defined and updated a list of tissue weighting factors estimating the relative contribution of different organs and tissues to the overall detriment of radiation-induced stochastic effects (Table I.1). Using these tissue weighting factors, the risk for non-uniform exposures (such as medical images) can be estimated.

It should be noted that, as stated in ICRP Publication 103, the equivalent and effective dose are not measurable quantities but so-called protection quantities. In practice, they are estimated by using reference test objects representing human anatomy (*i.e.* anthropomorphic phantoms) or by measuring other radiation quantities and applying conversion coefficients related to computational phantoms. In ICRP 103, the adult male and female computational phantoms reported in Publication 89 are proposed to compute absorbed organ doses for external exposures. However, as the weighting factors in Table I.1 are considered to be age- and sex-averaged, a variety of anthropomorphic phantoms are used to estimate organ and effective doses from all types of external radiation. Although these estimations cannot be considered as 'true' effective doses, as this would require an additional simulation step using the ICRP 89 reference voxel phantoms, they have been generally accepted in literature as being valid methods for estimating stochastic risks from external irradiation.

Table I.1 Tissue weighting factors for effective dose calculation according to ICRP Publication 26 (1977), 60 (1991) and 103 (2007)

Organ	Weighting factor		
	ICRP 26	ICRP 60	ICRP 103
Gonads	0.25	0.20	0.08
Red bone marrow[a]	0.12	0.12	0.12
Colon	-	0.12	0.12
Lung	0.12	0.12	0.12
Stomach	-	0.12	0.12
Bladder	-	0.05	0.04
Breast	0.15	0.05	0.12
Liver	-	0.05	0.04
Oesophagus	-	0.05	0.04
Thyroid[a]	0.03	0.05	0.04
Skin[a]	-	0.01	0.01
Bone surface[a]	0.03	0.01	0.01
Brain[a]	-	-	0.01
Salivary glands[a]	-	-	0.01
Remainder[a]	0.30	0.05	0.12[b]

[a]Head and neck or whole body organ.
[b]Adipose tissue, Adrenals, Extrathoracic region, Gall bladder, Heart, Kidneys, Lymphatic nodes, Muscle, Oral mucosa, Pancreas, Prostate, Small intestine, Spleen, Thymus, Uterus/cervix.

The relation between radiation dose and the induction of and mortality from stochastic effects has been under investigation for several decades, with the Life Span Study (LSS) of the Japanese atomic bomb survivors as primary source of epidemiological information. Several reports by national and international organisations such as the ICRP and the United Nations Scientific Committee on the Effects of Atomic Radiation (UNSCEAR) have reviewed these risks. A first assumption which is currently under investigation is the linear non-threshold (LNT) hypothesis, stating that the risk for stochastic effects induced by radiation decreases has a positive linear effect with radiation dose at doses below 100 mSv, with no threshold below which the risk is zero. At dose levels higher than 100 mSv, the dose-risk relationship has been accurately determined, but below this level there is a large degree of uncertainty caused by different confounding factors. The LNT hypothesis is considered as a conservative approach to estimate radiation risk, as there is evidence for hypersensitivy (*e.g.* bystander effect) to radiation at low doses, but also for counter-acting effects (*e.g.* adaptive response) which lower the risk. The consensus from all national and international bodies is to adhere to the LNT hypothesis, as there is currently no conclusive evidence against it. A

second issue is related to the actual quantification of the risk, using simple or more complicated models to estimate the risk for a given person exposed to radiation. The lifetime attributable risk (LAR) is a generally accepted quantity, which can be estimated for any cancer type by taking the attained age, age at exposure and dose into account.

Patient radiation dose in dental radiography

Radiographic examinations in dentistry have always represented a significant portion of the total frequency of X-ray images acquired for medical purposes. The first dental radiograph was acquired in 1896 by Friedrich Otto Walkhof, only 14 days after the report on the discovery by Roentgen. An exposure time of 25 minutes was used, resulting in exposures which were large enough to cause mild deterministic effects such as local hair loss. Evidently, there have been a series of developments in X-ray imaging since that point. For conventional 2-D intra- and extra-oral images, the exposure time is now a fraction of a second. The introduction of additional imaging techniques in dental practice has resulted in a degree of choice for the practitioner, enabling him to select the most appropriate imaging modality for any type of clinical indication. This choice is determined by different factors, with the radiation dose to the patient being a key determinant, as any unnecessary or excessive exposure should be avoided.

Generally, the radiation risk from exposures to the head and neck area can be considered as relatively low compared to other areas of the human body. The sole organ with a high radiosensitivity in the head and neck is the thyroid gland, with a w_T of 0.04. The salivary glands and brain both have a w_T of 0.01. Additionally, the oral mucosa and extrathoracic airways are both part of the large group of remainder tissues (w_T 0.12), giving them an actual w_T of approximately 0.01. Finally, there are a number of additional organs which are partly exposed during a dental X-ray examination, with the red bone marrow (w_T 0.12) being the most notable contributor to the effective dose.

The lowest patient doses are found for intra-oral and non-tomographic extra-oral radiographs. Reported effective doses for single intra-oral and cephalometric images are below 10 µSv (Ludlow *et al.* 2008), a level similar to the world-wide average of a single day of background radiation (Thorne 2003). For panoramic imaging, a range of dose values has been reported, with effective doses between 3 and 38 µSv (Garcia Silva *et al.* 2008, Gavala *et al.* 2009). For dental MSCT exposures, effective doses up to 1 mSv are seen, as well as

considerably reduced doses for reduced FOV (*e.g.* single jaw) or low-dose protocols (Loubele *et al.* 2005, Loubele *et al.* 2009).

Many authors have investigated organ and effective dose for one or more CBCT devices. Depending on different varying exposure parameters, estimated effective doses were between 13 and 1073 µSv (Loubele *et al.* 2009, Ludlow *et al.* 2008). Although an intercomparison of different studies should be avoided due to differences in methodology, it is clear that a wide exposure range is seen in dental CBCT imaging.

Image quality in medical imaging

In general, the image quality of any medical image can be described by four parameters: resolution, contrast, noise and artefacts. The (spatial) resolution or sharpness of an image can be interpreted as the ability to distinguish separate objects. Contrast is the difference in signal intensity (*e.g.* grey value) between regions in the image. The ubiquitous noise or graininess in an image is a result of the statistical nature of medical imaging. Artefacts refer to any type of image distortion caused by one or more aspects along the imaging chain: metal objects in CT and magnetic resonance imaging (MRI), object motion, film or detector damage, operator errors, *etc*. The appearance of different types of artefacts varies greatly, resulting in a slight, moderate or grave decrease in image quality.

When evaluating the image quality of a medical image, it is not practically possible to distinguish these four main parameters separately. Spatial resolution and contrast are co-dependent, as shown by the Modulation Transfer Function (MTF) which expresses the loss in contrast at increasing spatial frequencies. The noise affects both the sharpness and contrast of the image, and different types of artefacts can affect one or more of the other three parameters in (parts of) the image.

Practical parameters have been defined to quantify diverse image quality aspects. A variety of test objects and methods can be used to evaluate different image quality aspects of an imaging system. Certain parameters, such as the contrast-to-noise ratio (CNR), are directly linked to the actual diagnostic image quality and can be easily interpreted. Other parameters such as the noise power spectrum (NPS) are more abstract and serve as a more technical evaluation of imaging performance.

Image quality aspects of CBCT

Similar to its radiation dose, image quality of CBCT devices has been extensively studied since their introduction in dental practice. Most studies have focused on the use of CBCT scanners for specific imaging applications, such as the evaluation of bone quantity and quality for implant placement, visualization of the root canal for endodontic treatment, or the segmentation of 3-D models of the jaws and anterior skull for various applications (*e.g.* Suomalainen *et al.* 2009, Loubele *et al.* 2008, Liang *et al.* 2010, Kamburoğlu *et al.* 2011, Alqerban *et al.* 2011, Nackaerts *et al.* 2011, Lofthag-Hansen *et al.* 2011). Similar to the range in patient dose, a wide range in image quality performance has been reported for CBCT, affected by (but not solely determined by) the varying exposure levels which are applied.

CBCT images are generally considered to be of high resolution. The voxel sizes of reconstructed CBCT datasets, representing the upper limit of the actual resolution, ranges between 0.08 and 0.4 mm, and preliminary studies have pointed out that the sharpness of CBCT is superior to that of MSCT. It is therefore particularly useful for cases in which small structures (*e.g.* roots and periodontal tissues) need to be visualized in 3-D.

On the other hand, CBCT is considered to have relatively high noise levels and a limited soft tissue contrast, making it mainly suitable for the visualization of structures with a high inherent contrast: teeth, bony structures and canals, and air cavities. An absence of diagnostically valid soft tissue contrast on CBCT images limits its application range.

As mentioned above, the most commonly used reconstruction algorithm in CBCT is the original or modified Feldkamp algorithm, which is based on the principle of backprojection. Along with the physical properties of the imaging system (*e.g.* beam energy spectrum, tube output, detector efficiency, *etc.*), specific adaptations of this reconstruction algorithm can affect different image quality aspects. To some degree, limitations in terms of image quality are inherent to the reconstruction process, which is non-perfect in various ways. For example, it is based on discrete projections and is not able to take the poly-energetic nature of an X-ray beam into account. Furthermore, CBCT reconstruction is versatile to some degree, allowing the manufacturer to adapt various reconstruction parameters (*e.g.* voxel size, smoothening, sharpening, other pre- or post-reconstructions processing steps) with notable effects on image sharpness, contrast and noise.

Suboptimal use of CBCT in dental practice

Although the introduction of CBCT in dentistry has resulted in various improvements in patient treatment, the use of CBCT can still be considered suboptimal when taking the optimisation principle of ALARA into account. There are different aspects to the suboptimal use of CBCT, with many causes at different levels of the imaging process. The manufacturer plays a crucial part in the process of optimisation by providing a device that adheres to the ALARA principle as closely as possible. Medical physics experts (MPE) can aid the optimisation of CBCT by implementing dedicated acceptance tests and quality control (QC) using appropriate tools, figures of merit and reference levels. The clinical referrer should follow the justification principle by making a balanced decision on the need for a CBCT image for a certain patient, and by specifying the diagnostic image quality requirements for each referral (*e.g.* required FOV size and resolution). Finally, the operator of the device plays an important role as well, as they have varying degrees of choice of exposure parameters, depending on the available exposure range of the device and the referrer's specifications.

In the end, suboptimal uses will lead to unnecessary radiation dose for the patient. Optimisation should aim to reduce the dose for individual patients as well as population dose. A factor which complicated the optimisation of CBCT in practice is the variable implementation of the basic cone-beam principle by manufacturers. CBCT devices exhibit wide ranges of essential imaging parameters, affecting the exposure and/or image quality. Because of the difference in voltage peak (kVp) and filtration, the mean beam energy can vary, resulting in changes in both image quality and radiation dose due to different degrees of X-ray absorption and scatter. Varying tube currents (mA) and exposure times directly affect the radiation dose and image quality. The size of the FOV is one of the key determinants of the effective dose, also affecting the image quality in an indirect way. Furthermore, different detector types and specifications are used, and parameters associated with the reconstruction algorithm (*e.g.* voxel size) can show large variability, resulting in different image quality levels for a given exposure. It can be expected that for most of these adaptable imaging parameters, there is an optimum value of the ratio between image quality and radiation dose. However, there has been no large-scale evaluation of radiation dose or image quality for CBCT, and the imaging parameters are freely determined by the manufacturer as well as the user due to the lack of recommendations or guidelines. It should be noted that the user can be limited in his selection of exposure parameters, as they are often fixed by the manufacturer, thereby limiting the potential of dose optimisation by the operator.

A quality assurance (QA) protocol for CBCT would encompass a number of definitions, activities and requirements ensuring that the quality of each scanner can be assessed from a technical perspective. This should include the determination of specific procedures for acceptance testing and QC, enabling the MPE to properly evaluate the performance of different CBCT devices. An important aspect is the definition of figures of merit describing image quality, radiation dose or their ratio. These figures or measures need to be rational and fair, being applicable for any type of CBCT scanner and relevant in terms of clinical use and/or patient risk. Subsequently, ranges, thresholds or reference values need to be determined for all measures. A common approach in medical imaging QA is the definition of revision or suspension levels for all QC measures, providing the community with exposure and image quality levels that should be attained in practice. By including these reference levels in official guidelines or recommendations, a long-term follow-up of an individual scanner's performance and deterioration can be enabled; in addition, the reference levels could be implemented into International Electrotechnical Commission (IEC) standards for manufacturers.

The CBCT user, when provided with a selection of exposure protocols, should be properly educated and informed in order to choose the most appropriate exposure parameters for each individual patient, taking the referral into account. The wide-spread use of CBCT by various user groups (dentists, radiologists, radiation technicians, *etc.*), as well as the various dental and non-dental clinical applications with ranging image quality requirements, underlines the need for evidence-based guidelines on the use of CBCT and the implementation of appropriate theoretical and practical training for the user. Similar to the manufacturer's and MPE's issues mentioned above, a first step in the definition of guidelines and training is the assessment of radiation dose and image quality ranges, and a conversion of these findings to diagnostic reference levels. Clear imaging criteria would allow the CBCT user to make balanced, educated decisions for all types of patients and would likely result in significant dose reductions compared to current practice.

The SEDENTEXCT project

The work in this thesis was part of the multicentre project SEDENTEXCT: Safety and Efficacy of a New and Emerging Dental X-ray Modality, funded by the European Atomic Energy Community's Seventh Framework programme FP7/2007-2011 under grant agreement no. 212246.

The principal aim of the SEDENTEXCT project was the acquisition of the key information necessary for sound and scientifically based clinical use of CBCT. In order that safety and efficacy are assured and enhanced in actual practice, the parallel aim was to use the information to develop evidence-based guidelines dealing with justification, optimisation and referral criteria and to provide a means of dissemination and training for users of CBCT. The detailed objectives of the collaborative project were:

1. To develop evidence-based guidelines on use of CBCT in dentistry, including referral criteria, quality assurance guidelines and optimisation strategies.
2. To determine the level of patient dose in dental CBCT, paying special attention to paediatric dosimetry, and personnel dose.
3. To perform diagnostic accuracy studies for CBCT for key clinical applications in dentistry.
4. To develop a quality assurance programme, including a tool/tools for quality assurance work (including a marketable quality assurance phantom) and to define exposure protocols for specific clinical applications.
5. To measure cost-effectiveness of important clinical uses of CBCT compared with traditional methods.
6. To conduct valorisation, including dissemination, activities via an 'open access' website.

This thesis covers different dose- and image quality-related aspects of dental CBCT imaging. The various chapters each cover a particular topic related to CBCT exposures or images. The aim was to aid in all processes related to optimisation, standardization and guidelines for CBCT, as part of the SEDENTEXCT project (objectives 2 and 4 in the above list, in addition with input into objectives 1, 5 and 6).

Objectives & hypotheses

The overall aim of this thesis was to investigate the optimisation of CBCT imaging at different levels of the imaging chain. All chapters in this thesis cover a specific dosimetric or image quality-related topic. Apart from a particular focus on quality control aspects, this thesis provides a large-scale evaluation of CBCT scanners, exploring the current balance between patient risk and image quality, current and future optimisation schemes and diagnostic reference levels.

The following specific topics were addressed:

PART I: Dosimetry

Chapters 1, 2 and 3: The organ and effective dose range for CBCT scanners was assessed using thermoluminescent dosimeters attached to adult (*Chapters 1, 3*) and paediatric (*Chapter 2*) anthropomorphic phantoms. The effect of field of view reduction and partial rotation was quantified (*Chapter 3*). The effective dose also served as input for the individual patient dose estimations in *Chapter 4* and the validation of the dose index defined in *Chapter 6*.

Chapter 4: Estimation and variability of individual patient doses was evaluated *in vivo* by measuring entrance skin doses for different patient groups (based on clinical indication and demographic parameters). The relation between patient size and mass, exposure factors, patient age and radiation risk from CBCT exposures was assessed.

Chapters 5 and 6: The development of a specific dose index for dental CBCT was investigated in a two-part study. Using thermoluminescent dosimeter grids in water and PMMA phantoms, the three-dimensional dose distribution from various CBCT geometries was visualized (*Chapter 5*). Two potential dose indices were defined and validated using ion chamber measurements in a custom PMMA phantom (*Chapter 6*), with a special focus on the conversion to effective dose.

PART II: Image quality

Chapter 7: A prototype phantom containing inserts for technical image quality analysis was developed, and its applicability for CBCT imaging was assessed. The second version of this QC phantom was used for the experiments in *Chapters 8 to 11*, each focusing on a specific image quality aspect by evaluating various parameters on a large number of CBCT scanners involving numerous exposure protocols.

Chapter 8: The quantification of metal artefacts on CBCT datasets was evaluated using titanium and lead rods. The aims were to define a suitable quantitative parameter, to apply this parameter on datasets from CBCT and MSCT devices, and to investigate the possibility of metal artefact reduction by adapting exposure parameters.

Chapter 9: Visual analysis of spatial and contrast resolution was performed using line pair and rod (*i.e.* contrast-detail) inserts. The suitability of a visual check for quality control and acceptance testing was assessed, and the influence of imaging parameters such as mAs and voxel size was evaluated.

Chapter 10: Contrast, noise and uniformity was assessed using materials of ranging densities as well as homogeneous PMMA. The performance range in terms of contrast and noise of CBCT was determined and compared with MSCT and the intra- and inter-scan uniformity and its influence on the variability of grey values was calculated.

Chapter 11: The variability of CBCT grey values was evaluated using MSCT as a reference for correlation and calibration of grey values for density estimations. Different evaluations were included to quantify the suitability of CBCT grey values for (bone) density estimations.

Chapter 12: The relationship between technical and diagnostic image quality for CBCT was investigated. Contrast and noise measurements were obtained from homogeneous PMMA and an observer study was performed by scoring anatomical and diagnostic parameters on scans from an anthropomorphic phantom, using a step-wise reduction in exposure for different CBCT devices. An additional aim was to determine thresholds for diagnostic image quality, and correlating them to technical image quality parameters.

The various chapters and topics address the following hypotheses:

- Effective dose values for CBCT range between those of 2-D radiography and MSCT (*Chapters 1, 2, 3*).

- Radiation risk will be higher for children due to the relatively larger exposes area, in combination with the increased radiation sensitivity at lower ages (*Chapters 2, 4*).

- Significant dose reduction can be achieved by reducing the FOV or by use of a partial rotation (*Chapter 3*).

- Individual patient doses in CBCT depend on the size and mass of the patient (*Chapter 4*).

- Dose distribution in CBCT is highly affected by the exposure geometry (FOV diameter and height, FOV position, rotation arc)(*Chapter 5*).

- A dose index for CBCT, which takes the varying dose distribution into account, can be defined and converted to effective dose (*Chapter 6*).

- An image quality phantom, which can be applied to all types of CBCT devices on the market, can be developed (*Chapter 7* and following).

- Metal artefacts on CBCT or MSCT images can be quantified and compared (*Chapter 8*).

- Image quality (spatial resolution, contrast detail) in CBCT can be evaluated visually by use of suitable test objects (*Chapter 9*).

- CBCT images generally have a good contrast resolution for high-contrast materials, a poor contrast resolution for low-contrast materials, and a high degree of noise. Furthermore, uniformity within or between scans can be poor (*Chapter 10*).

- CBCT grey values can be used for (bone) density estimations, similar to the use of Hounsfield Units in MSCT (*Chapter 11*).

- Technical image quality can be linked to diagnostic image quality, and thresholds for acceptable image quality can be determined based on technical parameters (*Chapter 12*).

Preface

This thesis is based on the following papers:

Chapter 1:

Pauwels R, Beinsberger J, Collaert B, Theodorakou C, Rogers J, Walker A, Cockmartin L, Bosmans H, Jacobs R, Bogaerts R, Horner K; The SEDENTEXCT Project Consortium. Effective dose range for dental cone beam computed tomography scanners. Eur J Radiol 2012; 81: 267-271.

Chapter 2:

Theodorakou C, Walker A, Horner K, Pauwels R, Bogaerts R, Jacobs R, The SEDENTEXCT Project Consortium. Estimation of paediatric organ and effective doses from dental cone beam computed tomography using anthropomorphic phantoms. Br J Radiol 2012; 85: 153-160.

Theodorakou C, Pauwels R, Walker A, Horner K, Bogaerts R. Estimation of organ and effective doses in paediatric dental radiology. *In preparation.*

Chapter 3:

Pauwels R, Theodorakou C, Walker A, Bosmans H, Jacobs R, Bogaerts, Horner K, The SEDENTEXCT Project Consortium. Dose reduction in CBCT through field of view reduction and 180° scanning. *Submitted.*

Chapter 4:

Pauwels R, Cockmartin L, Ivanauskaité D, Urbonienė A, Gavala S, Jacobs R, Bosmans H, Bogaerts R, Horner K, The SEDENTEXCT Project Consortium. In vivo patient dose of CBCT. *In preparation.*

Chapter 5:

Pauwels R, Theodorakou C, Walker A, Bosmans H, Jacobs R, Bogaerts R, Horner K, The SEDENTEXCT Project Consortium. Dose distribution for dental cone beam CT and its implication for defining a dose index. Dentomaxillofac Radiol. *In press.*

Chapter 6:

Pauwels R, Theodorakou C, Walker A, Bosmans H, Jacobs R, Bogaerts R, Horner K, The SEDENTEXCT Project Consortium. A new dose index for cone beam CT and its correlation with organ and effective dose. *In preparation.*

Chapter 7:

Pauwels R, Stamatakis H, Manousaridis G, Walker A, Michielsen K, Bosmans H, Bogaerts R, Jacobs R, Horner K, Tsiklakis K, The SEDENTEXCT Project Consortium. Development and applicability of a quality control phantom for dental cone-beam CT. J Appl Clin Med Phys. 2011; 12: 245-260.

Chapter 8:

Pauwels R, Stamatakis H, Bosmans H, Bogaerts R, Jacobs R, Horner K, Tsiklakis K, The SEDENTEXCT Project Consortium. Quantification of metal artefacts on cone beam computed tomography images. Clin Oral Implants Res. 2011; Epub ahead of print.

Chapter 9:

Pauwels R, Beinsberger J, Stamatakis H, Tsiklakis K, Walker A, Bosmans H, Bogaerts R, Jacobs R, Horner K, The SEDENTEXCT Project Consortium. Comparison of spatial and contrast resolution for cone beam computed tomography scanners. Oral Surg Oral Med Oral Pathol Oral Radiol Endod. *In press.*

Chapter 10:

Pauwels R, Stamatakis H, Tsiklakis K, Walker A, Avontroodt P, Bosmans H, Bogaerts R, Jacobs R, Horner K, The SEDENTEXCT Project Consortium. Contrast, noise and uniformity of cone beam CT images. *In preparation.*

Chapter 11:

Pauwels R, Nackaerts O, Bellaiche N, Stamatakis H, Tsiklakis K, Walker A, Bosmans H, Bogaerts R, Jacobs R, Horner K, The SEDENTEXCT Project Consortium. Accuracy of CBCT grey values for density estimations. *Submitted.*

Chapter 12:

Pauwels R, Stamatakis H, Tsiklakis K, Walker A, Avontroodt P, Bosmans H, Bogaerts R, Jacobs R, Horner K, The SEDENTEXCT Project Consortium. Technical versus diagnostic image quality in CBCT imaging. *In preparation.*

As this thesis was part of a multicentric project, the experimental work in certain chapters was shared with different partners within the SEDENTEXCT project. Part of the dose measurements in *Chapters 1, 2, 5 and 6* were performed by the University of Manchester. Part of the skin measurements in *Chapter 4* were performed by Vilnius University and the University of Athens. CT scans used in *Chapter 7* were acquired by the University of Athens. The PhD student had personal or shared responsibility for the set-up and analysis of all experimental measurements. He also contributed to various other tasks within the SEDENTEXCT project which are not part of the current thesis.

PART I: DOSIMETRY

Chapter 1: Organ and effective dose ranges for CBCT scanners

1.1 Abstract

Objective: To estimate the absorbed organ dose and effective dose for a wide range of cone beam computed tomography scanners, using different exposure protocols and geometries.
Materials and methods: Two Alderson Radiation Therapy anthropomorphic phantoms were loaded with LiF detectors (TLD-100 and TLD-100H) which were evenly distributed throughout the head and neck, covering all radiosensitive organs. Measurements were performed on 14 CBCT devices: 3D Accuitomo 170, GALILEOS Comfort, i-CAT Next Generation, ILUMA Elite, Kodak 9000 3D, Kodak 9500, NewTom VG, NewTom VGi, Pax-Uni3D, Picasso Trio, ProMax 3D, SCANORA 3D, SkyView, Veraviewepocs 3D. Effective dose was calculated using the ICRP 103 (2007) tissue weighting factors.
Results: Effective dose ranged between 19 and 368 μSv. The largest contributions to the effective dose were from the remainder tissues (37%), salivary glands (24%), and thyroid gland (21%). For all organs, there was a wide range of measured values apparent, due to differences in exposure factors, diameter and height of the primary beam, and positioning of the beam relative to the radiosensitive organs.
Conclusions: The effective dose for different CBCT devices showed a 20-fold range. The results show that a distinction is needed between small-, medium-, and large-field CBCT scanners and protocols, as they are applied to different indication groups, the dose received being strongly related to field size. Furthermore, the dose should always be considered relative to technical and diagnostic image quality, seeing that image quality requirements also differ for patient groups. The results from the current study indicate that the optimisation of dose should be performed by an appropriate selection of exposure parameters and field size, depending on the diagnostic requirements.

1.2 Introduction

In recent years, the number of CBCT devices available on the market has increased substantially and new models are being developed and released on a continuous basis. These devices exhibit a wide variability in terms of crucial exposure parameters such as the X-ray

spectrum (voltage peak and filtration), X-ray exposure (mA and number of projections) and volume of the exposed field [1]. Also, many devices allow a degree of versatility regarding the exposure, allowing the operator to select certain exposure parameters. It is clear that the range of devices and imaging protocols that are available will result in different absorbed radiation doses for the patient with, to some extent, the amount of dose being reflected in the image quality of the scan. Radiation dose and image quality, together with the size of the field of view (FOV), determine whether or not a certain CBCT imaging protocol from a given device is suitable for a specific dental application by following the generally applied ALARA (As Low As Reasonably Achievable) principle of radiation exposure [2-3].

To measure the radiation risk for patients from a radiographic modality, the effective dose is still accepted as the most suitable figure of merit, even though alternatives are under consideration [4-7]. The effective dose is measured in practice using an anthropomorphic phantom, representing the shape and attenuation of an average human, most commonly an adult male [8]. There have been a number of studies measuring the effective dose on dental CBCT using thermoluminescent dosimeters (TLDs) in combination with a human phantom [9-19]. These studies provide some estimation of the range of doses that are obtained from these devices, but are not comparable, seeing that different types of phantoms are used as well as different TLD positioning schemes, with the number of TLDs applied to the different organs often being too low for an accurate and reproducible estimation of the organ and effective doses [11-18].

The aim of the current study was to perform a broad evaluation of the organ and effective doses obtained from CBCT, using a wide range of devices and imaging protocols.

1.3 Materials and methods

To estimate the effective dose for an average adult male, two similar types of anthropomorphic male Alderson Radiation Therapy (ART) phantoms (Radiology Support Devices Inc., CA, USA) were used (Figure 1.1). They represent an average man (175 cm tall, 73.5 kg) and consist of a polymer mould simulating the bone, embedded in soft tissue equivalent material. They are transsected into 2.5 cm thick slices, each containing a grid for TLD placement. The upper 11 slices (*i.e.* head and neck region) were used for TLD measurements, seeing that there is no significant dose found in the lower parts for dental examinations [19].

Figure 1.1 Alderson radiation therapy phantom, head and neck portion

The phantoms were scanned on a variety of available CBCT devices, combining different exposure protocols when possible. The phantoms were positioned as closely as possible to a typical patient with the help of local radiographic staff using the positioning aids provided for the scanner. The following CBCT devices were included: 3D Accuitomo 170, GALILEOS Comfort, i-CAT Next Generation, ILUMA Elite, Kodak 9000 3D, Kodak 9500, NewTom VG, NewTom VGi, Pax-Uni3D, Picasso Trio, ProMax 3D, SCANORA 3D, SkyView, Veraviewepocs 3D. Device parameters for different protocols that were included are given in Table 1.1.

Two types of TLDs were used for the measurements: TLD-100 (LiF:Mg,Ti) and TLD-100H (LiF:Mg,Cu,P). Calibration of the TLD-100H was performed free in air against an ionisation chamber with calibration traceable to national standards (National Physical Laboratory, London, UK), using a conventional diagnostic X-ray tube at 80 kVp. The chips were read using a Harshaw 5500 automatic TLD reader. Calibration of the TLD-100 was performed by irradiating internal calibration dosimeters for each experiment using a ^{90}Sr source. The source itself was calibrated using an ionisation chamber with a calibration factor traceable to a Secondary Standard Dosimetry Laboratory (SSDL, Gent, Belgium). The read-out of the TLDs was performed by a Harshaw 6600 reader. The total uncertainty of the TLD measurement procedure was estimated, taking into account all possible sources of uncertainty: TLD-related (batch inhomogeneity, energy dependence, linearity of response), reader-related or calibration-related (internal and external calibration factor). The total multiplicative uncertainty from these factors was estimated at 9%. A final source for uncertainty, with an absolute effect rather than a percentual one, is the residual TLD signal which ranges between 0 and 100 μGy. The effect of this residual signal was kept as low as possible by increasing the

obtained signal through repeated exposures, and by subtracting average residual values using non-irradiated background TLDs.

For each slice, placement of the TLDs was carefully considered with input from dental radiologists to ensure that there was an even spread over the different radiosensitive organs. Due to small differences between the two phantoms, TLD positioning was determined for each phantom separately. In total, 147 TLDs were used for one phantom and 152 for the other.

Two intercomparisons were performed to ensure that the variability between measurements performed on the two phantoms using different TLD types and positioning was within an acceptable range. Differences between TLD types were investigated, and identical exposures were applied to the two phantoms using one TLD type. Based on the results of the intercomparison, it was not deemed necessary to apply a correction factor.

The following calculation was used to determine the equivalent dose or radiation weighted dose H_T for all organs or tissues T:

$$H_T = w_R \, \Sigma_i \, f_i \, D_{Ti}$$

In this formula, w_R is the radiation weighting factor (being 1 for X-rays), f_i the fraction of tissue T in slice i, and D_{Ti} the average absorbed dose of tissue T in slice i, the summation being over all slices. For the brain, salivary glands, thyroid gland, oral mucosa and extrathoracic airways, calculation of H_T was straightforward since these organs are found completely within the head and neck. For bone and skin, the organ fractions reported by Huda *et al.* were used [8]. For muscle and lymph nodes, it was estimated that 5% of these organs are found within the head and neck, and an overall fraction of 0.05 was applied [16].

In order to calculate the contribution E_T of each organ to the effective dose, the organ radiation weighted dose is multiplied by the tissue weighting factor w_T, which expresses the contribution of this tissue to the overall radiation detriment from stochastic effects:

$$E_T = w_T \, H_T$$

The tissue weighting factors that are defined in the latest recommendations of the International Commission on Radiological Protection were applied (Table 1.2)[4]. The effective dose is calculated by taking the sum of the contribution E_T for all relevant organs as

shown in Table 2. The oesophagus was originally included in the calculation, but it was found that this organ does not provide a significant contribution to the effective dose.

Table 1.1 Technical parameters of CBCT devices

CBCT	Manufacturer	Protocol	FOV (cm)	Voltage (kVp)	mAs
3D Accuitomo 170	J. Morita Kyoto, Japan	Maxilla	10x5	90	87.5
		Lower jaw molar region	4x4	90	87.5
Galileos Comfort	Sirona Dental Systems Bensheim, Germany	Maxillofacial	15x15	85	28
I-CAT Next Generation	Imaging Sciences Int. Hatfield, PA, USA	Maxillofacial	16x13	120	18.5
		Mandible	16x6	120	18.5
ILUMA Elite	Imtec (3M) Ardmore, OK, USA	Maxillofacial	21x14	120	76
Kodak 9000 3D	Carestream Health Rochester, NY, USA	Upper jaw front region	5x3.7	70	107
		Lower jaw molar region	5x3.7	70	107
Kodak 9500	Carestream Health, Rochester, NY, USA	Maxillofacial	20x18	90	108
		Dentoalveolar	15x8	90	108
NewTom VG	Quantitative Radiology Verona, Italy	Maxillofacial	23x23	110	10.4
NewTom VGi	Quantitative Radiology Verona, Italy	Maxillofacial	15x15	110	8.8
		Dentoalveolar	12x8	110	43
PaX-Uni3D	VATECH Yongin, Rep. of Korea	Upper jaw front region	5x5	85	120
Picasso Trio	VATECH Yongin, Rep. of Korea	Dentoalveolar standard dose	12x7	85	127
		Dentoalveolar low dose			91
ProMax 3D	Planmeca Oy Helsinki, Finland	Dentoalveolar standard dose	8x8	84	169
		Dentoalveolar low dose			19.9
SCANORA 3D	Soredex Tuusula, Finland	Dentoalveolar	10x7.5	85	30
		Mandible	10x7.5		30
		Maxilla	10x7.5		30
		Maxillofacial	14.5x13.5		48
SkyView	MyRay Imola, Italy	Maxillofacial	17x17	90	51.5
Veraviewepocs 3D	J. Morita Kyoto, Japan	Dentoalveolar	8x8	70	51

As an additional evaluation, organ doses for red bone marrow, thyroid, salivary glands and remainder organs were recalculated using a limited number of selected TLDs, hereby mimicking the positioning protocol used by Ludlow *et al*. [12] which has been adapted by other authors [11,16,18]. Using this protocol, 24 TLDs are used for effective dose calculation.

The average and maximum variability between organ dose estimations using the two methods was calculated.

Table 1.2 ICRP 103 (2007) Tissue weighting factors

Organ or tissue	Weighting factor	Number of TLDs used
Gonads	0.08	/
Red bone marrow[a]	0.12	33[c]
Colon	0.12	/
Lung	0.12	/
Stomach	0.12	/
Bladder	0.04	/
Breast	0.12	/
Liver	0.04	/
Oesophagus	0.04	/
Thyroid[a]	0.04	7
Skin[a]	0.01	31
Bone surface[a]	0.01	36[c]
Brain[a]	0.01	27
Salivary glands[a]	0.01	17
Remainder[a,b]	0.12	27[c]

[a]Head and neck or whole body organ, included in current study
[b]Adipose tissue, Adrenals, Extrathoracic (ET) region, Gall bladder, Heart, Kidneys, Lymphatic nodes, Muscle, Oral mucosa, Pancreas, Prostate, Small intestine, Spleen, Thymus, Uterus/cervix.
[c]Including TLD locations for multiple purposes (*e.g.* bone marrow and bone surface)

1.4 Results

Due to the large differences in acquired volume, which is one of the main determinants of the effective dose, the results were split up by dividing the CBCT devices into three categories: large FOV (maxillofacial), medium FOV (dentoalveolar) and small FOV (localised). This allows for a fairer comparison between protocols, as different FOV sizes are used for different subsets of patients. It should be noted that some devices allow for a range of field sizes, and can therefore be found in more than one category, thereby widening their application range.

Table 1.3 gives the absorbed organ doses and effective dose for large FOV protocols. The effective dose ranged between 68 and 368 μSv. The highest absorbed dose was in the salivary glands, although the largest contribution to the effective dose was provided by the remainder tissue due to its higher weighting factor.

Table 1.3 Absorbed organ dose (µGy) and effective dose (µSv) for large FOV (maxillofacial) protocols

	Galileos	i-CAT N.G.	ILUMA Elite	Kodak 9500	NewTom VG	NewTom VGi	SCANORA 3D	SkyView
RBM	82	116	660	206	115	186	86	134
Thyroid	380	355	1230	585	354	2045	296	474
Skin	55	54	277	92	50	98	55	58
Bone surface	83	124	667	215	163	184	94	125
Salivary glands	2104	1830	7225	2676	1690	2855	1568	1582
Brain	124	375	3415	1205	251	605	255	719
Remainder	292	260	1034	380	281	436	221	224
Effective dose	84	83	368	136	83	194	68	87

Dose measurements from medium FOV protocols are shown in Table 1.4, showing effective doses between 28 and 265 µSv. Compared with the results from the large field protocols, organ doses were distributed similarly, although it is seen that the contribution of the brain was lower.

Table 1.5 shows the results for the small FOV protocols. The effective dose ranged between 19 and 44 µSv. From these results, the effect of FOV positioning can be observed. Comparing an upper jaw, frontal region with a lower jaw, molar region scan from the Kodak 9000 3D, it is seen that there were large differences regarding the absorbed dose for the salivary glands, thyroid gland, oral mucosa and extrathoracic airways.

The average doses for all devices for each FOV group are shown in Figure 1.2. The average doses for large, medium and small FOVs were 131, 88 and 34 µSv respectively. The standard deviations were 91 (70% of mean), 70 (83%) and 14 (37%), showing large variability of doses for large and medium FOV groups.

Figure 1.3 illustrates the average contribution of each of the measured organs to the effective dose. The remainder organs had the highest contribution, followed by the salivary glands and thyroid gland. Contributions of brain, bone surface and skin were almost negligible. No notable differences were seen when comparing the contributions for small, medium and large FOVs separately.

Table 1.4 Absorbed organ dose (µGy) and effective dose (µSv) for medium FOV protocols

	3D Accuitomo 170	i-CAT N.G.	Kodak 9500	NewTom VGi	Picasso Trio		ProMax 3D		SCANORA 3D			Veraviewepocs 3D
Protocol[a]	Upper jaw				High dose	Low dose	High dose	Low dose	Upper jaw	Lower jaw	Both jaws	
Red bone marrow	112	33	85	294	126	62	88	27	42	34	37	55
Thyroid	148	251	541	1293	551	583	1021	202	148	352	240	330
Skin	62	25	51	145	113	56	145	15	30	29	31	69
Bone surface	112	33	84	299	156	57	121	26	50	35	39	57
Salivary glands	2138	973	2166	6372	2982	1837	2576	596	1285	1052	1117	1956
Brain	189	46	91	431	134	39	53	28	45	25	31	40
Remainder	85	172	304	881	432	254	346	83	178	147	155	267
Effective dose	54	45	92	265	123	81	122	28	46	47	45	73

[a]If not specified, the positioning of the FOV is dentoalveolar (both jaws)

Table 1.5 Absorbed organ dose (µGy) and effective dose (µSv) for small FOV (localised) protocols

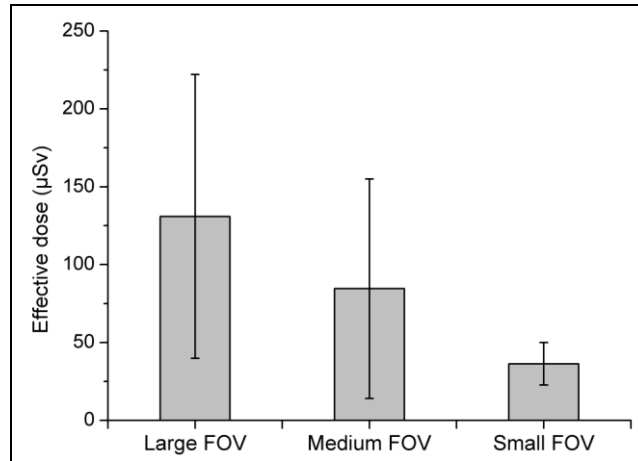|	3D Accuitomo 170	Kodak 9000 3D	Kodak 9000 3D	Pax-Uni3D
FOV positioning	Lower jaw, molar region	Upper jaw, front region	Lower jaw, molar region	Upper jaw, front region
Red bone marrow	37	21	78	47
Thyroid	195	30	251	209
Skin	32	25	24	55
Bone surface	37	27	35	49
Salivary glands	2120	523	709	1073
Brain	37	18	290	28
Remainder	70	74	86	146
Effective dose	43	19	40	44

Figure 1.2 Average effective dose for CBCT devices, divided into groups based on field of view size. Standard deviations are shown for each group.
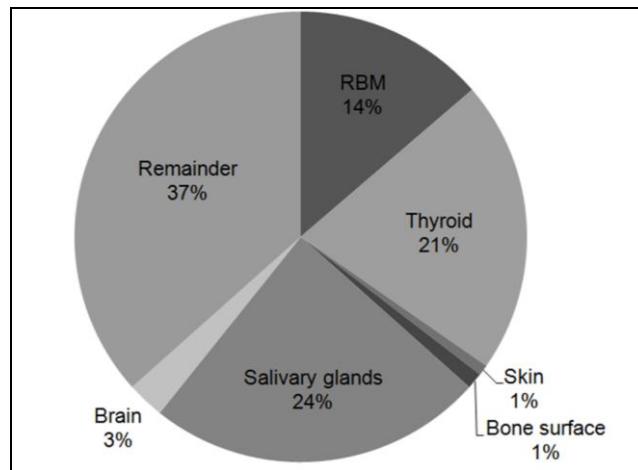

Figure 1.3 Average contributions of organs to effective dose.

Variability between organ doses estimations using the current TLD positioning, and recalculations using the positioning protocol devised by Ludlow *et al.* [16] are shown in Table 1.6. The largest deviations were seen for small FOV protocols, showing particularly high deviations for the salivary glands and remainder tissues. As seen in Figure 1.3, the four organs that were selected for dose recalculation comprise 95% of the effective dose.

Table 1.6 Variability of organ dose calculations using a low number of TLDs

Organ	Average deviation (%)	Maximum deviation (%)
Red bone marrow	21	40
Thyroid	18	26
Salivary glands	28	76
Remainder	25	80

Finally, an alternative recalculation of the effective doses was performed using 64 strategically selected TLD locations. 6 TLD locations were selected for skin, 7 for brain to 27 for bone. All TLDs for salivary glands, thyroid and remainder were withheld. The average variability of the recalculated effective doses was 0.6% with a maximum deviation of 1.2%.

1.5 Discussion

In the present study, effective dose estimations were performed on a wide range of dental CBCT devices, investigating the difference in dose due to variability in FOV size, tube output and exposure factors.

A large number of TLDs was used to ensure that the measurement was as accurate as possible. The TLDs were positioned throughout the head and neck to correctly cover all radiosensitive organs. By performing measurements on a large number of CBCT devices, differences in dose between the different CBCTs cold reliably be determined. Comparing these results with previous studies should be done with caution, as previous studies have used other phantoms and different numbers and positioning of TLDs, often using too few TLDs for an accurate measurement [11-18,20-21]. It must be stressed that for this type of dose measurement, the only way to estimate precisely the absorbed dose for any organ is to use TLDs at as many locations as possible for this organ, because the absorbed dose is an average dose. This is of particular concern in dental CBCT. Due to the large range of FOV sizes and the different possible positioning of this FOV within the dentomaxillofacial region, the position of the primary beam is variable, and each single location in the vicinity of the scanned region can show large variability depending on its relative position to the isocentre. This is shown by the different protocols for the SCANORA 3D; by changing the position of the FOV a few cm to move from a lower jaw to a dentoalveolar or an upper jaw examination, large differences are seen for individual TLD values. However, in the current study, these single TLDs have limited effect on the effective dose, seeing that only the thyroid dose changes significantly. Using a limited number of TLDs may underestimate or overestimate this kind of change in positioning. By recalculating the organ doses presented in this study, it was seen that organ dose estimations using a low number of TLDs can deviate 18-28% with differences up to 80%. These values indicate that a large number of TLDs is needed for accurate effective dose estimation, in particular for thyroid, salivary glands and remainder tissues.

From the results, it is seen that a single average effective dose is not a concept that should be used for the modality of CBCT as a whole, when comparing to alternative radiographic methods such as panoramic, intra-oral radiography and multislice CT (MSCT). The range of doses between the devices is too large to consider them as a single modality; even though the geometry of the image acquisition is basically the same, the differences in collimation of the cone beam, as well as the X-ray exposure factors, lead to considerable differences in absorbed dose for all organs in the head and neck region. However, a general conclusion based on the presented values is that the effective dose from most devices is found in the 20-100 μSv range, being higher than doses for 2-D radiographic methods used in dentistry but well below reported doses for common MSCT protocols [9-12,19-22]. Some devices show an elevated dose due to relatively high kV and mAs settings combined with a large FOV, attaining a dose range comparable with low-dose MSCT protocols [19].

The results should be interpreted carefully, due to the interplay between image quality, size of the scanned volume and absorbed radiation dose to different tissues. Therefore, the main goal of the study was not to compare the performance of different CBCT devices, as this cannot be done based on dosimetric results alone. Different studies have already pointed out that CBCT devices can have different application ranges, based on their maximum FOV size, collimation options, and diagnostic image quality [1,3,9,12,17]. Therefore, the radiation dose from these devices can be seen as a function of the diagnostic application. From that perspective, a key paradigm for dose optimisation is to ensure that patient scans are made using an exposure protocol which leads to an acceptable image for their specific indication [2,3]. The two key factors for an acceptable image are an appropriate size and positioning of the FOV and an acceptable quality of the reconstructed image. The only distinction made between the devices within this study was based on the size of the FOV, as this is a main determinant of possible diagnostic applications (Chapter 3). Further study is required to bring the image quality into play, on a technical and diagnostic level. By investigating technical image quality, the relation between the exposure from CBCT devices and the image quality performance in terms of noise, sharpness, contrast and artefacts, can be quantified (Chapters 7-11); diagnostic quality studies would link all quantifications of dose of image quality to performance evaluation on a clinical level (Chapter 12).

1.6 Conclusion

The effective dose for different CBCT devices showed a 20-fold range. The results show that a distinction is needed between small-, medium-, and large-field CBCT scanners and protocols, as they are applied to different indication groups, the dose received being strongly related to field size. Furthermore, the dose should always be considered relative to technical and diagnostic image quality, seeing that image quality requirements also differ for patient groups. The results from the current study indicate that the optimisation of dose should be performed by an appropriate selection of exposure parameters and field size, depending on the diagnostic requirements.

1.7 References

1. Scarfe WC, Farman AG, Sukovic P. Clinical applications of cone-beam computed tomography in dental practice. J Can Dent Assoc 2006; 72: 75–85.

2. Martin CJ, Sutton DG, Sharp PF. Balancing patient dose and image quality. Appl Radiat Isot 1999; 50: 1–19.

3. Farman AG. ALARA still applies. Oral Surg Oral Med Oral Pathol Oral Radiol Endod 2005; 100: 395–397.

4. International Commission on Radiological Protection. Recommendations of the International Commission on Radiological Protection. ICRP Publication 103. Ann ICRP 37. Oxford, UK: Pergamon Press, 2007.

5. Martin CJ. Effective dose: how should it be applied to medical exposures? Br J Radiol 2007; 80: 639–647.

6. Brenner DJ. Effective dose: a flawed concept that could and should be replaced. Br J Radiol 2008; 81: 521-523.

7. Thilander-Klang A, Helmrot E. Methods of determining the effective dose in dental radiology. Radiat Prot Dosimetry 2010; 139: 306-309.

8. Huda W, Sandison GA. Estimation of mean organ doses in diagnostic radiology from Rando phantom measurements. Health Phys 1984; 47: 463–467.

9. Loubele M, Bogaerts R, Van Dijck E, *et al.* Comparison between effective radiation dose of CBCT and MSCT scanners for dentomaxillofacial applications. Eur J Radiol 2009; 71: 461-468.

10. Okano T, Harata Y, Sugihara Y, *et al.* Absorbed and effective doses from cone beam volumetric imaging for implant planning. Dentomaxillofac Radiol 2009; 38: 79-85.

11. Suomalainen A, Kiljunen T, Käser Y, Peltola J, Kortesniemi M. Dosimetry and image quality of four dental cone beam computed tomography scanners compared with multislice computed tomography scanners. Dentomaxillofac Radiol 2009; 38: 367-78.

12. Ludlow JB, Ivanovic M. Comparative dosimetry of dental CBCT devices and 64-slice CT for oral and maxillofacial radiology. Oral Surg Oral Med Oral Pathol Oral Radiol Endod 2008; 106: 106-114.

13. Silva MA, Wolf U, Heinicke F, Bumann A, Visser H, Hirsch E. Cone-beam computed tomography for routine orthodontic treatment planning: a radiation dose evaluation. Am J Orthod Dentofacial Orthop 2008; 133: 640.e1-5.

14. Ludlow JB, Davies-Ludlow LE, Brooks SL, Howerton WB. Dosimetry of 3 CBCT devices for oral and maxillofacial radiology: CB Mercuray NewTom 3G and i-CAT. Dentomaxillofac Radiol 2006; 35: 219–226.

15. Tsiklakis K, Donta C, Gavala S, Karayianni K, Kamenopoulou V, Hourdakis CJ. Dose reduction in maxillofacial imaging using low dose Cone Beam CT. Eur J Radiol 2005; 56: 413–417

16. Roberts JA, Drage NA, Davies J, Thomas DW. Effective dose from cone beam CT examinations in dentistry. Br J Radiol 2009; 82: 35-40.

17. Hirsch E, Wolf U, Heinicke F, Silva MA. Dosimetry of the cone beam computed tomography Veraviewepocs 3D compared with the 3D Accuitomo in different fields of view. Dentomaxillofac Radiol 2008; 37: 268-273.

18. Mah JK, Danforth RA, Bumann A, Hatcher D. Radiation absorbed in maxillofacial imaging with a new dental computed tomography device. Oral Surg Oral Med Oral Pathol Oral Radiol Endod 2003; 96: 508-513.

19. Loubele M, Jacobs R, Maes F, *et al*. Radiation dose vs. image quality for low-dose CT protocols of the head for maxillofacial surgery and oral implant planning. Radiat Prot Dosimetry 2006; 117: 211–216.

20. Ngan DC, Kharbanda OP, Geenty JP, Darendeliler MA. Comparison of radiation levels from computed tomography and conventional dental radiographs. Aust Orthod J 2003; 19: 67-75.

21. Ludlow JB, Davies-Ludlow LE, White SC. Patient risk related to common dental radiographic examinations: the impact of 2007 International Commission on Radiological Protection recommendations regarding dose calculation. J Am Dent Assoc 2008; 139: 1237-1243.

22. Gijbels F, Jacobs R, Bogaerts R, Debaveye D, Verlinden S, Sanderink G. Dosimetry of digital panoramic imaging Part I: patient exposure. Dentomaxillofac Radiol 2005; 34: 145–149.

Chapter 2: Estimation of paediatric organ and effective doses from CBCT

2.1 Abstract

Objectives: To estimate organ and effective doses from CBCT exposures using paediatric phantoms, and to compare dose levels with conventional dental radiographic techniques and MSCT.

Materials and methods: Thermoluminescent dosimeters were attached to a 10-year-old and adolescent anthropomorphic phantom. Measurements were made with eight CBCT units for a range of imaging protocols, along with a MSCT device and a panoramic and cephalometric unit. Organ and effective doses were calculated using ICRP 103 weighting factors.

Results: Effective doses for CBCT ranged between 16 μSv and 282 μSv for the 10-year-old and between 18 μSv and 216 μSv for the adolescent phantoms, which is similar to adult dose ranges. Effective doses for the 10 year old and adolescent phantoms were 10 μSv and 6 μSv for panoramic radiography, 2 μSv and 1 μSv for cephalometry, and 605 μSv and 1047 μSv for MSCT. The salivary glands received the highest absorbed organ dose. There was a clear increase in the thyroid dose of the 10-year-old relative to that of the adolescent. The remainder tissues and salivary and thyroid glands contributed most significantly to the effective dose for a 10-year-old, whereas for an adolescent the remainder tissues and the salivary glands contributed the most.

Conclusion: It is of particular importance for young children to justify the use of dental CBCT over conventional X-ray imaging, and to optimise doses through mAs reduction and field of view collimation.

2.2 Introduction

Since its introduction, CBCT has notably altered the radiographic approach for children in dental practice. Because of their higher sensitivity for radiation, children were usually not subjected to CT scanning, unless it was fully justified. However, as CBCT has been advertised as a low-dose alternative to MSCT, the restraint of applying it to children was

overcome, and it is now routinely applied to children of various ages for different purposes: impacted teeth, other orthodontic purposes, trauma, and developmental disorders.

However, given the wide dose range presented in Chapter 1 and reported by various authors [1-11], it is crucial to reduce and optimise CBCT doses for children in particular. With a few exceptions, effective doses for CBCT are higher than those of 2-D radiographic techniques. Furthermore, low-dose MSCT protocols are able to achieve similar dose levels as certain CBCT exposure levels [1-4].

When estimating the actual radiation dose or risk for paediatric patients, there are a few considerations that need to be taken into account. Regarding the experimental measurement of absorbed doses in anthropomorphic phantoms, it is clear that existing dose reports are only applicable to adult patients. Furthermore, even within the adult patient populations, large deviations in dose uptake can occur because of variations in size, mass and anatomy. For paediatric patients, the main difference in absorbed dose will originate from the difference in the relative exposed area, as this is a crucial determinant of organ and effective dose (Chapters 1 and 3). A second consideration for paediatric dose assessments is that children are more sensitive to radiation than adults because of the higher number of dividing cells, which are sensitive to DNA mutagenesis. Furthermore, they have a longer time window to express stochastic radiation-induced effects. There is an order of magnitude increase in cancer risk between children and adults, and there is also a significant difference between young males and females, with the latter being more radiosensitive [12,13].

The aim of this study was to measure paediatric organ doses and effective doses using two anthropomorphic phantoms and TLDs for a range of CBCT units, and to compare dose levels with MSCT, panoramic radiography and cephalometry.

2.3 Materials and methods

Anthropomorphic phantoms

Two tissue-equivalent anthropomorphic phantoms (ATOM Model 702-C and ATOM Model 706-C; Computerized Imaging Reference Systems Inc, Norfolk, VA) were used, representing a 10-year old child and an adult female (Figure 2.1). The ATOM phantoms are transsected in 25mm slices, allowing for the placement of dosimeters. For this study the head, neck and shoulders of both phantoms were used. The female phantom closely represents an adolescent patient, according the ICRP 89 [14] report. The reference values in ICRP 89 for body height

for a 15-year-old male and female are 167 cm and 161 cm, respectively, compared with 160 cm for the female ATOM phantom. The weight of the female ATOM phantom is 55 kg compared with reference weight values of 56 kg and 53 kg for a 15-year-old male and female. The design of the phantoms was based on ICRP 23 [15] and ICRU 48 [16] and other available anatomical reference data. The tissues simulated in the ATOM phantoms are average bone, soft tissue, cartilage, spinal cord, spinal disks, lung, brain, sinus, trachea and bronchial cavities. The density of the simulated paediatric bone is adjusted to the represented age, and is an average of known cortical-to-trabecular ratios and age-based mineral densities.

Figure 2.1 Paediatric ATOM phantom model 702-C (left) and 706-C (right).

Thermoluminescent dosimeters

All dose measurements were performed using TLD-100 and TLD-100H chips (Harshaw Thermo Fisher Scientific Inc, Waltham, MA). Calibration procedures are detailed in Chapter 1. The chips were read using an automatic TLD reader (Harshaw 5500 and 6600; Harshaw Thermo Fisher Scientific Inc, Waltham, MA). A minimum of five TLDs were used for measuring the background signal. For the adolescent phantom, 140 TLDs were distributed throughout the head and neck. For the 10 year old phantom, 104 TLDs were used.

Organ and effective dose estimation

Organ and effective dose estimations were performed similarly to the adult phantom study in Chapter 1 by following the ICRP 103 recommendations, as the tissue weighting factors are sex- and age-averaged [17]. The absorbed dose to the salivary and thyroid glands, brain, red bone marrow, bone surface, oral mucosa, extrathoracic airway, lymph nodes, and muscle was measured. The bone surface dose was assumed to be equal to the red bone marrow dose. A few assumptions were made regarding the remainder tissues (*i.e.* oral mucosa, extrathoracic

airway, lymph nodes and muscle). Following ICRP 66 [18] along with previous studies [3-6], it was assumed that the dose to the oral mucosa equals the dose to the salivary glands; the dose to the lymph nodes and muscle equals the average dose to the thyroid gland, submandibular and parotid glands; and the dose to the extrathoracic airway equals the average dose to the thyroid gland, salivary glands, and bone marrow located at the anterior nasal cavity.

For organs not completely situated within the head and neck area, organ fractions were applied, following previous studies and the calculation method in Chapter 1. For skin, bone and red bone marrow, slice-specific organ fractions were applied to the average doses in each phantom slice, using fraction values from Huda *et al*. [20]. For the remainder tissues, it was assumed that 5% of the lymph nodes and muscle are located in the head and neck region [3].

Exposure protocols

Eight CBCT units were included. Table 2.1 lists the devices with exposure parameters for the imaging protocols applied in this study. A selection of clinically relevant imaging protocols was made with ranging FOV sizes and positions. kVp and mAs values were set according to the clinical situation, selecting paediatric exposure protocols when possible. The scanned region of interest was the same for the two phantoms for each exposure protocol, with the exception of small FOVs. For the 10-year-old phantom, small FOVs were focused on the maxillary anterior area, reflecting the use of imaging in orthodontic examinations of tooth eruption abnormalities in this area. For the adolescent phantom, the third molar area was included to reflect the increasing clinical use of three-dimensional imaging of this area. It should be noted that certain devices did not allow for the field of view (FOV) to be reduced to these regions of interest. For these devices, a large FOV was applied which reflects different clinical indications which require the full dentomaxillofacial region (orthodontic or other patients requiring maxillofacial surgery). For two devices, a medium-sized FOV was included, containing the teeth and associated structures of both jaws. Both phantoms were positioned as patients with the aid of the machines' alignment tools, such as lasers and scout images, ensuring reproducibility in phantom position. In addition, the paediatric phantoms were exposed using a MSCT device (Somatom Sensation 64, Siemens, Erlangen, Germany) using the exposure protocols listed in Table 2.1 A large, maxillofacial FOV size was selected, in correspondence with the large FOVs which was selected for certain CBCTs. For the 10 year old phantom, a child exposure protocol was applied, for the adolescent phantom a standard adult exposure was selected. Finally, panoramic and cephalometric exposures were

included using the Veraviewepocs 2D (J. Morita, Kyoto Japan) using standard exposure settings.

2.4 Results

Tables 2.1 and 2.2 show the calculated organ and effective doses calculated for the 10 year old and adolescent phantoms, respectively. Regarding CBCT, effective doses for the 10-year-old phantom ranged between 16 µSv and 282 µSv; for the adolescent phantom, effective doses were between 18 µSv and 216 µSv. For the large FOV protocols, effective doses were between 70 µSv and 282 µSv for the 10 year old phantom and between 71 µSv and 216 µSv for the adolescent phantom. For small fields of view, the highest effective dose was 28 µSv for the 10 year old phantom and 32 µSv for the adolescent phantom.

The salivary glands received the highest absorbed organ dose. There was a clear increase in the thyroid dose of the 10 year old phantom relative to that of the adolescent. The remainder tissues and salivary and thyroid glands contributed most significantly to the effective dose for a 10 year old, whereas for an adolescent the remainder tissues and the salivary glands contributed the most.

Effective doses for the 10 year old and adolescent phantoms were 10 µSv and 6 µSv for panoramic radiography, 2 µSv and 1 µSv for cephalometry, and 605 µSv and 1047 µSv for MSCT, respectively.

2.5 Discussion

In general, effective doses for the 10 year old phantom were higher than those of the adolescent phantom, when the same FOV size and position was applied. The larger relative exposed area for the 10 year old phantom overcompensated for the slight increase in absorption along the beam path for the adolescent phantom. However, there are a few notable exceptions, in which the exposure was adjusted either automatically or by following clinical exposure protocols. The clearest example is the MSCT, for which there was a considerable difference in dose between the phantoms. Following clinical guidelines for the MSCT, an adult exposure setting was applied to the adolescent phantom, whereas a low-dose exposure with kVp and mAs reduction was used for the 10 year old phantom. Furthermore, the relative FOV size was the same for both phantoms, as it could be manually collimated to contain the same anatomical region. Another example is the GALILEOS Comfort, for which a total of six

mAs options are available, which are selected manually depending on patient size. The lower mAs for the 10 year old phantom compensated for the relatively larger exposed area which was due to the fixed FOV size.

Even though most devices enable the selection of different exposure levels for patient of varying sizes, the results from the various CBCT devices and exposure protocols point out the importance of FOV selection. Similar to Chapter 1, three types of FOV sizes were included, covering different clinical indications. Small fields of view (*i.e.* <5x5 cm) allow for the scanning of a localized region, and could be suited for the scanning of impacted teeth (third molars, maxillary canines …), root problems, single implant sites or other indications. Medium fields of view (<10x10 cm) allow for the scanning of both dental arches, covering a wider array of indications. Another type of field of view, which could also be considered as medium-sized, has an extended diameter but is limited in height (*e.g.* 14x5 cm). This kind of FOV could be applied for scanning of third molars, temporomandibular joints or temporal bone providing that the left and right side of the patients are required; if not, a small FOV would suffice. Large fields of view are able to cover most of the anterior skull, and could be used for maxillofacial surgery planning, orthodontics, sinus evaluation, and other indications.

Along with Chapters 1 and 3, this study indicates that significant dose reduction could be achieved if the FOV could always be collimated depending on the clinical indication. This is accentuated by the current results, when looking at the difference in dose between the two phantoms in function of the FOV size. For those FOVs that could be considered as small or medium, effective doses for the two phantoms were similar if the anatomical position was the same. For large FOVs, this difference was clearer, at least when the difference in mAs for certain scanners is taken into account.

Table 2.1 Exposure parameters, absorbed organ doses (µGy) and effective dose (µSv) for the 10 year old phantom

Device	kVp	mAs	FOV	Position	RBM	Bone surface	Thyroid	Salivary glands	Remainder	Brain	Skin	Effective dose
i-CAT N.G.	120	18.5	16x6	Mandible	45	45	386	1584	210	78	30	63
i-CAT N.G.	120	18.5	16x6	Maxilla	86	85	190	1021	89	285	36	43
i-CAT N.G.	120	18.5	16x13	Maxillofacial	131	129	1398	1945	289	586	67	134
NewTom VG	110	Auto	15x11	Maxillofacial	103	103	1131	1901	273	327	52	114
Kodak 9000 3D	70	106.8	5x3.7	Maxilla anterior	51	51	43	273	30	33	72	16
ProMax 3D	84	19.6	8x8	Dentoalveolar	30	30	130	583	69	59	38	24
3D Accuitomo 170	90	87.5	17x12	Maxillofacial	381	377	1332	5949	763	2287	512	282
3D Accuitomo 170	90	87.5	14x10	Maxillofacial	309	306	943	5547	704	1503	411	237
3D Accuitomo 170	90	87.5	14x5	Mandible	138	135	1014	5858	778	166	240	214
3D Accuitomo 170	90	87.5	4x4	Maxilla anterior	82	82	90	546	58	78	76	28
GALILEOS Comfort	85	21	15x15	Maxillofacial	62	62	414	1668	210	305	46	70
SCANORA 3D	85	30	10x7.5	Dentoalveolar	42	42	41	1783	234	91	41	67
SCANORA 3D	85	48	14.5x13.5	Maxillofacial	113	113	383	1790	238	728	75	85
SkyView 3D	90	51.5	17x17	Maxillofacial	138	138	1054	1344	197	760	65	105
Somatom Sensation 64	100	80[a]	20x11.7	Maxillofacial	800	800	5963	7031	1086	5899	297	605
Veraviewepocs 2D Pano	61	48	N/A	N/A	3	3	36	326	38	10	7	10
Veraviewepocs 2D Ceph	80	44.6	N/A	N/A	2	2	14	22	3	14	1	2

[a]Based on reference mA; automatic exposure control enabled

RBM red bone marrow

Table 2.2 Exposure parameters, absorbed organ doses (µGy) and effective dose (µSv) for the adolescent phantom

Device	kVp	mAs	FOV	Position	RBM	Bone surface	Thyroid	Salivary glands	Remainder	Brain	Skin	Effective dose
i-CAT N.G.	120	18.5	16x6	Mandible	40	38	134	1427	195	47	25	49
i-CAT N.G.	120	18.5	16x6	Maxilla	58	57	68	1084	83	129	29	33
i-CAT N.G.	120	18.5	16x13	Maxillofacial	130	125	261	1914	259	352	73	82
NewTom VG	110	Auto	15x11	Maxillofacial	106	103	297	1970	272	228	63	81
Kodak 9000 3D	70	106.8	5x3.7	Mandible molar	31	31	18	932	75	18	48	24
ProMax 3D	84	19.6	8x8	Dentoalveolar	32	31	42	566	47	88	17	18
3D Accuitomo 170	90	87.5	17x12	Maxillofacial	327	320	494	5528	708	1158	176	216
3D Accuitomo 170	90	87.5	14x10	Maxillofacial	281	277	298	5153	653	800	157	188
3D Accuitomo 170	90	87.5	14x5	Maxilla	135	133	104	2218	193	261	62	70
3D Accuitomo 170	90	87.5	4x4	Mandible molar	59	59	31	1148	83	147	25	32
GALILEOS Comfort	85	21	15x15	Maxillofacial	73	73	162	2073	270	164	45	71
SCANORA 3D	85	30	10x7.5	Dentoalveolar	45	45	123	1588	201	48	28	52
SCANORA 3D	85	48	14.5x13.5	Maxillofacial	109	109	154	1933	255	290	67	74
SkyView 3D	90	51.5	17x17	Maxillofacial	195	195	399	1596	216	605	72	90
Somatom Sensation 64	120	150	20x12.8	Maxillofacial	2363	2363	3573	17391	2452	11948	921	1047
Veraviewepocs 2D Pano	61	48	N/A	N/A	4	4	12	216	27	4	5	6
Veraviewepocs 2D Ceph	80	44.6	N/A	N/A	2	2	3	19	2	14	1	1

[a]Based on reference mA; automatic exposure control enabled

RBM red bone marrow

Looking at the contribution of the different organs to the effective dose, findings are similar to those in Chapter 1. High contributions are seen from the remainder tissues, bone marrow, salivary glands and thyroid gland. The effect of the changes in the calculation for effective dose between ICRP 60 and ICRP 103 is clear. A few changes in the calculation were introduced with a significant impact on head and neck doses. In ICRP 60 [21], the remainder tissues were assigned a tissue weighting factor of 0.05 and, with the exception of muscle and brain, all of the remainder tissues were located outside the head and neck region. In ICRP 103 [17], the radiosensitivity of the remainder tissues was increased from 0.05 to 0.12 and the list of remainder tissues updated. The brain was assigned an individual weighting factor of 0.01 and removed from the list. Of particular relevance to dental CBCT, the oral mucosa and lymph nodes were added to the remainder tissues. In addition, the salivary glands received a weighting factor of 0.01 and the thyroid factor dropped from 0.05 to 0.04. For the 10-year-old phantom, the salivary glands, remainder tissues and thyroid glands contributed equally to the effective dose, while for the adolescent phantom the salivary glands and the remainder tissues gave the most significant contribution. Even though the red bone marrow dose was relatively small, its contribution to the effective dose was significant for both phantoms because of its high radiosensitivity. The contributions of the skin, brain and bone surface were small for both phantoms.

When comparing the CBCT doses for the 10 year old phantoms with those of panoramic and cephalometric radiography and MSCT, it can be seen that the dose range for both phantoms is situated between 2-D radiography and MSCT, which has also been demonstrated for adult phantoms [1-11]. However, similar to the adult phantom, an overlap can be seen. On the low end of the dose range, it is seen that small-volume CBCT exposures can result in similar dose levels to panoramic radiography, although clinically these two techniques are complimentary rather than supplementary. The use of a medium or large FOV CBCT scan could, in theory, replace a panoramic or cephalometric radiography, but this is clearly not justified for routine practice because of the increase in dose. The use of a large FOV CBCT scan could only be justified if there is a clear added value to the information provided by the scan. However, in many cases this decision can also be made after investigation of a conventional radiograph. This paradox shows that in general, large volume CBCTs should be used as an additional examination to 2-D radiography, providing that the benefit outweighs the increased radiation risk. It is important to note that doses for panoramic and cephalometric radiography can also vary between equipment. Furthermore, there was no

possibility for collimation of the FOV for these 2-D techniques, although this could lead to further dose reduction.

Comparing CBCT to MSCT, the situation is different, as they are applied for overlapping clinical purposes. In general, when a 3-D scan is required, CBCT is the preferred modality because of its lower dose. However, it depends on the context to some extent. For clinical indications requiring a small FOV size, CBCTs which allow FOV reduction would be preferred over MSCT. Even though the FOV can be collimated along the z-axis for MSCT scanners, resulting in lower doses than the ones reported in this study, doses will still be considerably higher than those of small-volume CBCT. For large FOV examinations, it can be seen that the difference between CBCT and MSCT can be rather small when a low-dose protocol is used for the latter, although doses for CBCT are still clearly lower. Although in certain cases a MSCT scan may be justified (*e.g.* when soft tissue diagnosis is need for cleft palate patients and other congenital deformities), the use of CBCT as an alternative will still be preferred.

Comparing adult and paediatric doses, the actual radiation risk for children should always be taken into account. The linear no-threshold (LNT) model suggests that the relationship between dose and risk is linear and there is no threshold below which the risk becomes zero. The resulting risk factors are primarily based on the life span study (LSS) of atomic bomb survivors [22,23]. For very low doses, the National Council on Radiation Protection and Measurements Report [24] supports the linear dose–response relation based on laboratory and epidemiological studies. Another conclusion from the LSS is that children are more sensitive to radiation than adults [12,13]. There is an order-of-magnitude increase in the attributable lifetime mortality risk between children and adults and there is also an increase in sensitivity between girls and boys. The effect of age on radiation risk is further investigated in Chapter 4.

2.6 Conclusion

This study investigated the organ and effective doses for paediatric dental CBCT using anthropomorphic phantoms, and compared dose levels to those for conventional dental radiography techniques and MSCT. Significant dose reduction can be achieved by adapting the FOV size and tube output, but this is not always possible in practice. Taking into account the higher radiosensitivity of children, it is imperative that the use of CBCT in paediatric

dentistry is fully justified over conventional X-ray imaging, and is only performed when the 3D information is crucial for patient treatment, providing that the exposure is optimised.

2.7 References

1. Cohnen M, Kemper J, Möbes O, Pawelzik J, Mödder U. Radiation dose in dental radiology. Eur Radiol 2002; 12: 634–637.

2. Loubele M, Bogaerts R, Van Dijck E, Pauwels R, Vanheusden S, Suetens P, Marchal G, Sanderink G, Jacobs R. Comparison between effective radiation dose of CBCT and MSCT scanners for dentomaxillofacial applications. Eur J Radiol 2009; 71: 461–468.

3. Roberts JA, Drage NA, Davies J, Thomas DW. Effective dose from cone beam CT examinations in dentistry. Br J Radiol 2009; 82: 35–40.

4. Ludlow JB, Ivanovic M. Comparative dosimetry of dental CBCT devices and 64-slice CT for oral and maxillofacial radiology. Oral Surg Oral Med Oral Pathol Oral Radiol Endod 2008; 106: 106–114.

5. Suomalainen A, Kiljunen T, Käser Y, Peltola J, Kortesniemi M. Dosimetry and image quality of four dental cone beam computed tomography scanners compared with multislice computed tomography scanners. Dentomaxillofac Radiol 2009; 38: 367–378.

6. Ludlow JB, Davies-Ludlow LE, Brooks SL, Howerton WB. Dosimetry of 3 CBCT devices for oral and maxillofacial radiology: CB Mercuray, NewTom 3G and i-CAT NG. Dentomaxillofac Radiol 2006; 35: 219–226.

7. Hirsch E, Wolf U, Heinicke F, Silva MA. Dosimetry of the cone beam computed tomography Veraviewepocs 3D compared with the 3D Accuitomo in different fields of view. Dentomaxillofac Radiol 2008; 37: 268–273.

8. Okano T, Harata Y, Sugihara Y, Sakaino R, Tsuchida R, Iwai K, Seki K, Araki K. Absorbed and effective doses from cone beam volumetric imaging for implant planning. Dentomaxillofac Radiol 2009; 38: 79–85.

9. Silva MA, Wolf U, Heinicke F, Bumann A, Visser H, Hirsch E. Cone-beam computed tomography for routine orthodontic treatment planning: a radiation dose evaluation. Am J Orthod Dentofacial Orthop 2008; 133: 640.e1–5.

10. Tsiklakis K, Donta C, Gavala S, Karayianni K, Kamenopoulou V, Hourdakis CJ. Dose reduction in maxillofacial imaging using low dose cone beam CT. Eur J Radiol 2005; 56: 413–417.

11. Mah JK, Danforth RA, Bumann A, Hatcher D. Radiation absorbed in maxillofacial imaging with a new dental computed tomography device. Oral Surg Oral Med Oral Pathol Oral Radiol Endod 2003; 96: 508–513.

12. Brenner DJ. Estimating cancer risks from pediatric CT: going from the qualitative to the quantitative. Pediatr Radiol 2002; 32: 228–3.

13. Pierce DA, Preston DL. Radiation-related cancer risks at low doses among atomic bomb survivors. Radiat Res 2000; 154: 178–86.

14. International Commission on Radiological Protection. Basic anatomical and physiological data for use in radiological protection: reference values. ICRP Publication 89. Oxford, UK: Pergamon Press, 2003.

15. International Commission on Radiological Protection. Reference manual: Anatomical, physiological and metabolic characteristics. ICRP Publication 23. Oxford, UK: Pergamon Press, 1975.

16. International Commission on Radiation Units and Measurements. Phantoms and computational models in therapy, diagnosis and protection. ICRU Report 48. Bethesda, MD: International Commission on Radiation Units and Measurements 1992.

17. International Commission on Radiological Protection. Recommendations of the International Commission on Radiological Protection. ICRP Publication 103. Annals of the ICRP 37. Oxford, UK: Pergamon Press, 2007.

18. International Commission on Radiological Protection. Human respiratory tract model for radiological protection. ICRP Publication 66. Ann ICRP. Oxford, UK: Pergamon Press, 1994.

19. Ludlow JB, Davies-Ludlow LE, Brooks SL, Howerton WB. Dosimetry of 3 CBCT devices for oral and maxillofacial radiology: CB Mercuray, NewTom 3G and i-CAT NG. Dentomaxillofac Radiol 2006; 35: 219–226.

20. Huda W, Sandison GA. Estimation of mean organ doses in diagnostic radiology from Rando phantom measurements. Health Phys 1984; 47: 463–467.

21. International Commission on Radiological Protection. 1990 Recommendations of the International Commission on Radiological Protection. ICRP Publication 60. Annals of the ICRP. Oxford, UK: Pergamon Press, 1991.

22. Preston DL, Shimizu Y, Pierce DA, Suyama A, Mabuchi K. Studies of mortality of atomic bomb survivors. Report 13: Solid cancer and noncancer disease mortality: 1950–1997. Radiat Res 2003; 160: 381–407.

23. Preston DL, Ron E, Tokuoka S, Funamoto S, Nishi N, Soda M, *et al*. Solid cancer incidence in atomic bomb survivors: 1958–1998. Radiat Res 2007; 167: 1–64.

24. National Council on Radiation Protection and Measurements. Evaluation of the linear-non threshold doseresponse model for ionizing radiation. Report No. 136. Bethesda, MD: NCRP, 2001.

Chapter 3: Dose reduction in CBCT through FOV reduction and 180° scanning

3.1 Abstract

Objective: To quantify the relationship between field of view (FOV) size, rotation arc and effective dose in dental cone-beam computed tomography imaging (CBCT) imaging.

Materials and methods: Organ and effective doses were estimated using 147 thermoluminescent dosimeters (TLD) were placed at various locations in an anthropomorphic phantom. The phantom was exposed with a dental CBCT scanner using various volume sizes ranging between 4x4 cm and 17x12 cm as well as full (360°) and half (180°) rotation protocols.

Results: For the full rotation protocols, effective dose ranged between 36 µSv (4x4 cm, upper jaw front region) and 296 µSv (17x12 cm). For half rotation protocols, effective dose was between 22 and 182 µSv. The average dose reduction for half rotation protocols was 36%. The relatively highest organ dose reduction owing to FOV reduction was seen for the brain and bone surface. Owing to half rotation, the highest reduction in organ dose was for the thyroid gland (49%).

Conclusions: Significant dose reduction can be achieved by reducing the FOV size of CBCT examinations to the actual region of interest. In some cases, a half rotation can be preferred, as it has the added value of reducing the acquisition time.

3.2 Introduction

Different studies have investigated the radiation dose for CBCT [1-18]. The general conclusion is that CBCT doses are found in a wide interval between conventional 2-D radiographic techniques (intra-oral, panoramic and cephalometric radiography) and multi-slice CT (MSCT). However, modern MSCT scanners allow for low-dose scanning of the head, reaching patient doses comparable or lower than those obtained for certain CBCT protocols. It is crucial to investigate all possible strategies for dose reduction in CBCT

imaging to ensure that the basic principles of justification and optimisation of patient dose are adhered [19].

From the available studies, it is clear that the size of the field of view (FOV) and its position relative to the radiosensitive organs are key factors determining the total effective dose of the patient [2-13]. However, it is not possible to directly compare radiation doses from CBCT devices with different FOV sizes since there are many other exposure factors affecting the dose (*e.g.* X-ray spectrum, tube current, exposure time, rotation arc). In terms of dose reduction, the FOV size can be one of the most important parameters, but its effect has not yet been clearly quantified. Another method for dose reduction is the use of a partial rotation. Some scanners expose using a full 360° rotation, other use a smaller rotation arc between 180° and 220°. Certain CBCTs include a standard protocol with a full rotation as well as a 180° protocol to reduce patient dose and scan time.

The objective of this study was to evaluate the effect of FOV size and position on the effective dose, using a CBCT scanner which allows for the selection of a wide range of field sizes. Furthermore, the effect of a 180° rotation arc was assessed for different FOVs.

3.3 Materials and methods

Dose measurements were performed on the 3D Accuitomo 170 (J. Morita, Kyoto, Japan), using the standard clinical exposure setting of 90 kVp, 87.5 mAs, 360° rotation. The following FOV sizes (diameter x height, cm) were used: 4x4, 6x6, 8x8,10x10, 14x5, and 17x12. The ratio in reconstructed volume size between the largest and smallest volume was approximately 54. For the clinically most common FOVs, as well as the smallest and largest available FOVs, additional measurements were obtained using a 180° rotation protocol with 90 kVp and 45 mAs.

The measurement methodology was highly similar to that in Chapter 1. The effective dose was estimated using an Alderson Radiation Therapy (ART) phantom (Radiology Support Devices Inc, CA, USA), representing an average adult male (height 175 cm, weight 73.5 kg). The phantom contains a polymer moulding representing the skeleton, which is embedded into a soft tissue-equivalent material (Figure 1.1, Chapter 1). It consists of slices with a thickness of 2.5 cm, containing a grid of holes allowing for the placement of dosimeters.

Thermoluminescent dosimeters (TLDs) were attached at various locations throughout the upper 11 slices (*i.e.* head and neck region) of the phantom. The type of TLD used was TLD-100 (LiF:Mg,Ti). For each measurement, 20 calibration TLDs were irradiated using a

Harshaw 6600 reader (Harshaw Thermo Fisher Scientific Inc, Waltham, MA) containing a ^{90}Sr source with a fixed dose rate. The internal source was calibrated for quantitative absorbed dose values using an ionisation chamber with a calibration factor traceable to a Secondary Standard Dosimetry Laboratory (SSDL, Gent, Belgium).

For an accurate estimation of the absorbed dose to the different radiosensitive organs throughout the head and neck region, 147 TLDs were distributed throughout the ART phantom. Additionally, 10 TLDs were used to estimate the background dose, which was subtracted from the measured values. Organs included in the effective dose calculation were: red bone marrow, bone surface, brain, extrathoracic airways, lymph nodes, muscle, oesophagus, oral mucosa, salivary glands, and thyroid gland. For each organ or tissue (T), the absorbed dose (or radiation weighted dose) was calculated as:

$$H_T = w_R \, \Sigma_i \, f_i \, D_{Ti}$$

With w_R the radiation factor for X-rays, being 1, f_i the fraction of tissue T in slice i, and D_{Ti} the average absorbed dose of tissue T in slice i. For the brain, salivary glands, thyroid gland, oral mucosa, and extrathoracic airways, calculation of D_T could be simplified as these tissues are found solely in the head and neck region, and the equivalent dose could be calculated as the average value for all TLDs used for these organs. For bone surface, bone marrow, muscle, lymph nodes and oesophagus, organ fractions were determined based on the estimated fractions of these tissues in the upper 11 slices of the ART phantom. Seeing that the TLDs were calibrated in water and given the different dose-energy relationships for different tissues, a tissue/water correction was applied for bone surface, bone marrow, muscle, lymph nodes, skin, brain and thyroid. For these tissues, the mass energy absorption coefficients from ICRU Publication 44 were selected for a beam energy of 50 keV [20]. This corresponds to the mean beam energy of the 3D Accuitomo 170 at 90 kVp, which was determined using full Monte Carlo simulation. The simulation model describes the actual tube/filter/collimation structure and performs the realistic photon/electron radiation transport [21]. The relative number of photons was calculated by collecting the photons of different energy bins over the entire radiation field, and normalised against the total number of X-ray photons generated out of the simulation.

The calculation of the contribution of each organ of interest to the effective dose is typically performed in two steps. First, the equivalent dose (or radiation weighted dose) is determined by multiplying the absorbed doses with a radiation weighting factor, which

expresses the relative biological damage for different types of radiation. Next, the equivalent organ dose is multiplied by the tissue weighting factor w_T, which expresses the contribution of this tissue to the overall radiation detriment from stochastic effects. Seeing that the radiation weighting factor for X-rays is 1, the tissue weighting factors could be directly applied to the absorbed dose values. The tissue weighting factors from the International Commission on Radiological Protection Publication 103 (2007) were applied (Table 1.2, Chapter 1)[22]. The effective dose is then calculated as the sum of all organ contributions.

3.4 Results

Table 3.1 shows equivalent organ doses and effective dose for all exposure protocols. For the full rotation protocols, the effective dose ranged between 36 μSv (4x4 cm, upper jaw front region) and 296 μSv (17x12 cm). For half rotation protocols, effective dose was between 22 and 182 μSv. When comparing the effective doses to the 17x12 cm protocol, ratios were between 0.07 and 0.85 (Table 3.1). Looking at the organ doses, the highest absorbed dose was from the salivary glands, showing a tenfold range between the lowest and highest salivary gland dose (573 - 5737 μGy). Considering the actual contribution of the different organs to the effective dose, the highest contribution is seen for the red bone marrow, thyroid gland, and salivary glands. The linear correlation between the absorbed organ doses and effective dose was calculated for each tissue. Correlation coefficients (R^2) ranged between 0.76 (brain) and 0.99 (remainder tissues). For single organs, the highest predictive value for effective dose was for the salivary glands ($R^2 = 0.99$) and skin ($R^2 = 0.98$).

A general consistency was found between FOV size and effective dose. The correlation between FOV size and effective dose was explored. A high correlation was seen when using the volumetric parameter (diameter x height^2) rather than the volume of the reconstructed cylinder. The selection of this volumetric parameter is supported by Table 3.1, as it is seen that the effective dose for the 10x10 cm FOV is 41% higher than the average dose for the 14x5 cm FOV even though the volume of the FOV cylinders is similar (*i.e.* 3142 cm^3 and 3078 cm^3), showing that the FOV height affect the effective dose more strongly than the FOV diameter. The volume-related parameter (diameter x height^2) showed a logarithmic relation with the effective dose ($R^2 = 0.976$). Figure 3.1 shows a scatter plot demonstrating the correlation between volume size and effective dose for the full rotation protocols. The effective doses for the varying positions of the 4x4, 6x6 and 14x5 cm FOVs were averaged. The graph shows that the effective dose increases sharply with increasing FOV height up to a

certain level. This level corresponds to the height at which all salivary glands are covered by the primary beam, and above which the additional exposure is given to the brain and small fraction of bone and skin, leading to a slighter increase in effective dose.

For the FOVs with limited height (4x4, 6x6 and 14x5 cm), the effective doses were larger for lower jaw exposures due to an increased contribution from the thyroid gland. Although the three types of salivary glands are exposed differently as well, the overall contribution of the salivary glands is similar for upper and lower jaw protocols.

Comparing 360° and 180° protocols, the average decrease in effective dose was 36% for a half rotation. The highest relative dose reduction was seen for the thyroid gland (49%); the lowest reduction was for the brain, oesophagus, salivary glands, and remainder tissues (31–34%).
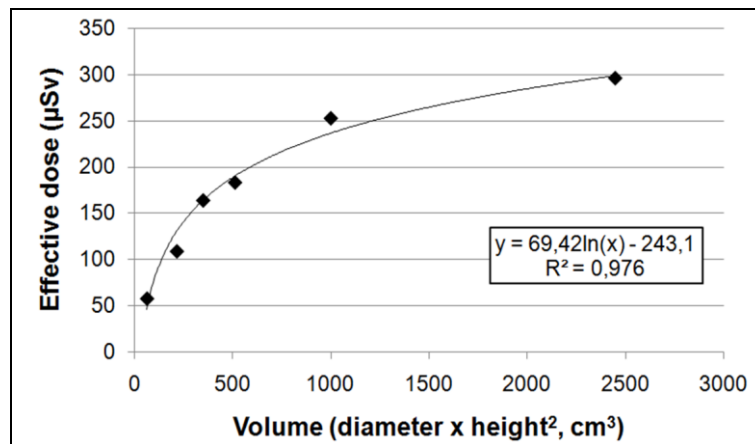

Figure 3.1 Scatter plot of effective dose for 360° exposure protocols versus volume size, expressed as (diameter x height^2). A logarithmic fit is shown.

3.5 Discussion

It is difficult to consider dental CBCT as a single imaging modality, due to the variety of scanners on the market. Although the basic exposure geometry is the same for these devices, there are many essential differences in terms of X-ray spectra, beam shape, FOV size, rotation arc, focus-skin/detector distance, detector specifications and reconstruction algorithms, resulting in wide ranges for image quality and radiation dose.

Table 3.1 Absorbed organ doses (µGy) and effective dose (µSv) for various FOV sizes and positions of the 3D Accuitomo 170 CBCT. The effective dose ratio compared with the highest exposure (17x12 cm, full rotation) is shown for each protocol.

FOV size (cm)[a]	4x4		4x4	6x6		6x6		14x5	14x5	8x8		10x10	17x12	
FOV position	Upper canine		Lower molar	Upper front		Lower molar		Upper jaw	Lower jaw	Both jaws		Both jaws	Maxillofacial	
Rotation	Full	Half	Full	Full	Half	Full	Half	Full	Full	Full	Half	Full	Full	Half
Red bone marrow	37	18	69	114	74	94	49	161	124	177	99	295	379	244
Oesophagus	38	25	174	74	44	295	219	127	508	331	232	428	475	287
Thyroid	108	50	236	175	88	433	254	296	813	651	338	799	847	426
Skin	44	27	30	70	49	82	52	106	103	116	67	161	207	125
Bone surface	250	114	178	724	448	305	158	1039	341	759	470	1789	2414	1432
Salivary glands	845	573	2011	2192	1583	3122	2083	3821	3879	4203	2946	5293	5737	3692
Brain	53	21	40	149	116	85	76	210	84	184	112	491	1469	1035
Remainder	118	79	268	313	224	426	281	545	526	586	407	760	832	515
Effective dose	36	22	79	93	63	127	82	153	175	184	119	253	296	182
Ratio ED/ED$_{MAX}$	0.12	0.07	0.27	0.31	0.21	0.43	0.28	0.52	0.59	0.62	0.40	0.85	1.00	0.62

[a]Diameter x height of cylindrical reconstructed FOV. A selection of clinically relevant FOV sizes, positions and rotation arcs is presented.
FOV field of view, *ED* effective dose

Previous studies on CBCT doses involved varying FOV sizes and positions [2-13]. However, the accuracy of certain previous dose evaluations is limited, as they have used a small number of TLDs (ranging between 16 and 25 phantom locations) to estimate organ doses for the entire head and neck [5-13]. This particularly affects the comparison of doses for varying FOV sizes, as organ doses can be over- or underestimated depending on the location of the FOV relative to the TLDs. The recalculation of effective doses in Chapter 1 has pointed out that large variability for organ doses may occur when excessively reducing the number of TLDs in the calculation of absorbed and effective doses [2]. Furthermore, when comparing devices with varying volume sizes, variations in dose will be determined through interplay of all exposure factors (*i.e.* voltage peak, filtration, beam size and geometry, and rotation arc). In this study, the effect of FOV size on patient dose was investigated using a single CBCT device, keeping all other exposure factors constant. Furthermore, the dose reduction from half-rotation scanning was quantified for different field sizes.

From a radioprotection point of view, the use of a FOV which is excessively larger than the region of interest (ROI) does not correspond to the requirement of optimisation [2,19]. Typically, a CBCT examination is preceded by a 2-D (intra-oral or panoramic) radiograph, enabling the exact determination of the required ROI. A common, but erroneous, counterpoint to this issue is that a large FOV could lead to diagnostic findings outside the ROI which may or may not be related to the clinical indication of the CBCT scan. This corresponds to a form of health screening, and a large-scale risk-benefit analysis may be able to weigh the increase of population dose due to the large FOV scanning with the possible improvement of patient treatment owing to additional findings. Furthermore, it should be taken into account that larger FOVs require more time and effort to be spent on clinical evaluation and, when the FOV extends outside the 'dental' region, the input of a radiologist.

Based on the current findings, it can be postulated that the FOV size should be determined based on the clinical application. When looking at the most common dental and head and neck applications for CBCT, it is clear that there are varying requirements in terms of image resolution and volume size for different clinical indications [1]. For partly or fully edentulous implant patients, it is sometimes needed to acquire the full dental arch. For certain patient subsets requiring maxillofacial surgery or orthodontic treatment, it can be required to scan the entire dentomaxillofacial area. On the other hand, a small FOV usually suffices for local implant planning and endodontic cases. For third molar extraction, temporomandibular joint evaluation or middle ear applications, depending on the requirement of scanning one side or both, the acquisition of one or two small-volume scans could be considered instead of

a single large-FOV scan. The added benefit of using a small FOV is the increase in spatial resolution in terms of voxel size. Whenever this increased resolution is not needed, the exposure could be lowered even further providing that the option of a low-resolution scan or a reduced tube output is available. The application range of CBCT devices will therefore depend on the range of available FOV sizes and resolution or exposure options. Ideally, the device should allow for versatile exposure factors (including paediatric exposure protocols), depending on the required application range. In practice, it is not needed for every device to cover a range of FOV sizes and voxel sizes, if it is primarily used for patient groups with identical imaging requirements. Still, devices with the sole option of a large FOV will often lead to unnecessary exposure to areas which are not of interest and which do not provide an added benefit in patient treatment.

Another dose optimisation strategy is the reduction of the rotation arc. In cone-beam imaging, projection acquired at a 180° arc suffice for reconstruction of the scanned volume. There are devices using a 180° or slightly larger rotation for all exposure protocols. Other devices allow for the selection of a full or half rotation. In terms of image quality, a reduction of the rotation has a similar effect as a reduction in tube current (mA) as they both affect the mAs. Fewer projections are acquired, resulting in a generally lower image quality. The reduction of image quality for a 180° rotation can be considered as comparable to a 50% reduction in tube current (mA). The effect of this mAs reduction on image quality is primarily reflected as an increase in noise. In Chapter 12, the relation between mAs and noise is investigated, showing a hyperbolic relationship. Therefore, the increase in noise will depend on the initial noise level for a 360° rotation along this hyperbolic curve. For the 3D Accuitomo 170 used in this study, Chapter 12 shows a 34% decrease in contrast-to-noise ratio for a 50% reduction in mAs compared to the default clinical protocol of 87.5 mAs. This indicates that, at least in this case, the dose reduction from a 180° rotation corresponds closely to the increase in noise. It should be taken into account that the same noise level could be achieved by reducing the mA by 50%, which would result in a 50% dose reduction which is considerably higher than the reduction found from a 180° rotation in this study. However, mirroring the tube-detector motion (*i.e.* letting the tube move at the anterior side) for a 180° rotation would, in theory, lead to a dose reduction greater than 50% and could be preferred over a reduction in mA. The current results indicate that manufacturers, when including a 180° protocol for their device, should let the tube pass anteriorly assuming that there is no significant difference in image quality between 180° protocols with anterior or posterior tube movement.

Regarding patient dose, it is seen that the dose reduction is less than 50%, averaging at 36% for the investigated FOVs. There is a twofold explanation for this. First of all, the mAs of the 180° protocol is not exactly half that of the 360° protocol but slightly higher (577 vs. 321 projections, including 47 dark frames for both protocols; verified by in-air ion chamber measurement at isocentre). Furthermore, during the 180° rotation, the tube starts its movement at the right side, passes at the posterior side of the scanned object and ends at the left side. This results in a back-to-front dose gradient, which is confirmed by the brain dose, for which the lowest relative dose reduction is seen for 180° scans. However, the FOV is always positioned anterior in the phantom's head. This leads to an asymmetry in exposure, resulting in a relatively higher dose uptake for almost all radiosensitive organs. It can be seen that the only organ that showed a dose reduction for 180° scans which corresponded closely to the mAs reduction was the thyroid gland. Seeing that this organ is below the primary beam, its dose consists of scattered radiation, which is not as sensitive to geometric factors such as the FOV position and the start and end angle of the rotation.

Apart from dose reduction, the use of a half rotation provides another benefit for certain patient groups. The decrease of the acquisition time can significantly reduce motion blur and motion artefacts. Patient motion is a relevant issue in CBCT imaging, as the images are reconstructed using small voxel sizes, and even the smallest movement will be reflected on the reconstructed image. Furthermore, in most cases patients are in a seated or standing position with limited fixation, and severe motion artefacts are possible for patients which have trouble staying still for the entire duration of the scan, which can be longer than 30 seconds. For certain patient groups (*e.g.* small children, older or insecure patients), the option of a 180° scan would not only lead to dose reduction, but the slight general loss in image quality will be compensated by the reduction of motion. Recent studies suggest that a 180° CBCT scan provides images of sufficient image quality for certain diagnostic tasks [23,24].

3.6 Conclusion

Significant dose reduction can be achieved by reducing the FOV size of CBCT examinations to the actual region of interest. In some cases, a half rotation can be preferred, as it has the added value of reducing the acquisition time. Both dose reduction strategies are particularly relevant for children.

3.7 References

1. Scarfe WC, Farman AG, Sukovic P. Clinical applications of cone-beam computed tomography in dental practice. J Can Dent Assoc 2006; 72: 75-80.

2. Pauwels R, Beinsberger J, Collaert B, Theodorakou C, Rogers J, Walker A, Cockmartin L, Bosmans H, Jacobs R, Bogaerts R, Horner K, The SEDENTEXCT Project Consortium. Effective dose range for dental cone beam computed tomography scanners. Eur J Radiol 2012; 81: 267-271.

3. Okano T, Harata Y, Sugihara Y, Sakaino R, Tsuchida R, Iwai K, Seki K, Araki K. Absorbed and effective doses from cone beam volumetric imaging for implant planning. Dentomaxillofac Radiol 2009; 38: 79-85.

4. Loubele M, Bogaerts R, Van Dijck E, Pauwels R, Vanheusden S, Suetens P, Marchal G, Sanderink G, Jacobs R. Comparison between effective radiation dose of CBCT and MSCT scanners for dentomaxillofacial applications. Eur J Radiol 2009; 71:461-468.

5. Davies J, Johnson B, Drage N. Effective doses from cone beam CT investigation of the jaws. Dentomaxillofac Radiol 2012; 41: 30-36.

6. Hirsch E, Wolf U, Heinicke F, Silva MA. Dosimetry of the cone beam computed tomography Veraviewepocs 3D compared with the 3D Accuitomo in different fields of view. Dentomaxillofac Radiol 2008; 37: 268-273.

7. Librizzi ZT, Tadinada AS, Valiyaparambil JV, Lurie AG, Mallya SM. Cone-beam computed tomography to detect erosions of the temporomandibular joint: Effect of field of view and voxel size on diagnostic efficacy and effective dose. Am J Orthod Dentofacial Orthop 2012; 140: e25-30.

8. Ludlow JB, Ivanovic M. Comparative dosimetry of dental CBCT devices and 64-slice CT for oral and maxillofacial radiology. Oral Surg Oral Med Oral Pathol Oral Radiol Endod 2008; 106: 106-114.

9. Ludlow JB, Davies-Ludlow LE, Brooks SL, Howerton WB. Dosimetry of 3 CBCT devices for oral and maxillofacial radiology: CB Mercuray, NewTom 3G and i-CAT. Dentomaxillofac Radiol 2006; 35: 219-226.

10. Qu XM, Li G, Ludlow JB, Zhang ZY, Ma XC. Effective radiation dose of ProMax 3D cone-beam computerized tomography scanner with different dental protocols. Oral Surg Oral Med Oral Pathol Oral Radiol Endod 2010; 110: 770-776.

11. Qu X, Li G, Zhang Z, Ma X. Thyroid shields for radiation dose reduction during cone beam computed tomography scanning for different oral and maxillofacial regions. Eur J Radiol 2012; 81: e376-380.

12. Roberts JA, Drage NA, Davies J, Thomas DW. Effective dose from cone beam CT examinations in dentistry. Br J Radiol 2008; 82: 35-40.

13. Suomalainen A, Kiljunen T, Käser Y, Peltola J, Kortesniemi M. Dosimetry and image quality of four dental cone beam computed tomography scanners compared with multislice computed tomography scanners. Dentomaxillofac Radiol 2009; 38: 367-378.

14. Chau AC, Fung K. Comparison of radiation dose for implant imaging using conventional spiral tomography, computed tomography, and cone-beam computed tomography. Oral Surg Oral Med Oral Pathol Oral Radiol Endod 2009; 107: 559-565.

15. Mah JK, Danforth RA, Bumann A, Hatcher D. Radiation absorbed in maxillofacial imaging with a new dental computed tomography device. Oral Surg Oral Med Oral Pathol Oral Radiol Endod 2003; 96: 508-513.

16. Silva MA, Wolf U, Heinicke F, Bumann A, Visser H, Hirsch E. Cone-beam computed tomography for routine orthodontic treatment planning: a radiation dose evaluation. Am J Orthod Dentofacial Orthop 2008; 133: 640.e1-5

17. Theodorakou C, Walker A, Horner K, Pauwels R, Bogaerts R, Jacobs R, The SEDENTEXCT Project Consortium. Estimation of paediatric organ and effective doses from dental cone beam CT using anthropomorphic phantoms. Br J Radiol 2012; 85: 153-160.

18. Tsiklakis K, Donta C, Gavala S, Karayianni K, Kamenopoulou V, Hourdakis CJ. Dose reduction in maxillofacial imaging using low dose Cone Beam CT. Eur J Radiol 2005; 56: 413-417.

19. Horner K, Islam M, Flygare L, Tsiklakis K, Whaites E. Basic principles for use of dental cone beam computed tomography: consensus guidelines of the European Academy of Dental and Maxillofacial Radiology. Dentomaxillofac Radiol 2009; 38: 187-195.

20. International Commission on Radiation Units and Measurements. Tissue Substitutes in Radiation Dosimetry and Measurement. ICRU Report 44. Bethesda, Maryland, USA: ICRU Publications 1989.

21. Zhang G, Pauwels R, Marshall N, Shaheen E, Nuyts J, Jacobs R, Bosmans H. Development and validation of a hybrid simulation technique for cone beam CT: application to an oral imaging system. Phys Med Biol; 56: 5823-5843.

22. International Commission on Radiological Protection. Recommendations of the International Commission on Radiological Protection. ICRP Publication 103. Ann ICRP 37. Oxford, UK: Pergamon Press 2007.

23. Lofthag-Hansen S, Thilander-Klang A, Gröndahl K. Evaluation of subjective image quality in relation to diagnostic task for cone beam computed tomography with different fields of view. Eur J Radiol 2011; 80: 483-488.

24. Durack C, Patel S, Davies J, Wilson R, Mannocci F. Diagnostic accuracy of small volume cone beam computed tomography and intraoral periapical radiography for the detection of simulated external inflammatory root resorption. Int. Endod J 2011; 44: 136-147.

Chapter 4: In vivo patient dose of CBCT

4.1 Abstract

Objectives: the aim of this study was to measure entrance skin doses on patients undergoing CBCT examinations, to establish conversion factors between skin and organ doses, and to estimate individual patient risk from CBCT exposures.

Materials and methods: 269 patients (age 8-83) were included, involving three imaging centres. CBCT scans were acquired using the SCANORA 3D and NewTom 9000. Eight thermoluminescent dosimeters (TLD) were attached to the patient's skin at standardized locations. Using previously published organ dose estimations on various CBCTs with an anthropomorphic phantom, the correlation between skin dose and organ doses was investigated and conversion factors were calculated to estimate individual organ doses based on skin measurements. An age-dependent risk model was applied to estimate the lifetime attributable cancer risk for each patient.

Results: For the SCANORA 3D, average skin doses over the eight locations varied between 484 and 1788 µGy (average 910 µGy) with individual TLD values ranging between 23 and 3843 µGy; for the NewTom 9000 the range was between 821 and 1686 µGy (TLD values between 60 and 3980 µGy) for Centre 1 and between 292 and 2325 µGy (TLD values from 6 to 6682 µGy) for Centre 2. The individual lifetime attributable cancer risk estimation varied between 0.000042% and 0.0023%. There was no clear correlation between BMI and entrance skin dose for any CBCT.

Conclusions: entrance skin dose measurements demonstrated the combined effect of exposure and patient factors on the dose uptake. The actual radiation risk was primarily influenced by the age at exposure, pointing out the need for justification and optimisation of CBCT exposures, with a specific focus on children.

4.2 Introduction

Currently, a vast amount of dental cone beam computed tomography (CBCT) devices are available, and a large variability is seen between these devices in terms of exposure. Using

anthropomorphic phantoms, it has been shown that there is a wide radiation dose range in CBCT due to difference in beam energy, tube output, and beam geometry [1-5]. The dose metric which is typically reported in literature is the effective dose as defined by the International Commission on Radiological Protection (ICRP), which is estimated as a weighted sum of absorbed doses from different radiosensitive organs [6]. Although it is a useful quantity to express the overall risk for cancer-induced effects from radiation exposure, there are a few drawbacks to the effective dose which limits its applicability in patient dose management. The main issue with the effective dose in the context of CBCT imaging is that this modality is used for various age groups. When measured in a standard phantom, the effective dose provides a risk estimation for an average adult male. In actuality, patient dose will vary between individuals, with patient size and mass as main factors [7,8]. For dental CBCT, this is of particular relevance, as it is frequently used for young children for orthodontic treatment planning, traumas and developmental defects. It can be expected that the absorbed dose to the different head and neck organs will be higher for children for a given exposure, as relatively more tissue is included in the primary beam [9-18]. Another limitation to the effective dose values reported in literature is the age-dependent sensitivity of cancer effects from radiation. Depending on the age of an individual, the relative risk for a certain exposure ranges from fourfold for young children to a negligible risk for old patients, when compared to an adult [19]. Based on these considerations, it can be seen that the actual patient risk from dental CBCT exposures has not yet been estimated.

The aim of this study was to measure entrance skin dose on CBCT patients, involving different patient groups with varying ages and sizes. Additionally, the purpose was to investigate the variability in skin dose values and its relation with demographic parameters, and to estimate the individual patient risk based on skin dose.

4.3 Materials and methods

Five patients groups were determined based on the clinical indication. The investigated indications were: dental implant planning impacted teeth, orthodontic planning, maxillofacial trauma/tumours/developmental abnormalities and sinus visualization. There were no exclusion criteria regarding age, weight or any other parameter; all patients corresponding to one of these indications were eligible for inclusion. Three CBCT devices were included in this study: the SCANORA 3D (Soredex, Tuusula, Finland) and two NewTom 9000 (QR, Verona, Italy) devices. Ethical approval was obtained at the three involved centres: the University of

Leuven (SCANORA 3D) and the universities of Athens and Vilnius (NewTom 9000). Only patients who were actually referred for a CBCT examination were included; no additional exposure was given to any patient. An informed consent form was signed by the patient or its guardian before the examination. Before exposure, demographic and anatomic data was recorded: age, gender, height, weight, interpupillary distance and chin-thyroid distance. The BMI was calculated as the conventional Quetelet index, dividing the weight (in kg) by the square of the height (in m). Exposure parameters were recorded, with the kVp being fixed for each device but the FOV size, scanned region and exposure (mAs) varying between patients according to the existing clinical exposure protocol.

To measure entrance skin dose, thermoluminescent dosimeters (TLD-100) were attached to eight locations on the face of the patient: eyebrows/eyelids (2), parotid gland (2), submandibular gland (2), mouth (1), and thyroid gland (1). Bilateral palpation was performed for placement of the TLDs on the salivary glands. For each patient, two TLDs were used to estimate background radiation. A calibrated TLD reader was used for read-out. Background dose values were measured using two non-irradiated TLDs for each patient and subtracted from entrance skin doses.

To estimate individual patient risk based on the measured entrance skin dose, previously published organ and effective dose measurements obtained from an Alderson Radiation Therapy phantom were used, involving a wide range of CBCT devices and exposure protocols. Organ doses were estimated by attaching TLDs at various locations throughout the head and neck, corresponding to radiosensitive organs and tissues. The effective dose was calculated according to the ICRP 103 Publication [20], applying weightings to the different involved tissues. Tissues included in the calculation of the effective dose were: bone marrow, bone surface, brain, extrathoracic airways, lymph nodes, muscle, oesophagus, oral mucosa, salivary glands, and thyroid gland. From the 31 TLDs used to estimate the skin dose, 8 TLD locations were selected, closely corresponding to the placement of the 8 skin TLDs for patients. Using this selection, the prediction of organ doses using 1 or more skin measurement locations was investigated. For each organ or tissue, the combination of skin TLDs providing the highest correlation with the absorbed organ dose was found. The slope of the linear fit with intercept (0,0) was used as a conversion factor. Using these conversion factors, organ doses were estimated for each individual patient. The weighting factors from ICRP 103 were then applied to each organ dose estimation. Mass energy absorption coefficients from ICRU Publication 44 were used, assuming a mean energy of 50 keV for the SCANORA 3D and 60 keV for the NewTom 9000 [21].

Finally, an estimation of the age-dependent risk for radiation-induced stochastic effects was applied for each patient, as the effective dose is not a suitable quantity for individual radiation risk estimation [22]. Although the weighting factors defined in ICRP 103 are assumed to be valid for both genders and all age groups, correction factors for radiation exposures to varying age groups have been defined in the ICRP 60 recommendations (Table 4.1)[19]. More recently, the influence of the age at exposure on radiation risk has been further analyzed and reported in the Biological Effects of Ionizing Radiation (BEIR) VII report from the United States National Research Council [23], enabling a continuous modelling of the lifetime attributable risk (LAR) for cancer induction or mortality. Figure 4.1 shows the overall LAR for a 10 mGy dose as a function of gender and age at exposure. Using the effective dose estimations for each patient, the gender-averaged LAR was estimated using the curve in Figure 4.1.

4.4 Results

A total of 269 patients were included. Demographic and anatomical data is summarized in Table 4.2. For each scanner, the age range, gender distribution, and ranges for BMI, interpupillary and chin-thyroid distances are shown. Overall, the subject's ages ranged between 8 and 83 years, with BMIs ranging between 12.7 and 40.4. The gender distribution was 42% male and 58% female.

Entrance skin dose measurements are illustrated in Table 4.3. Values for left-right symmetrical TLD locations (*i.e.* eyes, parotid and submandibular glands) were averaged. For the SCANORA 3D, average skin doses over the eight locations varied between 484 and 1788 µGy (average 910 µGy) with individual TLD values ranging between 23 and 3843 µGy; for the NewTom 9000 the range was between 821 and 1686 µGy (TLD values between 180 and 3980 µGy) for Centre 1 and between 292 and 2325 µGy (TLD values from 6 to 3690 µGy) for Centre 2. Figure 4.2 shows the average skin dose for all patients for the three devices. The highest entrance skin doses were found at the mouth; the lowest dose was at the eyes and thyroid, which also showed the largest variability in entrance doses between patients.

72

Table 4.1 Relative lifetime risk for radiation detriment for different age groups from ICRP Publication 60 [19]

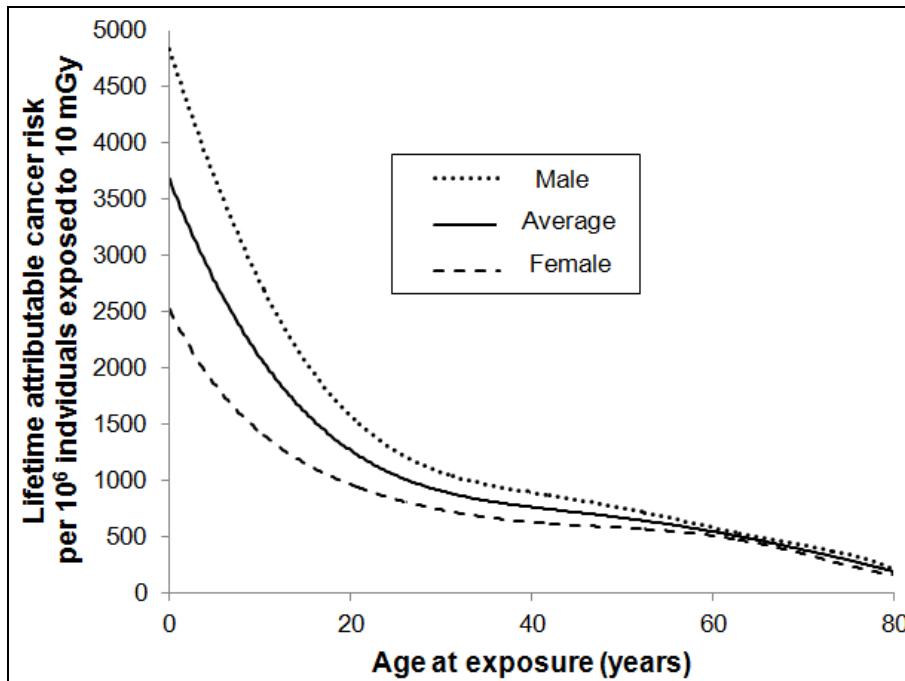| Age group (years)	Risk factor
<10	x3
10-20	x2
20-30	x1.5
30-50	x0.5
50-80	x0.3
80+	Negligible

Figure 4.1 Estimated lifetime attributable cancer risk from radiation as a function of age at exposure, based on BEIR VII risk models [23,24]

The relation between BMI and entrance skin dose is shown in Figure 4.3. The TLD value at the mouth was used, as it can be assumed that it was in the primary beam for all exposures. There was no clear correlation between BMI and entrance skin dose for any CBCT. For the NewTom 9000, a normalisation was attempted by dividing the doses by the mAs, which is determined automatically based on the density distribution of the scout image. However, there was no improvement in correlation for the normalised values.

Table 4.2 Patient information for skin dose measurements

	SCANORA 3D				NewTom 9000 (Centre 1)				NewTom 9000 (Centre 2)			
	Min	Med	Max	Avg	Min	Med	Max	Avg	Min	Med	Max	Avg
Age (years)	10	41	64	37.5	12	42	61	37.8	8	32	83	34.4
Interpupillary distance (mm)	5	6	8	6.2	5.6	6.2	6.5	6.2	4.6	5.8	7	6
Chin-thyroid distance (mm)	5	7	8.5	6.9	5.5	6.5	7	6.4	4.2	6	7	5.9
Length (cm)	135	169	194	167.9	152	168	185	168	135	168	198	167.3
Weight (kg)	27	65	116	64.2	43	66	95	65.5	25	65	176	67
BMI (kg/m^2)	13.8	22.4	34.5	22.5	18.1	24.2	29.3	23.1	12.7	23.7	40.4	23.7
	Male	Female	Total		Male	Female	Total		Male	Female	Total	
Percentage	43%	57%	100%		N/A	N/A	N/A		41%	59%	100%	
Number of patients	37	50	87		N/A	N/A	38		59	85	144	

Table 4.3 Entrance skin doses for SCANORA 3D and NewTom 9000

|	SCANORA 3D				NewTom 9000 (Centre 1)				NewTom 9000 (Centre 2)			
	Min	Avg	Max	SD	Min	Avg	Max	SD	Min	Avg	Max	SD
Eyes	44	196	1968	228	180	669	1630	360	20	581	2337	536
Parotid	102	1236	2524	443	690	1341	2770	376	71	1115	2625	373
Mouth	265	2076	3843	439	1530	2299	3980	631	147	2327	3690	929
Submandibular	66	1029	2317	760	430	1211	1785	217	138	718	1875	411
Thyroid	23	284	2559	421	400	1007	1600	377	6	131	1027	143
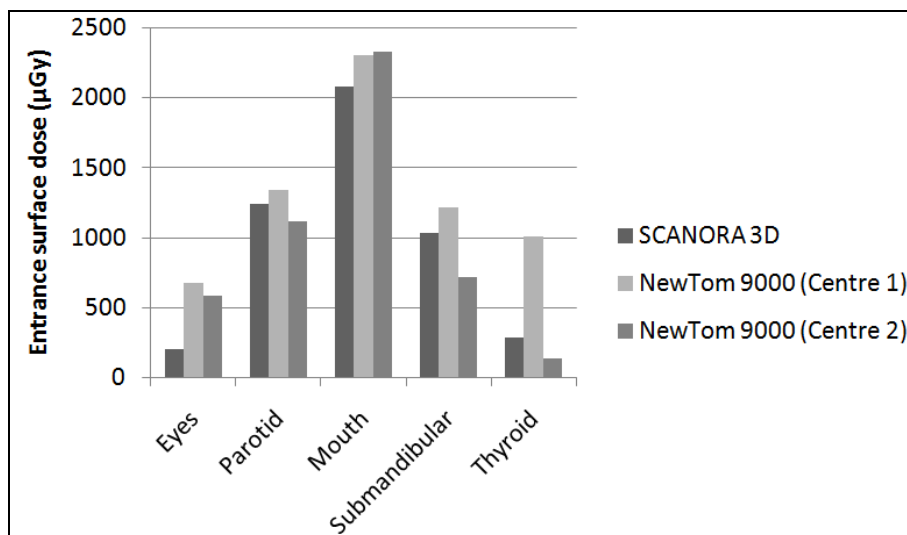
Figure 4.2 Average entrance skin dose for three CBCT devices at 5 skin locations

Correlation coefficients and conversion factors between selected skin TLDs and organ doses from ART phantom measurements are depicted in Table 4.4. For red bone marrow and skin, the average of all 8 TLD locations resulted in the best correlation. For all other organs, a selection of TLD locations ranging between 2 (brain) and 7 (bone surface) was made to obtain the highest possible correlation. Figure 4.4 shows scatter plots for the organs with the highest contribution to the effective dose.

Using the mass energy absorption coefficients from ICRU Publication 44, the skin-to-organ conversion factors from Table 4.4 and the age-dependent risk estimation shown in Figure 4.1, the lifetime attributable cancer risk was calculated for each patient. For the SCANORA 3D, the incidence risk varied between 0.00016% (49 y.o.) and 0.0023% (10 y.o.). For the NewTom 9000, the risk varied between 0.00034% (61 y.o.) and 0.0014% (15 y.o.) for Centre 1 and between 0.000042% (83 y.o.) and 0.001485% (14 y.o.) for Centre 2. The ratio between the highest and lowest risk for the three centres was 14, 4 and 36, respectively. The sum of each individual estimated risk for the 269 patients included in this study was 0.17%.

There was no clear relation between the clinical indication and entrance skin dose for any device. For the SCANORA 3D, the FOV size was fixed at the clinically used value of 100x75 mm for all except two (145x75 mm) exposures, and the tube current was fixed at 8 for all but one (15 mA) exposures. For the NewTom 9000, the FOV height was manually adjusted based on patient size and mAs was automatically determined using the scout image. Therefore, for the two devices in this study, there was no clear distinction for the entrance skin dose between different clinical indications. However, the risk estimations did vary

between indication due the varying age distribution, with the highest risk seen for the orthodontic and impacted teeth groups and the lowest risk for the implant group.
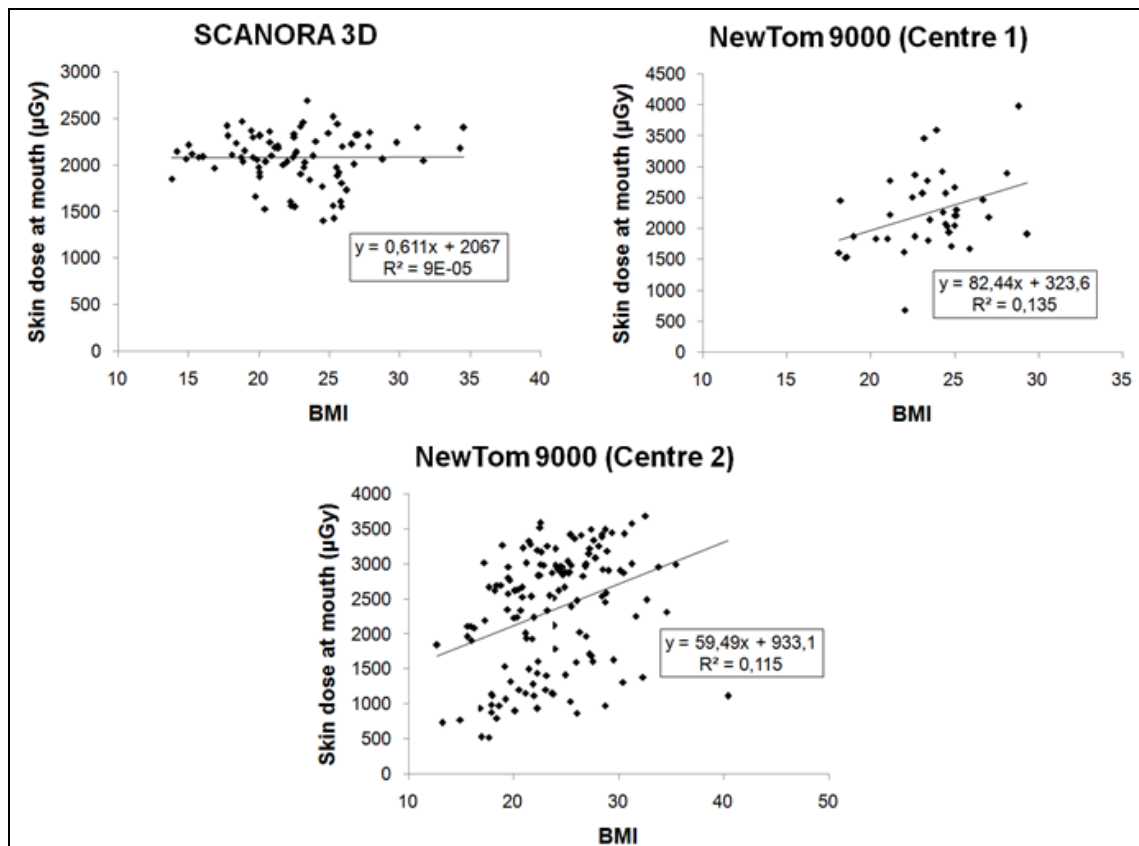

Figure 4.3 Relation between BMI and entrance skin dose at the mouth area. Three values from non-standard exposure protocols were removed for the SCANORA 3D. One value with assumed non-direct exposure to the mouth was removed for NewTom 9000 (Centre 2).

Table 4.4 TLD locations and conversion factors used for individual absorbed organ dose estimations based on entrance skin dose.

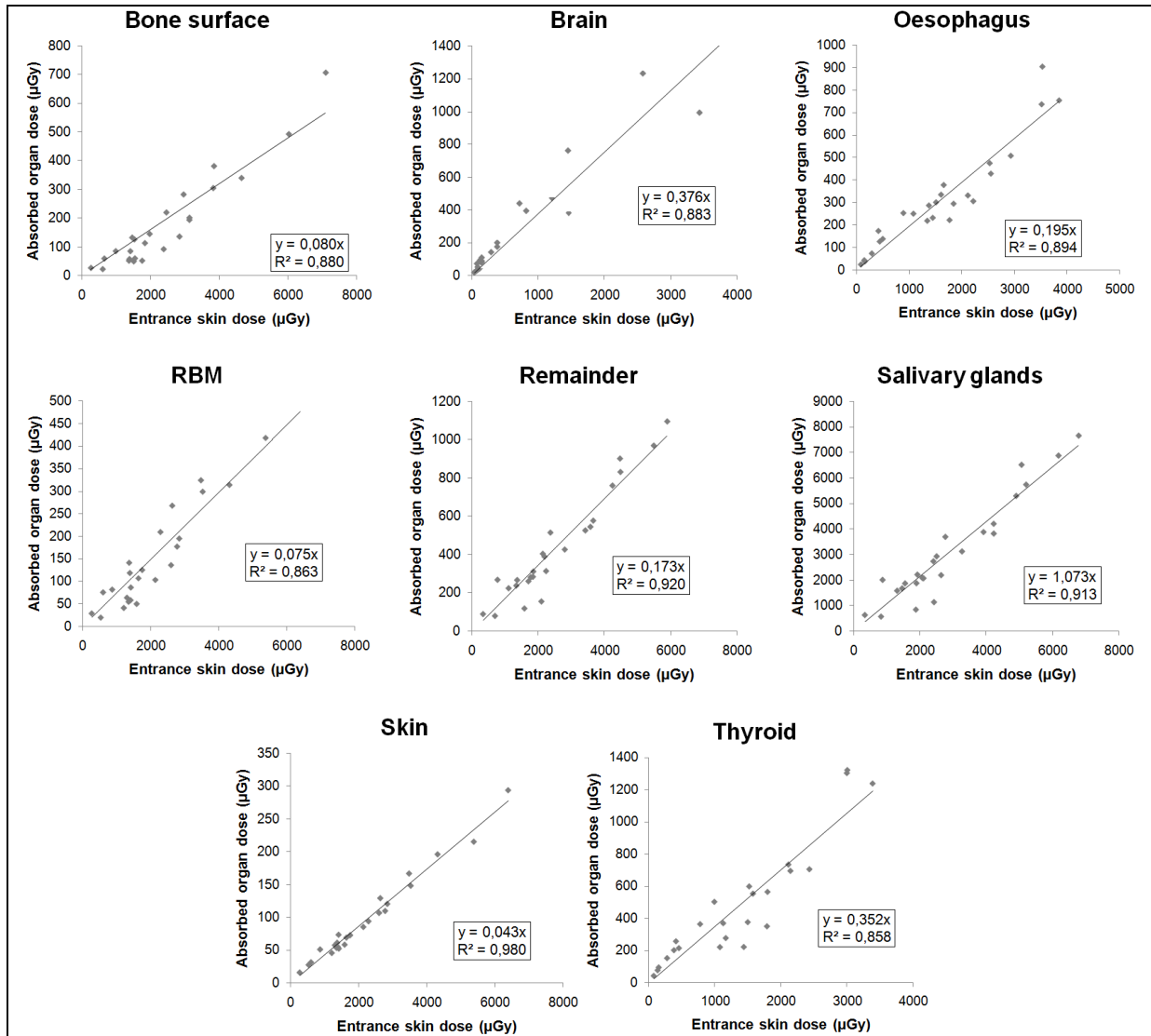|	Skin TLD locations	Number of skin TLD locations	Conversion factor
Bone surface	All except thyroid	7	0.080
Brain	Eyes	2	0.376
Oesophagus	Thyroid, submandibular	3	0.194
RBM	All	8	0.075
Remainder	All except eyes	6	0.173
Salivary	Parotid, submandibular, mouth	5	1.073
Skin	All	8	0.043
Thyroid	Thyroid, submandibular	3	0.352

Figure 4.4 Correlation between entrance skin dose and organ doses using anthropomorphic phantom data from various CBCT devices

4.5 Discussion

Patient risk from radiation has been a continuing concern in dental imaging, due to the frequency of X-ray examinations in dental practice. The introduction of CBCT in dentistry has brought an opportunity for dose reduction, as it generally operates at lower exposure levels compared to MSCT, and can be a useful alternative for certain applications [1]. However, as CBCT doses are higher than those of conventional 2-D radiographic techniques, its use as a replacement or complement to intra-oral, panoramic or cephalometric radiography should be considered with great care, particularly for children. Radiation dose for dental CBCT has been thoroughly assessed in many studies by estimating organ and effective doses

using anthropomorphic phantoms [2-5]. Most of these phantoms represent an average adult male, although paediatric phantoms representing varying ages are commercially available [14]. Still, doses obtained from these reference phantoms cannot be directly applied as patient risks. The effective dose, as defined by the ICRP, can only be measured using these reference phantoms; for patients, the actual risk from exposures to ionising radiation is determined by additional patient-specific factors (*i.e.* age at exposure, size and weight, anatomical characteristics)[20,22,23]. In this study, the estimation of individual patient risks from dental CBCT examinations was performed, using entrance skin dose measurements, conversion factors for organ doses based on anthropomorphic phantom measurements, and age-dependent risk estimations.

Entrance skin doses were similar for most TLD locations for the three devices included in this study. These devices, however, do not represent the dose range found in dental CBCT; lower doses can be achieved by devices with smaller FOV sizes, and much higher doses (with entrance skin dose values above 10 mGy) have been reported for other devices. It is therefore not feasible to use the values from this study in the context of diagnostic reference levels (DRL); reference levels based on dosimetry can only be proposed when this dosimetric parameter (*i.e.* a suitable dose index) has been applied to a large sample of the available CBCT devices and exposure protocols. For many radiographic techniques, an appropriate dose index is available, and many authors have proposed DRLs for a variety of medical X-ray techniques based on large-scale dose surveys [25-36]. For dental CBCT, a dosimetric study by Holroyd and Walker on 41 CBCT units measuring the dose-area product (DAP) resulted in a proposal of a DAP of 250 mGy.cm² for a specific indication (*i.e.* implant placement, upper molar region, adult patient), by normalising their measured value to a 4x4 cm² beam area [36]. Although it provides a useful starting point, the definition of appropriate DRLs (without the need for normalisation) should be further explored, taking all different clinical indications and age groups into account.

A particular finding in this study is that the entrance skin dose in the thyroid area was much higher for one of the centres using the NewTom 9000. It was found that the FOV is routinely positioned lower at this centre, due to the lack of detailed positioning criteria for CBCT. As the thyroid gland is one of the key organs affecting the total risk from head and neck exposures, a significant dose reduction could be achieved by positioning the field as high as possible at all times. Because of the sharp dose gradient at the edge of the beam [37], a clear reduction in thyroid dose could be achieved by adjusting the FOV, placing it as cranially as possible.

78

The conversion from skin dose to organ dose was calculated using conversion factors derived from the measurements on the Alderson Radiation Therapy phantom, representing an average adult male. Using a large number of TLDs carefully distributed over the head and neck of the phantom, it was ensured that the uncertainty of the organ dose estimations was kept as low as possible. However, there are additional uncertainties involved in the conversion between skin and organ doses performed in this study. First of all, as seen in Figure 4.4, the relation between skin dose and organ doses varied somewhat between CBCT devices and exposure protocols, due to the interplay between different variable exposure parameters (*e.g.* beam energy, FOV size and position). R^2 values for the scatter plots in Figure 4.4 ranged between 0.858 and 0.960, showing reasonable deviations from a linear relation. As this study involved only two CBCT devices with a limited variety of exposure protocols, it can be assumed that the error in organ dose conversion due to variety in exposure parameters did not vary considerably between individuals.

The second uncertainty regarding the conversion to organ dose is related to the fact that this conversion did not take differences in individual anatomy into account. The use of a single anthropomorphic phantom for the calculation of conversion factors assumes that the relative distribution of the different radiosensitive organs in relation with the skin TLD positions is identical for each individual, and equal to the organ distribution in the Alderson Radiation Therapy phantom In reality, variations in patient size, gender, age and anatomy will affect the size and position of radiosensitive organs related to the selected locations for skin dose measurements. This anatomical variation is partly picked up by the skin dose measurements, as they are affected to some extent by patient size and anatomy. However, for each organ dose there is a degree of uncertainty due to potential differences between individuals. For most organs (*i.e.* red bone marrow, bone surface, skin, brain, oesophagus), this uncertainty is reasonable. For the salivary glands and thyroid, some anatomical variation may occur; in addition, the size and shape of the thyroid varies with age. To investigate the actual variability of organ distributions in the head and neck and their effect on patient dose and risk, Monte Carlo simulations using deformable models or actual patient data should be performed [38]. Based on the distribution of entrance skin dose values for the patients in this study, it is clear that the effect of the BMI is limited, or at least obscured by other factors. From the scatter plots in Figure 4.3, it can be concluded that skin doses in the mouth area were normally (or bivariate normally, for NewTom 9000 at Centre 2) distributed with no clear effect from the BMI, even after normalising the values for tube output. The entrance skin dose can therefore be considered as a result from different exposure factors (*i.e.* tube output, FOV

size and position, patient factors) with a minor influence from the BMI. However, it is possible that doses for non-surface organs are affected by the BMI more clearly, as the skin dose will be mainly composed of direct (unattenuated) exposure, whereas organ doses are more susceptible to varying degrees of beam attenuation. This is another limitation to the conversion from skin dose to organ doses, as the conversion factors were determined using the ART phantom, assuming similar beam attenuation levels for different patients. The effect of patient size on organ doses should be further explored using dose simulation on varying model sizes.

Using a gender-averaged risk estimation based on the BEIR VII report, an age-dependant risk estimation was performed [19,22,23]. The individual patient risks calculated in this study showed a wide range, determined by both the entrance skin dose values (*i.e.* the combination of exposure factors and patient factors) and the age at exposure. Although there was no distinction possible between clinical indication groups based on entrance skin dose, it was clear that paediatric indications (*e.g.* impacted teeth, orthodontic planning) showed higher risk levels than adult indications (*e.g.* implant planning). The evaluation of effective doses of CBCT using paediatric phantoms showed that dose levels were similar to adult dose ranges, as most CBCT devices have implemented paediatric exposure protocols (*i.e.* FOV and/or tube output reduction). However, the actual risk for children will always be higher due to the effect of the age at exposure. Therefore, the added value of a CBCT scan to a conventional 2-D radiographic examination should always be judged with great care for children, and optimisation of exposures is pivotal seeing that a suboptimal exposure protocol may lead to considerable dose levels. After a quick search of the available CBCT patient databases, we found that the youngest patient referred for a CBCT scan was found to be 3 years and 5 months at the time of the exposure, corresponding to a risk multiplication of x3.4 compared to a 30 year old according to Figure 4.1. CBCT users and referrers should be aware of the increased radiation risk for children, and apply the ALARA principle even more strictly compared to adult patients [39].

4.6 Conclusion

The entrance skin dose measurements in this study demonstrated the combined effect of exposure and patient factors on the dose uptake. Conversion factors were determined to estimate absorbed organ doses using skin measurements, and age-dependent cancer risk was estimated. The actual radiation risk was primarily influenced by the age at exposure, pointing

out the need for age-related justification and optimisation of CBCT exposures. Special attention for optimised radiation is needed for children.

4.7 References

1. Jacobs R. Dental cone beam CT and its justified use in oral health care. JBR-BTR 2011; 94: 254-265.

2. Pauwels R, Beinsberger J, Collaert B, Theodorakou C, Rogers J, Walker A, Cockmartin L, Bosmans H, Jacobs R, Bogaerts R, Horner K, The SEDENTEXCT Project Consortium. Effective dose range for dental cone beam computed tomography scanners. Eur J Radiol 2012; 81: 267-271.

3. Suomalainen A, Kiljunen T, Käser Y, Peltola J, Kortesniemi M. Dosimetry and image quality of four dental cone beam computed tomography scanners compared with multislice computed tomography scanners. Dentomaxillofac Radiol 2009; 38: 367-378.

4. Loubele M, Bogaerts R, Van Dijck E, Pauwels R, Vanheusden S, Suetens P, Marchal G, Sanderink G, Jacobs R. Comparison between effective radiation dose of CBCT and MSCT scanners for dentomaxillofacial applications. Eur J Radiol 2009; 71: 461-468

5. Silva MA, Wolf U, Heinicke F, Bumann A, Visser H, Hirsch E. Cone-beam computed tomography for routine orthodontic treatment planning: a radiation dose evaluation. Am J Orthod Dentofacial Orthop 2008; 133: 640.e1-5.

6. International Commission on Radiological Protection. Recommendations of the International Commission on Radiological Protection. ICRP Publication 103. Ann ICRP 37. Oxford, UK: Pergamon Press 2007.

7. Marine PM, Stabin MG, Fernald MJ, Brill AB. Changes in radiation dose with variations in human anatomy: larger and smaller normal-stature adults. J Nucl Med 2010; 51: 806-811.

8. Cassola VF, Milian FM, Kramer R, de Oliveira Lira CA, Khoury HJ. Standing adult human phantoms based on 10th, 50th and 90th mass and height percentiles of male and female Caucasian populations. Phys Med Biol 2011; 56: 3749-3772.

9. Borisova R, Ingilizova Ch, Vassileva J. Patient dosimetry in paediatric diagnostic radiology. Radiat Prot Dosimetry 2008; 129: 155-159.

10. Sorantin E, Weissensteiner S, Hasenburger G, Riccabona M. CT in children - dose protection and general considerations when planning a CT in a child. Eur J Radiol. 2012 Jan 5. [Epub ahead of print]

11. Frush DP, Frush KS. In a New Kind of Light: Patient Safety in Pediatric Radiology. Clin Ped Emerg Med 2006; 7: 255-260.

12. Azevedo AC, Osibote OA, Boechat MC. Paediatric x-ray examinations in Rio de Janeiro. Phys Med Biol 2006; 51: 3723-3732.

13. Lee C, Lee C, Staton RJ, Hintenlang DE, Arreola MM, Williams JL, Bolch WE. Organ and effective doses in pediatric patients undergoing helical multislice computed tomography examination. Med Phys 2007; 34: 1858-1873.

14. Theodorakou C, Walker A, Horner K, Pauwels R, Bogaerts R, Jacobs R; The Sedentexct Project Consortium. Estimation of paediatric organ and effective doses from dental cone beam CT using anthropomorphic phantoms. Br J Radiol 2012; 85: 153-160

15. Gogos KA, Yakoumakis EN, Tsalafoutas IA, Makri TK. Radiation dose considerations in common paediatric X-ray examinations. Pediatr Radiol 2003; 33: 236-240.

16. Kiljunen T, Tietäväinen A, Parviainen T, Viitala A, Kortesniemi M. Organ doses and effective doses in pediatric radiography: patient-dose survey in Finland. Acta Radiol. 2009; 50: 114-124.

17. Montgomery A, Martin CJ. A study of the application of paediatric reference levels. Br J Radiol 2000; 73: 1083-90.

18. Sulieman A, Theodorou K, Vlychou M, Topaltzikis T, Kanavou D, Fezoulidis I, Kappas C. Radiation dose measurement and risk estimation for paediatric patients undergoing micturating cystourethrography. Br J Radiol 2007; 80: 731-737.

19. International Commission on Radiological Protection (1990) Recommendations of the International Commission on Radiological Protection. ICRP Publication 60. Ann ICRP. Oxford, UK: Pergamon Press, 1991.

20. International Commission on Radiological Protection. Recommendations of the International Commission on Radiological Protection. ICRP Publication 103. Ann ICRP 37. Oxford, UK: Pergamon Press 2007.

21. International Commission on Radiation Units and Measurements. Tissue Substitutes in Radiation Dosimetry and Measurement. ICRU Report 44. Bethesda, Maryland, USA: ICRU Publications 1989.

22. Brenner DJ. Effective dose: a flawed concept that could and should be replaced. Br J Radiol 2008; 81: 521-523.

23. National Research Council of the National Academies. Health Risks from Exposure to Low Levels of Ionizing Radiation - BEIR VII. Washington, DC: The National Academies Press 2006.

24. Hall EJ, Brenner DJ. Cancer risks from diagnostic radiology. Br J Radiol 2008; 81: 362-378.

25. Berni D, Gori C, Lazzari B, Mazzocchi S, Rossi F, Zatelli G. Use of TLD in evaluating diagnostic reference levels for some radiological examinations. Radiat Prot Dosimetry 2002; 101: 411-413.

26. Freitas MB, Yoshimura EM. Diagnostic reference levels for the most frequent radiological examinations carried out in Brazil. Rev Panam Salud Publica 2009; 25: 95-104.

27. González L, Vañó E, Fernández R. Reference doses in dental radiodiagnostic facilities. Br J Radiol. 2001; 74: 153-156.

28. Hart D, Hillier MC, Wall BF. National reference doses for common radiographic, fluoroscopic and dental X-ray examinations in the UK. Br J Radiol 2009; 82:1-12.

29. Hatziioannou K, Psarouli E, Papanastassiou E, Bousbouras P, Kodona H, Kimoundri O, Delichas M. Quality control and diagnostic reference levels in intraoral dental radiographic facilities. Dentomaxillofac Radiol 2005; 34: 304-307.

30. Helmrot E, Alm Carlsson G. Measurement of radiation dose in dental radiology. Radiat Prot Dosimetry 2005; 114: 168-171.

31. Ziliukas J, Krynke L, Urboniene A. Management of patient doses and diagnostic reference levels in X-ray radiography in Lithuania. Radiat Prot Dosimetry 2010; 139: 313-316.

32. Padovani R, Vano E, Trianni A, Bokou C, Bosmans H, Bor D, Jankowski J, Torbica P, Kepler K, Dowling A, Milu C, Tsapaki V, Salat D, Vassileva J, Faulkner K. Reference levels at European level for cardiac interventional procedures. Radiat Prot Dosimetry 2008; 129: 104-107.

33. Papageorgiou E, Vardalaki E, Hourdakis CJ, Dimitriou P. Estimation of doses received by patients undergoing radiological examinations in Greece. Radiat Prot Dosimetry 2001; 93: 31-41.

34. Vassileva J, Dimov A, Slavchev A, Karadjov A. Bulgarian experience in the establishment of reference dose levels and implementation of a quality control system in diagnostic radiology. Radiat Prot Dosimetry 2005; 117: 131-134.

35. Walker C, van der Putten W. Patient dosimetry and a novel approach to establishing Diagnostic Reference Levels in dental radiology. Phys Med 2012; 28: 7-12.

36. Holroyd JR, Walker A. Recommendations for the Design of X-ray Facilities and the Quality Assurance of Dental Cone Beam CT (Computed Tomography) Systems – A report of the HPA Working Party on Dental Cone Beam CT. HPA-RPD-065. Health Protection Agency, March 2010.

37. Pauwels R, Theodorakou C, Walker A, Bosmans H, Jacobs R, Bogaerts, Horner K, The SEDENTEXCT Project Consortium. Dose distribution for dental cone beam CT and its implication for defining a dose index. Dentomaxillofac Radiol. In press.

38. Zhang G, Pauwels R, Marshall N, Shaheen E, Nuyts J, Jacobs R, Bosmans H. Development and validation of a hybrid simulation technique for cone beam CT: application to an oral imaging system. Phys Med Biol; 56: 5823-5843.

39. Horner K, Islam M, Flygare L, Tsiklakis K, Whaites E. Basic principles for use of dental cone beam computed tomography: consensus guidelines of the European Academy of Dental and Maxillofacial Radiology. Dentomaxillofac Radiol 2009; 38: 187-195.

Chapter 5: Dose distribution for CBCT and its implication for defining a dose index

5.1 Abstract

Objectives: to characterise the dose distribution for a range of cone beam computed tomography (CBCT) units, investigating different field of view sizes, central and off-axis geometries, full or partial rotations of the X-ray tube and different clinically applied beam qualities. The implications of the dose distributions on the definition and practicality of a CBCT dose index were assessed.

Materials and methods: Dose measurements on CBCT devices were performed by scanning cylindrical head size water and polymethyl methacrylate (PMMA) phantoms, using thermoluminescent dosimeters (TLD), a small-volume ion chamber and radiochromic films.

Results: It was found that the dose distribution can be asymmetrical for dental CBCT exposures throughout a homogeneous phantom, due to an asymmetrical positioning of the isocentre and/or partial rotation of the X-ray source. Furthermore, the scatter tail along the z-axis was found to have a distinct shape, generally resulting in a strong (90%) drop in absorbed dose outside the primary beam.

Conclusions: There is no optimal dose index available due to the complicated exposure geometry of CBCT and the practical aspects of quality control measurements. Practical validation of different possible dose indices is needed, as well as the definition of conversion factors to patient dose.

5.2 Introduction

As seen in the previous chapters, there is an increasing number of manufacturers of CBCT units offering a large variety of devices with considerable differences in exposure parameters, such as field of view (FOV) size, beam quality (tube voltage and filtration), X-ray exposure (mAs) and rotation angle [1]. Chapters 1-3 and various other studies have pointed out the wide range of effective doses for CBCT devices, and many authors have indicated that the exposure used for different types of patients should be adjusted based on patient size, image

quality requirements and field size requirements [2-7]. Such optimisations require a standardised dose index, which can be any dose descriptor that can be measured in practice and allows for dose characterisation, device intercomparison and estimation of patient risk.

In single and multi-detector CT (MDCT) scanners, the computed dose index (CTDI) is the international dose assessment metric (IEC 60601-2-44 2002) that is used to quantify the radiation output of the scanners. $CTDI_{100}$ is the 100 mm long integral of the dose profile along a line perpendicular to the axial (XY) plane divided by the beam collimation. It can be determined using a 100 mm long ionisation chamber either free in air or in CT dosimetry phantoms. The weighted CTDI ($CTDI_w$) can be calculated by combining central and peripheral measurements and represents the average dose in the scan plane. CTDI measurements are part of standardised quality assurance protocols and are generally used for dose optimisation in CT. Moreover, CTDI allows the estimation of the effective dose to the patient using conversion factors [8]. The use of $CTDI_{100}$ has been under investigation lately for both CBCT and MDCT [8-15]. It has been shown by different authors that the increasing beam width used by modern MDCT scanners leads to a significant underestimation of the axial (z-axis) dose when measuring the $CTDI_{100}$, as the scatter tails are not fully measured by the 100 mm pencil ion chamber [9-12]. In addition, there are commercially available dental CBCT units that offer FOVs that exceed the length of the 100 mm pencil ionisation chamber. Different solutions for capturing the entire scatter tail have been proposed, and the current state of the technology leads to believe that a small-volume ion chamber is currently the best option to measure an appropriate dose index for MDCT in the field [9].

CBCT devices used in dentistry are inherently different from MDCT scanners, and it has been pointed out before that the CTDI is not applicable for CBCT [10,15]. Because of its particular exposure geometry, a separate dose index needs to be defined which is applicable to all dental CBCT devices. There are a few factors distinguishing CBCT from MDCT which need to be taken into account before adapting or defining a suitable dose index. Dental CBCT devices exhibit a wide range of FOV sizes, ranging from a few cm in diameter and height to a FOV which can cover the entire head. It can be expected that dose distributions vary considerably for different FOV sizes [16]. In addition, the isocentre (*i.e.* the centre of the FOV) can be positioned centrally or peripherally in the patients head, affecting the dose distribution to all head and neck organs [15]. Another source of asymmetrical dose distribution is a partial exposure along a rotation arc ranging between 180° and 200°, which is implemented by different CBCT manufacturers. Furthermore, a number of devices use a 'half

beam' scanning technique, resulting in an overlapping exposed region surrounding the isocentre, leading to further inhomogeneities in dose distribution.

As an alternative dose index for CBCT, the dose area product (DAP) measured with a transmission ionisation chamber has been proposed [15,17-19]. The DAP provides an estimation of the tube output in terms of dose and field size. However, the use of DAP as a dose index is limited because it does not take any of the specific geometric exposure issues in dental CBCT into account. It is possible for two CBCT exposure protocols to have the exact same DAP value, despite having considerable differences for all exposure factors mentioned above (*i.e.* beam quality, mAs, FOV size, FOV position, rotation arc, half beam). As all of these factors determine the actual distribution of dose throughout the patient, it is not possible at this moment to link DAP values to patient dose.

All of these pieces of information must be considered when developing a dose index for dentomaxillofacial CBCTs. An improved knowledge of the complex dose distributions associated with available CBCT systems would aid the definition of a dose index that can be measured during routine quality control and is relevant for patient dose estimation. The aim of this study, therefore, was to perform dose distribution measurements on a range of CBCT devices using cylindrical phantoms and different dosimetric methods.

5.3 Materials and methods

Two types of phantoms were used for dose measurements: a cylindrical water phantom and a customized cylindrical PMMA phantom. Both phantoms allowed different types of dose measurements to be undertaken. Measurements were made on eight dental CBCT units, across the axial, coronal and sagittal planes and for a range of FOVs, isocentre positions and rotation arcs. The coordinate system and definitions used throughout this article are illustrated in Figure 5.1. Table 5.1 provides an overview of the different CBCT devices that were involved and the different exposure protocols that were investigated.

Phantoms and dosimeters

A water phantom was used for measuring the dose distributions across all planes. The phantom consists of a plastic cylinder of 15 cm diameter and 25.5 cm height which was filled with water, enabling measurements at various positions using TLDs and an ionisation chamber (Figure 5.2). Additionally, a PMMA phantom was developed for measuring the dose distributions along the x-y plane using TLDs and radiochromic film. It was manufactured by

Leeds Test Objects Ltd (Boroughbridge, UK). It consists of 7 interchangeable slices of 16cm diameter and 2.8 cm thickness (Figure 5.3). Two dedicated slices were manufactured to accommodate TLDs and films. An extra disc positioned at the top of the phantom was designed to allow alignment of the phantom with the laser beams of the CBCT units.
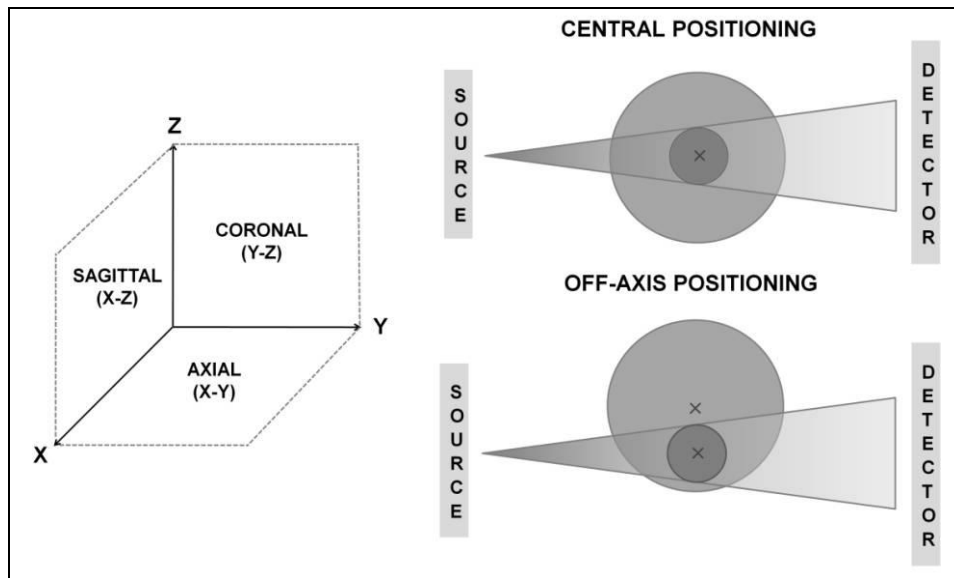

Figure 5.1 Coordinate system and terminology used for dose measurements.

Two types of TLDs (Harshaw Thermo Fisher Scientific Inc, Waltham, USA) were used in this study: TLD-100 (LiF:Mg,Ti) at Leuven and TLD-100H (LiF:Mg,Cu,P) at Manchester. The TLD-100 were calibrated using an ionisation chamber with a calibration factor traceable to a Secondary Standard Dosimetry Laboratory (SSDL, Gent, Belgium). The TLD-100H were individually calibrated against an ionisation chamber with calibration traceable to national standards (National Physical Laboratory, London, UK), using a conventional diagnostic X-ray tube at 80 kVp. For both TLD types, a selection was performed by repeating the calibration process and discarding TLDs if the read-out value from the repeated exposures varied more than 3%. Furthermore, a series of inter-comparison measurements was performed to ensure consistency between the measurements from the two TLD types.
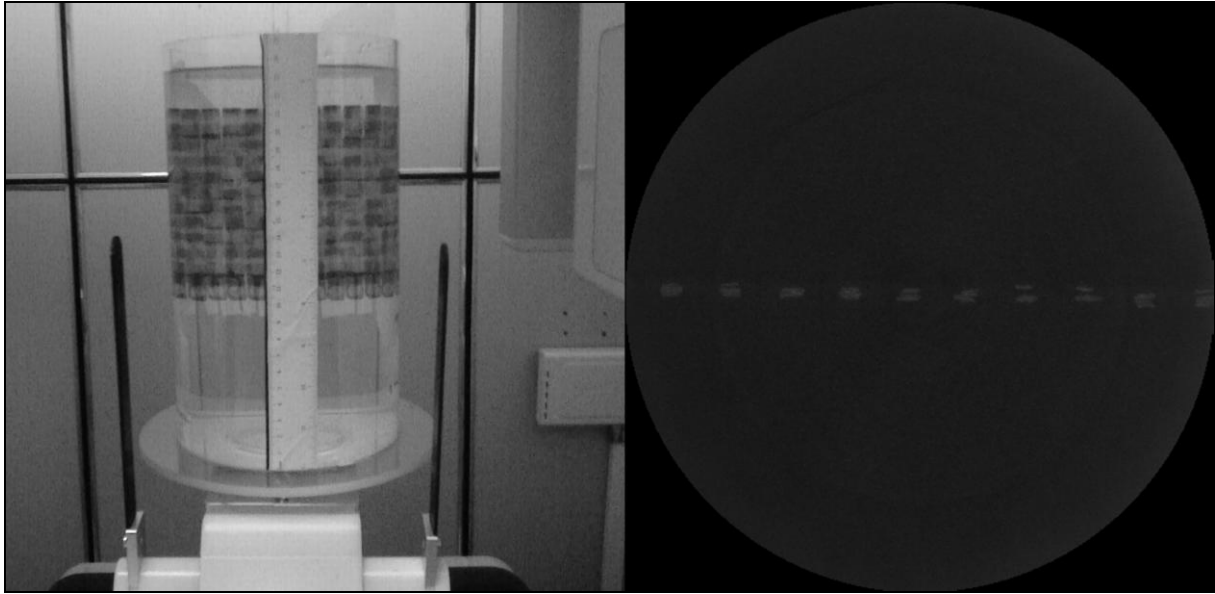
Figure 5.2 Left: Water phantom positioned in the SCANORA 3D, showing 14x11 TLD grid in the y-z plane. Right: axial (x-y) maximum intensity projection image of the reconstructed scan, superposing all TLDs within the FOVs. The distribution of the TLDs in the x-y plane was within a 3 mm margin.
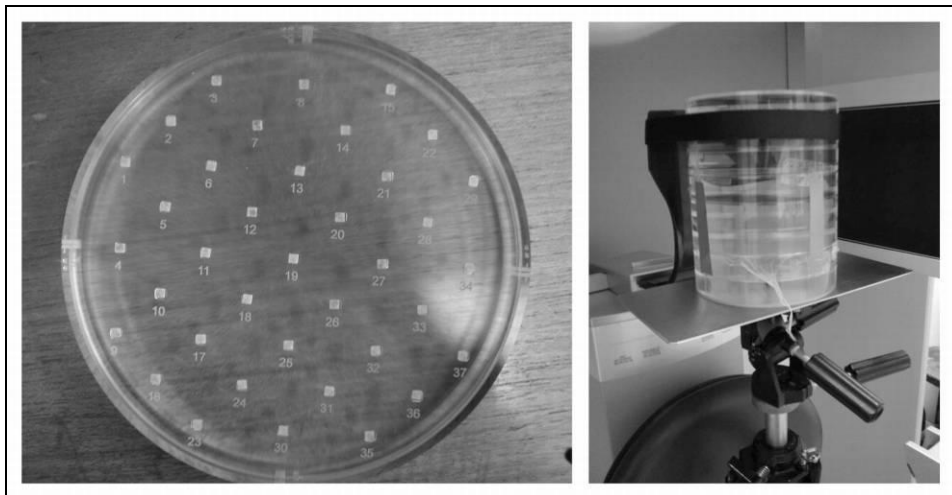

Figure 5.3 PMMA phantom for dose distribution. Left: slice loaded with TLDs. Right: phantom in position for measurement.

Table 5.1 Exposure factors used for water and PMMA phantom measurements

Device	Rotation	Phantom positioning	kVp	mAs	FOV size (cm)[a]
Ion chamber measurements in water phantom, x-z plane					
SCANORA 3D	360	central	85	30	10x7.5
TLD measurements in water phantom, x-z and y-z planes					
SCANORA 3D	360	central	85	30	10x7.5
SCANORA 3D	360	off-axis	85	36	6x6
3D Accuitomo XYZ	360	off-axis	80	70	4x3
TLD measurements in water & PMMA phantoms, x-y plane					
GALILEOS	200	off-axis	85	28	15x15
SCANORA 3D	360	off-axis	85	30	10x7.5
ILUMA Elite	360	central	120	76	21x14
ILUMA Elite	360	off-axis	120	76	21x14
NewTom VG	360	central	110	9.6	23x23
NewTom VG	360	off-axis	110	6.1	23x23
3D Accuitomo 170	360	central	90	87.5	4x4, 6x6, 8x8, 14x5,14x10
3D Accuitomo 170	360	off-axis	90	87.5	4x4
3D Accuitomo 170	180	central	90	45	10x10
i-CAT N.G.	360	central	120	18.5	8x8, 16x6
i-CAT N.G.	360	off-axis	120	18.5	8x8, 16x6
i-CAT N.G.	180	central	120	9.3	8x8
ProMax 3D	200	central	84	17.1	8x5, 8x8
ProMax 3D	200	off-axis	84	17.1	8x5

PMMA, polymethyl methacrylate; *FOV*, field of view; *TLD*, thermoluminescent dosimeter
[a]diameter x height

For ionisation chamber measurements a 0.6 cm^3 chamber (Farmer FC65-G, IBA Dosimetry, Schwarzenbruck, Germany) was used, which was calibrated in a RQR5 diagnostic beam. Radiochromic films (XR-QA, Gafchromic, International Specialty Products, USA) were used to visualize the two dimensional axial dose distribution, but were not calibrated for absorbed dose as it is difficult to obtain accurate quantitative results from film measurements [20].

Measurements in x-z and y-z planes

A first measurement was performed by placing 154 TLDs in the water phantom in a vertical grid pattern in the y-z plane at 1 cm intervals (Figure 5.2). The grid contained 11 rows and 14 columns, spanning an area of 13x10 cm. It was attached to a sheet of transparent paper which was fixed in the cylindrical phantom. The grid was exposed with the SCANORA 3D unit, using the standard protocol for adult patients (Table 5.1) and placing the isocentre of the x-ray

beam at the midpoint of the grid (both horizontally and vertically), which coincided with the midpoint of the cylinder. Using this scanning protocol and phantom set-up, rotational symmetry of the dose distribution can be assumed. Therefore, the angle of the grid could be chosen freely. The y-z plane was selected to allow for accurate phantom and grid positioning. The placement of the grid was verified after scanning.

As a subsequent evaluation of scattered radiation along the z-axis, ion chamber measurements were performed on the SCANORA 3D (Table 5.1) at 1 cm intervals along the z-axis at four different x-coordinates corresponding to a central, peripheral and two mid-peripheral positions in the FOV. Measurements were repeated for each position to check for consistency, and corrected for temperature and pressure.

Further measurements with TLDs were performed to completely visualise the scatter tails. Firstly, the SCANORA 3D's small FOV was used, using standard exposure settings (Table 5.1). The field was positioned non-centrally, with the isocentre placed at 5 cm from the central point of the cylinder, simulating a dental examination (incisor/canine region). For this measurement, a grid of 76 TLDs was used. This grid contained 4 columns of 19 TLDs each, interspaced at 1 cm. Due to z-axis symmetry, the columns were positioned on one side of the central x-y plane, covering coordinates from z = 0 cm up to z = 18 cm. The 4 columns were positioned with variable intervals along the y-axis: centrally in the FOV, 1.5 cm from the isocentre (on the midpoint between the isocentre and border of the FOV), and at 4.5 cm and 6 cm from the isocentre (both outside the FOV). For a further evaluation, the 3D Accuitomo XYZ was used. This device uses a small-sized FOV of 4x3cm. For this measurement, a TLD distribution was used similar to the previous with a grid of 76 TLDs divided into 4 columns with a 1 cm interspace along the z-axis. The isocentre was placed at 5.5 cm from the centre of the cylinder. The placement of the columns was adapted to obtain the same relative positions compared to the previous measurement (*i.e.* at 0 cm, 1 cm, 3 cm and 4 cm from the isocentre).

Measurements in x-y plane

Two different measurement grids were used for the x-y plane, using the water phantom and PMMA phantom. For the water phantom, 69 TLDs were used. The distance between adjacent TLDs in any row was 2 cm, and adjacent rows were shifted 1 cm. For the PMMA phantom, 37 TLDs were used, positioned 3 cm apart. Measured values were inserted into a matrix, and empty cells were interpolated. Measurements were performed on seven CBCTs, combining central and off-axis positioning as well as full and partial rotation arcs (Table 5.1). For all x-y measurements, the beam was positioned at the vertical centre of the phantom, corresponding

with the height of the TLD grid. As a result, all measurements were performed in the mid-axial plane.

5.4 Results

Measurements in x-z and y-z planes

Figure 5.4 shows a surface plot of the dose distribution in water measured by TLDs using a 14x11 grid in the y-z plane and positioning the phantom centrally in the FOV. The position of the 154 TLDs within the y-z plane was within a 3 mm margin inside the FOV (Figure 5.2). Doses are highest in the isocentre, and remain high along the x-axis, also when measuring outside the reconstructed volume. Along the z-axis, a clear drop in dose values is shown outside the primary beam area, although the evaluated area is not wide enough to get a clear view on the amount of scattered radiation.

Figure 5.5 shows ion chamber dose values at different coordinates, using a central position of the SCANORA 3D device. A drop in dose values can be perceived when measuring at coordinates which are outside the primary beam. This drop is gradual because the ion chamber, which measures the dose of a certain volume, progressively moves out of the primary beam.
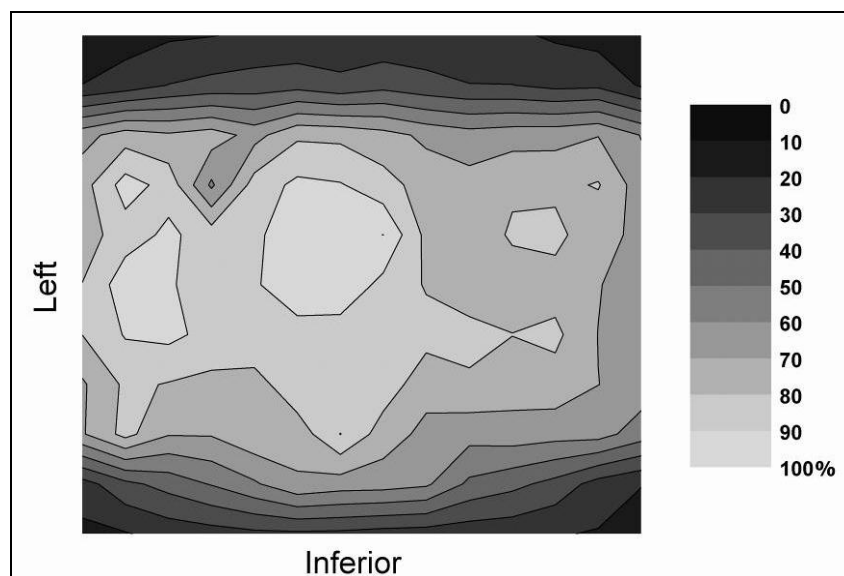

Figure 5.4 Relative dose distribution (%) at the y-z plane from TLD measurements in water, using the SCANORA 3D.

Further scatter tail measurements using TLDs are depicted in Figure 5.6. Similar results can be observed for the SCANORA 3D and 3D Accuitomo XYZ. With the present

set-up of TLDs the scatter tail is shown more extensively, demonstrating a clear, but smooth drop in dose when measuring outside the primary beam. It is seen that there can be a noticable dose deposition just above or below the FOV. The scatter tails are shown to extend to a distance of twice or more the height of the FOV.
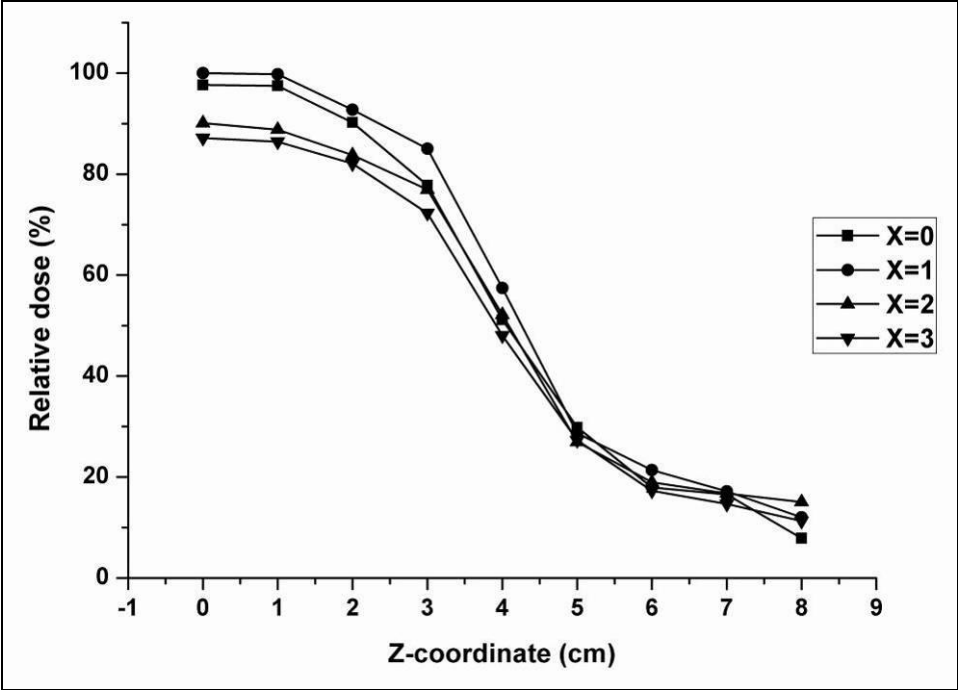

Figure 5.5 Relative dose (%) from ion chamber measurements in water, using the SCANORA 3D (isocentre at z=0, nominal FOV border at 3.75 cm).
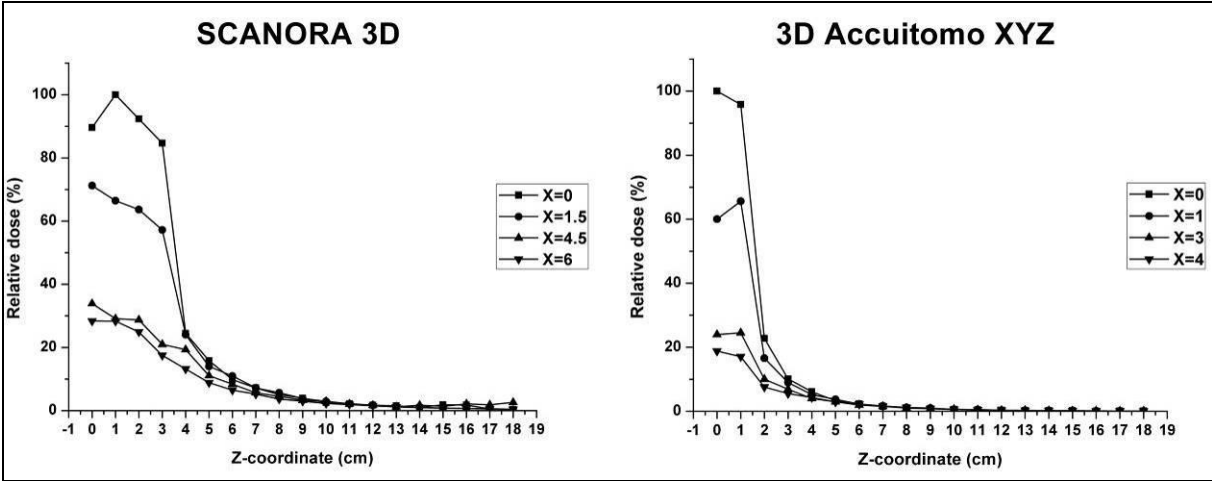

Figure 5.6 Relative dose (%) from TLD measurements in water, using the SCANORA 3D CBCT (isocentre at z=0, nominal FOV border at z=3.75cm) and 3D Accuitomo XYZ (isocentre at z=0, nominal FOV border at z=1.5 cm).

Measurements in x-y plane

Figure 5.7 shows all measurements performed in the x-y plane using the water phantom, involving three CBCT devices. As shown on the graphs, the bottom of each 2-D distribution represents the front (anterior) side of the phantom, whereas the left side of the graph corresponds to the left side of the phantom. Only one scan shows a homogeneous distribution, as it is a 360° scan with central positioning and a large FOV. All others exhibit a gradient of dose (which can be higher or lower in the anterior region), due to either a partial rotation or off-axis phantom positioning.
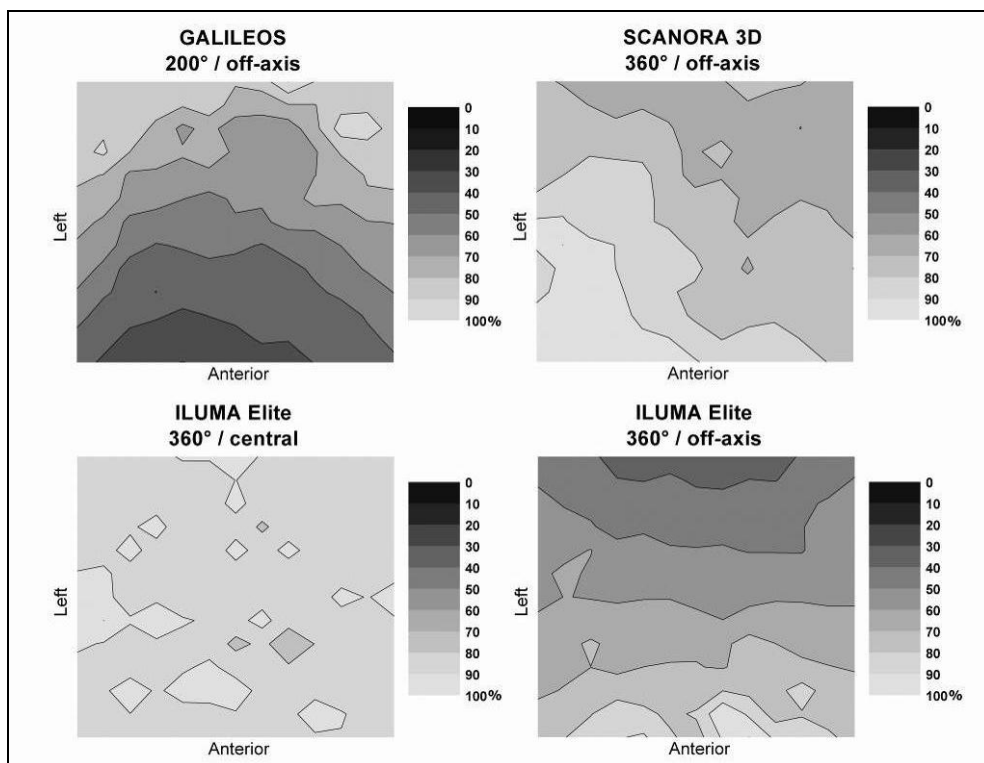

Figure 5.7 Relative dose distributions (%) at the x-y plane in water for different CBCT units and exposure settings.

Figure 5.8 shows the dose distribution for three protocols of the ProMax 3D. Dose distributions were nonuniform for all three measurements because the device scans using a 200° rotation. The dose distributions for the two FOVs are similar. The highest dose area is shifted to the back and right of the phantom with two hot spots at similar positions in the two set-ups. For off-axis positioning, the dose distribution was more uniform in the central region of the phantom than for the other two measurements but showed two hot spots at the front and back of the phantom.

Dose distributions for the NewTom VG are shown in Figure 5.8. These distributions show a homogeneous dose distribution for central positioning, and a front-back dose gradient

94

for off-axis positioning. Figure 5.9 shows the dose distributions for all 3D Accuitomo 170 protocols. Large differences can be seen between the different protocols, due to variations in field size, rotation, and positioning. Dose distributions for all i-CAT N.G. protocols are displayed in Figure 5.9. Again, there is a clear change in dose distributions when scanning using half a rotation, or by scanning the phantom off-axis.
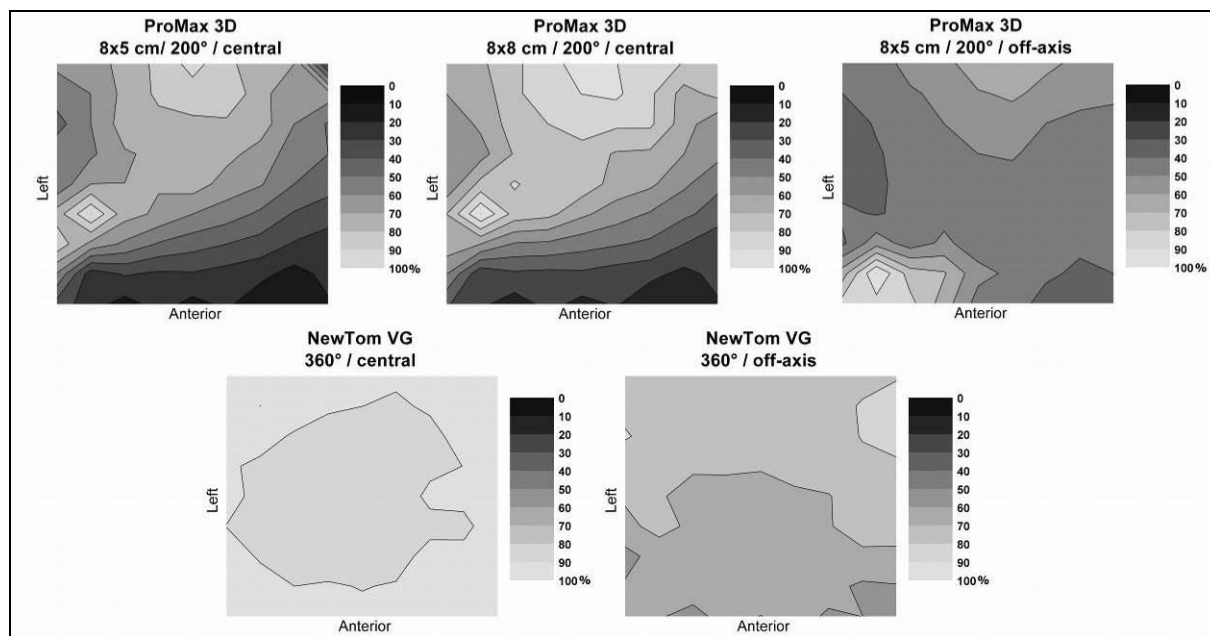

Figure 5.8 Relative dose distributions (%) at the x-y plane in PMMA for the ProMax 3D and NewTom VG.

Film distributions obtained from various CBCT devices showed dose gradients corresponding to the obtained TLD dose distributions at a higher spatial resolution. These measurements were performed in parallel with the TLD measurements to investigate the applicability of film, but could not be calibrated for absolute dose values.

5.5 Discussion

In this study, the results of different types of dose distribution measurements in homogeneous phantoms are presented. A wide range of dose measurements, using different CBCT devices, exposure protocols, phantoms and dosimeters have been carried out. A water phantom was used for measurements in the x-y and y-z planes and along the z-axis using TLDs and a small-volume ion chamber. The PMMA phantom allowed for TLD measurements in the x-y plane and the placement of radiochromic film. Although the use of film allowed for the visualisation of dose distribution at a high spatial resolution, there are a few drawbacks that inhibit its

application as a tool for dosimetry in this context. A highly sensitive film type is required to avoid the need for a large number of exposures. Furthermore, there are a number of measurement uncertainties associated with film [20]. To obtain accurate quantitative results, it is needed to perform batch calibration, or even individual film calibration, at beam energies corresponding to the CBCT exposure. In this study, film distributions were used as an additional visual analysis of dose gradients in the x-y plane, but no quantitative assessment was made.
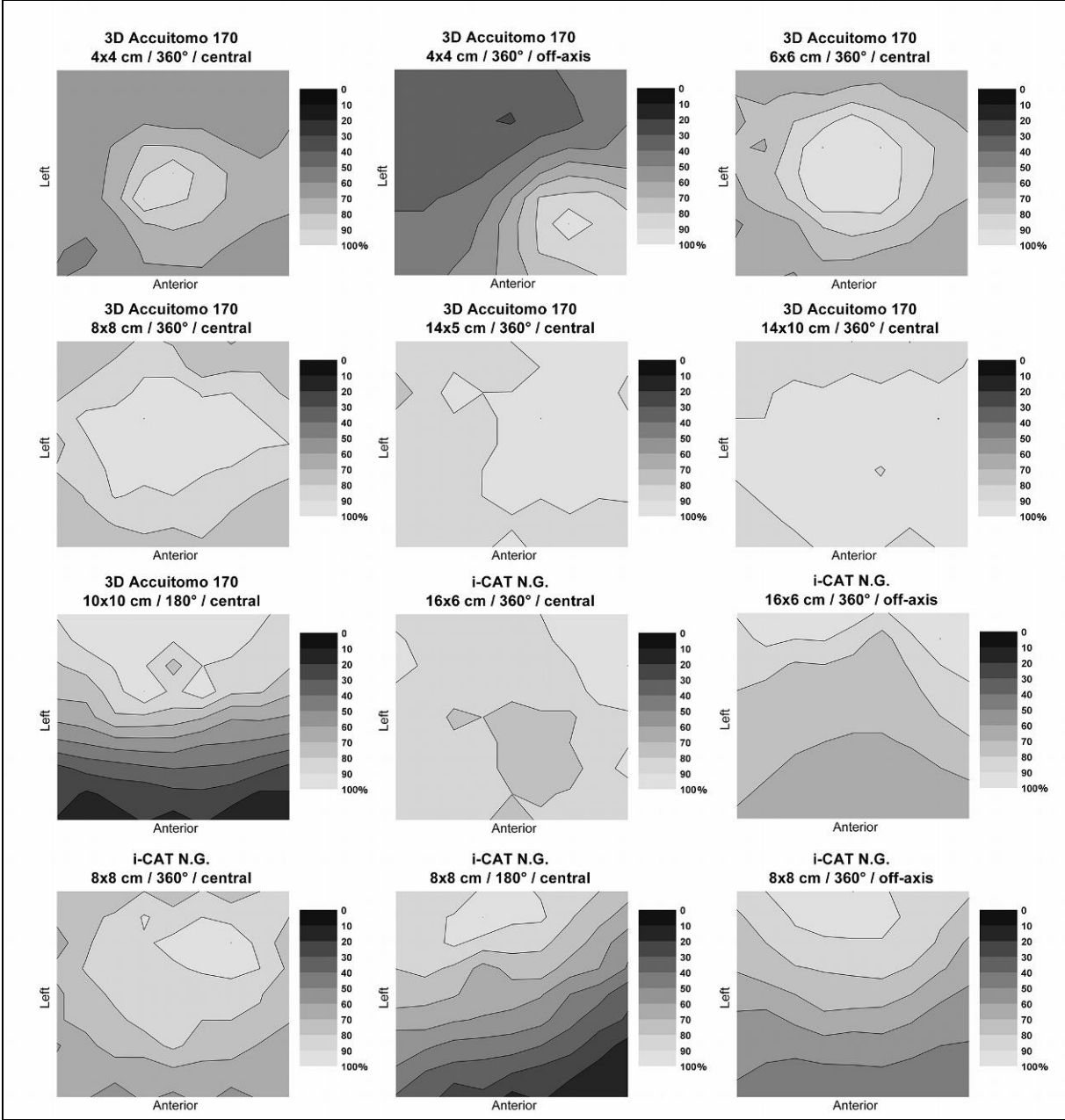

Figure 5.9 Relative dose (%) at the x-y plane in PMMA for the 3D Accuitomo 170 and i-CAT N.G.

As shown by ion chamber and TLD measurements in water, the dose showed variations up to 20% along the z-axis within the primary beam. For large-field FOVs (but especially for wide cone angles), the difference in dose will be more pronounced due to a longer attenuation path for angled X-rays. When moving the measuring point outside the primary beam, distinctive scatter tails were observed. A few cm outside the primary beam, the dose showed a sharp drop to about 10% of the maximum dose, after which a gradual further decline can be seen. These scatter tails confirm the inadequacy of using a 100mm pencil chamber as a dosimetry tool, as this type of ion chamber cannot cope with the wide range of beam widths used in dental CBCT.

In contrast with MDCT scanners, the dose distributions of CBCTs were asymmetric in the x-y plane when using off-axis positioning or partial rotation. For full rotation exposures using central positioning, the dose distribution was symmetric and generally showed a central dose peak with a concentric dose gradient towards the periphery. For large FOVs, dose variations up to 20% were perceived, whereas small FOVs showed variability up to 40% as peripheral parts of the phantom were outside the primary beam for part of the rotation. A clear difference was observed between central and off-axis positioning, which is more pronounced for small FOVs. The general pattern of the dose distribution remains the same for different FOV positions, showing concentric (and left-right symmetrical) isodose curves around a dose peak in the isocentre. For off-axis positioning, this resulted in a semi-concentric dose gradient from the isocentre towards the opposing side of the phantom. Similar to central positioning, the magnitude of this gradient depended on the FOV diameter, but generally the dose dropped to 50% or less at the opposing side. Furthermore, it was shown that an exposure with a less than full rotation also influences the shape of the dose distribution. A gradient is apparent with dose values dropping to 20% and below, with the highest dose being found on the X-ray tube side of the phantom but keeping left-right symmetry.

The results show that there are three key factors determining the shape of the dose distribution as well as the magnitude of the dose gradient: the size and position of the FOV and the rotation arc. Another aspect which may lead to variations in distribution is the X-ray spectrum (voltage peak and filtration), as this determines the amount of attenuation and beam hardening. However, in this study, it was not possible to isolate the effect of the voltage peak. Most CBCT devices are found between 80 and 120 kVp, and this value is usually fixed for each device. The only kVp variation possible in practice was between 60 and 90 kVp, which is not a relevant range. All of the exposure factors combined provide evidence that dental

CBCT requires the definition of a specific dose index, which is able to cope with the different types of dose distributions depicted in the current study.

It has been shown in previous studies reporting TLD measurements in anthropomorphic phantoms that the effective dose and the individual organ absorbed doses can vary depending on the FOV size and positioning, and the amount and energy of exposure [5-7]. It was also shown that the effective dose from a dental CBCT exposure is mainly defined by the absorbed dose of the salivary glands, thyroid gland, remainder tissues (esp. oral mucosa and extrathoracic airways) and bone marrow. These findings suggest that the risk to the patient may be characterized by the absorbed dose at a few anatomical positions. This opens up the possibility for an anatomical dose index, which would be based on measurements performed at specific locations in a customized (head-like) phantom, and would provide an estimation of patient dose without a need for conversion. However, it is not feasible to put this type of index into routine practice. Therefore, the focus should be to establish a technical dose index as well as conversion factors linking it to patient dose.

Different dose indices can be proposed based on the results of this study. Although a variety of distribution patterns are observed for different exposure geometries, it should still be possible to define an index that is measured using a PMMA phantom and a small volume ion chamber. Due to practical constrains (*i.e.* no possibility for fast rescanning) the number of measurements should be limited and focus on the mid-axial plane (z=0) without measuring the scatter tails along the z-axis. It has been pointed out by Dixon and Boone that dose measurements in the central axial plane suffice for dose index determination [14], indicating that conversion factors relative to the height of the FOV can be applied when relating an index to patient dose. However, these findings cannot be directly applied to dental CBCT. For some devices, z-axis symmetry cannot be assumed, seeing that the beams can be tilted or shaped asymmetrically. This complicates the definition of a dose index using a limited number of measurements positions in the central axial plane. For CBCT devices using non-symmetrical beams, additional measurements may be needed along the z-axis to verify dose symmetry and apply specific correction factors if needed. Furthermore, the x-y dose distribution in MDCT can be described using a limited number of measurements, as the FOV always covers the entire object leading to a distribution with rotational symmetry. The x-y distributions from the CBCTs presented in this study indicate that a different combination of measurement points is needed compared to the central and four peripheral points used for the $CTDI_w$.

98

The CBCT dose index should be able to cope with different exposure geometries, meaning that it should be sensitive to differences in FOV diameter and positioning and non-full rotations. Based on the axial dose distributions in this study, two dose indices can be proposed (Chapter 6). First of all, an index could be defined using a small-volume ion chamber, measuring centrally and at four peripheral positions in a cylindrical phantom. The FOV would have to be positioned centrally for these measurements at all times, as it would not be possible to measure the dose peak with the isocentre being positioned between centre and edge. The current results show rotational symmetry for small and large FOVs positioned centrally, indicating that four peripheral measurements would suffice. Front-back gradients due to partial rotations would be reflected by the difference in dose between the peripheral measurements. This index is similar to the $CTDI_w$ used in MDCT but should be interpreted different because of the difference in exposure geometry between MDCT and CBCT. Conversion factors to patient dose could be determined separately for different FOV sizes. A second possibility for a dose index measured in a cylindrical phantom is to measure at different points along the diameter of the cylinder. Using this kind of index, the FOV can be positioned off-axis (at one of the points along the diameter). By measuring at a number of additional positions between centre and periphery, the gradient of doses due to off-axis positioning and partial rotation would be reflected. The FOV positioning used for this index would reflect the clinical situation and facilitate conversion to patient dose. The index assumes left-right symmetry, which is seen in the x-y dose distributions for the protocols involved in this study. To cope with potential left-right asymmetry, two additional peripheral measurements could be obtained.

A third possible dose index for dental CBCT is the DAP. Measurement of the DAP requires no customised phantom, and can be performed with a single exposure which is of practical importance. Conversion coefficients between DAP and effective dose have been determined for intraoral, panoramic and cephalometric radiography [21-23]. For CBCT, the conversion between DAP and effective dose is far more complicated, as the irradiated field size and positional factors need to be taken into account, which may complicate interpretation of this index [24]. A study by Lofthag-Hansen *et al.* converted DAP values to effective dose using conversion factors determined for panoramic radiography [15]. However, before the DAP can be applied to estimate the effective dose for CBCT examinations, it is needed to determine specific conversion factors which take the entire exposure geometry into account. Monte Carlo simulations could be used to investigate the conversion between DAP and effective dose [17].

The determination of an optimal dose index and conversion factors could lead to Diagnostic Reference Levels (DRL) for dental CBCT. Specific DRLs will need to be defined for all patient groups undergoing CBCT examinations in dentistry. Combining DAP measurements from 41 CBCT units, Holroyd and Walker proposed an achievable DAP of 250 mGycm² for the placement of an implant in the upper molar region of an adult patient [19]. This DRL was based on normalised values for a 4x4 cm² field size, and is not achievable in practice as most CBCT devices have much larger minimal FOV sizes. Nonetheless, the proposed achievable DAP value, also recommended in the recent SEDENTEXCT Guidelines [25], reflects the importance of FOV reduction for dose optimisation in CBCT, and can be a useful starting point for the determination of achievable dose levels for other patient groups.

5.6 Conclusion

The variety of dose distributions for CBCT indicate the need for a specific dose index and appropriate conversion factors to link the index to effective patient dose. Further investigations should be made to assess the validity and practicality of dose indices using a small ion chamber and a suitable PMMA phantom and the use of DAP. Furthermore, the relationship between the dose indices and the effective dose should be investigated by defining conversion factors based on experimental results or dose simulations.

5.7 References

1. Scarfe WC, Farman AG. What is cone-beam CT and how does it work? Dent Clin North Am 2008; 52: 707-730.

2. Horner K, Islam M, Flygare L, Tsiklakis K, Whaites E. Basic principles for use of dental cone beam CT: consensus guidelines of the European Academy of Dental and Maxillofacial Radiology. Dentomaxillofac Radiol 2009; 38: 187-195.

3. Scarfe WC, Farman AG, Sukovic P. Clinical applications of cone-beam computed tomography in dental practice. J Can Dent Assoc 2006; 72: 75–85.

4. Farman AG. ALARA still applies. Oral Surg Oral Med Oral Pathol Oral Radiol Endod 2005; 100: 395–397.

5. Ludlow JB, Ivanovic M. Comparative dosimetry of dental CBCT devices and 64-slice CT for oral and maxillofacial radiology. Oral Surg Oral Med Oral Pathol Oral Radiol Endod 2008; 106: 106-114.

6. Hirsch E, Wolf U, Heinicke F, Silva MA. Dosimetry of the cone beam computed tomography Veraviewepocs 3D compared with the 3D Accuitomo in different fields of view. Dentomaxillofac Radiol 2008; 37: 268-273.

7. Pauwels R, Beinsberger J, Collaert B, Theodorakou C, Rogers J, Walker A, Cockmartin L, Bosmans H, Jacobs R, Bogaerts R, Horner K, The SEDENTEXCT Project Consortium. Effective dose range for dental cone beam computed tomography scanners. Eur J Radiol 2012; 81: 267-271.

8. Fujii K, Aoyama T, Yamauchi-Kawaura C, Koyama S, Yamauchi M, Ko S, Akahane K, Nishizawa K. Radiation dose evaluation in 64-slice CT examinations with adult and paediatric anthropomorphic phantoms. Br J Radiol 2009; 82: 1010-1018.

9. Dixon RL. A new look at CT dose measurement: beyond CTDI. Med Phys 2003; 30: 1272-1280.

10. Mori S, Endo M, Nishizawa K, Tsunoo T, Aoyama T, Fujiwara H, Murase K. Enlarged longitudinal dose profiles in cone-beam CT and the need for modified dosimetry. Med Phys 2005; 32: 1061-1069.

11. Nakonechny KD, Fallone BG, Rathee S. Novel methods of measuring single scan dose profiles and cumulative dose in CT. Med Phys 2005; 32: 98-109.

12. Perisinakis K, Damilakis J, Tzedakis A, Papadakis A, Theocharopoulos N, Gourtsoyiannis N. Determination of the weighted CT dose index in modern multi-detector CT scanners. Phys Med Biol 2007; 52: 6485-6495.

13. Dixon RL. Restructuring CT dosimetry--a realistic strategy for the future Requiem for the pencil chamber. Med Phys 2006; 33: 3973-3976.

14. Dixon RL, Boone JM. Cone beam CT dosimetry: a unified and self-consistent approach including all scan modalities--with or without phantom motion. Med Phys 2010; 37: 2703-2718.

15. Lofthag-Hansen S, Thilander-Klang A, Ekestubbe A, Helmrot E, Gröndahl K. Calculating effective dose on a cone beam computed tomography device: 3D Accuitomo and 3D Accuitomo FPD. Dentomaxillofac Radiol 2008; 37: 72-79.

16. Boone JM, Cooper VN 3rd, Nemzek WR, McGahan JP, Seibert JA. Monte Carlo assessment of computed tomography dose to tissue adjacent to the scanned volume. Med Phys 2000; 27: 2393-2407.

17. Vassileva J, Stoyanov D. Quality control and patient dosimetry in dental cone beam CT. Radiat Prot Dosim 2010; 139: 310-312.

18. Thilander-Klang A, Helmrot E. Methods of determining the effective dose in dental radiology. Radiat. Prot. Dosim 2010; 139, 306–309.

19. Holroyd JR, Walker A. Recommendations for the Design of X-ray Facilities and the Quality Assurance of Dental Cone Beam CT (Computed Tomography) Systems – A report of the HPA Working Party on Dental Cone Beam CT. HPA-RPD-065. Health Protection Agency, March 2010.

20. Rampado O, Garelli E, Deagostini S, Ropolo R. Dose and energy dependence of response of Gafchromic XR-QA film for kilovoltage x-ray beams. Phys Med Biol 2006; 51: 2871-2881.

21. Looe HK, Eenboom F, Chofor N, Pfaffenberger A, Sering M, Rühmann A, Poplawski A, Willborn K, Poppe B. Dose-area product measurements and determination of conversion coefficients for the estimation of effective dose in dental lateral cephalometric radiology. Radiat Prot Dosim 2007; 124: 181-186.

22. Looe HK, Eenboom F, Chofor N, Pfaffenberger A, Steinhoff M, Rühmann A, Poplawski A, Willborn K, Poppe B. Conversion coefficients for the estimation of effective doses in intraoral and panoramic dental radiology from dose-area product values. Radiat Prot Dosim 2008; 131: 365-373.

23. Helmrot E, Alm Carlsson G. Measurement of radiation dose in dental radiology. Radiat Prot Dosim 2005; 114: 168–171.

24. Wise KN, Sandborg M, Persliden J, Alm Carlsson G. Sensitivity of coefficients for converting entrance surface dose and kerma-area product to effective dose and energy imparted to the patient. Phys Med Biol 1999; 44: 1937–1954.

25. Radiation protection: cone beam CT for dental and maxillofacial radiology. Evidence Based Guidelines [Online]. Report prepared by the SEDENTEXCT project. [updated 2011 Mar; cited 2011 May 13]. Available from http://www.sedentexct.eu/guidelines_v1.1.pdf/.

Chapter 6: A new dose index for CBCT and its correlation with patient dose

6.1 Abstract

Objectives: To define a suitable dose index for dental cone beam computed tomography (CBCT) based on the known dose distribution, to evaluate the practical use of this index for varying CBCT geometries, and to investigate the relation between the index and effective dose.

Materials and methods: A customized cylindrical PMMA phantom, containing holes along its diameter for ion chamber insertion, was developed. Two possible dose indices were defined by (1) measuring at 7 locations along the diameter and (2) measuring at the centre and at four peripheral locations. Two small-volume ion chambers were used to measure the indices on three CBCT devices (3D Accuitomo 170, Cranex 3D, SCANORA 3D). A total of 15 combinations of field of view (FOV) sizes and full or partial rotations were included. The effect of tube voltage (kVp) on the indices was verified. Conversion factors to effective dose were calculated using the 3D Accuitomo 170. Effective doses were estimated for the other devices based on the two indices.

Results: Index values ranged between 1.2 and 8.8 mGy for the 3D Accuitomo 170, and between 1.7 and 2.3 mGy for the SCANORA 3D. Values for both indices were similar, with an average deviation of 3.7%. After correcting for beam height, beam diameter and rotation arc, conversion of the indices resulted in effective dose values between 30 and 302 µSv.

Conclusions: Both indices are suitable for the evaluation of the dose distribution in the mid-axial plane for various CBCT exposure geometries. Conversion to effective dose was fairly straightforward, although the proposed conversion factors should be further explored.

6.2 Introduction

The radiation dose of CBCT has been an ongoing concern, as there is a wide range of doses seen in practice, as seen in Chapters 1-3 [1-4]. An aspect of dose optimisation which is currently not feasible in CBCT imaging is the determination of diagnostic reference levels (DRL) for the different potential clinical indications in dentistry [5-7]. A first step in the

103

process of determining DRLs is the definition of a suitable dose index, which takes into account the variety of exposure geometries (*e.g.* beam size, angle and shape, isocentre position, rotation arc), by assessing the dose distribution of CBCT using tools and methods which can be applied in routine practice (*e.g.* in acceptance testing or quality control)[8].

Patient dose for CBCT has been investigated by many authors, mainly focusing on the assessment of organ and effective doses for reference phantoms using thermoluminescent dosimeters (TLD)[2-4]. A wide dose range is seen for all radiosensitive organs in the head and neck area. Although an accurate estimation of organ doses in anthropomorphic phantoms provides useful information regarding patient dose levels and dose optimisation strategies, the measurement process is labour-intensive, and there is no standardized method for TLD placement. Furthermore, the dosimetric tools needed for organ dose estimations (phantom, TLDs and reader) are not generally available for medical physicists performing acceptance test or quality control. A suitable dose index would enable a routine measurement of CBCT exposures as well as patient dose estimations based on this index [9-11].

The predicament of defining a suitable dose index for the cone-beam exposure geometry has been investigated for dental and non-dental CBCT. To some extent, the issue with CBCT is similar to that of MSCT, seeing that the classic $CTDI_{100}$ is inapplicable due to the large beam widths [12]. However, the limited beam diameter seen in dental CBCT (*i.e.* as small as 4 cm) leads to additional considerations, seeing that the dose distribution will not be symmetrical, with dose peaks and gradients depending on the field of view (FOV) size and position [13,14]. Additionally, certain CBCT devices do not use a full 360° rotation arc, leading to additional inhomogeneities in dose distribution [14]. The dose-area product (DAP) has been used by manufacturers and researchers as an estimation of tube output [15-18]. Although it can be a practical dose index which takes the FOV size into account, it is difficult to relate the DAP to patient dose, as it does not provide any information on the actual dose distribution.

The aim of this study was to investigate the applicability of a newly defined dose index for dental CBCT. The index was measured using a wide range of exposure geometries and its relation and conversion to organ and effective dose was evaluated.

6.3 Materials and methods

Two dose indices are proposed, taking different factors into account which affect the dose distribution (Chapter 5):

- FOV diameters may vary between 4 cm and more than 20 cm, and can be placed centrally or off-axis in clinical practice

- FOV heights show equal variation, but a dose index could be measured in the midaxial plane (z=0), and corrected for beam height, as proposed by Dixon and Boone for MSCT beams

- Partial rotations (180-220°) keep left-right symmetry and lead to a front-to-back or back-to-front dose gradient

- Other slight variations in dose distribution (*e.g.* asymmetrical beam shape, circular vs. pyramid-shaped beam) cannot be practically measured using a dose index, but could be used as correction factors when correlating the index to patient risk

The proposed indices are measured in a typical head-size PMMA phantom, similar to existing CTDI head phantoms. However, as the use of the pencil beam ion chamber has been disputed for modern MSCT scanners and is clearly not feasible for dental CBCT dosimetry, a small-volume ion chamber is needed.

The two indices are illustrated in Figure 6.1, showing an axial diagram of a cylindrical phantom with different possible measuring points. Both indices are measured in the mid-axial plane. A first index (Index 1) would be measured along the front-to-back diameter of the phantom, be measuring at points 4B, 3B, 2B, 1, 2F, 3F and 4F, and is calculated as the arithmetic mean of all measurement positions:

$$Index1 = \frac{1}{7} \sum_{i=4F}^{4B} (D_i)$$

with D_i the absorbed dose at measuring point *i*. For this index, the isocentre of the image could be placed according to the clinical situation (*i.e.* central for large FOVs, peripheral for small FOVs, in-between for medium FOVs). However, the isocentre needs to be placed at one of the measuring points along the front-back axis. Positioning criteria were determined according to the FOV diameter: <6 cm in 4F, 6-8 cm in 3F, 9-13 cm in 2F and >13 cm in 1.

A second index (Index 2) is measured using point 1, 4B, 4R, 4F, and 4L *i.e.* five measuring points in the centre and along the periphery of the phantom. For this index, which closely resembles the weighted CTDI, the isocentre needs to be positioned centrally (at point 1) for all FOV sizes. It is calculated as the mean between the central measuring point and the four peripheral points, using a ½ weighting:

$$Index2 = \frac{1}{2}(D_1) + \frac{1}{2}(\frac{D_{4F} + D_{4B} + D_{4R} + D_{4L}}{4})$$

with D_1, D_{4F}, D_{4B}, D_{4R}, and D_{4L} the absorbed doses in the measuring points shown in Figure 6.1.
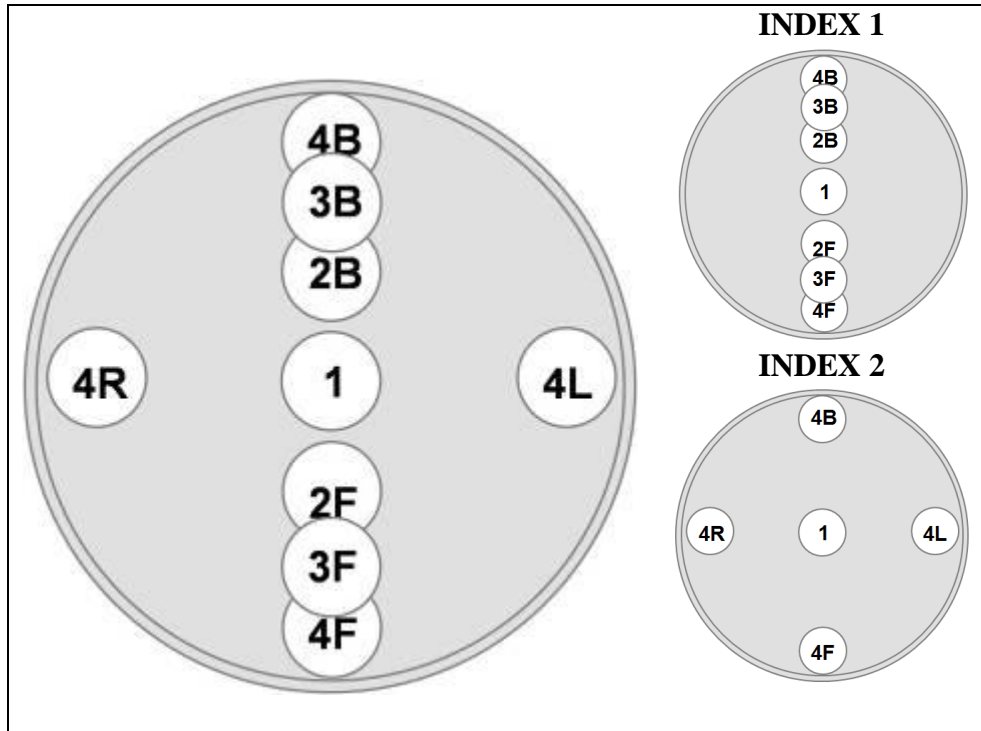

Figure 6.1 Left: nine possible measuring points on the phantom. Right: selected measuring points for Index 1(top) and Index 2 (bottom). F = front, B = back, R= right, L = left.

For the measurement of the two indices, a customized cylindrical (16x16 cm) PMMA phantom was created by Leeds Test Objects (Boroughbridge, United Kingdom), according to the configuration of the measuring points in Figure 6.1. To allow for the use of varying small-volume ion chambers, the holes of the phantom would need to be larger than those of existing CTDI phantoms. A 25 mm diameter for the holes was chosen. Inserts were designed to fill up holes which are not used when measuring the dose at one of the locations (Figure 6.2).

The phantom was scanned on two CBCT devices: 3D Accuitomo 170 (J. Morita, Kyoto, Japan) and SCANORA 3D (Soredex, Tuusula, Finland), involving a vast amount of exposure protocols, varying all possible exposure factors (FOV size, kVp, mAs, rotation arc). Two types of ion chambers were used: a 0.6 cm^3 chamber (Farmer FC65-G, IBA Dosimetry, Schwarzenbruck, Germany), which was calibrated in a RQR5 diagnostic beam, and a 6 cm^3 thimble ionisation chamber (Radcal 9010, Radcal Corporation, California, USA) coupled with an electrometer with calibration traceable to national standards (National Physical

Laboratory). An intercomparison was performed to ensure consistency in measurements between the two ion chambers. For the Farmer ion chamber, a custom insert containing a 13mm diameter hole was manufactured to fit the chamber.
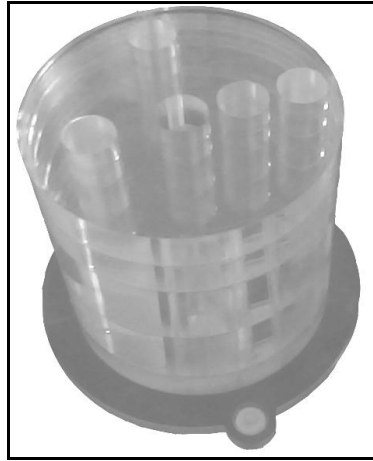

Figure 6.2 Phantom for dose index validation, containing holes at different locations and inserts to fill up unused holes.

The clinical relevance of the dose indices was verified with the 3D Accuitomo 170, by relating them to effective dose measurements using an Alderson Radiation Therapy phantom. A selection of clinically applied FOV sizes was made for these measurements, applying both 360° and 180° rotation protocols (Chapter 3). No kVp variation was used for the anthropomorphic phantom measurements. Organ doses were estimated by attaching TLDs at various locations throughout the head and neck, corresponding to radiosensitive organs and tissues. The effective dose was calculated according to the ICRP 103 Publication, applying weightings to the different involved tissues. Tissues included in the calculation of the effective dose were: bone marrow, bone surface, brain, extrathoracic airways, lymph nodes, muscle, oesophagus, oral mucosa, salivary glands, and thyroid gland. Correlation between effective doses for varying FOV sizes, FOV positions and rotation arcs was explored.

6.4 Results

Table 6.1 shows the dose index measurements for the different exposure protocols of the 3D Accuitomo 170 and SCANORA 3D. Index 1 ranged between 1.2 mGy and, 8.7 mGy. For Index 2, calculated values were between 1.9 mGy and 8.8 mGy. It can be seen that both indices are affected by the amount of exposure and geometric factors (FOV size and position). Generally, there is a good consistency between the two indices; the largest differences are

seen for 180° scans, as they show larger dose gradients, and for the medium and small FOV protocols of the SCANORA 3D, likely caused by an increased exposure at the start/end-point of the tube.

The effect of the kVp on the indices is illustrated in Figure 6.3, showing the dose ratio between 90, 80 and 70 kVp for various FOV sizes of the 3D Accuitomo 170. For both indices, it can be seen that they are sensitive to dose variation due to kVp adjustment, and that the ratio is stable for varying FOV sizes and consistent between the two indices.
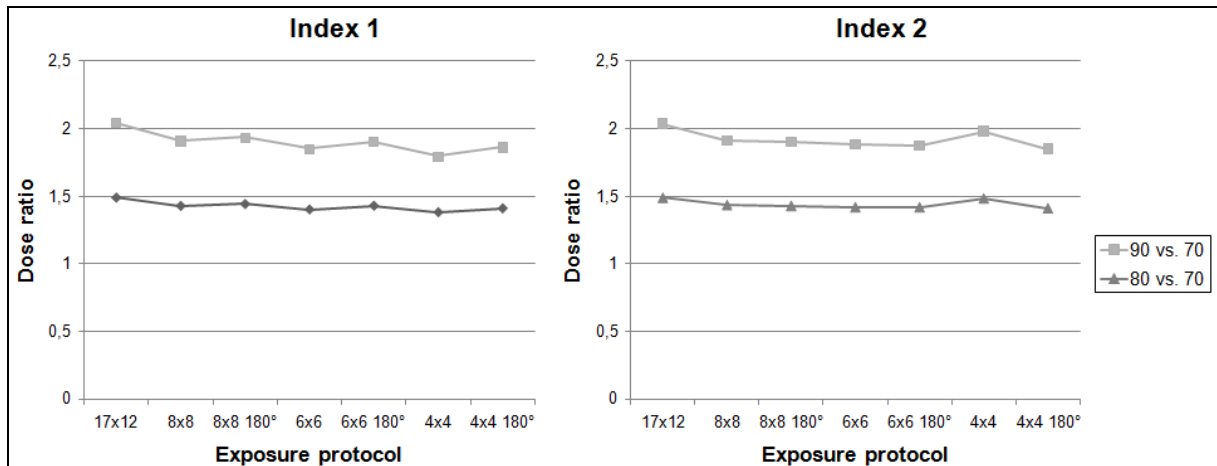

Figure 6.3 Dose ratios for 90, 80 and 70 kVp for Index 1 and Index 2, using various FOV sizes

The conversion to effective dose was investigated for both indices, using effective dose measurements with an anthropomorphic phantom on the 3D Accuitomo 170. The most optimal fit between dose index and effective dose was obtained using different corrections:

1. **Height correction:** Both indices were multiplied with the height of the FOV to obtain a metric similar to the Dose Length Product (DLP) used in MSCT [19-22]. For FOV heights above 11 cm, the multiplication factor would be limited to 11.

2. **Rotation correction:** For 180° rotations, an additional correction factor was applied, which decreased for increasing FOV sizes for Index 1 (ranging between 1.21 and 1.70) but was more stable for Index 2 at 1.23 +/- 0.05 (Table 6.2) .

3. **Diameter correction:** For FOV sizes with a large diameter but limited height (*i.e.* 14x5 cm), the effective doses are relatively higher, and a correction factor of 1.39 was applied.

Table 6.1 Dose index, corrected dose index and converted effective dose calculations

Device	kVp	mAs	FOV	Rotation	Index 1 (mGy)	Index 2 (mGy)	Corr.	Corr. Index 1 (mGy.cm)	Corr. Index 2 (mGy.cm)	Diff. (%)		Eff. dose from Index 1 (μSv)	Eff. dose from Index 2 (μSv)	Diff. (%)
3D Accuitomo 170	90	87.5 (360)	17x12	360	8.7	8.8	H	96.0	96.9	1.0		300	302	0.4
		45 (180)		180	4.4	4.5	H,R	59.0	59.6	1.0		190	192	1.0
			17x5	360	7.5	7.4	H,D	52.0	51.1	-1.7	Max	159	157	-1.1
											Mand	180	177	-1.4
			14x10	360	8.6	8.6	H	86.0	86.1	0.1		271	270	-0.3
			14x5	360	7.1	7.2	H,D	49.5	50.3	1.6	Max	152	155	1.9
											Mand	172	175	1.7
			10x10	360	7.6	7.9	H	76.0	78.6	3.4		241	248	2.9
			8x8	360	6.4	6.5	H	50.9	51.9	2.0		166	170	2.1
				180	2.9	3.3	H,R	33.1	33.8	2.0		113	116	2.9
			6x6	360	5.2	5.2	H,P	31.3	31.0	-1.0	Max	94	95	1.0
											Mand	122	122	0.2
				180	2.1	2.7	H,R,P	20.8	20.6	-1.0	Max	68	70	2.2
							H,R,P	20.8	20.6	-1.0	Mand	85	86	1.3
			4x4	360	3.4	3.7	H,P	13.6	14.7	7.7	Max	40	44	11.1
											Mand	70	76	8.9
				180	1.2	1.9	H,P	8.2	8.9	7.7	Max	30	34	12.8
											Mand	48	53	10.2
SCANORA 3D	90	24	15x8	360	2.1	2.2	H	16.0	16.2	1.5		62	65	4.6
		30	10x8	360	2.1	2.3	H	15.4	17.1	10.9		60	67	11.7
		36	6x6	360	1.7	2.0	H,P	10.2	11.9	16.0	Max	40	47	16.3
											Mand	50	58	15.9

H height correction, *R* rotation arc corrections, D, diameter correction, *P* positional correction (upper vs. lower jaw), *Max* maxilla, *Mand* mandible

Table 6.2 Correction factors for 180° rotation protocol, in function of FOV size

	Index 1	Index 2
4x4 cm	1.70	1.17
6x6 cm	1.63	1.27
8x8 cm	1.42	1.26
17x12 cm	1.21	1.21

Figure 6.4 shows the correlation between dose indices and effective dose using the corrected data, averaging mandibular and maxillary protocols for the 4x4, 6x6 and 14x5 FOVs. An excellent linear correlation is seen because of the combination of approximate (*i.e.* correction 1) and exact (*i.e.* corrections 2 and 3) correction factors. As effective dose varies between small-height FOVs positioned on the upper and lower jaw, a final additional correction factor was calculated (Table 6.3). It can be seen that the correction factor for FOV positioning decreases with increasing volume (*i.e.* actual volume size, not FOV height); for the 4x4 cm FOV, the effective dose for the lower jaw is double that of the upper jaw, for the 14x5 cm FOV effective doses are almost the same. This final correction based on FOV position is not applicable for FOV height of 8 cm or greater.
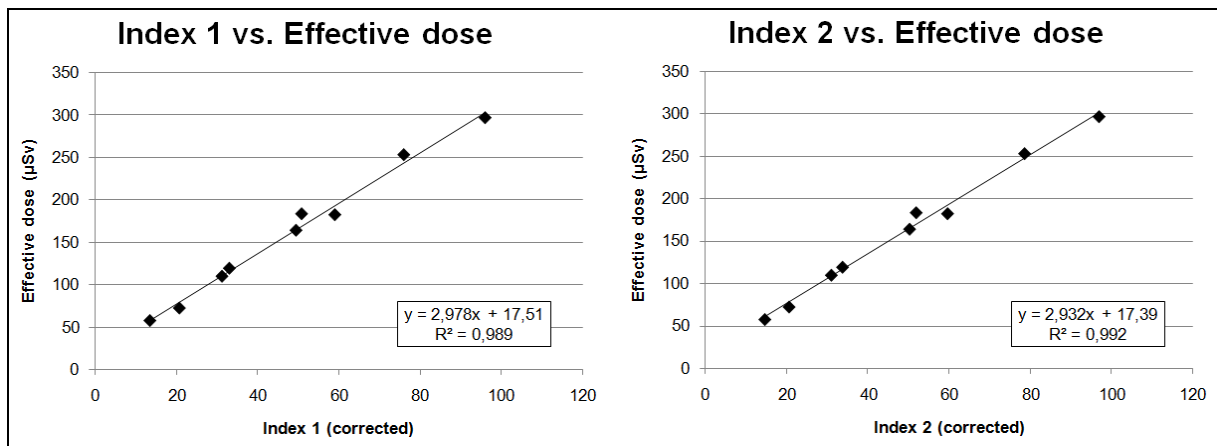

Figure 6.4 Correlation between dose indices and effective dose after height, diameter and rotation correction. Effective dose values for upper and lower jaws were averaged for small FOVs.

Using these correction factors, the effective dose was estimated using the two dose indices for all CBCT devices and protocols, with values ranging between 30 μSv (3D Accuitomo 170, 4x4 cm, 180°, maxilla) and 302 μSv (3D Accuitomo 170, 17x12 cm, 360°)(Table 6.1).

Table 6.3 Correction factors for FOV position, in function of FOV size

FOV size	4x4 cm	6x6 cm	6x6 cm 180°	14x5 cm
Upper jaw	0.63	0.85	0.87	0.93
Lower jaw	1.37	1.15	1.13	1.07

6.5 Discussion

It has been pointed out by various authors that the dose distribution in dental CBCT can be complicated due to the variety of exposure geometries [14-16]. The varying FOV sizes in terms of diameter and height, as well as different beams shapes and rotations arcs ranging between 180° and 360° can lead to sharp dose gradients along the antero-posterior, left-right or cranial-caudal direction. A suitable dose index for CBCT has be able to cope with this, allowing for a routine dose measurement by researchers, manufacturers and medical physicists, using tools and phantoms that are commonly available. A crucial aspect of the dose index is that it should relate to effective dose using (variable, exposure protocol-specific) conversion factors.

Based on the known three-dimensional dose distribution in CBCT, two potential dose indices were defined, and a customized PMMA phantom was developed to allow for the validation of both indices. Both indices are sensible, and provide both parallel and complimentary information. Index 1, measured along the diameter of the phantom, allows for a detailed estimation of front-back dose gradients, which makes it particularly useful for partial rotation protocols. Furthermore, using Index 1, the isocentre can be placed according to the clinical situation, as long as it is placed along one of the 4 possible locations (*i.e.* central or at 3 possible distances from the centre). Index 2 is measured similarly to the CTDI$_w$ but, measuring only at the mid-axial plane and using ½ weighting between central and peripheral measurements, resulting in a more reasonable dose estimation for small-diameter CBCTs.

The index was validated using the 3D Accuitomo 170 and applied to other CBCT devices. For the 3D Accuitomo 170, a large amount of dosimetric data was available using an anthropomorphic phantom, allowing for the investigation of the conversion between the indices and effective dose. It was seen that both indices are both suitable for conversion after applying a few corrections. However, a few of the applied conversion factors need further investigation, as they were now calculated in a custom way for the included protocols of the 3D Accuitomo 170 and cannot be readily applied to exposure protocols from other devices.

The rotation correction for non-360° exposure geometries will depend on the actual rotation arc, which can be between 180° and 220° in dental CBCT. Furthermore, this rotation correction was highly dependent on the FOV size for Index 1, as it is affected more gravely by front-back dose gradients than Index 2, for which the rotation correction was relatively constant. In addition, the tube passes at the posterior side for 180° protocols of the 3D Accuitomo 170, and the rotation correction will be different (presumably inverse) if the tube passes at the anterior side of the head.

The height correction appeared to be suitable in general, with two exceptions: the 17x12 cm and the 14x5 cm FOVs. For the former, a height correction of 11 rather than 12 was used; for the latter an additional correction factor of 1.39 was calculated in addition to the use of the FOV height. Both can be explained anatomically when looking at the position and distribution of radiosensitive organs in the head. Assuming that the lower border of a FOV is never positioned lower than the soft tissue of the chin, FOVs of 10 cm and larger will always result in similar exposure to all salivary glands, thyroid gland, oral mucosa, extrathoracic airways, lymph nodes, and oesophagus. FOVs larger than 10 cm will only result in a small additional exposure to red bone marrow, bone surface, muscle and skin. The only clear increase in absorbed dose will be for the brain. However, the increase in effective dose will be limited, and certainly not proportional to the height of the FOV. The slight increase for the dose index values due to the increase in scatter will reflect the marginal increase in effective dose for these FOV sizes. Therefore, a maximal height correction factor of 11 was proposed. For the 14x5 cm FOV, the normal height multiplication would lead to an underestimation of the effective dose. Irrespective of the position of a 14x5 cm FOV (*i.e.* upper or lower jaw), part of the salivary glands, red bone marrow and bone surface and remainder tissues will be in the primary beam during the entire exposure, leading to relatively high absorbed doses compared with a FOV with small height and diameter (*e.g.* 4x4 cm, 6x6 cm) for which the dose distribution in the xy-plane is more localized. Thus, an additional diameter correction was needed for the 14x5 cm FOV. This was calculated in an exact way due to the lack of multiple reference points (*e.g.* 10x5, 15x5 or similar) which would enable a more exact definition of a diameter correction.

From the available data, it is seen that the values and conversion factors are similar for Index 1 and 2. From a rational point of view, Index 1 appears to make more sense to measure the CBCT dose distribution for different reasons: there are two additional measuring points compared to Index 2 (7 vs. 5), it allows for the FOV to be positioned similar to the clinical situation (closer to the periphery for smaller FOV diameters), and it measures the front-back

gradient which is seen for off-axis field positions and non-360° rotation arcs. However, for the variety of exposure geometries included in this study, both indices showed similar values, with an average difference of 3.7% and a maximal difference of 16% (SCANORA 3D, 6x6 cm). From this preliminary evaluation, it seems that Index 2 is more practical. It can be measured using a standard CTDI head phantom, using central FOV positioning. For compact CBCT devices using small FOVs, it could be impossible to place the FOV centrally without removing the head and/or chin support, but for most devices it should be possible to measure both indices practically. In that case, Index 2 would be preferred as it does not require a custom phantom. Furthermore, as most CBCT devices have a significant waiting time between exposures due to reconstruction or tube cool-down, the practicality of an index is also defined by the total measurement time. Therefore, the lower number of measurement points for Index 2 is an important practical advantage. For full rotation protocols, two measurements (*i.e.* one central, one peripheral) could even suffice to calculate this index, although some slight discrepancies would then be ignored (*e.g.* attenuation by the chair or head support, overshooting at the beginning and end of the rotation).

Further in-depth investigation is needed to evaluate whether or not Index 1 truly has an added value in terms of correlation with patient dose. Furthermore, the preliminary correction factors need to be evaluated and defined more precisely if needed. Monte Carlo simulations will play a crucial role in this type of investigation, as they allow for the simulation of any beam quality and beam geometry [23]. Using voxel models of cylindrical PMMA phantoms and segmented anthropomorphic phantoms, more evidence can be provided regarding the use of both indices.

A third possible dose index which could be suitable for dental CBCT is the dose-area product (DAP), which is measured using a transmission ionisation chamber and is routinely applied in two-dimensional radiography [9,10]. Different authors have investigated the use of DAP for dental CBCT, but there has not been a true validation of its use [15-18]. Furthermore, the conversion to effective dose has not yet been thoroughly investigated. The evaluation of the use of the DAP could easily be implemented into a Monte Carlo framework, similar to the two indices proposed in this study.

6.6 Conclusion

Both indices are suitable for the evaluation of the dose distribution in the mid-axial plane for various CBCT exposure geometries. Conversion to effective dose was relatively

straightforward, although the proposed conversion and correction factors should be further explored.

6.7 References

1. Scarfe WC, Farman AG, Sukovic P. Clinical applications of cone-beam computed tomography in dental practice. J Can Dent Assoc 2006; 72: 75–85.

2. Pauwels R, Beinsberger J, Collaert B, Theodorakou C, Rogers J, Walker A, Cockmartin L, Bosmans H, Jacobs R, Bogaerts R, Horner K, The SEDENTEXCT Project Consortium . Effective dose range for dental cone beam computed tomography scanners. Eur J Radiol 2012; 81: 267-271.

3. Suomalainen A, Kiljunen T, Käser Y, Peltola J, Kortesniemi M. Dosimetry and image quality of four dental cone beam computed tomography scanners compared with multislice computed tomography scanners. Dentomaxillofac Radiol 2009; 38: 367-378

4. Loubele M, Bogaerts R, Van Dijck E, Pauwels R, Vanheusden S, Suetens P, Marchal G, Sanderink G, Jacobs R. Comparison between effective radiation dose of CBCT and MSCT scanners for dentomaxillofacial applications. Eur J Radiol 2009; 71: 461-468

5. Hart D, Hillier MC, Wall BF. National reference doses for common radiographic, fluoroscopic and dental X-ray examinations in the UK. Br J Radiol. 2009; 82: 1-12.

6. Hatziioannou K, Psarouli E, Papanastassiou E, Bousbouras P, Kodona H, Kimoundri O, Delichas M. Quality control and diagnostic reference levels in intraoral dental radiographic facilities. Dentomaxillofac Radiol. 2005; 34: 304-307.

7. Walker C, van der Putten W. Patient dosimetry and a novel approach to establishing Diagnostic Reference Levels in dental radiology. Phys Med. 2012; 28: 7-12.

8. Radiation protection: cone beam CT for dental and maxillofacial radiology. Evidence Based Guidelines [Online]. Report prepared by the SEDENTEXCT project. [updated 2011 Mar; cited 2011 May 13]. Available from http://www.sedentexct.eu/guidelines_v1.1.pdf/.

9. Looe HK, Eenboom F, Chofor N, Pfaffenberger A, Sering M, Rühmann A, *et al*. Dose-area product measurements and determination of conversion coefficients for the estimation of effective dose in dental lateral cephalometric radiology. Radiat Prot Dosim 2007; 124: 181-186.

10. Looe HK, Eenboom F, Chofor N, Pfaffenberger A, Steinhoff M, Rühmann A, *et al*. Conversion coefficients for the estimation of effective doses in intraoral and

panoramic dental radiology from dose-area product values. Radiat Prot Dosim 2008; 131: 365-373.

11. Wise KN, Sandborg M, Persliden J, Alm Carlsson G. Sensitivity of coefficients for converting entrance surface dose and kerma-area product to effective dose and energy imparted to the patient. Phys Med Biol 1999; 44: 1937–1954.

12. Dixon RL. Restructuring CT dosimetry--a realistic strategy for the future Requiem for the pencil chamber. Med Phys 2006; 33: 3973-3976.

13. Boone JM, Cooper VN 3rd, Nemzek WR, McGahan JP, Seibert JA. Monte Carlo assessment of computed tomography dose to tissue adjacent to the scanned volume. Med Phys 2000; 27: 2393-2407.

14. Pauwels R, Theodorakou C, Walker A, Bosmans H, Jacobs R, Bogaerts R, Horner K, The SEDENTEXCT Project Consortium. Dose distribution for dental cone beam CT and its implication for defining a dose index. Dentomaxillofac Radiol. In press.

15. Lofthag-Hansen S, Thilander-Klang A, Ekestubbe A, Helmrot E, Gröndahl K. Calculating effective dose on a cone beam computed tomography device: 3D Accuitomo and 3D Accuitomo FPD. Dentomaxillofac Radiol 2008; 37: 72-79.

16. Vassileva J, Stoyanov D. Quality control and patient dosimetry in dental cone beam CT. Radiat Prot Dosim 2010; 139: 310-312.

17. Thilander-Klang A, Helmrot E. Methods of determining the effective dose in dental radiology. Radiat. Prot. Dosim 2010; 139, 306–309.

18. Holroyd JR, Walker A. Recommendations for the Design of X-ray Facilities and the Quality Assurance of Dental Cone Beam CT (Computed Tomography) Systems – A report of the HPA Working Party on Dental Cone Beam CT. HPA-RPD-065. Health Protection Agency, March 2010.

19. Dixon RL, Boone JM. Cone beam CT dosimetry: a unified and self-consistent approach including all scan modalities--with or without phantom motion. Med Phys 2010; 37: 2703-2718.

20. Fujii K, Aoyama T, Yamauchi-Kawaura C, Koyama S, Yamauchi M, Ko S, *et al*. Radiation dose evaluation in 64-slice CT examinations with adult and paediatric anthropomorphic phantoms. Br J Radiol 2009; 82: 1010-1018.

21. Dixon RL. A new look at CT dose measurement: beyond CTDI. Med Phys 2003; 30: 1272-1280.

22. Nakonechny KD, Fallone BG, Rathee S. Novel methods of measuring single scan dose profiles and cumulative dose in CT. Med Phys 2005; 32: 98-109.

23. Zhang G, Pauwels R, Marshall N, Shaheen E, Nuyts J, Jacobs R, Bosmans H. Development and validation of a hybrid simulation technique for cone beam CT: application to an oral imaging system. Phys Med Biol 2011; 56:5823-5843.

PART II: IMAGE QUALITY

Chapter 7: Development and applicability of a quality control phantom for CBCT

7.1 Abstract

Objectives: To develop a quality control phantom which is suited for dental CBCT imaging, can be used on any CBCT device and allows for the measurement of parameters which are relevant to dental imaging requirements.

Materials and methods: To investigate the application of different image quality parameters for CBCT, a prototype polymethyl methacrylate (PMMA) cylindrical phantom with inserts for image quality analysis was developed. Applicability and reproducibility of the phantom were assessed using seven CBCT devices with different scanning protocols. Image quality parameters evaluated were: CT number correlation, contrast resolution, image homogeneity and uniformity, point spread function, and metal artefacts.

Results: Deviations of repeated measurements were between 0.0% and 3.3%. Correlation coefficients of CBCT voxel values with CT numbers ranged between 0.68 and 1.00. Contrast-to-noise ratio (CNR) values were much lower for hydroxyapatite ($0 < CNR < 7.7$) than for air and aluminium ($5.0 < CNR < 32.8$). Noise values ranged between 35 and 419. The uniformity index was between 3.3% and 11.9%. Full Width at Half Maximum (FWHM) measurements varied between 0.43 mm and 1.07 mm. The increase of mean voxel values surrounding metal objects ranged between 6.7% and 43.0%.

Conclusions: Results from preliminary analyses of the prototype quality control phantom showed its potential for routine quality assurance on CBCT. Large differences in image quality performance were seen between CBCT devices. Based on the initial evaluations, the phantom can be optimised and validated.

7.2 Introduction

Due to the increasing use of Cone Beam CT (CBCT) in dental practice and the large number of devices on the market, there is a need for a quantified and objective analysis of the technical image quality and radiation dose to enable an optimal use for this imaging modality [1,2]. Three different aspects have to be considered in the optimisation of an X-ray imaging

modality: quantifying the radiation dose and risk for patients, assessment of technical image quality and assessment of diagnostic image quality. By means of an appropriate test object, the first and second aspect can be studied in one investigation process. Ideally, the development of test objects goes along with the formation of quality assurance (QA) protocols. During these activities, the diagnostic image quality must always be considered, implying that dose measurements are to be reported in terms of diagnostic needs, and technical image quality assessments need to be evaluated for their diagnostic relevance. This is particularly the case for dental imaging, as it involves a large variety of diagnostic indications requiring different imaging approaches [3].

There is a lack of standardized tools for image quality analysis for dental CBCT. To develop such a tool, all available knowledge regarding image quality assessment on other 3D or pseudo-3D imaging modalities (spiral CT, tomosynthesis, kV-CBCT used in radiotherapy, *etc.*)[4-7] needs to be combined with the existing knowledge of CBCT and previous studies on CBCT image quality [2,8-16]. Even though a large number of CBCT image quality studies have been published over the last few years, most have focused on the diagnostic image quality. However, a number of studies have already assessed technical image quality for one or more CBCT devices, using an existing commercial quality control (QC) phantom [8,9], a phantom provided by a CBCT manufacturer [2,10], a water phantom [8,11], a customized test object [12-15] or clinical data [16,17]. Although these studies have provided useful insights regarding certain image quality aspects, they also show the need for a standardized QC phantom which is suited for use on all CBCT devices, and which provides results that are relevant to dental imaging and that can be compared between systems. Commercial QC phantoms have been described for conventional CT, but these are not applicable for dental CBCT due to the difference in performance for certain image quality aspects. CT phantoms use soft tissue-equivalent materials for gray value analysis, which are not relevant for dental CBCT [6,7]. Furthermore, dental imaging requires a high spatial resolution and a limitation of metal artefacts, both of which are not assessed by conventional CT phantoms.

A CBCT system uses a cone- or similarly shaped X-ray beam that rotates around an object and acquires two-dimensional projections, reconstructed into a three-dimensional volume [18]. There is a variety of CBCT devices available with large differences for a number of imaging parameters: peak voltage, amount of filtration, quantity of X-rays (mAs), pulsed versus continuous exposure, beam geometry, number of projections, detector type, field of view (FOV) size, reconstruction algorithm, reconstructed voxel size, pre- and post-processing of raw and reconstructed data, *etc*. Designing a QC phantom requires a cross-

section of all available CBCT devices, identifying common properties. These properties, most of which are intertwined, are (ordered from general to specific):

- CBCT images show very poor soft tissue differentiation, as they are meant for the visualization of hard tissues (bone, teeth) and air (sinus and air cavities).
- Spatial resolution is high (voxel sizes are generally below 0.4 mm) and nominally identical in all planes (isotropic).
- Most devices expose at a kVp below 100, and a low mAs.
- There is a relatively large degree of scattered radiation resulting in image noise and non-uniformity.
- Voxel values are not standardized and cannot directly be used as quantitative CT numbers for use in bone mineral density (BMD) evaluation.
- High density tissues and metal objects result in metal artefacts due to scatter, beam hardening and photon starvation.

All of these considerations affect the design of a QC phantom. Another limitation is the minimum FOV size of all currently available CBCT devices; the phantom must be suitable for all CBCTs, including those with a FOV of a few cubic centimetres.

The objective of the current study is to develop a quality control phantom which is suited for dental CBCT imaging, can be used on any CBCT device and allows for the measurement of parameters which are relevant to dental imaging requirements. As an initial evaluation of the phantom, it was scanned using a variety of CBCT devices to evaluate the reproducibility and applicability of the evaluated parameters and to investigate CBCT imaging performance.

7.3 Materials and methods

Development of quality control phantom

The phantom was designed by Leeds Test Objects Ltd. in the frame of the EC project SEDENTEXCT. For the first prototype, a head-size cylindrical polymethyl methacrylate (PMMA) phantom (160 mm diameter, 162 mm height) was designed with seven cylindrical holes positioned at the centre and vertices of a regular hexagon (Figure 7.1).

Along with this phantom, 8 different cylindrical inserts (35 mm diameter, 20 mm height) were developed to test a total of 6 image quality parameters. A listing of currently

evaluated image quality parameters including the different materials and patterns that were used for each analysis is shown in Table 7.1. For metal artefact analysis, titanium was selected because of the increasing use of titanium implants in dentistry.

Figure 7.1 First prototype QC phantom and inserts

Table 7.1 Listing of inserts developed for image analysis

Parameter	Insert design	Image analysis
CT number	Cylinders of five different materials (hydroxyapatite of varying density (50, 100 and 200 mg.cm^{-3}), aluminium, air) in PMMA surrounding	Average voxel value compared to Hounsfield Units obtained from MSCT scanners in correlation plot
Contrast resolution	Same as CT number	Contrast-to-noise ratio calculation using central material and surrounding PMMA
Image homogeneity	PMMA inserts	Normalised standard deviation
Image uniformity	PMMA inserts	Difference in average voxel value between insert columns
Point spread function	Steel wire (0.25 mm) suspended in air	1D integrated full width at half maximum calculation
Metal artefacts	Three in-line titanium rods	Increase of voxel values in vicinity of rods

Scanning of the phantom and inserts on CBCT and MSCT systems

To evaluate the reproducibility of the evaluated parameters before applying them to scans of various CBCT devices, the phantom and inserts were scanned 5 consecutive times using the SCANORA 3D CBCT (Soredex, Tuusula, Finland), with a clinical standard resolution protocol as depicted in Table 7.2. Measurements of all image quality parameters described below were performed on each scan. Also, measurements were repeated 5 times for one scan, to evaluate the reproducibility of the measurement itself.

Table 7.2 CBCT and spiral CT scan parameters

CBCT				
	Field size (cm)	Tube potential (kVp)	mAs	Voxel size (mm)
GALILEOS Comfort	15x15	85	28	0.3
i-CAT Classic High dose	16x8	120	35	0.2
i-CAT Classic Low dose	16x8	120	10	0.4
ILUMA Elite	21x14	120	76	0.2
ProMax 3D High dose	8x8	84	168	0.16
ProMax 3D Low dose	8x8	84	20	0.32
SCANORA 3D High dose	6x6	85	36	0.13
SCANORA 3D Low dose	6x6	85	24	0.2
SCANORA 3D (Reproducibility)	14.5x7.5	85	24	0.35
SkyView High dose	17.3x17.3	90	96	0.34
SkyView Low dose	17.3x17.3	90	52	0.34
Veraviewepocs 3D	8x8	70	51	0.13
Spiral CT				
	Field size	Tube potential (kV)	mA	Slice Thickness (mm)
GE Prospeed	N/A	120	200	1
Siemens SOMATOM Sensation 64	N/A	80 / 100	208 / 199	1 / 2.5

[a] diameter x height

Subsequently, the inserts were scanned on 7 CBCT devices: GALILEOS Comfort (Sirona Dental Systems, Bensheim, Germany), i-CAT Classic (Imaging Sciences International, Hatfield, PA, USA), ILUMA Elite (IMTEC, Ardmore, OK, USA), ProMax 3D (Planmeca Oy, Helsinki, Finland), SCANORA 3D (Soredex, Tuusula, Finland), SkyView (MyRay, Imola, Italy), Veraviewepocs 3D (J. Morita, Kyoto, Japan). Exposure parameters for all devices can be found in Table 7.2. All selected protocols are used in clinical practice.

All inserts were placed in the PMMA holder phantom for scanning. For all scanners with a small or medium-sized field of view (FOV), which were unable to scan the entire

phantom, the insert of interest was positioned in one of the peripheral holes to mimic an actual dental scan. The inserts were scanned centrally in the FOV. Holes not containing the insert were filled up using blank PMMA inserts. For scanners with a large FOV (~15 cm diameter or more), inserts were positioned at the six peripheral positions of the holder phantom. The holder phantom was scanned centrally in the FOV, to mimic a full head scan. For all scanners, three insert rows were used: the bottom row contained blank PMMA inserts, the middle row contained the metal artefact insert, and the top row was used for all other inserts (Figure 7.2). An exposure used for a standard adult patient was selected for each CBCT. Whenever possible, high and low dose clinical protocols were selected by varying the mAs. For CBCT, high dose protocols typically imply a smaller voxel size owed to a modified reconstruction.
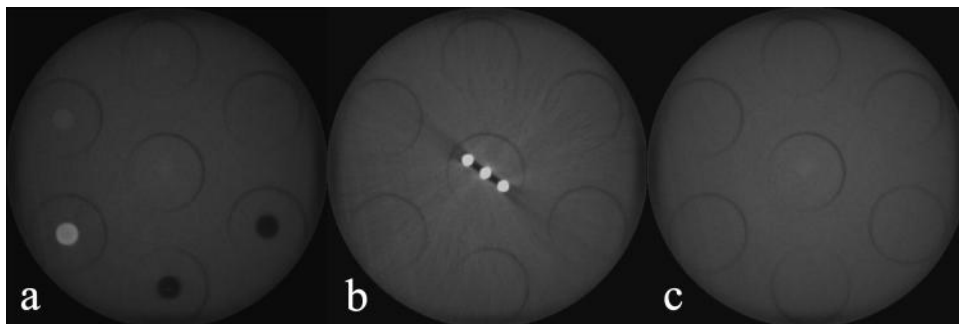

Figure 7.2 Axial slices of SCANORA 3D phantom scan, using the large FOV: (a) top row containing CT number / contrast resolution inserts and point spread function insert; (b) middle row with metal artefact insert; (c) bottom row containing PMMA inserts.

In addition to CBCT scans, spiral CT scans were acquired from the inserts to obtain CT number measurements serving as the gold standard. Three scanning protocols were used from two different scanners: GE Prospeed (General Electric, Fairfield, CT, USA) and SOMATOM Sensation 64 (Siemens AG, Erlangen, Germany) (Table 7.2).

Analysis of image quality inserts

All datasets were evaluated with the ImageJ software (National Institutes of Health, Bethesda, MD, USA, http://rsb.info.nih.gov/ij/) using a combination of different image analysis methods. For all measurements except point spread function, the measurement was performed on ten consecutive axial slices to obtain a sufficient sample size. Measured parameters (mean voxel value, standard deviation) were averaged over these slices. The top and bottom of the insert were avoided because of possible interference by adjacent inserts.

The inserts for CT number evaluation, containing rods of five different densities, were analyzed by measuring the mean voxel value obtained from circular ROIs along different

axial slices through the insert. Apart from the five materials involved in the insert, the voxel value from PMMA was obtained using a blank insert. From all six materials, corresponding CT numbers obtained from spiral CT scans by taking the average value from the three CT protocols that were applied. Correlation coefficients were determined for a linear fit.

The same inserts were used to determine the contrast-to-noise ratio (CNR) for the five different materials. To calculate the CNR, circular regions of interest (ROI) were positioned on the inner part of the materials and on the adjacent PMMA (Figure 7.3). The mean voxel value and standard deviation were determined, and the CNR was calculated using the formula:

$$CNR = \frac{MVV_m - MVV_b}{SD_{m,\,b}}$$

where MVV_m and MVV_b are the mean voxel values for the evaluated material and the (PMMA) background, respectively, and $SD_{m,b}$ is the average standard deviation of the voxel values within the material and background.
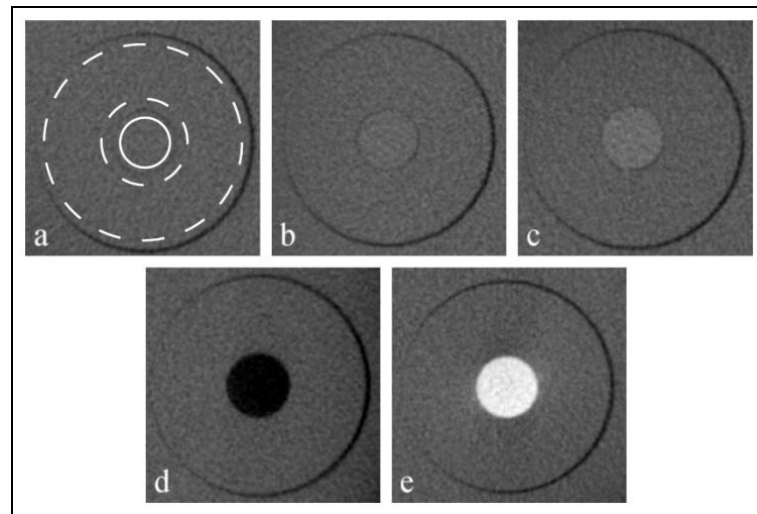

Figure 7.3 Contrast resolution inserts, containing five rods of different materials: (a) hydroxyapatite 50 mg/cm³; (b) hydroxyapatite 100 mg/cm³; (c) hydroxyapatite 200 mg/cm³; (d) air; (e) aluminium. The ROIs used for the material (solid circle) and PMMA background (area between dashed circles) are shown in (a).

Blank PMMA inserts were used to evaluate image homogeneity and uniformity. The noise was determined by measuring the standard deviation of voxel values within a blank PMMA insert. It was chosen not to calculate a signal-to-noise ratio (SNR) as voxel values of homogeneous PMMA do not represent the amount of signal. It was seen that most CBCT datasets use a conventional 12 bit scale, but some use a higher or lower bit depth which makes

it impossible to compare standard deviations of voxel values. Therefore, the measured values were converted to a 12 bit scale where needed. Uniformity of voxel values in the XY-plane was determined for large-volume scanners by filling the central and peripheral holes of the phantom with blank PMMA inserts and positioning the phantom centrally in the FOV, thus yielding 7 ROIs. For small-volume scanners, the FOV was positioned on a peripheral PMMA insert and the adjacent areas were used as peripheral ROIs. All measurements of voxel values were converted to a 12 bit scale with the lowest possible voxel value being 0. The uniformity parameter was defined as the percentage of mean voxel value difference between the areas with the highest and lowest value.

The point spread function (PSF) insert was evaluated by determining the 2-D profile from the wire and surrounding air, and integrating this along the y-axis to yield a one-dimensional PSF. The resulting distribution was fitted to a Cauchy distribution (*i.e.* Lorentz distribution, a continuous probability distribution similar to the Student's *t* distribution) using EasyFit 5.0 (MathWave Technologies), enabling the determination of the full width at half maximum (FWHM) value (Figure 7.4).

For measuring the extent of metal artefacts, the average voxel value from the PMMA insert was subtracted from the scan of the metal artefact insert. Subsequently, the average voxel value was measured at two ROIs surrounding the titanium rods. All steps are illustrated in Figure 7.5.
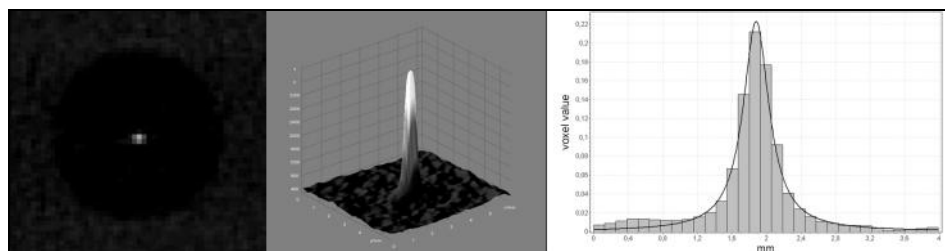

Figure 7.4 Point spread function of 0.25 mm wire, showing an example axial slice (left), a 2-D surface plot from a small central ROI (middle), and an integrated one-dimensional profile fitted to a Cauchy distribution (right).
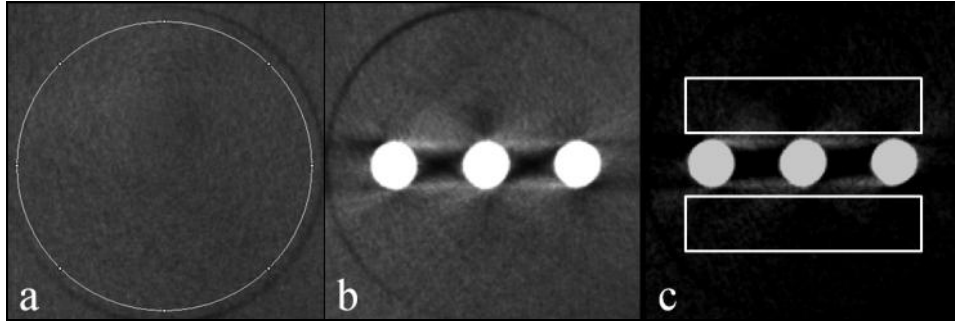
Figure 7.5 Consecutive steps in streak artefact measurement: (a) measurement of PMMA mean voxel value; (b) example axial slice of metal artefact insert; (c) after subtraction of PMMA mean voxel value, showing regions of interest.

The 'artefact added value' (AAV) was then defined as

$$AAV = \frac{MVV_{art} + MVV_{PMMA}}{MVV_{PMMA}}$$

where MVV_{art} and MVV_{PMMA} are the mean voxel values for the artefact after subtraction and the blank PMMA insert, respectively. The AAV is independent of factors such as noise and bit depth. Its value is mainly defined by those parts of the metal artefact which show higher values than that of PMMA, seeing that all values below that of PMMA are subtracted to the lowest possible voxel value. The value of AAV increases when white streaks originating from the metal object cover a larger area or when they are more pronounced.

7.4 Results

Reproducibility of image quality parameters

Average and maximal deviations of repeated measurements obtained from 5 consecutive scans using an identical exposure and 5 repeated measurements on a single dataset are shown in Table 3. This deviation represents the inter-scan and intra-scan reproducibility of the phantom and measuring methods. For the different materials involved in contrast analysis, the measurement of mean voxel value was used rather than the CNR. The average deviation for all investigated parameters was 1.3% for consecutive scans and 1.0% for measurements on an identical scan. The highest deviations were seen for the measurements of hydroxyapatite (2.2%-3.3%) and the FWHM of the point spread function (2.0%-2.7%). The highest reproducibility was seen for the CT number correlation coefficient (0.01%-0.02%).

Table 7.3 Reproducibility of repeated measurements on consecutively scanned (Inter) and identical (Intra) CBCT datasets

	Average deviation (%)		Maximal deviation (%)	
	Inter	*Intra*	*Inter*	*Intra*
Air	0.2	0.2	0.4	0.4
PMMA	0.7	0.4	1.7	0.7
HA50	2.2	1.2	5.6	2.7
HA100	3.3	2.6	5.9	6.8
HA200	2.8	2.7	4.3	4.6
Aluminium	0.5	0.3	0.8	0.5
Artefacts	1.1	0.5	2.2	1.4
Noise	0.3	0.4	0.8	0.9
Uniformity	0.8	0.7	1.6	1.7
FWHM	2.7	2.0	5.2	4.2
CT number correlation	0.0	0.0	0.0	0.0
Average of all parameters	1.3	1.0	2.6	2.2

Analysis of image quality inserts

Example slices from scans obtained from the 5 different inserts used for CT number and contrast analysis are depicted in Figure 7.3. Table 7.4 shows the correlation coefficients between CT numbers measured on spiral CT scans and voxel values measured on CBCT scans. Correlation coefficients ranged between 0.6864 and 0.9996 (average: 0.9689) when including all materials. For the medium density range (Hydroxyapatite 50, 100 and 200 mg/cm³ and PMMA) the correlation coefficient ranged between 0.7303 and 0.9909 (average: 0.9156).

Table 7.4 depicts CNR values obtained from the inserts. Contrast was shown to be low in general for all three hydroxyapatite densities ($0 < CNR < 7.7$), and high for aluminium and air ($5.0 < CNR < 32.8$), showing a large range between the different CBCT devices and protocols.

Table 7.4 shows noise values for all CBCT datasets. Large differences are seen between devices, with standard deviations of voxel values ranging between 35 and 419. When considering high and low dose protocols, it is shown that there is no clear correlation between dose and noise for different CBCT devices, seeing that the images are reconstructed using different voxel sizes.

Uniformity index calculations also vary between devices (Table 4). Generally, uniformity is better for high dose scans.

Table 7.4 contains FWHM values, which range between 0.43 mm and 1.07 mm, showing clear differences between high and low resolution scans of certain CBCT devices.

Example slices of the metal artefact insert for each are shown in Figure 7.6. Table 7.4 shows results for the artefact added value (AAV), which ranged between 10.4 and 40.6. No clear difference is seen for high and low dose protocols of any device ($P > 0.05$ for Wilcoxon signed rank test).
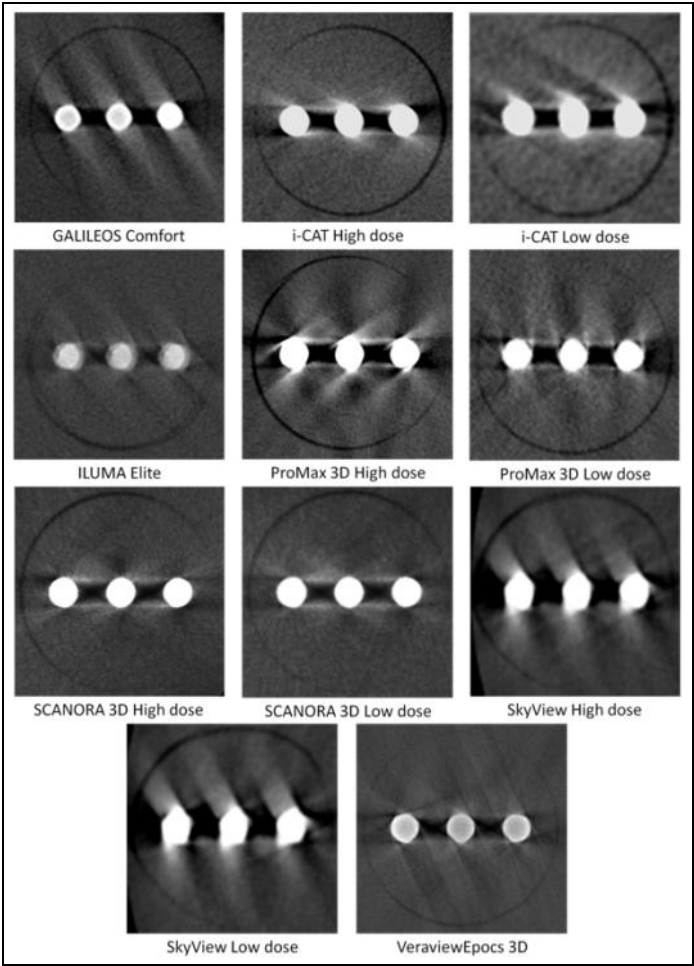

Figure 7.6 Example axial slices for metal artefact inserts, showing three titanium rods.

Table 7.4 Image analysis results for CBCT scanners

Device	CNR_{HA50}	CNR_{HA100}	CNR_{HA200}	CNR_{AIR}	CNR_{AL}	CT_{ALL}	CT_{MED}	AAV(%)	Noise	Unif. (%)	FWHM (mm)
GALILEOS Comfort	0.0	1.0	1.0	5.0	8.7	0.9980	0.8159	14.3	89.4	8.1	0.57
i-CAT High dose	1.7	2.6	3.8	15.0	21.0	0.9973	0.9070	19.2	69.1	11.8	0.49
i-CAT Low dose	0.4	2.6	4.4	17.3	21.2	0.9870	0.9661	24.3	56.6	21.1	0.97
ILUMA Elite	0.0	0.0	0.8	13.6	15.0	0.9946	0.7303	6.7	82.6	3.3	0.70
ProMax 3D High dose	0.0	0.4	2.1	11.4	19.9	0.9996	0.9614	23.4	70.6	11.9	0.77
ProMax 3D Low dose	0.0	0.1	1.0	6.5	10.8	0.9993	0.9236	24.0	126.5	11.2	0.97
SCANORA 3D High dose	0.5	0.8	2.0	8.9	9.4	0.9988	0.9909	11.6	81.6	7.9	0.43
SCANORA 3D Low dose	0.0	0.9	1.7	9.4	9.5	0.9993	0.9781	11.2	80.6	13.5	0.45
SkyView High dose	2.5	4.1	7.7	19.2	32.8	0.9990	0.9679	40.2	35.1	4.0	0.68
SkyView Low dose	2.2	3.5	7.3	16.5	28.5	0.9986	0.9719	43.0	41.2	4.9	0.71
Veraviewepocs 3D	0.6	1.3	1.6	6.4	13.0	0.6864	0.8581	9.4	418.6	6.4	1.07

CNR contrast-to-noise ratio, CT_{ALL} overall correlation coefficient with CT numbers, CT_{MED} correlation coefficient for medium densities only, *AAV* artefact added value, *Noise* standard deviation of PMMA voxel values, *FWHM* full width at half maximum

7.5 Discussion

In this study, the applicability of a first prototype quality control phantom for CBCT was evaluated. Reproducibility of the measurements of image quality parameters was assessed, and the range of values obtained from all parameters was investigated for a wide range of devices and exposure protocols to assess the applicability of the selected insert designs, materials and image analysis methods.

The design of the phantom was tailored for its application on dental CBCT devices. A head-sized PMMA cylinder was selected to ensure a simplified yet proper simulation of the average attenuation of the head. PMMA is a standard material used for dosimetric and image quality phantoms [5-7,9,10,12,15]. Although the human head contains a number of air cavities, most notably the oral cavity and sinuses, there are a number of high-density structures as well, such as the temporal bone, mandibular cortical bone and tooth enamel. Therefore, the PMMA phantom used in this study can be considered to result in comparable detector photon fluencies as the human head. As a result, the different technical image parameters measured using this phantom can be related to the CBCT devices' clinical performance.

Furthermore, all selected materials for image quality evaluation are relevant for dental imaging. For contrast resolution and voxel value analysis, different densities of hydroxyapatite were selected to represent various bone densities, and aluminium was used to represent dense cortical bone. For metal artefact evaluation, titanium rods resembling dental implants were used, bearing in mind that titanium implants are major contributors to image quality degradation for dental CBCT [19]. The nominally high spatial resolution of CBCT devices was assessed by choosing a thin wire to estimate the point spread function. By using small size inserts the phantom can be applied to all CBCT devices, as the smallest FOV of all CBCT devices on the market (40x30 mm) is larger than the insert size (35x20 mm). Furthermore, placing these inserts peripherally in the phantom is clinically relevant, seeing that almost all tissues that are investigated in dentomaxillofacial imaging are found peripherally in the head (teeth, jaw bones, sinuses, temporomandibular joint). It is especially important for CBCT devices with small FOVs to mimic this clinical situation, as it has been shown that the size and position of a FOV can affect the image quality for these devices [12,14].

Another specific issue in CBCT imaging is the wide cone angle used by some devices, which leads to image quality degradation and artefacts. These artefacts may occur at the top

or bottom of the FOV, and result in voxel values that are unsuitable for image quality analysis. However, seeing that three rows of inserts were used, the part of the phantom that was used for image analysis was limited to 6 cm in height. Furthermore, for those scanners with a small FOV height, insert rows were scanned separately to avoid these artefacts for the top and bottom inserts. In addition, measurements of all image quality parameters were performed in slices around the centre of the height of the insert, avoiding any interference that may occur at the border between adjacent inserts.

It was possible to accurately position and scan the phantom on the different CBCT devices with supine, seated and standing patient positioning. The total time needed to obtain a full phantom dataset depended largely on the FOV size. For some devices, a single scan sufficed to include all inserts, while for others it was necessary to scan each insert separately leading to an increase in the total time needed to obtain a full set of scans of the phantom. This total time is a summation of the time needed to position the phantom, the lag time between consecutive scans, and the time needed to reconstruct and export datasets; all of these factors are affected by the available FOV size. This implies that the insert size, but also the number of inserts, is limited by the small-volume CBCTs, as it is not practical to perform a large number of scans for an image quality QC procedure. For further prototyping, it will therefore be investigated whether the number of inserts can be lowered by combining the different materials used for contrast resolution analysis into a single insert.

All measurements of image quality parameters were proven to be reproducible for consecutive scans as well as for identical scans. It can be expected that consecutive scans differ slightly in terms of voxel values due to slight variability in tube output, and this was generally reflected in the measurements, seeing that the deviations on consecutive scans were typically larger than for repeated measurements on a single scan, which shows the sensitivity of the image quality assessment for small variations of image quality. The largest variability was found for low contrast resolution, which is susceptible for slight variations in voxel value or noise measurements, seeing that the low contrast resolution for dental CBCT is generally poor. Variability was also seen for the point spread function analysis, most likely due to undersampling which is of specific concern for low resolution datasets. An image analysis technique using oversampling can increase the accuracy of the FWHM estimation [10].

For most devices, there was a good overall correlation between voxel values from different materials and CT numbers obtained from spiral CT scanners, but the correlation for medium-density materials was worse. Two important factors contribute to this finding. First, voxel values are affected by the amount of mass outside the reconstructed volume, seeing that

132

that this mass results in variable projection data due to different amounts of scattered radiation. This is especially the case for small-volume CBCTs. Katsumata *et al.* showed a relation between density variability and imaging volume, and the present study is in accordance with those findings [14]. Secondly, the amount of mass within the FOV may affect the gray value distribution, depending on the reconstruction algorithm used. Therefore, the presence of high- or low-density materials in the FOV can affect the distribution of voxel values. Similar findings were reported by Bryant *et al.* [12]. In contrast to the current results, Lagravère *et al.* and Naitoh *et al.* have stated that a linear conversion can be made between density measurements on a CBCT scan and CT numbers [15,17]. Furthermore, density measurements were independent of the position in the volume [15]. However, one must take care when applying statistical analysis methods to this type of measurements, as a statistical significance or insignificance can be difficult to interpret. In order to claim an accurate and stable relation between CT numbers and CBCT voxel values, there is not only the requirement of a high correlation, but CBCT values also need to be independent of exposure and positioning factors to allow rescaling to CT numbers. The presented results do not support this claim for the investigated devices.

Contrast measurements further confirmed the general poor contrast between materials of intermediate density. CNR measurements showed that the noise is often similar or larger than the measured difference in mean voxel value between low-density hydroxyapatite and PMMA. For air and aluminium, large differences were seen for CNR values between devices.

The present study showed that image homogeneity and uniformity values were not only affected by the exposure. The reconstructed voxel size, the size of the imaging field and the amount of mass outside the volume were additional factors leading to differences in device performance. Bryant *et al.* have defined the "exo-mass" effect as the gradient of voxel values appearing for asymmetrical phantom positioning, leading to a shift in density response throughout the entire volume, as well as a decrease in uniformity [12]. This results in different noise and uniformity values for small- and large-field CBCTs.

A general consistency could be observed between FWHM values obtained from the point spread function and voxel sizes of the CBCT images. However, it can be clear that the voxel size itself provides only a crude prediction of the spatial accuracy [2,16]. The voxel size, determined by the manufacturer, should ideally provide a balance between spatial resolution and noise. It is seen that for some devices, pre-defined exposure protocols using different mAs values are reconstructed at different voxel sizes. As seen from the FWHM measurements, high dose protocols showed an increased spatial resolution in most cases. Two

exceptions were found, for which there was no clear difference in FWHM values between exposure protocols from the same device. For these exceptions, high and low dose protocols were reconstructed at similar or identical voxel sizes, and the increase in mAs did not result in an improved spatial resolution. It must be noted that the point spread function can be influenced by a number of additional factors, being the difference in voxel values for the steel wire and the surrounding air, and the presence of small streak artefacts.

Metal artefacts from titanium rods appear different when comparing CBCT devices and protocols. A method was established to quantify streaks by subtracting background voxel values and calculating an artefact added value (AAV). The AAV provides a relevant description of the net effect of streaks on image quality, but provides no information regarding beam hardening and photon starvation artefacts. Imai *et al.* proposed a statistical analysis of streak artefacts on CT images, using the extreme value theory [20]. This approach may provide a partial solution regarding a full artefact analysis for CBCT.

From a QC perspective, the variability of all image quality parameters show that a general threshold or range for acceptable parameter values cannot be established for CBCT and quality control should be based on the initial performance of the device at the time of installation and acceptance testing. These initial image quality results would then serve as baseline values for further tests on this particular device. Large deviations of QC results compared with the initial performance would then point out that the performance of the device needs to be assessed by the equipment installer, the manufacturer or that the device should be temporarily suspended from clinical use until the performance issue has been fixed.

In addition to this type of baseline QC evaluation, it could be possible to establish specific image quality criteria for CBCT. To enable this, an evaluation of the diagnostic relevance is required for all technical image quality parameters to establish a QA protocol based on these parameter values. For some parameters, this relevance is obvious, but their true diagnostic effect is not always clear. Based upon a poor correlation between voxel values and CT numbers, along with a high degree of noise and poor image uniformity, it may be concluded that CBCT images are not useful for quantitative analysis of bone quality. Bone analysis methods do not, however, necessarily rely on absolute or relative voxel values [21]. The results demonstrate that a CT number correlation analysis should not be part of a QC procedure for dental CBCT, as many manufacturers do not claim to have an accurate correlation with CT numbers for their device. Nevertheless, these devices can still be used in clinical practice for analysis of bone quality. As another example, a high contrast between aluminium and PMMA can partly predict a good bone segmentation quality in vivo, but the

latter also depends on factors such as geometric accuracy and spatial resolution of the system, and artefacts originating from the cortical bone and other high-attenuation objects such as implants and metallic restorations [16]. The further development of the QC phantom and the formation of a QA protocol will therefore be conducted in parallel with research on diagnostic image quality, which could allow determination of specific ranges or thresholds for certain image quality parameters. Our results suggest that different ranges may have to be applied for large and small FOV devices, as they perform differently in terms of noise and uniformity.

There are a number of possible improvements for the phantom, which will be implemented and evaluated in further development stages. Regarding the choice of materials, the results indicate that low-density hydroxyapatite is not a suitable material for contrast evaluation, due to the poor performance for most CBCT devices in terms of low-contrast resolution. Alternative materials will be investigated. Furthermore, the analysis of point spread function and metal artefacts will be fine-tuned. The measurements of the FWHM would be more accurate if an oversampling technique is used [10]. Also, the current phantom provides no analysis of spatial resolution along the z-axis, as the FWHM estimation if performed in the axial (x-y) plane. Although CBCT datasets are nominally isotropic, it is worthwhile to verify this by measuring the spatial resolution along all axes. The analysis of metal artefacts used in the current study provides a useful estimation of the artefact's effect on the adjacent region, but should be altered to involve the entire insert rather than a fixed region of interest. Furthermore, the image quality parameter used for artefacts should be independent of actual voxel values, as these values are not standardized in CBCT imaging. Further in-depth study is required to determine the ideal image analysis method for metal artefacts.

The measurement of radiation dose was not included in the current study, even though a comparison of high and low dose protocols provided certain insights concerning the relation between image quality and radiation dose. To establish a correct definition of image quality, there is a need for an accurate but relatively simple method for estimating the corresponding radiation dose using routine measurements, and relating these measurements to patient risk. Existing methods do not cope well with the exposure geometry and dose distribution of CBCT [22,23]. The development of a suitable dose index will establish the possibility for an extensive evaluation of CBCT performance, optimising image quality versus radiation dose (Chapters 5 and 6).

7.6 Conclusion

The currently evaluated phantom has shown promising potential for technical image quality evaluation of CBCT. Different image quality parameters were measured for a wide range of CBCT devices and protocols. Future work should focus on optimising the phantom and insert design, while establishing a QA protocol with appropriate criteria or ranges for each image quality parameter.

7.7 References

1. Horner K, Islam M, Flygare L, Tsiklakis K, Whaites E. Basic principles for use of dental cone beam CT: consensus guidelines of the European Academy of Dental and Maxillofacial Radiology. Dentomaxillofac Radiol 2009; 38: 187-195.

2. Loubele M, Jacobs R, Maes F, *et al*. Image quality vs radiation dose of four cone beam computed tomography scanners. Dentomaxillofac Radiol 2008; 37: 309-318.

3. Scarfe WC, Farman AG, Sukovic P. Clinical applications of cone-beam computed tomography in dental practice. J Can Dent Assoc 2002; 72: 75-80.

4. Du LY, Umoh J, Nikolov HN, Pollmann SI, Lee TY, Holdsworth DW. A quality assurance phantom for the performance evaluation of volumetric micro-CT systems. Phys Med Biol 2007; 52: 7087-7108.

5. Daly MJ, Siewerdsen JH, Moseley DJ, Jaffray DA, Irish JC. Intraoperative cone-beam CT for guidance of head and neck surgery: Assessment of dose and image quality using a C-arm prototype. Med Phys 2006; 33: 3767-3780.

6. McCann C, Alasti H. Comparative evaluation of image quality from three CT simulation scanners. J Appl Clin Med Phys 2004; 5: 55-70.

7. Suess C, Kalender WA, Coman JM. New low-contrast resolution phantoms for computed tomography. Med Phys 1999; 26: 296-302.

8. Jaffray DA, Siewerdsen JH. Cone-beam computed tomography with a flat-panel imager: initial performance characterization. Med Phys 2000; 27: 1311-1323.

9. Marguet M, Bodez V. [Quality control of a kV cone beam computed tomography imaging system]. Article in French. Cancer Radiother 2009; 13: 345-352.

10. Watanabe H, Honda E, Kurabayashi T. Modulation transfer function evaluation of cone beam computed tomography for dental use with the oversampling method. Dentomaxillofac Radiol 2010; 39: 28-32.

11. Vassileva J, Stoyanov D. Quality control and patient dosimetry in dental cone beam CT. Radiat Prot Dosimetry 2010; 139: 310-312.

12. Bryant JA, Drage NA, Richmond S. Study of the scan uniformity from an i-CAT cone beam computed tomography dental imaging system. Dentomaxillofac Radiol 2008; 37: 365-374.

13. Lascala CA, Panella J, Marques MM. Analysis of the accuracy of linear measurements obtained by cone beam computed tomography (CBCT-NewTom). Dentomaxillofac Radiol 2004; 33: 291-294.

14. Katsumata A, Hirukawa A, Okumura S, *et al*. Relationship between density variability and imaging volume size in cone-beam computerized tomographic scanning of the maxillofacial region: an in vitro study. Oral Surg Oral Med Oral Pathol Oral Radiol Endod 2009; 107: 420-425.

15. Lagravère MO, Carey J, Ben-Zvi M, Packota GV, Major PW. Effect of object location on the density measurement and Hounsfield conversion in a NewTom 3G cone beam computed tomography unit. Dentomaxillofac Radiol 2008; 37: 305-308.

16. Loubele M, Maes F, Schutyser F, Marchal G, Jacobs R, Suetens P. Assessment of bone segmentation quality of cone-beam CT versus multislice spiral CT: a pilot study. Oral Surg Oral Med Oral Pathol Oral Radiol Endod 2006; 102: 225-234.

17. Naitoh M, Hirukawa A, Katsumata A, Ariji E. Evaluation of voxel values in mandibular cancellous bone: relationship between cone-beam computed tomography and multislice helical computed tomography. Clin Oral Implants Res 2009; 20: 503-506.

18. Scarfe WC, Farman AG. What is cone-beam CT and how does it work? Dent Clin North Am 2008; 52: 707-730.

19. Schulze RKW, Berndt D, d'Hoedt B. On cone-beam computed tomography artifacts induced by titanium implants. Clin Oral Impl Res 2010; 21: 100–107.

20. Imai K, Ikeda M, Enchi Y, Niimi T. Statistical charachteristics of streak artifacts on CT images: relationship between streak artifacts and mA s values. Med Phys 2009; 36: 492-499.

21. Jiang C, Giger ML, Chinander MR, Martell JM, Kwak S, Favus MJ. Characterization of bone quality using computer-extracted radiographic features. Med Phys 1999; 26: 872-879.

22. Dixon RL. Restructuring CT dosimetry – a realistic strategy for the future Requiem for the pencil chamber. Med Phys 2006; 33: 3973–3976.

23. Lofthag-Hansen S, Thilander-Klang A, Ekestubbe A, Helmrot E, Gröndahl K. Calculating effective dose on a cone beam computed tomography device: 3D Accuitomo and 3D Accuitomo FPD. Dentomaxillofac Radiol 2008; 37: 72-79.

Chapter 8: Quantification of metal artefacts on CBCT images

8.1 Abstract

Objectives: To quantify metal artefacts obtained from a wide range of cone beam computed tomography (CBCT) devices and exposure protocols, to compare their tolerance to metals of different densities, and to provide insights regarding the possible implementation of metal artefact analysis into a QC protocol for CBCT.

Materials and methods: A customized polymethyl methacrylate (PMMA) phantom, containing titanium and lead rods, was fabricated. It was scanned on 13 CBCT devices and 1 multi-slice computed tomography (MSCT) device, including high-dose and low-dose exposure protocols. Artefacts from the rods were assessed by two observers by measuring the standard deviation of voxel values in the vicinity of the rods, and normalising this value to the percentage of the theoretical maximum standard deviation.

Results: For CBCT datasets, artefact values ranged between 6.1% and 27.4% for titanium, and between 10.0% and 43.7% for lead. Most CBCT devices performed worse than MSCT for titanium artefacts, but all of them performed better for lead artefacts. In general, no clear improvement of metal artefacts was seen for high dose protocols, although certain devices showed some artefact reduction for large FOV or high mAs protocols.

Conclusions: Regions in the vicinity of the metal rods were moderately or gravely affected, particularly in the area between the rods. In practice, the CBCT user has very limited possibilities to reduce artefacts. Researchers and manufacturers need to combine their efforts in optimising exposure factors and implementing metal artefact reduction algorithms.

8.2 Introduction

An increasing number of CBCT devices have become available over the last years, exhibiting a wide range in exposure parameters such as field of view (FOV) size, beam quality (voltage peak and filtration), amount of X-rays (anode current and exposure time) and rotation arc. Furthermore, different sizes and types of detectors are used, and different reconstruction algorithms are applied. All of these parameters affect the diagnostic image quality in terms of

image noise, high- and low-contrast resolution, and artefacts [1]. Metal artefacts are one of several types of artefacts found in all types of CT imaging [2,3]. There is a variety of small and large inserted metal objects found throughout the human body, especially in the head and neck area. Metallic restorations, crowns, brackets and implants affect the image quality of a reconstructed CT image due to effects such as beam hardening, scatter, quantum noise and photon starvation [3,4]. Beam hardening results in the increase of the mean beam energy after passing through the metal object due to the predominant absorption of low-energy X-rays. Scatter refers to X-rays deflecting from their original path but still reaching the detector, leading to faulty projection data. Quantum noise increases the graininess of the image due to a contamination of the detector signal. Furthermore, complete absorption (*i.e.* starvation) of all photons along certain beam paths may occur. These effects result in different types of image deterioration, ranging from bright streaks radiating from the metallic object to darkening of areas in its vicinity and even the complete loss of grey values between adjacent metallic objects (Figure 8.1). As a result, regions of interest for diagnosis, planning or follow-up are not properly visualized.
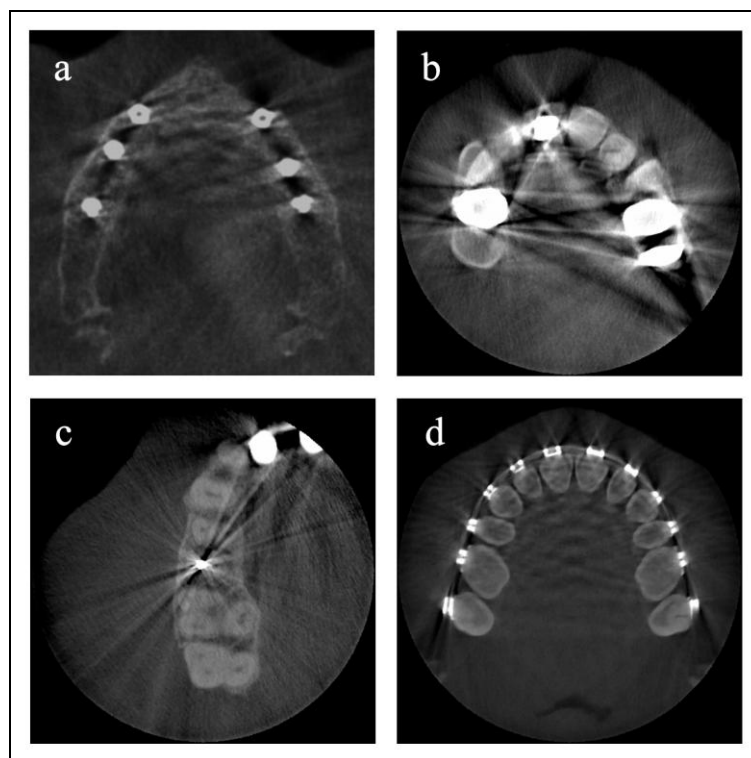

Figure 8.1 Examples of metal artefacts on cone beam computed tomography images in clinical practice due to (a) dental implants, (b) crowns, (c) endodontic filling and (d) orthodontic brackets.

The effects of metallic objects in CBCT imaging are similar to those observed in conventional CT. It has been reported by many authors that the diagnostic image quality of

head and neck CT or CBCT is hampered by the presence of metallic objects in the dental area [5-11]. Also, several authors have investigated metal artefact reduction using adapted scanning techniques [12,13] or specific reconstruction algorithms or post-processing techniques [14-18]. The majority of these studies use observers to evaluate artefact-related parameters, which can be useful to evaluate artefact reduction and diagnostic effects. However, this type of subjective evaluation cannot provide a comparison of the performance of different devices and protocols and cannot be used in routine quality control. Some studies have investigated the quantification of metal artefacts using different approaches [10,11,19]. However, there is no standardized parameter available to quantify the effect of metals on the surrounding voxel values.

The aim of this study was to quantify metal artefacts on CBCT images using a quality control phantom, involving a wide range of CBCT devices and exposure protocols. This quantification would serve as a comparison of the tolerance of different system and protocols to metals of different densities, and provides insights regarding the possible implementation of metal artefact analysis into a QC protocol for CBCT.

8.3 Materials and methods

Phantom and metal artefact inserts

A second prototype of the head-size cylindrical polymethyl methacrylate (PMMA) phantom developed in Chapter 7 was manufactured by Leeds Test Objects Ltd (Bouroughbridge, UK). As described in Chapter 7, the phantom contained seven cylindrical holes, allowing the placement of inserts for image quality analysis.

Two types of inserts (35 mm diameter, 20 mm height) were used for the analysis of metal artefacts. Both inserts consisted of three metal rods of 5.2 mm, positioned in-line and surrounded by PMMA. For one insert, titanium was used to investigate the effect of dental implants. For the other, lead was selected to investigate artefacts from high-density metals used in dental fillings and crowns.

CBCT scanning

The inserts were placed in the peripheral columns of the head-size phantom. Two inserts of each type (titanium and lead) were used, positioned in a different orientation. One insert was positioned parallel to the phantom edge, the other perpendicular to this edge. Inserts of the

same type were positioned at the same height. Empty columns were filled using blank PMMA inserts.

The phantom was scanned using 13 CBCT devices: 3D Accuitomo 170 (J. Morita, Kyoto, Japan), 3D Accuitomo XYZ image intensifier version (J. Morita, Kyoto, Japan), GALILEOS Comfort (Sirona Dental Systems, Germany), i-CAT Next Generation (Imaging Sciences International, Hatfield, PA, USA), Kodak 9000 3D (Carestream Health, New York, NY, USA), Kodak 9500 (Carestream Health, New York, NY, USA), NewTom VGi (Quantitative Radiology, Verona, Italy), Pax-Uni3D (Value Added Technologies, Korea), Picasso Trio (Value Added Technologies, Yongin, Republic of Korea), ProMax 3D (Planmeca Oy, Helsinki, Finland), SCANORA 3D (Soredex, Tuusula, Finland), SkyView (Cefla Dental Group, Imola, Italy) and Veraviewepocs 3D (J. Morita, Kyoto, Japan). The phantom was also scanned with a multi-slice computed tomography (MSCT) device (Somatom Sensation 64, Siemens, Erlangen, Germany). Different exposure protocols were used where possible, generally involving a change in the FOV size, amount of exposure (mAs) and/or voxel size of the reconstructed image. All exposure protocols are shown in Table 8.1. A total of 30 protocols were included for CBCT. For MSCT, a soft tissue (H30s) and bone (H60s) protocol were included.

Image analysis

All datasets of were evaluated with the ImageJ software version 1.41o (National Institutes of Health, Bethesda, MD, USA). Datasets in compressed DICOM format were uncompressed with a custom-made tool before import into the software, seeing that ImageJ cannot open compressed images.

Table 8.1 Selected exposure protocols and measurement results for CBCT and MSCT devices

CBCT	Protocol[a]	FOV (cm)	kVp	mA	Exposure time (s)	Voxel size (mm)	Ti	Pb
3D Accuitomo 170	LV HI	17x12	90	5	31	0.25	6.3	11.5
	LV LO	17x12	90	5	18	0.25	6.1	11.9
	SV HI*	6x6	90	5	31	0.08	8.3	19.3
	SV LO	6x6	90	5	18	0.08	8.1	19.9
3D Accuitomo XYZ	SV*	4x3	80	4	18	0.125	13.6	15.6
Galileos Comfort	LV HI*	15x15	85	7	4	0.29	14.8	24.3
I-CAT Next Generation	XLV HI	23x16	120	5	7	0.3	8.4	16.9
	XLV LO	23x16	120	5	4	0.3	8.7	19.7
	LV XHI	16x13	120	5	7	0.25	8.5	17.7
	LV HI*	16x13	120	5	4	0.25	8.9	18.2
	LV LO	16x13	120	5	4	0.4	9.0	21.4
	LV XLO	16x13	120	5	2	0.4	10.1	22.9
Kodak 9000 3D	SV*	5x3.6	70	10	11	0.076	16.3	14.9
Kodak 9500	XLV	20x18	90	10	11	0.3	9.5	14.1
	LV*	14.5x8.3	90	10	11	0.2	15.1	21.1
NewTom VGi	MV HI*	12x8	110	12	15	0.24	10.2	22.5
	MV LO	12x8	110	4	10	0.24	10.7	21.9
PaX-Uni3D	SV*	5x5	85	6	20[b]	0.2	9.3	20.5
Picasso Trio	MV HI*	12x7	85	4.8	24[b]	0.2	26.6	41.7
	MV LO	12x7	85	4.8	15[b]	0.3	27.4	43.7
ProMax 3D	MV HI1*	8x8	84	14	12	0.16	17.8	32.4
	MV HI2	8x8	84	14	12	0.32	17.7	32.3
	MV LO	8x8	84	7	3	0.32	18.6	32.7
SCANORA 3D	MV HI	10x7.5	85	15	3.8	0.2	19.8	30.2
	MV ME*	10x7.5	85	8	3.8	0.2	19.9	30.3
	MV LO	10x7.5	85	8	2.5	0.3	18.0	30.0
SkyView	LV HI	17x17	90	6.5	15	0.34	20.0	31.4
	LV ME*	17x17	90	6.5	8	0.34	22.2	34.1
	LV LO	17x17	90	6.5	6	0.34	25.8	39.9
Veraviewepocs 3D	MV*	8x8	70	3	17	0.125	10.7	10.0
MSCT		FOV	kVp	mA	Exposure time (s)	Voxel size (mm)	Ti	Pb
Somatom Sensation 64	H30s	Full	120	139	1	0.39	9.6	58.3
	H60s*	Full	120	127	1	0.39	13.4	62.6

[a]A selection of protocols was made based on the availability of the device and the clinical relevance of the protocol. Other clinical exposure protocols may be available. The mentioning of HI, ME or LO refers only to the exposure range of that specific device, the exposure of different devices cannot be compared based on this terminology.

[b]These values are for acquisition time, actual exposure time not known and not shared by manufacturer.

*Exposure protocols selected for Figure 8.2.

FOV field of view, *SV* small volume, *MV* medium volume, *LV* large volume, *HI* high dose; *ME* medium dose, *LO* low dose, *X* extra, *Ti* titanium, *Pb* lead

A fixed region of interest (ROI) was used in the axial view. This ROI encompassed the entire insert, with the exception of the metal itself (Figure 8.2). Removing the metal from the selection was performed manually, as it was seen that no standardized segmentation method was appropriate; in some cases, voxel values well outside the metal area were saturated, in other cases non-saturated voxel values were found in the centre of the metal. Within the selected ROI, the standard deviation (SD) of all voxel values was determined. Seeing that not all CBCT datasets use the conventional 12 bit scale (4096 grey values), it is not possible to compare measured SDs from different CBCT datasets directly. A correction was applied to the measured SDs by measuring minimum and maximum grey values within the datasets. Based on the actual grey value range, a correction factor was calculated. This factor ensures that all SDs correspond to 12 bit images. Next, the values were normalised a second time to facilitate their interpretation. Seeing that the theoretical maximum SD for 12 bit images is 2048 (*i.e.* half of the voxels is black, the other half is white), the SDs were normalised to a percentage, with 2048 being equal to 100%. Consequently, the results can be interpreted as the percentage of the maximum SD.
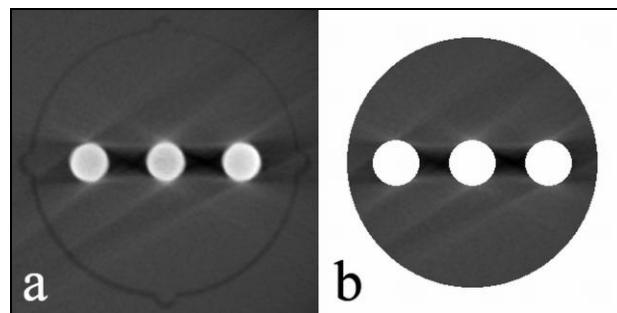

Figure 8.2 Selection of region of interest (ROI) for metal artefact measurements. (a) Example axial slice of metal artefact insert. (b) ROI, avoiding metal rods and air spaces.

All measurements were performed by two observers with extensive experience in image analysis. One observer performed the measurements twice to estimate intra-observer variability. Inter-observer agreement between the measurements was also investigated. In rare cases where the deviation between the two observers was higher than 5% of the measured value, the measurements were discarded and carefully repeated by both observers to achieve an acceptable consistency. The average value of all measurements was used, with the exception of those which were discarded due to the 5% threshold. For both titanium and lead, the mean value from the two inserts containing the material was used as it was seen that there was no perceived difference between values from the two insert orientations (parallel and perpendicular to the edge).

8.4 Results

Figure 8.3 shows close-ups of axial slices of the titanium insert for each scanner type. Although an automatic window/level setting was used, these figures should not be used for metal artefact evaluation, as the appearance of these artefacts is affected by the grey level display. Still, it can be seen that the artefacts appear different for the included devices and protocols. Similar artefacts are found in the PMMA region between the rods, which contains no projectional information from exposure angles running through the three rods, as those X-rays are completely absorbed. The grey values of this region are therefore gravely underestimated.

The mean variability between measurements performed by the two observers, after discarding and repeating measurements that varied more than the acceptable threshold of 5%, was 3%. The mean deviation between repeated measurements by the same observer was 1%; the maximum deviation was 4%.

Table 8.1 shows the measured values for all devices and protocols, expressed as the percentage of the theoretical maximum standard deviation. This value represents an overall estimation of the metal's influence on voxel values in the neighboring region, and higher values correspond to more extensive artefacts. For titanium, the artefact value ranged from 6.1 (3D Accuitomo 170, LV LO) to 27.4 (Picasso Trio, MV LO) with an average of 14.2 for all CBCT datasets. For lead, the artefact value was found between 10.0 (Veraviewepocs 3D) and 43.7 (Picasso Trio, MV LO) with an average of 24.1 for all CBCTs. For the two MSCT protocols, the averages values were 12.4 for titanium and 52.8 for lead.

With two exceptions (Kodak 9000 3D and Veraviewepocs 3D), all protocols showed considerably higher values for lead than for titanium. When focusing on the variability between different exposure protocols from the same device, the clearest difference is seen for the 3D Accuitomo 170, for which the large FOV performed better than the small FOV. For the i-CAT Next Generation, the largest FOV also performed better, although differences were smaller given that both FOVs can be considered as relatively large. For both FOVs, high dose protocols performed better than low dose protocols, although differences were rather small. For the ProMax 3D and SCANORA 3D, there was no clear difference between high- and low-dose protocols. For the SkyView, the low dose protocol performed worse.
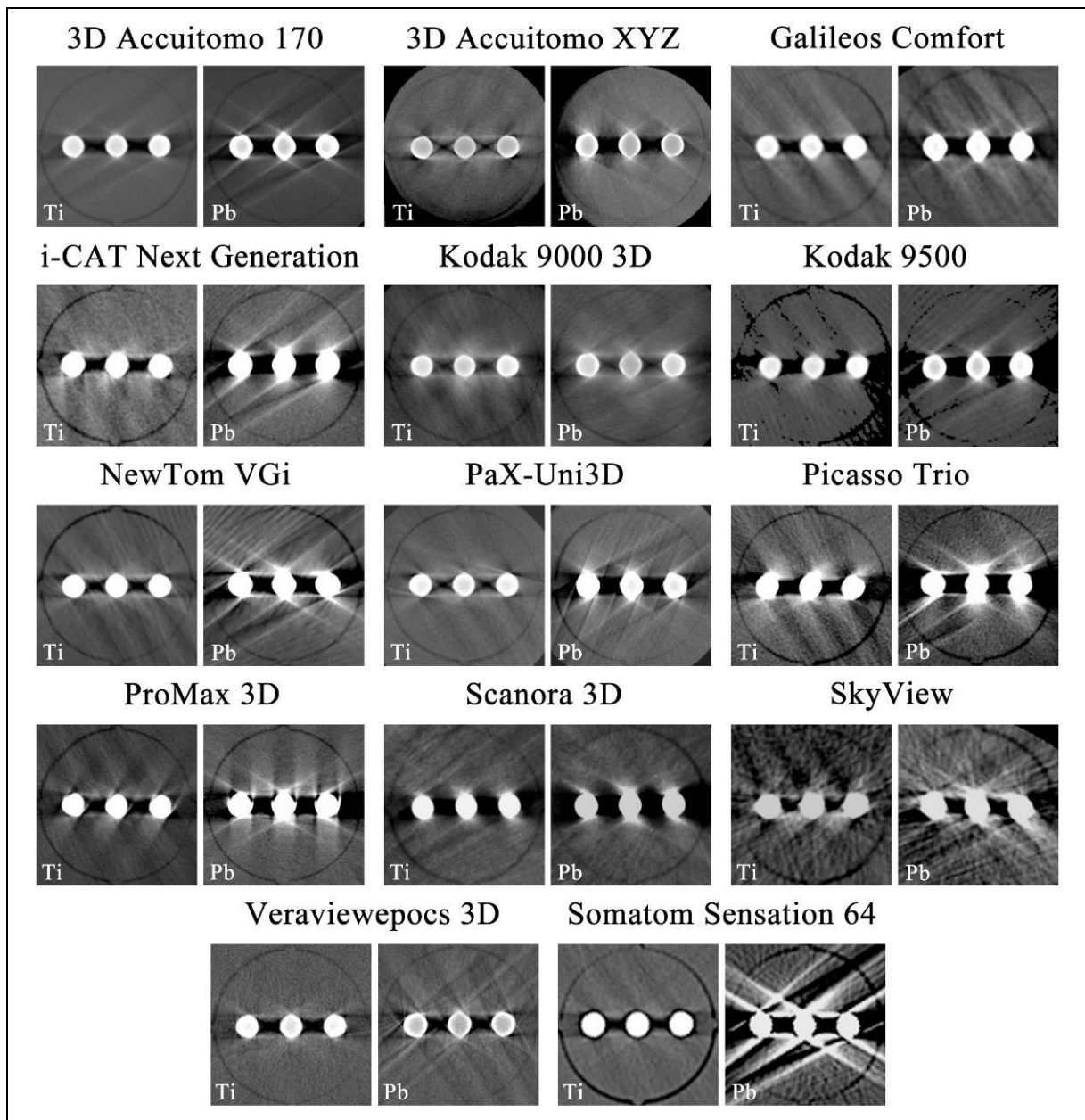
Figure 8.3 Axial slices of titanium and lead inserts for selected cone beam computed tomography and multi-slice computed tomography protocols. An automatic window/level setting was chosen in most cases; manual window/level adjustment was performed if the automatic setting was suboptimal. Visual evaluation of these artefacts should be avoided.

8.5 Discussion

The current study investigates metal artefacts on CBCT images by measuring the effect of titanium and lead rods on surrounding voxel values in a PMMA phantom. A wide range of devices was involved and differences between devices and exposure protocols were assessed. A prototype QC phantom was used for the evaluation, containing two types of insert for metal artefact analysis. This head-sized PMMA phantom has similar attenuation properties to a

146

human head, ensuring that voxel values are distributed similarly to actual clinical scans. Naturally, the phantom does not contain the distinctive features found in the dentomaxillofacial region, but this is not needed for the analysis of technical image quality performance, seeing that voxel values and noise are primarily affected by the total mass inside and outside the FOV, and not by the shape or attenuation range of the scanned object.

The phantom was scanned on 13 CBCT devices and one MSCT device. In total, 32 exposure protocols were evaluated. For some devices, a single protocol was selected as it was seen that this particular protocol was the only one used in clinical practice. For other devices, multiple protocols were selected, varying the FOV size and the dose. Large differences are seen for the CBCT devices with regards to the tube voltage peak (70-120 kVp), tube current-time product (10-180 mAs) field of view size (4x3-20x18 cm) and reconstructed voxel size (0.08-0.4 mm). Furthermore, different types of detectors are used; most CBCT devices use flat panel detectors instead of image intensifiers, as they are proven to result in lower noise levels [20]. Also, different reconstruction algorithms are applied; although most devices use a modified filtered backprojection algorithm, algebraic reconstruction techniques are being applied for a few years. All of these factors combined imply that there is a wide range of radiation dose for these devices, and that considerable differences in image quality can be expected.

For the analysis of metal artefacts, small rods of titanium and lead were used to represent metals of relatively low density that are used in implants and restorations, and high-density metals that are used in crowns and bridges, respectively. To obtain an overall assessment of the effect of these two metals on the surrounding voxel values, the standard deviation (SD) was selected. This parameter provides an overall estimation of the extent of darkening and brightening caused by metals. Although it is a useful parameter for comparing different devices and protocols, there are a few important considerations. First of all, there is a wide range of voxel sizes used in CBCT imaging which influences the noise, although this should not affect the SD when measuring large, non-uniform regions as in the current study. It was considered to resample all images to one voxel size (*e.g.* 1 mm) but preliminary tests pointed out that this would not affect the measurements. Also, different degrees of inherent image noise could affect the SD value. It was considered to measure the noise in a homogeneous region and use this as a correction factor to obtain an 'artefact-to-noise' ratio, but this type of parameter would be difficult to interpret as it involves two quasi-independent image quality values.

147

When comparing the current results with the metal artefact analysis in Chapter 7, a few tendencies can be seen. Considering the five CBCT devices which are included in both chapters, the best and worst performing CBCTs are the same. When intercomparing other devices, it is seen that their performance is different for the analysis in Chapter 7, which focused on white artefact streaks, than for the current analysis, which provided an overall estimate of the artefact including the areas between the rods. Furthermore, in both studies, little or no difference is seen between different high- and low-dose exposure protocols from the same CBCT device.

As expected, a wide range is seen for artefact values for the CBCT devices and protocols that are investigated. A 5-fold range is seen for titanium artefacts, and a 4-fold range for lead artefacts. When comparing exposure protocols from the same device, a few remarks can be made. The only significant difference between these protocols is the mAs, seeing that differences in voxel size do not directly affect the measurement of standard deviations in large heterogeneous regions. In most cases, the mAs varied between protocols because of a difference in the number of acquired projections (exposure time) rather than the anode current. Although it can be expected that a larger number of projections leads to artefact reduction, there was no perceptible difference between high-mAs and low-mAs protocols for some devices. For one device, an 88% increase in mA at constant exposure time did not result in any artefact improvement. For others, a certain degree of artefact reduction could be spotted. Large differences between protocols were seen if the size of the FOV was varied. Large FOV performed better in these cases, presumably because of the local tomography effect for small FOVs. In this case, tissues or materials outside the ROI contribute to the detector signal for part of the rotation arc. The affected projection data leads to additional errors in image reconstruction [21].

The results from this study are difficult to interpret in terms of QC, as there is no reference frame for metal artefact-related parameters. Based on these measurements, it can be clearly seen that some devices perform worse than others when metals are introduced in the images. However, there is no evidence that some of these devices are unacceptable for clinical use. Previous studies have pointed out that there is a large range in the perceived or measured image quality for CBCT devices in dentistry [22-24]. However, there are no specific guidelines regarding clinical imaging performance requirements for dental CBCT devices. Furthermore, no large-scale studies on diagnostic image quality are available, which are needed to assess the relation between technical parameters that can be measured in quality control and diagnostic validity. Clear diagnostic criteria are needed to ensure that technical

image parameters like the one measured in this study can be interpreted in a relevant way. This can lead to a detailed QA protocol containing revision or suspension thresholds for these parameters.

In terms of artefact reduction, the most relevant conclusion based on the current results is that the possibility for artefact reduction based on the adjustment of exposure parameters is very limited and clinically not feasible. From the results, two possibilities are shown to reduce the effect of artefacts: increasing the FOV size and increasing the mAs. The former is not feasible in practice, seeing that the FOV should always be limited to the area of interest to limit the radiation dose; the increase of dose by using larger FOVs for the sole purpose of reducing artefacts cannot be justified [25]. For the latter, it was seen that only a limited improvement is seen for some devices. Again, the small gain in image quality is outweighed by the increase in dose, which is linearly related to the mAs if the beam quality, FOV size and position are kept constant. Another option for artefact reduction which is not covered by the current study is the adjustment of the tube voltage. It has been shown that there is a considerable difference between low-energy and high-energy beams in the attenuation by high-density objects [11]. However, for this study it was chosen not to vary the kV, seeing that the devices that allow for voltage selection are found in the 60-90 kVp range. This does not represent the typical voltage range of CBCT devices, most of which are found between 80 and 120 kVp. Therefore, it was not possible to study the absolute effect of kVp within a relevant range.

This study points out that, because of the limited possibility for artefact reduction by the operator, the devices need to be optimised by enabling exposure factors that are appropriate for artefact reduction and other image quality parameters, finding a balance with the radiation dose. An additional aspect is the optimisation and clinical implementation of specific metal artefact reduction (MAR) algorithms, which have been under investigation for several years. Different approaches have been used for MAR. Most of the algorithms under investigations can be categorized as projection interpolation, iterative reconstruction and filtering algorithms, using different approaches or combinations thereof to limit the effect of metal objects in the image [14-18]. There seems to be a general consensus that the continuous increase in computational power will lead to an increasing clinical implementation of artefact reduction using iterative reconstruction algorithms [11,26]. However, the cone beam geometry provides additional challenges in artefact reduction compared to parallel or fan-beam reconstruction. It may take several more years before iterative MAR algorithms are implemented in routine clinical practice.

8.6 Conclusion

The measurement of metal artefacts on CBCT devices shows a wide range of values, which can be expected from the variety of imaging parameters used. In clinical practice, diagnosis of the area between adjacent metal objects should be avoided, seeing that these region show excessive loss of projectional information. For other affected regions in the vicinity of the metal, image evaluation should be done with care and quantitative measurements based on voxel values (*e.g.* bone quantity) should be particularly avoided. Although some possibility for artefact reduction could be seen when comparing different exposure protocols from the same device, it cannot be justified to increase the radiation dose for the sole purpose of MAR, as the effect on the artefacts is too limited.

8.7 References

1. Goldman LW. Principles of CT: radiation dose and image quality. J Nucl Med Technol 2007; 35: 213-225.

2. Barrett JF, Keat N. Artifacts in CT: recognition and avoidance. Radiographics 2004; 24: 1679-1691.

3. Schulze R, Heil U, Groβ D, Bruellmann D, Dranischnikow E, Schwanecke U, Schoemer E. Artefacts in CBCT: a review. Dentomaxillofac Radiol 2011; 40: 265-273.

4. De Man B, Nuyts J, Dupont P, Marchal G, Suetens P. Metal streak artifacts in X-ray computed tomography: A simulation study. IEEE Trans Nucl Sci 1999; 46: 691–696.

5. Draenert FG, Coppenrath E, Herzog P, Müller S, Mueller-Lisse UG. Beam hardening artefacts occur in dental implant scans with the NewTom cone beam CT but not with the dental 4-row multidetector CT. Dentomaxillofac Radiol 2007; 36: 198-203.

6. Holberg C, Steinhäuser S, Geis P, Rudzki-Janson I. Cone-beam computed tomography in orthodontics: benefits and limitations. J Orofac Orthop 2005; 66: 434–444.

7. O'Daniel JC, Rosenthal DI, Garden AS, Barker JL, Ahamad A, Ang KK, Asper JA, Blanco AI, de Crevoisier R, Holsinger FC, Patel CB, Schwartz DL, Wang H, Dong L. The effect of dental artifacts, contrast media, and experience on interobserver contouring variations in head and neck anatomy. Am J Clin Oncol 2007; 30: 191-198.

8. Perrella A, Lopes PM, Rocha RG, Fenyo-Pereira M, Cavalcanti MG. Influence of dental metallic artifact from multislice CT in the assessment of simulated mandibular lesions. J Appl Oral Sci 2010; 18: 149-154.

9. Razavi T, Palmer RM, Davies J, Wilson R, Palmer PJ. Accuracy of measuring the cortical bone thickness adjacent to dental implants using cone beam computed tomography. Clin Oral Implants Res 2010; 21: 718–725.

10. Sanders MA, Hoyjberg C, Chu CB, Leggitt VL, Kim JS. Common orthodontic appliances cause artifacts that degrade the diagnostic quality of CBCT images. J Calif Dent Assoc 2007; 35: 850–857.

11. Schulze R, Berndt D, d'Hoedt B. On cone-beam computed tomography artifacts induced by titanium implants. Clin Oral Implants Res 2010; 21:100-107.

12. Haramati N, Staron RB, Mazel-Sperling K, Freeman K, Nickoloff EL, Barax C, Feldman F. CT scans through metal scanning technique versus hardware composition. Comput Medical Imaging Graph 1994; 18: 429–434.

13. Nakae Y, Sakamoto K, Minamoto T, Kamakura T, Ogata Y, Matsumoto M, Johkou T. Clinical evaluation of a newly developed method for avoiding artifacts caused by dental fillings on X-ray CT. Radiol Phys Technol 2008; 1: 115-122.

14. Bal M, Spies L. Metal artifact reduction in CT using tissue-class modeling and adaptive prefiltering. Med Phys 2006; 33: 2852-2859.

15. Prell D, Kyriakou Y, Beister M, Kalender WA. A novel forward projection-based metal artifact reduction method for flat-detector computed tomography. Phys Med Biol 2009; 54: 6575-6591.

16. Wang G, Vannier MW, Cheng PC. Iterative X-ray cone-beam tomography for metal artifact reduction and local region reconstruction. Microsc Microanal 1999; 5: 58–65.

17. Watzke O, Kalender WA. A pragmatic approach to metal artifact reduction in CT: merging of metal artifact reduced images. Eur Radiol 2004; 14: 849-856.

18. Zhang Y, Zhang L, Zhu XR, Lee AK, Chambers M, Dong L. Reducing metal artifacts in cone-beam CT images by preprocessing projection data. Int J Radiat Oncol Biol Phys 2007; 67: 924-932.

19. Imai K, Ikeda M, Enchi Y, Niimi T. Statistical characteristics of streak artifacts on CT images: relationship between streak artifacts and mA s values. Med Phys 2009; 36: 492-9.

20. Baba R, Ueda K, Okabe M. Using a flat-panel detector in high resolution cone beam CT for dental imaging. Dentomaxillofac Radiol 2004; 33: 285-290.

21. Siltanen S, Kolehmainen V, Järvenpää S, Kaipio JP, Koistinen P, Lassas M., Pirttilä J, Somersalo E. Statistical inversion for medical x-ray tomography with few radiographs: I. General theory. Phys Med Biol 2003; 48: 1437-1463.

22. Liang X, Jacobs R, Hassan B, Li L, Pauwels R, Corpas L, Souza PC, Martens W, Shahbazian M, Alonso A., Lambrichts, I. A comparative evaluation of Cone Beam Computed Tomography (CBCT) and Multi-Slice CT (MSCT) Part I. On subjective image quality. Eur J Radiol 2010; 75: 265-269.

23. Loubele M, Maes F, Schutyser F, Marchal G, Jacobs R, Suetens P. Assessment of bone segmentation quality of cone-beam CT versus multislice spiral CT: a pilot study. Oral Surg Oral Med Oral Pathol Oral Radiol Endod 2006; 102: 225-234.

24. Suomalainen A, Kiljunen T, Käser Y, Peltola J, Kortesniemi M. Dosimetry and image quality of four dental cone beam computed tomography scanners compared with multislice computed tomography scanners. Dentomaxillofac Radiol 2009; 38: 367-378.

25. Horner K, Islam M, Flygare L, Tsiklakis K, Whaites E. Basic principles for use of dental cone beam CT: consensus guidelines of the European Academy of Dental and Maxillofacial Radiology. Dentomaxillofac Radiol 2009; 38: 187-195.

26. Wang G, Yu H, De Man B. An outlook on x-ray CT research and development. Med Phys 2008; 35: 1051-1064.

Chapter 9: Comparison of spatial and contrast resolution for CBCT scanners

9.1 Abstract

Objective: The purpose was to evaluate the perceived spatial and contrast resolution for a wide range of CBCT devices.

Materials and methods: A customized polymethyl methacrylate (PMMA) phantom was used. Inserts containing a line pair and rod pattern were used. The phantom was scanned using thirteen CBCT devices and one MSCT device, using a variety of scanning protocols. The images were presented to four observers for scoring.

Results: The observer scores showed excellent agreement. A wide range was seen in image quality between CBCT exposure protocols. Compared to the average CBCT scores, the MSCT protocols scored lower for the line pair insert but higher for the rod insert.

Conclusions: CBCT devices are generally suitable for the visualization of high-contrast structures. Certain exposure protocols can be used for depicting low-contrast structures or fine details. The user should be able to select appropriate exposure protocols according to varying diagnostic requirements.

9.2 Introduction

Over the last decade, many studies have evaluated one or more aspects of image quality of dental CBCT [1-5]. Many authors compared the quality of CBCT with MSCT or two-dimensional radiography [6-15]. Some included different CBCT devices in their study, resulting in a clearer depiction of the range in imaging performance seen in CBCT [8-10]. Also, a wide variety of phantoms and test objects have used in the evaluation of CBCT. The use of skulls [3-8,13], anthropomorphic phantoms [14] or patient data [15-17] leads to results that are clinically relevant, providing that an appropriate simulation of the total density of the head is used. However, many studies use observers to grade the visibility of anatomical landmarks, which is prone to subjectivity due to the calibration of the observer and their background. Also, it is difficult to standardize these types of studies, as there are different experimental setups and analysis methods used in practice.

Alternatively, geometrical phantoms are used which allow for the quantification of different image quality parameters [9-12]. Although these types of studies are useful for device intercomparison and quality control and allow for a degree of standardization, it is difficult to relate technical image quality parameters (*e.g.* contrast-to-noise ratio) to the clinical situation and to obtain threshold values for clinical use (Chapter 12). There has been no wide-scale evaluation of the imaging performance of CBCT and the tools used for analysis are suboptimal, being prone to a large degree of subjectivity or leading to results that are difficult to relate to the diagnostic performance.

The aim of this study is to investigate the possibility of a routine observer evaluation of spatial resolution and contrast in CBCT using a customized geometrical phantom and involving a wide range of CBCT devices and exposure protocols.

9.3 Materials and methods

Phantom and inserts

A second prototype of the cylindrical polymethyl methacrylate (PMMA) phantom described in Chapter 7 was manufactured by Leeds Test Objects Ltd (Bouroughbridge, UK). The phantom contained seven cylindrical holes, allowing the placement of inserts for image quality analysis [18]. Two types of inserts (3.5 cm diameter, 2 cm height) were used for the analysis of spatial and contrast resolution. For the first insert, a line pair (lp) pattern was designed using alternating aluminium and polymer sheets with different thickness, ranging between 1 and 10 lp/mm. Two inserts of this type were produced, allowing for an evaluation in the axial (XY) and transaxial (XZ/YZ) planes. The second type of insert contained five cylindrical rods of different sizes (1 to 5 mm) positioned at the vertices of a regular pentagon, using PMMA as a background material. For this type, five different inserts were produced, using air, aluminium and three different densities of hydroxyapatite (HA): 50 mg/cm³, 100 mg/cm³, and 200 mg/cm³.

CBCT scanning

The inserts were placed in the peripheral columns of the head-size phantom. Empty columns were filled using uniform PMMA inserts. The phantom was scanned using 13 CBCT devices: 3D Accuitomo 170, 3D Accuitomo XYZ image intensifier version and Veraviewepocs 3D (J. Morita, Kyoto, Japan), GALILEOS Comfort (Sirona Dental Systems, Germany), i-CAT Next

Generation (Imaging Sciences International, Hatfield, PA, USA), Kodak 9000 3D and Kodak 9500 (Carestream Health, New York, NY, USA), NewTom VGi (Quantitative Radiology, Verona, Italy), Pax-Uni3D and Picasso Trio (Value Added Technologies, Yongin, South Korea), ProMax 3D (Planmeca Oy, Helsinki, Finland), SCANORA 3D (Soredex, Tuusula, Finland), and SkyView (Cefla Dental Group, Imola, Italy). The phantom was also scanned with a MSCT device (Somatom Sensation 64, Siemens, Erlangen, Germany). A total of 30 clinically applied exposure and/or reconstruction protocols were selected for the included CBCT devices, varying different parameters such as the size of the FOV, the amount of exposure (mAs) and the reconstructed voxel size. Table 8.1 (Chapter 8, p.141) provides an overview of all scanning protocols.

Observer evaluation

Images were exported in Digital Imaging and Communications in Medicine (DICOM) format for further processing using ImageJ (version 1.41, National Institutes of Health, Bethesda, MD, USA). The original axial slices were used for all inserts except for the transaxial line pair pattern, for which oblique reformatting was performed using OnDemand3D (version 1.0.6.9457, CyberMed, Seoul, South Korea). For each insert, a single slice in the middle of the insert was selected and cropped to contain only the insert of interest, and the grey scale window and level was manually set to optimise contrast and to avoid subjective adjustment of the grey scale by the observers.

All images were assessed by four observers. Two observers had a background in Biomedical Sciences, two in Medicine. All observers were experienced in the evaluation of radiographic images; no specific dental expertise was needed as the observers looked at geometric patterns rather than anatomical structures. All observations were done in a darkened room using a SyncMaster 971p (Samsung, Seoul, South Korea) display with a luminance of 250 cd/m^2, contrast ratio of 1500:1 (*i.e.* stated by the manufacturer) and pixel resolution of 1280x1024. The CBCT and MSCT images of the inserts were evaluated in a random order. For the line pair insert, the axial and transaxial images were shown together. For the rod insert, slices from all five inserts were presented together. The observers were calibrated prior to the actual observations using a few selected insert images from datasets of poor, intermediate and good image quality, representing the range of image quality from the actual observation data. Each observation was performed twice with a one-week interval to assess intra-observer agreement.

For the line pair inserts, it was found during the preparation of the observation that counting the number of distinguishable lines would not lead to useful results. As opposed to what could be expected from the nominal voxel size, the actual spatial resolution of all devices was found to be less than 3 lp/mm seeing that line pairs at a higher resolution were indistinguishable for all datasets. As a result, when using line counting only three different scores would be possible (*i.e.*, 0-1, 1-2, and 2-3 lp/mm). To obtain more differentiated results, it was chosen to score the general visibility of the line pattern. A scoring system of 0 to 5 was used. The observers were instructed to provide one score per insert based on three criteria: the ability to distinguish adjacent lines, the geometric shape of the lines and their sharpness. It can therefore be considered as a combined analysis of spatial resolution, contrast resolution, geometric distortion and noise. For the rod insert, scoring was more straightforward. For the five included materials, the observers counted the number of rods that could be distinguished from the PMMA background, resulting in scores from 0 to 5 for each material.

To assess the inter- and intra-observer agreement, Kappa statistics was done using MedCalc (version 11.2, MedCalc Inc, Mariakerke, Belgium). To investigate the difference in performance between the CBCT units and exposure protocols, the Newman-Keuls Multiple Comparison Test was performed using Prism (version 5, GraphPad Software Inc., San Diego, CA, USA).

9.4 Results

Intra- and inter-observer agreement

The linear weighted kappa was determined for the scores of each insert type separately. The air and aluminium rod inserts were not included in this analysis, as it was seen that the inter- and intra-observer agreement was perfect. When comparing the intra-observer scores for sessions 1 and 2, kappa ranged between 0.603 and 0.898 with an average of 0.755 for the line pair inserts, and between 0.682 and 1.000 with an average of 0.852 for the rod inserts.

When comparing the inter-observer scores, the weighted kappa was between 0.686 and 0.869 (average 0.768) for the line pair insert and between 0.651 and 1.000 (average 0.844) for the rod insert. It can be seen that for the intra- and inter-observer comparisons, all kappa values were found in the 0.6-0.8 (substantial agreement) or 0.8-1 (almost perfect agreement) range [19]. On average, the agreement scores were considerably higher for the rod insert than for the line pair insert.

Insert evaluation results

Figure 9.1 shows example CBCT and MSCT images for both inserts. The average scores for the two line pair inserts and three rod inserts are shown in Table 9.2. Significant differences for pairwise comparison of exposure protocols are shown by the Rank number. This number is calculated as the sum of significant pairwise comparisons with all other exposure protocols. A significant difference with a lower-scoring protocol is counted as +1, with a higher-scoring protocol it is counted as -1. The highest possible Rank value is +31 (*i.e.* if the highest scoring protocol shows a significant difference with all 31 other protocols) and the lowest theoretical Rank is -31. For the line pair inserts, the average score for the axial and transaxial inserts were used, as there was no consistent difference between the two inserts, showing average scores of 1.96 and 1.98 respectively. For the rod inserts the average score for the three HA inserts was used, as it was seen that all rods were visible for the air and aluminium inserts for all protocols.
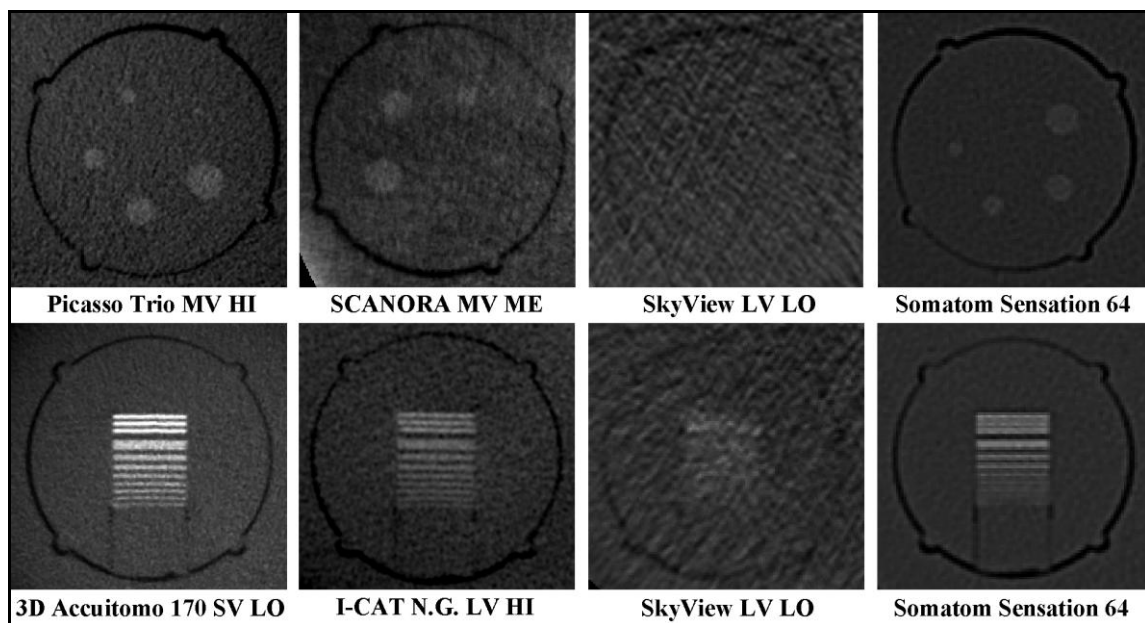

Figure 9.1 Example slices of line pair and rod inserts. The HA200 rod insert (top row) and the axial line par insert (bottom row) are shown. The best scoring (first column), median scoring (second column) and worst scoring (third column) CBCT protocols were selected for each insert, as well as the MSCT H60s protocol (right column).

Scores for the line pair inserts varied between 0 (SkyView, all three protocols) and 4.0 (3D Accuitomo 170, SV LO), showing a large inter-CBCT variability. The average score for all CBCT protocols was 2.0, for the two MSCT protocols it was 1.1. When comparing different intra-CBCT exposure protocols, it can be seen that small FOV protocols generally score better than large FOV scans. This is the case for the 3D Accuitomo 170, Kodak 9500

and to a lesser extent for the i-CAT Next Generation. For these devices, the tube output (mAs) for their large and small FOV protocols is identical, but the small FOV protocols are reconstructed using a smaller voxel size. When comparing intra-CBCT high and low dose protocols, scores were similar for the Picasso Trio, SCANORA 3D, the small FOV protocols of the 3D Accuitomo 170 and the largest FOV protocols of the i-CAT Next Generation. For the ProMax 3D and NewTom VGi and the large FOV protocols of the 3D Accuitomo 170, the high dose protocol scored substantially higher. For the smaller FOV protocols of the i-CAT Next Generation (LV), the two high dose protocols performed better than the two low dose protocols. For the ProMax 3D, two selected protocols used the same amount of exposure (FOV, mAs) but were reconstructed at a different voxel size. The decrease in voxel size resulted in an improved score for this insert.

For the rod inserts, as mentioned above, all air and aluminium rods were visible for each exposure protocols. For the HA rods, average scores varied between 0.1 (SkyView, LV LO) and 3.4 (Picasso Trio, MV HI). The average score for all CBCT protocols was 2.0, compared with 2.7 for the MSCT protocols. It was seen that for most devices, none of the HA50 rods could be detected, as the largest HA50 rod was only distinguished on seven occasions. For the HA100 and HA200 inserts, more differentiation between the datasets could be seen resulting in a wide range of scores. The difference between high and low dose datasets was clear for the Picasso Trio, ProMax 3D and the large FOV protocols of the 3D Accuitomo 170. For the SCANORA 3D and SkyView, the lowest dose protocol scored worse than the medium and high dose protocols, which scored similar. For the NewTom VGi, both protocols scored similar. No consistent relation between dose and observer scores was found for this insert for the i-CAT Next Generation.

Using the Newman-Keuls Multiple Comparison Test, from the 496 pairwise comparisons (*i.e.* (32 x 31) / 2) of exposure protocols per insert type, 363 were found to be significant ($P < 0.05$) for the line pair insert, and 235 for the rod insert. The Rank value, with possible values between +31 and -31, ranged between +29 and -29 for the line pair insert, and between +26 and -31 for the rod insert, showing a wide spread in image quality performance for both inserts.

Table 9.2 Average observer scores for both insert types.

CBCT device	Protocol	Score line pair insert	Rank line pair insert[a]	CBCT device	Protocol	Score rod insert	Rank rod insert[a]
3D Accuitomo 170	SV LO	4.00	29	Picasso Trio	MV HI	3.42	26
3D Accuitomo 170	SV HI	4.00	29	3D Accuitomo 170	SV HI	3.08	18
Kodak 9000 3D	SV	3.94	29	NewTom VGi	MV HI	3.00	18
NewTom VGi	MV HI	3.38	21	3D Accuitomo 170	SV LO	2.96	18
PaX-Uni3D	SV	3.25	21	Somatom Sensation 64	H30s	2.83	16
ProMax 3D	MV HI1	3.25	21	NewTom VGi	MV LO	2.79	15
3D Accuitomo XYZ	SV	3.19	21	Picasso Trio	MV LO	2.67	13
Picasso Trio	MV HI	3.06	20	ProMax 3D	MV HI1	2.63	12
VeraviewEpocs 3D	MV	2.69	14	VeraviewEpocs 3D	MV	2.63	12
Picasso Trio	MV LO	2.50	6	Somatom Sensation 64	H60s	2.58	12
ProMax 3D	MV HI2	2.50	6	3D Accuitomo 170	LV HI	2.46	12
3D Accuitomo 170	LV HI	2.13	2	ProMax 3D	MV HI2	2.46	12
Kodak 9500	LV	2.13	2	Kodak 9500	XLV	2.29	6
SCANORA 3D	MV HI	2.06	2	PaX-Uni3D	SV	2.29	6
NewTom VGi	MV LO	1.94	0	I-CAT Next Generation	LV LO	2.13	1
I-CAT Next Generation	LV HI	1.88	0	I-CAT Next Generation	LV XHI	2.08	1
I-CAT Next Generation	LV XHI	1.88	0	SCANORA 3D	MV HI	2.00	-1
ProMax 3D	MV LO	1.88	0	SCANORA 3D	MV ME	1.96	-3
SCANORA 3D	MV ME	1.75	-2	3D Accuitomo XYZ	SV	1.83	-5
SCANORA 3D	MV LO	1.56	-8	3D Accuitomo 170	LV LO	1.67	-11
3D Accuitomo 170	LV LO	1.50	-8	Kodak 9500	LV	1.67	-11
Galileos Comfort	LV	1.31	-11	I-CAT Next Generation	XLV HI	1.63	-11
Somatom Sensation 64	H60s	1.31	-11	ProMax 3D	MV LO	1.58	-11
Kodak 9500	XLV	1.06	-16	Kodak 9000 3D	SV	1.54	-11
I-CAT Next Generation	XLV HI	1.06	-16	Galileos Comfort	LV	1.50	-11
I-CAT Next Generation	LV XLO	1.00	-16	I-CAT Next Generation	LV HI	1.42	-13
I-CAT Next Generation	LV LO	1.00	-16	SCANORA 3D	MV LO	1.42	-13
I-CAT Next Generation	XLV LO	1.00	-16	I-CAT Next Generation	LV XLO	1.21	-15
Somatom Sensation 64	H30s	0.94	-16	I-CAT Next Generation	XLV LO	1.17	-16
SkyView	LV LO	0.00	-29	SkyView	LV HI	1.04	-17
SkyView	LV ME	0.00	-29	SkyView	LV ME	0.96	-18
SkyView	LV HI	0.00	-29	SkyView	LV LO	0.08	-31

[a]Sum of pairwise significant differences between exposure protocols.
SV small volume, *MV* medium volume, *LV* large volume, *HI* high dose, *ME* medium dose, *LO* low dose, *X* extra

Figure 9.2 shows the correlation between the average observer scores for the two insert types and the mAs value and voxel size of the CBCT dataset. The coefficient of determination (R^2) is shown for each scatter plot. The outlying values for the SkyView were not included in these graphs; for the line pair insert this resulted in a clear increase of the coefficient, for the rod insert the coefficients were similar with or without the three SkyView

datasets. The Picasso Trio and Pax-Uni3D were not included in the plots as the exact mAs for these devices is not known. The coefficient of determination was moderate for the comparison between mAs and rod insert ($R^2 = 0.41$) and line pair insert ($R^2 = 0.40$) scores. A good correlation ($R^2 = 0.72$) is seen between the voxel size and line pair insert results. No clear correlation is seen between the voxel size and the rod insert scores ($R^2 = 0.20$).
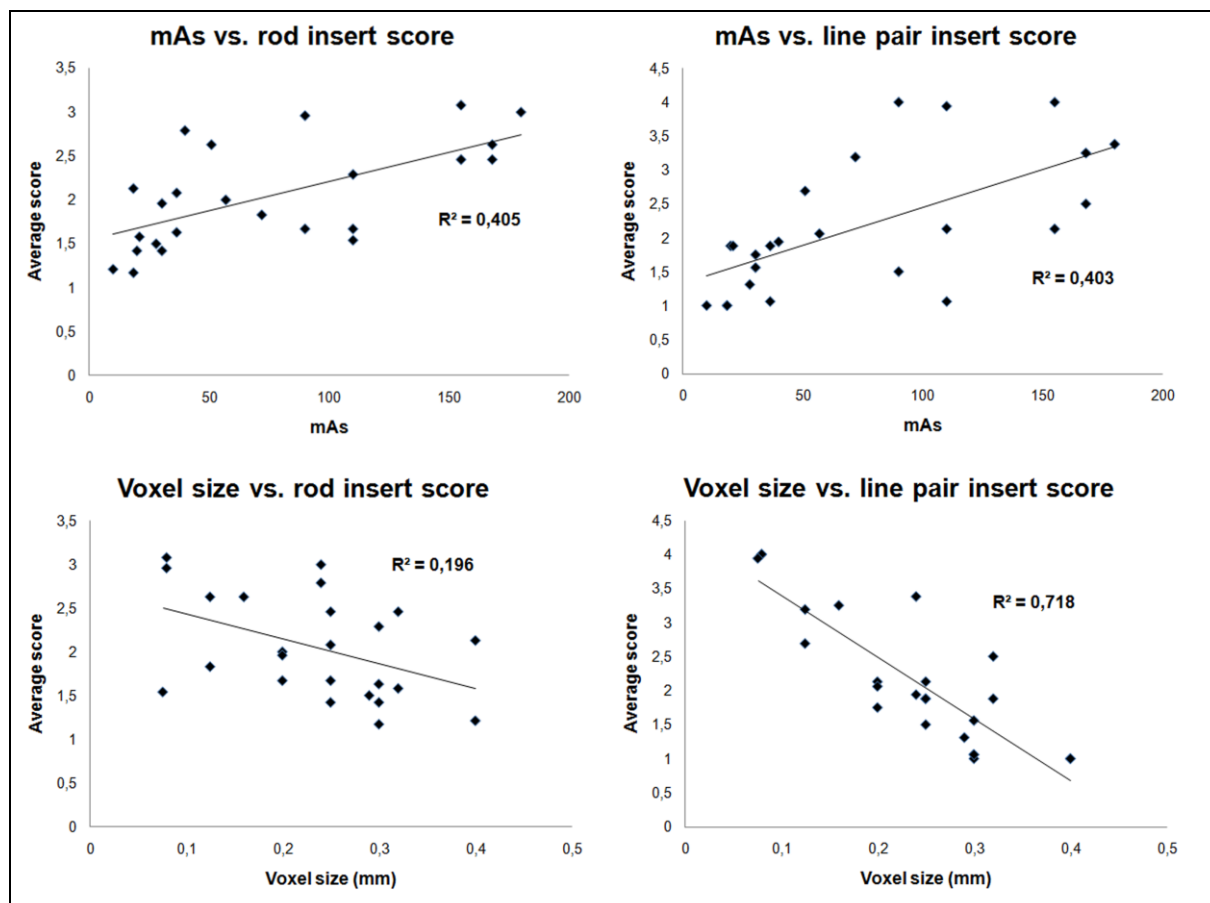

Figure 9.2 Scatter plots showing correlation between average insert scores and mAs and voxel size. The coefficient of determination (R^2) for a linear fit is shown for each plot.

9.5 Discussion

The use of CBCT has been described for a variety of dentomaxillofacial applications. The 3-D information obtained is complementary to the 2-D overviews provided by conventional radiographic techniques, and can greatly facilitate diagnosis and surgery planning. Although there have been many studies evaluating the clinical image quality of CBCT using a variety of experimental setups and evaluated parameters, these results cannot be directly compared and were often limited to a single CBCT device. Conclusions drawn from these studies were often limited to the particular study set-up and subject to the author's interpretation of the results.

The current study attempts to evaluate the image quality of CBCT using a phantom and evaluation protocol which could be routinely implemented in acceptance testing or quality control. The evaluation was performed on a wide range of CBCT devices, using a variety of clinically applied exposure protocols.

For both the line pair insert and rod insert, inter- and intra-observer agreement was high. In many previous studies evaluating the image quality in CBCT using observers, kappa values below 0.5 and even below 0 are seen [6-8,13,14]. As can be expected, the observer agreement was larger for the rod insert, as the evaluation of this insert was more straightforward and less prone to subjective interpretation. Still, the level of agreement for the line pair insert was in the top end of the 'substantial' range (0.61-0.8)[19]. The range of scores obtained by the line pair inserts show that this type of insert is applicable for CBCT. Its evaluation can be optimised by providing an appropriate lp/mm range, with a sufficient number of intervals between 1 and 3 lp/mm, which would enable the evaluation to be performed as line counting instead of a general visual evaluation.

Using the two types of inserts, the interplay of various image quality parameters is evaluated. The visibility of the line pairs is not only determined by the spatial resolution of the imaging system, but is influenced by the contrast resolution, noise and geometric accuracy as well. Similarly, the visibility of the cylindrical rods is not only determined by the contrast. For the smallest rods, it is seen that the spatial resolution and noise are additional factors determining the scores in Table 9.2.

From the results, a wide range in performance is seen for CBCT. It can be expected from the wide range of radiation doses measured in dental CBCT imaging that there could be substantial differences in terms of spatial and contrast resolution between high dose and low dose protocols [2]. However, comparing scores from different CBCT devices should be done with great care, as the evaluation of the image quality of a certain exposure protocol should be done in relation with the corresponding dose [20]. It cannot be concluded from these observer results alone that higher scoring protocols are superior in terms of dose optimisation. Even though effective dose values have been reported for most devices included in this study, these cannot be directly correlated to the image quality scores because the effective dose is greatly influenced by the FOV size and position, which determines the range of clinical indications for a given scanning protocol [2,9,20].

The results provide useful insights regarding inter- and intra-CBCT variability of image quality performance. As seen in Figure 9.2, there is a moderate correlation between the mAs and the insert scores for the two insert types, but it is clear that the mAs is only one of

161

many factors affecting the image quality in the current evaluation. Also, a good correlation is seen between the voxel size and the line pair insert scores, showing that the voxel size provides a reasonable estimation of the actual spatial resolution. When comparing different scanning protocols from certain CBCT devices, most exposure and reconstruction factors are kept constant, and the effect of certain changes in individual scanning parameters can be singled out. Furthermore, providing that the FOV size is the same, the relative dose of intra-CBCT protocols can be easily determined as it is linearly related to the mAs. This leads to a number of findings. First of all, there was a clear effect of the reconstructed voxel size on observers scores for both inserts. High-mAs protocols reconstructed with a smaller voxel size generally outperformed their low-mAs counterparts. For the SCANORA 3D, an increase from 8 to 15 mA (*i.e.* 87.5% increase in radiation dose) at fixed exposure time and voxel size did not result in a significant improvement in scores, although the noise for the latter protocol will have been somewhat lower. On the other hand, a 50% increase in mAs (*i.e.* 50% increase in radiation dose) coinciding with a smaller voxel sizes did lead to higher scores for this device, although the difference was small for the line pair insert. An improvement of scores was seen for most datasets with identical mAs but reconstructed at smaller voxel sizes (esp. 3D Accuitomo 170, Kodak 9500, ProMax 3D). Ideally, the voxel size determined by the manufacturer should be smaller than the actual spatial resolution of the dataset, ensuring that the voxel size is not the bottleneck determining the spatial resolution. Furthermore, excessive detector binning should be avoided, balancing the resulting noise reduction with the loss of image detail. In reality, it is seen that certain protocols are deliberately reconstructed at a larger voxel size to limit the reconstruction time and/or the file size of the reconstructed dataset. For the 3D Accuitomo 170 and Kodak 9500, the FOV size is different for high- and low-resolution protocols, resulting in varying application ranges. For clinical indications requiring large FOV CBCT scanning, in general there is no need for a high spatial resolution. Still, the current results indicate that it could be possible to improve the image quality for datasets by reconstructing them at lower voxel sizes. In practice, this is not yet feasible as the file size and reconstruction time of these datasets would increase excessively. This implies that the justification principle of medical radiation exposures is not always correctly adhered to in dental CBCT imaging, seeing that datasets can be reconstructed at a sub-optimal spatial resolution because of practical limitations. For these protocols, it could be possible to achieve significant dose reduction without affecting image quality. Manufacturers should ensure that the image quality is determined by the exposure, and that reconstruction algorithms are

adapted for each exposure ensuring that the maximal image quality is obtained for each exposure protocol.

Comparing the results from the CBCT devices with the MSCT scores, it is seen that most CBCTs perform better for the line pair insert, but worse for the rod insert. The H60s MSCT protocol can be considered to be more relevant than the H30s protocol for dental imaging, as the former is a bone kernel. However, both protocols resulted in similar scores. Although the low-contrast resolution for MSCT is generally considered to be superior to that of CBCT and noise is much lower, the results indicate that some CBCT devices outperform MSCT scans for the visualization of structures in the mm and sub-mm range owing to a higher spatial resolution [7,8,11,14].

The ranges of scores for both inserts point out that certain CBCT protocols are suitable for an overall assessment of the jaw bone and surrounding tissues, and others are more suitable for the depiction of small localized structures such as the periodontal ligament space and root canal. The latter type of protocols generally has a small FOV size, in order to limit the radiation dose and to enable image reconstruction at small voxel sizes. In practice, the CBCT user should be able to select different exposure protocols based on the varying diagnostic needs for different patient subsets [17,20]. The FOV should be limited to the diagnostic region of interest to limit the absorbed radiation dose to organs outside this region, and the image quality of the dataset should be selected according to the required amount of detail and contrast.

The image quality test objects developed in this study can serve different purposes. They can be used in research as a straightforward comparison between different exposure protocols or to investigate the effect of new reconstruction algorithms. However, a more technical analysis of image quality may be preferred for these assessments. The main use of the test objects is found in quality control [18]. During acceptance testing of a newly installed CBCT device, images of both types of insert can be acquired, either to investigate if the spatial resolution and contrast resolution is suitable or as baseline images for QC analysis over time. In the latter case, acceptance testing would be primarily based on technical image quality parameters, which can be objectively quantified. However, as it is difficult to establish ranges for these parameters, it could be valuable to have these types of visual test objects as well, providing that they represent the threshold of acceptable image quality. When performing periodical QC, identical scans of the inserts can be obtained and evaluated. The scans could be assessed using the method proposed in this study or by visually comparison to the scans obtained at acceptance testing to investigate image degradation over time. Long

term follow-up studies investigating image quality performance and reduction for a range of CBCT devices may lead to the definition of reference levels for both technical and visual image quality parameters.

9.6 Conclusion

A wide range in image quality was seen due to differences in spatial resolution, contrast resolution and noise for the investigated CBCT and MSCT devices. The current image quality assessment shows that CBCT devices are generally suitable for the visualization of high-contrast structures in the mm range. Certain exposure protocols can be used for evaluation of low-contrast structures or fine details. The user should be able to select appropriate exposure protocols according to the varying diagnostic requirements in dental practice.

9.7 References

1. Scarfe WC, Farman AG, Sukovic P. Clinical applications of cone-beam computed tomography in dental practice. J Can Dent Assoc 2006; 72: 75-80.

2. Pauwels R, Beinsberger J, Collaert B, Theodorakou C, Rogers J, Walker A, *et al*. Effective dose range for dental cone beam computed tomography scanners. Eur J Radiol 2012; 81: 267-271.

3. Sur J, Seki K, Koizumi H, Nakajima K, Okano T. Effects of tube current on cone-beam computerized tomography image quality for presurgical implant planning in vitro. Oral Surg Oral Med Oral Pathol Oral Radiol Endod 2010; 110: e29-33.

4. Lofthag-Hansen S, Thilander-Klang A, Gröndahl K. Evaluation of subjective image quality in relation to diagnostic task for cone beam computed tomography with different fields of view. Eur J Radiol. 2011; 80: 483-488.

5. Kwong JC, Palomo JM, Landers MA, Figueroa A, Hans MG. Image quality produced by different cone-beam computed tomography settings. Am J Orthod Dentofacial Orthop 2008; 133: 317-327.

6. Alqerban A, Jacobs R, Fieuws S, Willems G. Comparison of two cone beam computed tomographic systems versus panoramic imaging for localization of impacted maxillary canines and detection of root resorption. Eur J Orthod 2011; 33: 93-102.

7. Hashimoto K, Kawashima S, Kameoka S, Akiyama Y, Honjoya T, Ejima K, *et al*. Comparison of image validity between cone beam computed tomography for dental

use and multidetector row helical computed tomography. Dentomaxillofac Radiol 2007; 36: 465-471.

8. Liang X, Jacobs R, Hassan B, Li L, Pauwels R, Corpas L, *et al*. A comparative evaluation of Cone Beam Computed Tomography (CBCT) and Multi-Slice CT (MSCT) Part I. On subjective image quality. Eur J Radiol 2010; 75: 265-269.

9. Suomalainen A, Kiljunen T, Käser Y, Peltola J, Kortesniemi M. Dosimetry and image quality of four dental cone beam computed tomography scanners compared with multislice computed tomography scanners. Dentomaxillofac Radiol 2009; 38: 367-378.

10. Loubele M, Jacobs R, Maes F, Denis K, White S, Coudyzer W, *et al*. Image quality vs radiation dose of four cone beam computed tomography scanners. Dentomaxillofac Radiol 2008; 37: 309-318.

11. Watanabe H, Honda E, Tetsumura A, Kurabayashi T. A comparative study for spatial resolution and subjective image characteristics of a multi-slice CT and a cone-beam CT for dental use. Eur J Radiol 2011; 77: 397-402.

12. Loubele M, Maes F, Jacobs R, van Steenberghe D, White SC, Suetens P. Comparative study of image quality for MSCT and CBCT scanners for dentomaxillofacial radiology applications. Radiat Prot Dosimetry 2008; 129: 222-6.

13. Soğur E, Baksi BG, Gröndahl HG. Imaging of root canal fillings: a comparison of subjective image quality between limited cone-beam CT, storage phosphor and film radiography. Int Endod J 2007; 40: 179-185.

14. Hashimoto K, Arai Y, Iwai K, Araki M, Kawashima S, Terakado M. A comparison of a new limited cone beam computed tomography machine for dental use with a multidetector row helical CT machine. Oral Surg Oral Med Oral Pathol Oral Radiol Endod 2003; 95: 371-377.

15. Dreiseidler T, Mischkowski RA, Neugebauer J, Ritter L, Zöller JE. Comparison of cone-beam imaging with orthopantomography and computerized tomography for assessment in presurgical implant dentistry. Int J Oral Maxillofac Implants 2009; 24: 216-25.

16. Mischkowski RA, Scherer P, Ritter L, Neugebauer J, Keeve E, Zöller JE. Diagnostic quality of multiplanar reformations obtained with a newly developed cone beam device for maxillofacial imaging. Dentomaxillofac Radiol 2008; 37: 1-9.

17. Ritter L, Mischkowski RA, Neugebauer J, Dreiseidler T, Scheer M, Keeve E, *et al*. The influence of body mass index, age, implants, and dental restorations on image

quality of cone beam computed tomography. Oral Surg Oral Med Oral Pathol Oral Radiol Endod 2009; 108: e108-16.

18. Pauwels R, Stamatakis H, Manousaridis G, Walker A, Michielsen K, Bosmans H, *et al*. Development and applicability of a quality control phantom for dental cone-beam CT. J Appl Clin Med Phys 2011; 12: 245-260.

19. Landis JR, Koch GG. The measurement of observer agreement for categorical data. Biometrics 1977; 33: 159-74.

20. Horner K, Islam M, Flygare L, Tsiklakis K, Whaites E. Basic principles for use of dental cone beam computed tomography: consensus guidelines of the European Academy of Dental and Maxillofacial Radiology. Dentomaxillofac Radiol 2009; 38: 187-95.

Chapter 10: Contrast, noise and uniformity of cone beam CT images

10.1 Abstract

Objectives: The aim of this study was to investigate the contrast, homogeneity (noise) and uniformity of a variety of cone beam computed tomography (CBCT) scanners.

Materials and methods: A polymethyl methacrylate (PMMA) phantom was used, containing inserts of different density: air, PMMA, hydroxyapatite (HA) 50 mg/cm^3, HA 100, HA 200, and aluminium. The phantom also contains a homogeneous PMMA portion. Scans were acquired on thirteen CBCT devices and one MSCT device. The contrast-to-noise ratio (CNR) was calculated for all materials using PMMA as background. The homogeneity was determined as the standard deviation of voxel values in PMMA, normalising the values by taking the grey value range (actual bit depth) and voxel size into account. The intra-scans and inter-scan uniformity of PMMA voxel values was determined for large and small-FOV protocols as the difference in mean grey value between regions, normalised to the grey value range.

Results: CNR values for CBCT ranged between 4 and 45 for air, 0 and 11 for HA 50, 0 and 11 for HA 100, 2 and 23 for HA 200 and 3 and 72 for aluminium. CNR values for MSCT were generally higher, although gravely affected by the reconstruction kernel. Intra-scan uniformity values were between 3 and 67, inter-scan uniformity between 11 and 1358.

Conclusions: Varying performance was seen for high- and low-contrast resolution. When evaluating noise, it is important to take the voxel size into account. When translating the results to the clinical situation, the main difference between CBCT exposure protocols will be reflected in the low-contrast resolution. Uniformity was variable among scanners; the stability of grey values is mainly questionable for small FOVs.

10.2 Introduction

Cone beam computed tomography (CBCT) has been applied in dentistry for over ten years. It has now become an indispensable radiographic tool for a range of dental applications, including implant surgery, orthodontics and endodontics. The main benefits to the CBCT

technique are the possibility to acquire a three-dimensional image of the dentomaxillofacial area at a high spatial resolution and a relatively low patient radiation dose.

Over the years, dosimetric and image quality aspects of first- and current-generation CBCT devices have been thoroughly investigated, and the need for optimisation of this modality in dental practice has been emphasized by different authors [1-4]. Although in most studies, there was a practical limitation to the number of CBCT devices that could be included, it can be clear from the current literature that there is a wide range in patient dose and image quality for CBCT, depending on the interplay of various exposure factors, imaging hardware and image reconstruction [2,4]. Unfortunately, the discussion of image quality evaluations is often limited to the author's subjective interpretation, as there are no reference or threshold values or ranges determined for any dose or image quality index [5,6].

From a technical point of view, the image quality of any radiographic image is determined by four parameters: spatial resolution, contrast, noise and artefacts. In practice, each of these factors is closely or indirectly related to another, and different figures of merit are available to quantify the quality of a radiographic image in terms of these parameters. A first index is the contrast-to-noise ratio (CNR), which balances the image contrast with the overall homogeneity [7-8]. It is a useful parameter for all kinds of medical imaging, as it does not require absolute reference values for the pixels or voxels, such as Hounsfield Units in MSCT [9-10]. Seeing that absolute grey values are not applicable in CBCT imaging, the CNR is a useful index to evaluate the visualization of high- and low-contrast structures, and can be related to diagnostic image quality as opposed to more abstract image quality indices such as the Modulation Transfer Function (MTF) or the Noise Power Spectrum (NPS)[11-13]. Additional to the CNR, the pure noise (or homogeneity) can be measured using an image of a homogeneous object, by measuring the standard deviation of grey values. A final parameter which describes a specific aspect of image quality is image uniformity, which expresses the consistency of grey values throughout an image. As opposed to the measurement of noise, the uniformity is estimated as a difference of mean grey vales between areas rather than using a standard deviation.

The aim of this study was to quantify image contrast, noise and uniformity for a variety of CBCT scanners, using materials of different densities. Secondly, using the ranges of the measured image quality parameters, preliminary reference values for dental CBCT imaging are proposed.

10.3 Materials and methods

A second prototype of the cylindrical polymethyl methacrylate (PMMA) phantom described in Chapter 7 was manufactured by Leeds Test Objects Ltd (Bouroughbridge, UK). It consists of a large cylindrical holder, containing a variety of interchangeable inserts for the analysis of different image quality parameters. Five cylindrical inserts (diameter 3.5 cm, height 2.0 cm) were used for the measurement of CNR. They contain a 10 mm central rod surrounded by PMMA. Five materials of different density were used in the inserts: air, aluminium, and hydroxyapatite (HA) of varying density (50, 100 and 200 mg/cm^3). The inserts have the same size, materials and shape as those used in Chapters 7 and 11 for CNR and CT number analysis. At the bottom of the phantom, a 25 mm homogeneous PMMA section was added to allow for the measurement of noise and uniformity.

The five CNR inserts were placed in the peripheral columns of the phantom holder. The other columns and rows of the phantom were filled up using PMMA inserts, ensuring an adequate simulation of the total attenuation of an average human head. The inserts and homogeneous PMMA section were scanned using thirteen CBCT devices: 3D Accuitomo 170, 3D Accuitomo XYZ image intensifier version and Veraviewepocs 3D (J. Morita, Kyoto, Japan), GALILEOS Comfort (Sirona Dental Systems, Bensheim, Germany), i-CAT Next Generation (Imaging Sciences International, Hatfield, PA, USA), Kodak 9000 3D and Kodak 9500 (Carestream Health, New York, NY, USA), NewTom VGi (Quantitative Radiology, Verona, Italy), Pax-Uni3D and Picasso Trio (Value Added Technologies, Yongin, South Korea), ProMax 3D (Planmeca Oy, Helsinki, Finland), SCANORA 3D (Soredex, Tuusula, Finland), and SkyView (Cefla Dental Group, Imola, Italy). In addition, the phantom was scanned with a MSCT device (Somatom Sensation 64, Siemens, Erlangen, Germany). Depending on the available clinical exposure protocols for each device, multiple exposure and reconstruction parameters (*i.e.* field of view (FOV) size, mAs, voxel size) were used for most devices. A total of 30 selected clinical CBCT scanning protocols and 2 MSCT protocols were included. All varied imaging parameters are provided in Chapter 8, Table 8.1, p.141.

For image analysis, the CBCT and MSCT images were exported as axial stacks using the Digital Imaging and Communications in Medicine (DICOM) file format. The stacks were imported into ImageJ software (version 1.41, National Institutes of Health, Bethesda, MD, USA). All analyses were performed by two researchers with extensive experience in medical image analysis, using a detailed measurement protocol for each parameter.

For the calculation of CNR, a circular region of interest (ROI) was used, covering all but the edge of the five investigated materials. Another ROI was placed on the adjacent PMMA. The mean vale and standard deviation for each ROI was determined using 5 consecutive axial slices. The CNR was calculated for each material (M) using the formula:

$$CNR_M = \frac{\left|MGV_M - MGV_{PMMA}\right|}{\sqrt{(SD_{PMMA}.Voxel^{0.608})^2 + (SD_M.Voxel^{0.608})^2}}$$

with MGV the mean grey value, SD the standard deviation, and Voxel the voxel size (in mm) of the image.

To find the most appropriate correction factor for voxel size, different tests were performed. First, an artificial 2-D noisy image was resampled at varying pixel size using bicubic interpolation, finding an inverse relation between noise and pixel size in the form of $y=a.x^{-b}$. To determine the most appropriate correction factor (*i.e.* voxel size multiplied by $-b$ from the above equation), two approaches were investigated. Reconstructed DICOM images of homogeneous PMMA from various CBCT devices were resampled at increasingly larger voxel sizes (Figure 10.1). Similar to the 2-D noisy image, the relation between voxel size and noise was inverse, but it was seen that there was no consistency for the power factor $-b$, which varied not only between CBCT devices but also for varying FOV sizes and even changes in mA for the same device. As a final investigation, raw projection data from the 3D Accuitomo 170 was reconstructed at varying voxel sizes (0.08-0.3 mm for 3D Accuitomo 170) using the manufacturer's own reconstruction algorithm. A comparison between the resampling and reconstruction method is shown in Figure 10.2. The reconstruction approach using the raw data is more relevant than post-reconstruction resampling and showed a stable value for $-b$ at varying exposure levels (Figure 10.3), although the available voxel size range was somewhat limited.
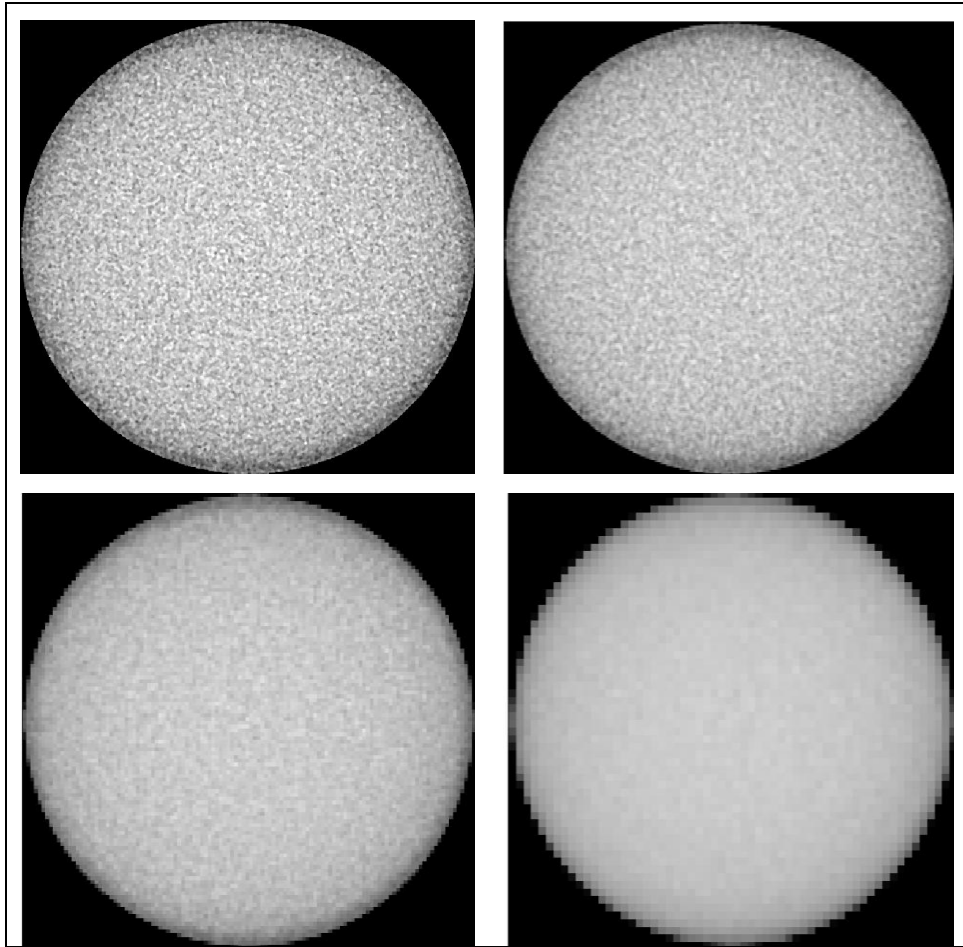
Figure 10.1 Effect of voxel size on image noise. Resampling method using reconstructed data. Top left: 0.125 mm (original data). Top right: 0.250 mm. Bottom left: 0.5 mm. Bottom right: 1 mm.
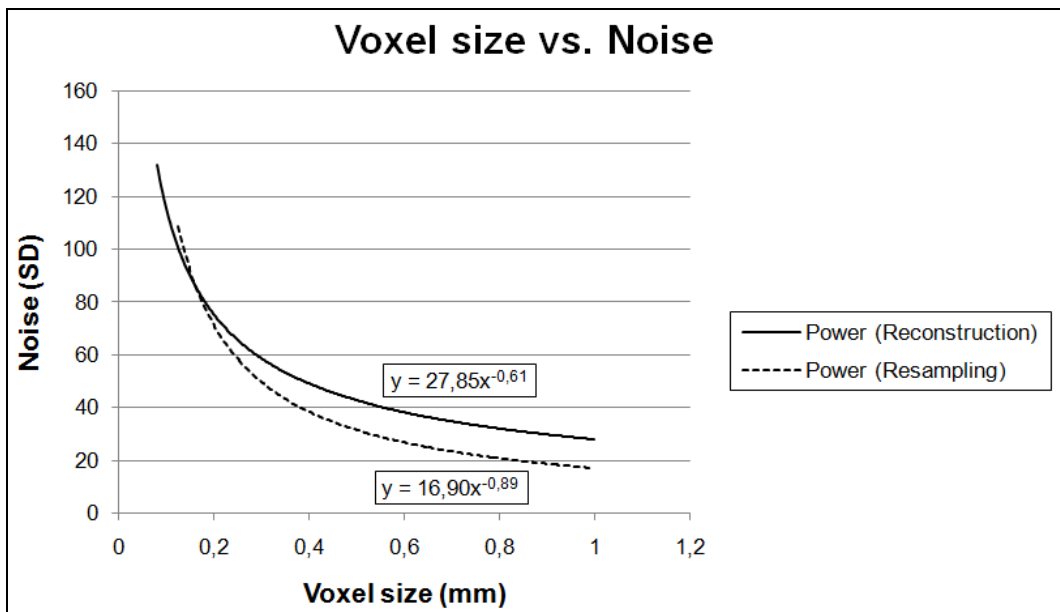

Figure 10.2 Difference in relation between voxel size and noise for two approaches, using the same dataset (3D Accuitomo 170, 6x6 cm, 5 mA).
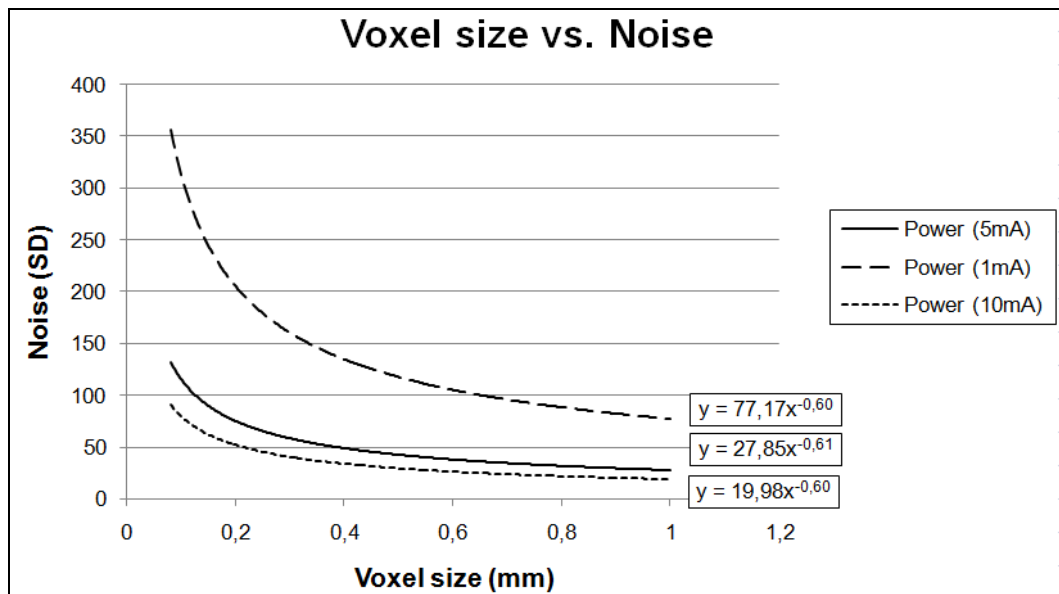
Figure 10.3 Stability of noise correction using reconstruction method. The highest, lowest and standard mA setting of the 3D Accuitomo 170 is shown. The negative power factor is stable, with an average value of 0.608.

The uniformity was calculated differently for large FOV ($\geq$ 14 cm diameter) and medium and small FOV ($\leq$ 12 cm diameter) scans. For the former, all ROIs were determined on a single scan, using a central and four peripheral ROIs (Figure 10.4). For the latter, the central and peripheral part of the PMMA portion was scanned separately, and one ROI was used for each scan, covering a large portion of the available FOV but avoiding the edges (Figure 10.4). For the large FOVs, the difference between the central and peripheral ROIs was calculated (*i.e.* intra-scan uniformity). For small and medium FOVs, as there is no significant variation of grey values within the FOV, it was chosen to determine the uniformity between the scan of the central and peripheral portion of the phantom (*i.e.* inter-scan uniformity). The uniformity (U) was calculated as the ratio of the difference in voxel value between two ROIs and the normalised grey value range:

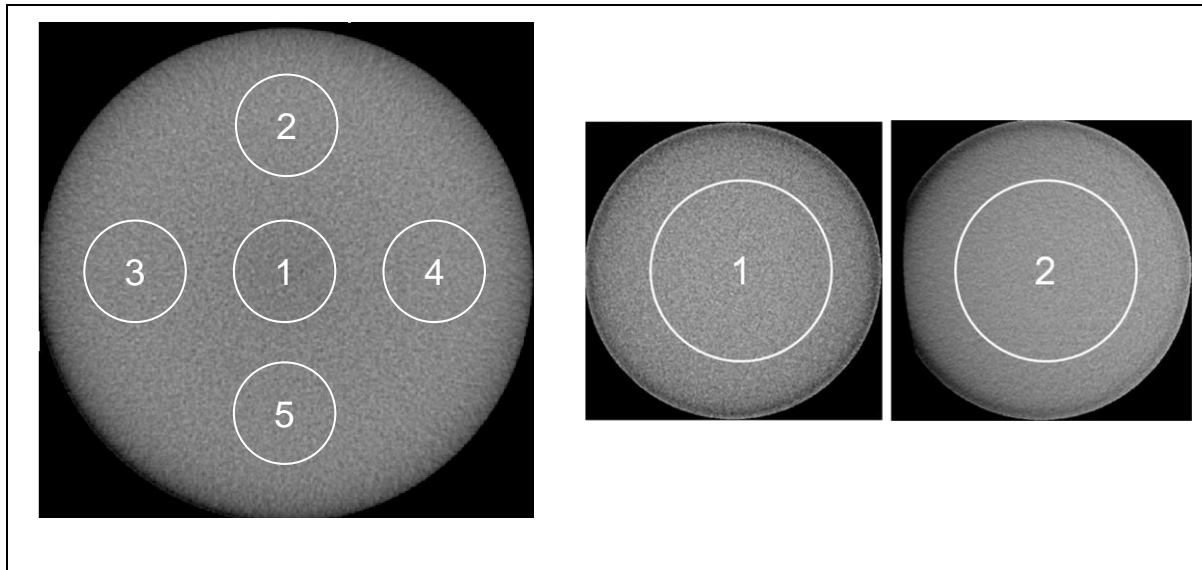$$U = \frac{|MVV_1 - MVV_2|}{\dfrac{Range}{4096}}$$

172

Figure 10.4 Measurement of intra-scan (left) and inter-scan (right) grey value uniformity. Inter-scan uniformity was calculated by averaging values from ROIs 2-4 and comparing with ROI 1. Inter-scan uniformity was determined as the difference in grey values between central (1) and peripheral (2) scans of the PMMA section of the phantom.

10.4 Results

Table 10.1 shows CNR, noise, inter- and intra-scan uniformity values for all included CBCT and MSCT protocols. Considering the CBCT protocols, CNR values for air (4-45) and aluminium (3-72) were generally much higher than corresponding values for HA50 (0-11), HA100 (0-11) and HA200 (2-23). The average CNR for the five materials was between 2 and 24 for CBCT and 13 and 82 for MSCT. A large difference was seen between the H30s and H60s MSCT protocols due to the difference in noise.

A varying uniformity is seen between scanners. Intra-scan uniformity was between 9 and 67 for the CBCTs and 3 and 5 for the MSCT. Inter-scan uniformity was between 11 and 1358.

Table 10.1 Contrast-to-noise ratio and uniformity results.

Device	FOV	Dose	CNR$_{AL}$	CNR$_{HA50}$	CNR$_{HA100}$	CNR$_{HA200}$	CNR$_{AIR}$	CNR$_{AVG}$	U$_{INTRA}$	U$_{INTER}$
3D Accuitomo 170	LV	HI	39	0	2	6	23	14	20	
3D Accuitomo 170	LV	LO	31	0	2	5	18	11	20	
3D Accuitomo 170	SV	HI	49	0	6	9	24	18		37
3D Accuitomo 170	SV	LO	41	1	5	7	20	15		33
3D Accuitomo XYZ	SV		3	1	1	4	4	2		108
GALILEOS Comfort	LV		23	0	2	4	16	9	9	
I-CAT N.G.	LV	HI	20	1	2	4	15	8	67	
I-CAT N.G.	LV	XHI	29	0	2	4	20	11	19	
I-CAT N.G.	LV	XLO	26	1	3	6	21	11	71	
I-CAT N.G.	LV	LO	38	1	3	6	29	15	25	
I-CAT N.G.	XLV	HI	52	1	6	8	36	21	31	
I-CAT N.G.	XLV	LO	35	1	4	5	25	14	31	
Kodak 9000 3D	SV		72	11	11	23	4	24		1081
Kodak 9500	XLV		24	1	1	4	18	10	45	
Kodak 9500	LV		32	1	0	3	19	11	43	
NewTom VGi	MV	HI	49	1	2	8	45	21		34
NewTom VGi	MV	LO	47	4	5	11	36	21		11
PaX-Uni3D	SV		24	9	10	9	7	12		805
Picasso Trio	MV	HI	34	1	2	7	18	13		N/A
Picasso Trio	MV	LO	30	2	4	7	13	11		N/A
ProMax 3D	MV	HI1	36	1	2	6	19	13		128
ProMax 3D	MV	HI2	17	0	1	2	10	6		151
ProMax 3D	MV	LO	15	1	1	3	8	5		128
SCANORA 3D	MV	HI	22	1	1	4	15	8		14
SCANORA 3D	MV	ME	19	1	0	3	15	7		31
SCANORA 3D	MV	LO	12	0	0	2	9	5		52
SkyView 3D	LO	LO	9	1	1	2	4	3	69	
SkyView 3D	ME	ME	13	1	2	3	6	5	56	
SkyView 3D	HI	HI	18	2	3	5	8	7	62	
Somatom Sensation 64		H30s	150	3	13	35	217	83	5	
Somatom Sensation 64		H60s	33	0	2	3	24	13	3	
Veraviewepocs 3D	MV		29	11	13	16	1	14		1358

SV small volume, *MV* medium volume, *LV* large volume, *HI* high dose, *ME* medium dose, *LO* low dose, *X* extra, *CNR* contrast-to-noise ratio, *AVG* average

10.5 Discussion

This study focused on the evaluation of contrast, noise and uniformity for a wide range of CBCT and MSCT scanners. Compared with the measurements which are part of Chapter 7, a few changes were implemented to the measurement methodology. The measurements were applied to a wide array of devices and exposure protocols.

The CNR values could be interpreted using a statistical approach. When considering the grey values to be normally distributed, the CNR could be regarded as a one-sided t-distribution with infinite degrees of freedom. In this case, a CNR value greater than 1.65 would correspond to a significance level of α=0.05, and a value of 2.33 to a level α=0.01. Although this provides useful reference values for the interpretation of CNR, it should be noted that in a statistical test, the sample size is always taken into the equation. This is not quite applicable to the CNR. It can be seen that the calculation of a CNR closely resembles the Welch's t-test, which is used for two samples with unequal sample size and variances:

$$t = \frac{\overline{X}_1 - \overline{X}_2}{\sqrt{\dfrac{s_1^2}{N_1} + \dfrac{s_2^2}{N_2}}}$$

With X, s^2 and N as mean, variance and sample size, respectively. In this case, the sample size corresponds to the number of voxels in the ROI. However, when measuring mean grey values and standard deviations in homogeneous regions, these values are independent of the size of the area providing that the area of the ROI is large enough. This would render the equation useless, as the t-value could be steadily increased by measuring larger ROIs. On the other hand, the noise correction factor used in the current CNR calculation can be seen as a rational replacement for the sample size, as the voxel size determines the number of voxels in the ROI if the measured area is consistent. The CNR calculation can therefore be seen as an adapted Welch's t-test. When applying this statistical interpretation to the current results, it shows that there is no 'significant' contrast (CNR > 1.65) for most of the HA50 and HA100 measurements, indicating that the low-contrast resolution for most CBCT devices is outweighed by the noise.

Although it provides a reference frame, a statistical analysis of CNR values for different materials cannot be directly interpreted in terms of clinical image quality. From the current results, it could be concluded that CBCT is generally suited for the visualisation of high-contrast structures, but has a poor low-contrast resolution, confirming the findings from the previous/parallel evaluations in Chapters 7 and 9. In clinical practice, a higher CNR value

for air and aluminium corresponds to a variety of diagnostic image quality parameters: visibility of cortical bone, trabecular bone and bony canals, bone and teeth segmentation quality, sinus visualization, *etc*. CNR values for HA mainly reflect soft tissue discrimination, which is generally considered to be low in CBCT due to the relatively large amount of noise, which is confirmed in the current study. However, for certain CBCT imaging protocols, CNR values for HA are reasonable, which corresponds to the clinical situation where limited soft tissue contrast is perceived for certain devices. However, imaging of soft tissues in dentistry is generally limited to the measurement of thickness and displacement rather than the discrimination of different soft tissues [14-17]. The majority of dental imaging focuses on hard tissue diagnostics; rarely, there is need for soft tissue contrast in dental X-ray imaging [18,19]. For specific diagnostic applications involving soft tissues, non-ionising imaging methods are used [20-23].

Average CNR values for the two MSCT protocols were higher than those of CBCT, although it can be seen that there is six-fold difference in average CNR for the two reconstruction kernels. The H30s (soft tissue) protocol smoothens the images, leading to considerably higher CNR values. However, the H60s (bone) protocol is more relevant for dental applications. For a number of CBCT devices, CNR values are higher than that of the H60s protocol, although this is partly caused by the correction for voxel size. Although the increased noise levels in CBCT imaging compared to MSCT are well documented [4,24], it is an important consideration that this may be related to (and possibly outweighed by) the higher spatial resolution of CBCT.

Compared to CNR, image homogeneity or noise is a more fundamental image quality parameter. However, noise in CBCT is more difficult to interpret, mainly due to the varying voxel sizes used. It was chosen not to measure pure noise, as was done in Chapter 7, as an additional technical parameter in this study. Estimating noise by means of a SD not only requires a correction for voxel size, similar to the denominator of the CNR; the SD also needs to be normalised to the grey value range. For most CBCT devices, grey values are distributed along a 12 bit (*i.e.* 4096 grey values) range. For devices not using this 12 bit range, the difference between the minimum and maximum value could be used for normalisation of the SD. This correction was used for the noise measurements in Chapter 7 and the metal artefact quantifications in Chapter 8. Another approach, which takes the shape of the histogram into account, would be to measure the grey value of two materials in each dataset (*e.g.* air and PMMA) and using the difference between them for normalisation of the SD. However, this

kind of calculation actually represents a noise-to-contrast ratio, and will not provide any added value to the CNR.

The uniformity of images is mainly related to the use of grey values for quantitative evaluations. In this study, an important distinction was made between intra- and inter-scan uniformity, which should be interpreted in a different way. Intra-scan uniformity, although it could be measured on any FOV size, is mainly relevant for large-diameter FOVs as these are prone to center-to-periphery grey value gradients caused by beam hardening. The occurrence of inter-scan uniformity issues is opposite to intra-scan uniformity, as it is primarily an issue for small-volume scans. The grey values for these scans are not only affected by the mass inside the reconstructed area, but also by the mass and its spatial distribution outside the FOV [25,26]. From the results, it is seen that the inter-scan uniformity is reasonable for most CBCT scanners, but lower than that of MSCT. Intra-scan uniformity is severely compromised in certain cases. An important clinical implication for this uniformity issue is that grey values will not be reproducible for different scans (*i.e.* different patient sizes or scanned regions) and cannot be used quantitatively [27]. The quantitative use of CBCT grey values for density estimations, which was already covered to some extent in Chapter 7, is further explored in Chapter 11.

10.6 Conclusion

Varying performance was seen for high- and low-contrast resolution. When evaluating noise, it is important to take the voxel size into account. When translating the results to the clinical situation, the main difference between CBCT exposure protocols will be reflected in the low-contrast resolution. The clinical relevance of CNR and noise measurements is further evaluated in Chapter 12. Uniformity was variable among scanners; the stability of grey values is mainly questionable for small FOVs. The use of CBCT grey values for density estimations is investigated in depth in Chapters 7 and 11.

10.7 References

1. European Commission. Cone Beam CT for Dental and Maxillofacial Radiology: Evidence Based Guidelines, Radiation Protection Publication 172. Luxembourg: European Commission. 2012.

2. Pauwels R, Beinsberger J, Collaert B, Theodorakou C, Rogers J, Walker A, Cockmartin L, Bosmans H, Jacobs R, Bogaerts R, Horner K, The SEDENTEXCT Project Consortium. Effective dose range for dental cone beam computed tomography scanners. Eur J Radiol 2012; 81: 267-271.

3. Liang X, Jacobs R, Hassan B, Li L, Pauwels R, Corpas L, *et al*. A comparative evaluation of Cone Beam Computed Tomography (CBCT) and Multi-Slice CT (MSCT) Part I. On subjective image quality. Eur J Radiol 2010; 75: 265-269.

4. Suomalainen A, Kiljunen T, Käser Y, Peltola J, Kortesniemi M. Dosimetry and image quality of four dental cone beam computed tomography scanners compared with multislice computed tomography scanners. Dentomaxillofac Radiol 2009; 38: 367-78.

5. Vassileva J, Stoyanov D. Quality control and patient dosimetry in dental cone beam CT. Radiat Prot Dosimetry 2010; 139: 310-312.

6. Jessen KA. The quality criteria concept: an introduction and overview. Radiat Prot Dosimetry 2001; 94: 29-32.

7. Funama Y, Sugaya Y, Miyazaki O, Utsunomiya D, Yamashita Y, Awai K. Automatic exposure control at MDCT based on the contrast-to-noise ratio: Theoretical background and phantom study. Phys Med 2011. Epub ahead of print.

8. Muhogora WE, Devetti A, Padovani R, Msaki P, Bonutti F. Application of European protocol in the evaluation of contrast-to-noise ratio and mean glandular dose for two digital mammography systems. Radiat Prot Dosimetry 2008; 129: 231-236.

9. Schreiber JJ, Anderson PA, Rosas HG, Buchholz AL, Au AG. Hounsfield units for assessing bone mineral density and strength: a tool for osteoporosis management. J Bone Joint Surg Am 2011; 93: 1057-1063.

10. Sogo M, Ikebe K, Yang TC, Wada M, Maeda Y. Assessment of Bone Density in the Posterior Maxilla Based on Hounsfield Units to Enhance the Initial Stability of Implants. Clin Implant Dent Relat Res 2011. Epub ahead of print.

11. Watanabe H, Honda E, Kurabayashi T. Modulation transfer function evaluation of cone beam computed tomography for dental use with the oversampling method. Dentomaxillofac Radiol 2010; 39: 28-32.

12. Benítez RB, Ning R, Conover D, Liu S. Measurements of the modulation transfer function, normalized noise power spectrum and detective quantum efficiency for two flat panel detectors: a fluoroscopic and a cone beam computer tomography flat panel detectors. J Xray Sci Technol 2009; 17: 279-293.

13. Padgett R, Kotre CJ. Development and application of programs to measure modulation transfer function, noise power spectrum and detective quantum efficiency. Radiat Prot Dosimetry 2005; 117: 283-287.

14. Januário AL, Barriviera M, Duarte WR. Soft tissue cone-beam computed tomography: a novel method for the measurement of gingival tissue and the dimensions of the dentogingival unit. J Esthet Restor Dent 2008; 20: 366-373.

15. Barriviera M, Duarte WR, Januário AL, Faber J, Bezerra AC. A new method to assess and measure palatal masticatory mucosa by cone-beam computerized tomography. J Clin Periodontol 2009; 36: 564-568.

16. Shawky MM, El-Ghareeb TI, Hameed Abu Hummos LA. Evaluation of the three-dimensional soft tissue changes after anterior segmental maxillary osteotomy. Int J Oral Maxillofac Surg 2012. Epub ahead of print.

17. Hwang HS, Kim K, Moon DN, Kim JH, Wilkinson C. Reproducibility of facial soft tissue thicknesses for craniofacial reconstruction using cone-beam CT images. J Forensic Sci 2012; 57: 443-448.

18. Li B, Long X, Cheng Y, Wang S. Cone beam CT sialography of Stafne bone cavity. Dentomaxillofac Radiol 2011; 40: 519-523.

19. Jadu FM, Hill ML, Yaffe MJ, Lam EW. Optimization of exposure parameters for cone beam computed tomography sialography. Dentomaxillofac Radiol. 2011; 40: 362-368.

20. Stoianovici C, Wilder-Smith P, Choi B. Assessment of pulpal vitality using laser speckle imaging. Lasers Surg Med 2011; 43 :833-837.

21. Karayilmaz H, Kirzioğlu Z. Comparison of the reliability of laser Doppler flowmetry, pulse oximetry and electric pulp tester in assessing the pulp vitality of human teeth. J Oral Rehabil 2011; 38: 340-347.

22. Lopes S, Costa A, Cruz A, Li L, de Almeida S. Clinical and MRI investigation of temporomandibular joint in major depressed patients. Dentomaxillofac Radiol 2012; 41: 316-322.

23. Li C, Su N, Yang X, Yang X, Shi Z, Li L. Ultrasonography for Detection of Disc Displacement of Temporomandibular Joint: A Systematic Review and Meta-Analysis. J Oral Maxillofac Surg 2012. Epub ahead of print.

24. Loubele M, Maes F, Jacobs R, van Steenberghe D, White SC, Suetens P. Comparative study of image quality for MSCT and CBCT scanners for dentomaxillofacial radiology applications. Radiat Prot Dosimetry 2008; 129: 222-226.

25. Elstrøm UV, Muren LP, Petersen JB, Grau C. Evaluation of image quality for different kV cone-beam CT acquisition and reconstruction methods in the head and neck region. Acta Oncol 2011; 50: 908-917.

26. Bryant JA, Drage NA, Richmond S. Study of the scan uniformity from an i-CAT cone beam computed tomography dental imaging system. Dentomaxillofac Radiol 2008; 37: 365-374.

27. Nackaerts O, Maes F, Yan H, Couto Souza P, Pauwels R, Jacobs R. Analysis of intensity variability in multislice and cone beam computed tomography. Clin Oral Implants Res 2011; 22: 873-879.

Chapter 11: Accuracy of CBCT grey values for density estimations

11.1 Abstract

Objectives: The aim of this study was to investigate the use of dental cone beam computed tomography (CBCT) grey values for density estimations by calculating the correlation with MSCT values as well as the grey value error after recalibration.

Materials and methods: A polymethyl methacrylate (PMMA) phantom was developed, containing inserts of different density: air, PMMA, hydroxyapatite (HA) 50 mg/cm^3, HA 100, HA 200, and aluminium. The phantom was scanned on thirteen CBCT devices and one MSCT device. Correlation between CBCT grey values and CT numbers was calculated, and the average error of the CBCT values was estimated in the medium-density range after recalibration.

Results: Pearson correlation coefficients ranged between 0.7014 and 0.9996 in the full density range and between 0.5620 and 0.9991 in the medium-density range. The average error of CBCT voxel values in the medium density range was between 35 and 1562.

Conclusions: Even though most CBCT devices showed a good overall correlation with CT numbers, large errors can be seen when using the grey values in a quantitative way. Although it could be possible to obtain pseudo-Hounsfield Units from certain CBCTs, alternative methods of assessing bone quality should be further investigated.

11.2 Introduction

A variety of radiographic tools has been applied in dentistry for the preoperative planning of implant placement. Conventional two-dimensional (2-D) projection techniques are still used routinely as primary assessment of the jaw bones and for certain linear measurements [1]. However, the superposition of various tissues in 2-D radiography is an important limitation which inhibits an appropriate evaluation of potential implant sites in many cases. Apart from the localization of various anatomical structures, three-dimensional (3D) radiography can be used for the evaluation of bone quantity (*i.e.* bone volume, width and depth) and quality (*i.e.* bone density and structure)[1-3].

Different 3D imaging modalities are available for implant planning. In the past years, multi-slice computed tomography (MSCT) has been gradually replaced with alternatives such as conventional (linear or spiral) tomography and cone beam computed tomography (CBCT)[2]. CBCT allows for the acquisition of true volumetric images of the dentomaxillofacial area at a high spatial resolution. Furthermore, as seen in Chapters 1-3, patient radiation doses from CBCT are generally low, although a wide dose range with organ and effective doses between those of 2-D radiographic techniques and MSCT has been reported [4]. Many authors have proposed to consider CBCT as the modality of choice for dental implant planning [2,5-7].

The accuracy of CBCT for bone quantity measurements has been thoroughly investigated, using a variety of available scanners. Current-generation CBCT scanners allow for linear and volumetric measurements at potential implant sites in the jaw bones at sub-millimetre accuracy [7-11]. However, there are contradictory reports as to whether CBCT can be used for bone quality evaluations by means of density estimations [10-22], similar to the use of Hounsfield Units (HU) in MSCT which can be related to absolute density [3,23-27]. Although most CBCT devices use 12 bit images (*i.e.* 4096 grey values) scaled in a HU-like fashion (*i.e.* between -1000 and +3000), it is assumed by many that CBCT grey values cannot be accurately calibrated as HU due to the relatively large amount of noise, different types of artefacts, the cone-beam geometry and the limited field of view (FOV) size. Previous investigations and applications of CBCT grey values as HU were often limited to a single device, and may have been too optimistic about the actual accuracy of density estimations in practice.

The aim of this study was to investigate the relationship between CBCT and MSCT grey values for a variety of scanners. The linearity and calibration error of grey values from a range of materials were assessed.

11.3 Materials and methods

For the evaluation of CBCT grey values, a second prototype of the cylindrical polymethyl methacrylate (PMMA) phantom described in Chapter 7 was manufactured by Leeds Test Objects Ltd (Bouroughbridge, UK). Five cylindrical inserts (diameter 3.5 cm, height 2.0 cm) were used for the measurement of CNR. They contain a 10 mm central rod surrounded by PMMA. Five materials of different density were used in the inserts: air, aluminium, and hydroxyapatite (HA) of varying density (50, 100 and 200 mg/cm^3). The inserts have the same

size, materials and shape as those used in Chapters 7 and 10 for CNR and CT number analysis.

Thirteen CBCT devices were used for the scanning of the phantom: 3D Accuitomo 170, 3D Accuitomo XYZ image intensifier version and Veraviewepocs 3D (J. Morita, Kyoto, Japan), GALILEOS Comfort (Sirona Dental Systems, Bensheim, Germany), i-CAT Next Generation (Imaging Sciences International, Hatfield, PA, USA), Kodak 9000 3D and Kodak 9500 (Carestream Health, New York, NY, USA), NewTom VGi (Quantitative Radiology, Verona, Italy), Pax-Uni3D and Picasso Trio (Value Added Technologies, Yongin, South Korea), ProMax 3D (Planmeca Oy, Helsinki, Finland), SCANORA 3D (Soredex, Tuusula, Finland), and SkyView (Cefla Dental Group, Imola, Italy). The phantom was also scanned with a MSCT device (Somatom Sensation 64, Siemens, Erlangen, Germany) using a bone and soft tissue protocol to obtain reference grey values for the correlation analysis and the recalibration of the CBCT grey values. Where available, scanning was performed using different exposure and reconstruction parameters (*e.g.* FOV size, mAs, voxel size). A total of 30 selected clinical CBCT scanning protocols were included (Table 8.1, Chapter 8, p. 141). Axial CBCT and MSCT slices from each insert are shown in Figure 11.1.

All datasets were exported as axial stacks using the Digital Imaging and Communications in Medicine (DICOM) file format. ImageJ software (version 1.41, National Institutes of Health, Bethesda, MD, USA) was used for measurements on the CBCT and MSCT images. For all six materials inside the inserts, the mean grey value was determined using a circular ROI of approximately 2 cm^2. Measurements from ten consecutive axial slices were averaged, leading to a total measurement area of 20 cm^2. The number of voxels included in the ROI was between 12 500 (voxel size 0.4 mm) and 346 260 (voxel size 0.076 mm). All measurements were performed by two researchers with extensive experience in image analysis.
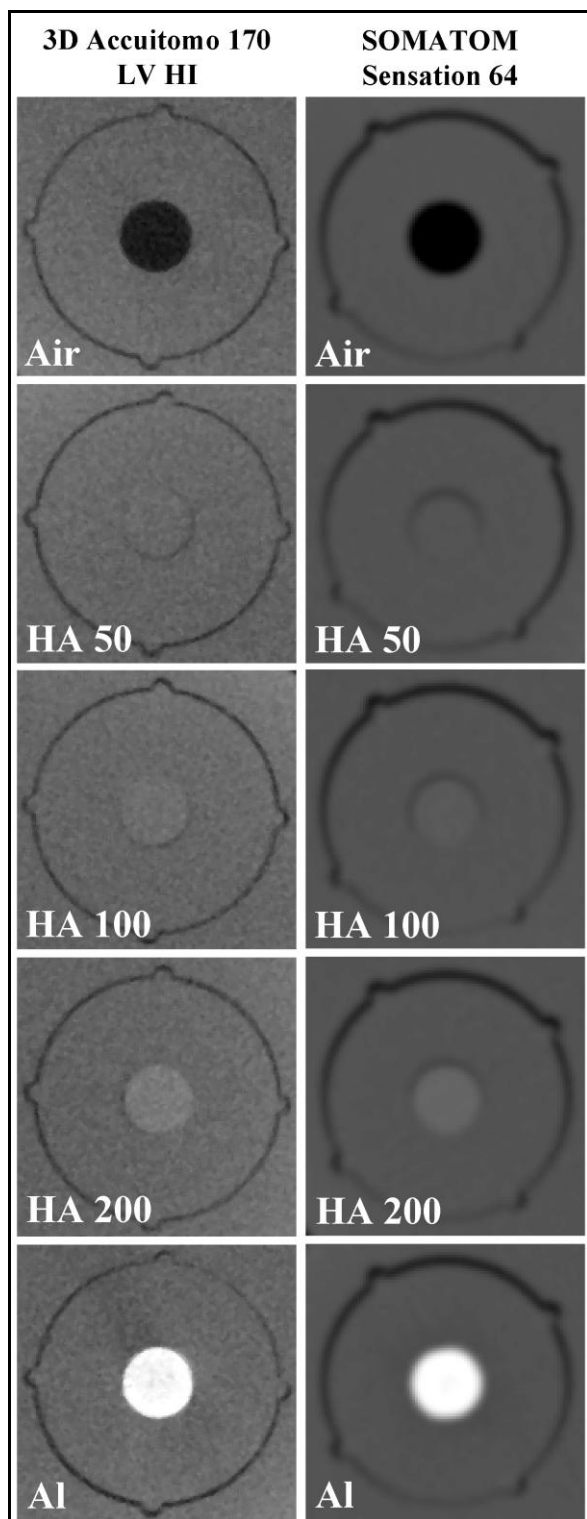
Figure 11.1 Example CBCT slices of five inserts used for grey value correlation analysis. PMMA insert not shown. For the MSCT, the H60s bone protocol is shown.

Grey value measurements from the two MSCT protocols were averaged and used as reference values for correlation analysis. For all 30 CBCT protocols, Pearson's sample correlation coefficient was calculated for a linear fit using all six materials, with the formula:

$$r_{ALL} = \frac{1}{n-1} \sum_{i=ALL}^{n} \left(\frac{X_i - \overline{X}}{s_X} \right) \left(\frac{Y_i - \overline{Y}}{s_Y} \right)$$

In this formula, X_i and Y_i are the mean grey values for the CBCT and MSCT for the different materials, $\overline{X}$ and $\overline{Y}$ are the sample means, s_X and s_Y are the sample standard deviation, and n equals six (*i.e.* air, PMMA, HA 50, HA 100, HA 200, aluminium). A second correlation coefficient was determined by excluding the air and aluminium measurements:

$$r_{MED} = \frac{1}{n-1} \sum_{i=MED}^{n} \left(\frac{X_i - \overline{X}}{s_X} \right) \left(\frac{Y_i - \overline{Y}}{s_Y} \right)$$

In this formula, n equals four (*i.e.* PMMA, HA 50, HA 100, HA 200).

As an additional measurement of grey value accuracy in the medium-density range, the CBCT measurements were rescaled using the measured MSCT values for air and aluminium as reference points. For the four other materials, the deviation ("error") in grey value between the MSCT and the rescaled CBCT values was calculated and averaged, using the formula:

$$Error = \frac{1}{4} \sum_{i=MED}^{4} (GV_i - GV_{AIR}) . \left(\frac{GVR_{MSCT}}{GVR_{CBCT}} \right)$$

GV is the measured mean grey value on the CBCT image, GVR_{MSCT} is the grey value range (*i.e.* the difference in GV for air and aluminium) for the MSCT device and GVR_{CBCT} is the grey value range for the CBCT in question.

11.4 Results

Table 11.2 shows the Pearson sample correlation coefficients (r-value) for the full density range (r_{ALL}) as well as the medium density range (r_{MED}). The exposure protocols are ranked from high to low according to the value for r_{ALL}. The ranking for r_{MED} is also included. The difference between the two r-values is shown, as well as the difference between the two ranks. For the thirty investigated CBCT exposure protocols, r_{ALL} ranged between 0.7014 (3D Accuitomo XYZ, SV) and 0.9996 (SCANORA 3D, MV ME). Three protocols showed r_{ALL} values below 0.8, all other had coefficients of 0.96 or higher. Apart from five protocols, all r_{ALL} values were higher than 0.99.

The r_{MED} value was between 0.5620 (Pax-Uni3D, SV) and 0.9991 (I-CAT Next Generation, LV XHI). Compared to their value for r_{ALL}, most exposure protocols showed a drop for r_{MED}. For five protocols, changes in r-value were minimal (<0.006). It is noteworthy that four of these five protocols are from the i-CAT Next Generation LV, whereas the XLV protocols from this device did show a decrease for r_{MED}. For 22 protocols, a clear drop for r_{MED} was seen with a decrease ranging between 0.011 and 0.398 with an average of 0.073. For three protocols (Veraviewepocs 3D MV, 3D Accuitomo XYZ SV, Kodak 9000 3D SV) the coefficient showed an increase for r_{MED} ranging between 0.050 and 0.261 with an average of 0.175. These three protocols showed the worst score for the full density range, but rank at 6, 18 and 28 for the medium density range, respectively.

When considering the ranking of the protocols for the two calculated r-values, large differences in ranks can be seen for most exposure protocols. Only four exposure protocols are ranked in the upper third (*i.e.* ten or higher) for both r-values, showing a consistent correlation irrespective of the density range. For twelve protocols, the difference in rank was 5 or lower. For eight protocols, the difference was 15 or higher.

The average grey value deviation of the four medium density materials after rescaling to the MSCT values was 241, corresponding to 5.9% of the total grey value range after rescaling to the MSCT values (*i.e.* 12 bit or 4096 grey values). The range of errors was between 35 (SCANORA 3D MV ME and Kodak 9500 LV) and 1562 (3D Accuitomo XYZ SV). For the protocols with an r-value higher than 0.99 for the full density range, the average error was 110 (2.7%). The three protocols with the lowest r_{ALL}-value (<0.80) had an average error of 1265 (30.9%). A good correlation was seen between r_{ALL} and the calculated error (inverse linear relationship, r=-0.986). No correlation was seen between the r_{MED} and the average error (r=-0.046).

11.5 Discussion

Three parameters were used to evaluate the linearity of CBCT grey values, providing complementary information. Correlation coefficients were generally high for the full density range between air and aluminium. Most CBCT protocols showed an r_{ALL} value higher than 0.99, implying an excellent linear fit between the CBCT and MSCT grey values. However, the possibility for CBCT voxel values to be calibrated for density measurements cannot be evaluated solely based on the overall correlation with MSCT. Especially for large FOV

devices containing all inserts in a single scan, a general correlation between grey values and density is self-evident, as it would be for any X-ray modality.

Table 11.2 Results of correlation analysis using MSCT grey values as a reference

Device	Protocol		r_{ALL}	r_{MED}	r_{MED}-r_{ALL}	Rank r_{ALL}	Rank r_{MED}	Rank r_{ALL}-Rank r_{MED}	Error
	FOV	Dose							
SCANORA 3D	MV	ME	0.9996	0.9820	-0.02	1	10	-9	35
Kodak 9500	LV		0.9991	0.9820	-0.02	2	9	-7	35
3D Accuitomo 170	LV	HI	0.9984	0.9797	-0.02	3	12	-9	55
NewTom VGi	MV	HI	0.9983	0.9135	-0.08	4	22	-18	54
SCANORA 3D	MV	LO	0.9982	0.8514	-0.15	5	27	-22	77
NewTom VGi	MV	LO	0.9982	0.9186	-0.08	6	21	-15	54
3D Accuitomo 170	LV	LO	0.9982	0.9809	-0.02	7	11	-4	63
I-CAT N.G.	LV	LO	0.9980	0.9969	-0.00	8	2	6	117
I-CAT N.G.	LV	XHI	0.9972	0.9991	+0.00	9	1	8	143
3D Accuitomo 170	SV	LO	0.9969	0.9773	-0.02	10	13	-3	100
SCANORA 3D	MV	HI	0.9967	0.8381	-0.16	11	29	-18	98
3D Accuitomo 170	SV	HI	0.9967	0.9767	-0.02	12	14	-2	105
Galileos Comfort	LV	HI	0.9965	0.9402	-0.06	13	19	-6	84
Kodak 9500	XLV		0.9959	0.9713	-0.02	14	15	-1	91
SkyView	LV	HI	0.9958	0.9677	-0.03	15	16	-1	99
Picasso Trio	MV	HI	0.9957	0.9660	-0.03	16	17	-1	166
SkyView	LV	ME	0.9957	0.9840	-0.01	17	7	10	109
ProMax 3D	MV	HI1	0.9954	0.9043	-0.09	18	24	-6	88
I-CAT N.G.	XLV	HI	0.9951	0.9135	-0.08	19	23	-4	196
I-CAT N.G.	XLV	LO	0.9948	0.9190	-0.08	20	20	0	202
SkyView	LV	LO	0.9947	0.9838	-0.01	21	8	13	134
ProMax 3D	MV	HI1	0.9942	0.8832	-0.11	22	26	-4	92
ProMax 3D	MV	HI2	0.9941	0.8877	-0.11	23	25	-2	91
Picasso Trio	MV	LO	0.9936	0.9963	+0.00	24	3	21	196
I-CAT N.G.	LV	XLO	0.9905	0.9963	+0.01	25	4	21	273
I-CAT N.G.	LV	HI	0.9885	0.9932	+0.00	26	5	21	307
PaX-Uni3D	SV		0.9595	0.5620	-0.40	27	30	-3	365
Kodak 9000 3D	SV		0.7997	0.8497	+0.05	28	28	0	972
VeraviewEpocs 3D	MV		0.7777	0.9921	+0.21	29	6	23	1261
3D Accuitomo XYZ	SV		0.7014	0.9625	+0.26	30	18	12	1562

r_{ALL}, correlation coefficient for all six materials; r_{MED}, correlation coefficient for medium density materials, excluding air and aluminium; r_{MED}-r_{ALL},absolute difference between correlation coefficients; Error, average deviation of medium density grey values after recalibration; SV, small volume; MV, medium volume; LV, large volume; HI, high dose; ME, medium dose; LO, low dose; X, extra.

The second correlation coefficient which was calculated for the four materials in the medium density range provided further insights regarding the use of CBCT grey values for

density measurements. When considering only the medium density range, the correlation coefficient is more sensitive to variability in grey values. The r_{MED} was clearly lower than the r_{ALL} for most devices, although for some protocols the difference was minimal. Seeing that previous studies have found correlation coefficients which were interpreted as 'high' but were lower than most of the r_{MED} values in this study [15,16], additional information was needed to evaluate the coefficients calculated in this study, avoiding subjective interpretation. The error values after recalibration demonstrate whether or not the generally high correlation coefficients imply that the currently investigated CBCT devices are useful for density assessment. The average error for the materials in the medium density range clearly shows the error margin that can be expected when using CBCT grey values in a quantitative way. The two exposure protocols with the highest r_{ALL} value both had an average error of 35; for all other protocols this error was larger than 50. Half of the exposure protocols showed an error value larger than 100.

When looking at the use of HU in dental practice, the implication of the grey value errors which were calculated in this study can be investigated. The main use for density estimations would be in the evaluation of bone quality before implant placement. Different studies have investigated bone quality based on HU from MSCT scans from implant patients [3,23-27]. Classification of bone quality based on HU has been assessed, and ranges for bone quality groups have been proposed [27]. It can be seen that the error margins for some CBCT protocols are well below the proposed HU ranges, showing that density estimations with reasonable accuracy would be possible for implant planning using these CBCT protocols. However, previous studies have used CBCT grey values for the differential diagnosis and follow-up of bony lesions [28-31]. Based on the current results, the quantitative use of CBCT grey values for differentiating lesions should be generally avoided. Even the best performing devices will not enable to distinguish different types of lesions (*e.g.* cysts and granulomas) based on grey values. For the detection of root lesions and the evaluation of bone healing over time, the added value of CBCT grey values is questionable, as visual inspection typically provides the required information [32-34]. Furthermore, no thresholds or ranges for bone healing based on HU have been determined.

It is important to note that the current evaluation did not take the absolute grey values into account, as they are often dynamically distributed along an extended (*e.g.* 16 bit) scale. Before actually using CBCT grey values for density estimations, a histogram calibration is needed. This calibration process can be taken care of by the manufacturer, but it is also possible for the user to implement it in clinical practice. The use of a reference object in the

FOV containing at least two materials of known density could allow for a routine HU calibration, similar to the use of reference phantoms in quantitative computed tomography (QCT). Further investigation is needed to assess the accuracy and clinical applicability of this kind of calibration method.

There are different CBCT exposure factors which contribute to the deviation of grey values. Exposures in dental CBCT imaging yield doses far below conventional MSCT protocols. Although the spatial resolution of CBCT is considered to be higher than MSCT, the amount of noise is higher as well. Excessive noise may lead to aberrant grey values when measuring the mean voxel value of small areas. However, in this study the effect of noise has been limited because of the large measurement area. For most devices, correlation coefficients were similar for high- and low-dose protocols, showing that noise and voxel size did not affect the measurements. In practice, when small bony lesions or areas adjacent to planned implants would be investigated, the noise will randomly affect the measured mean grey value.

Another factor is beam hardening, which occurs primarily with low-energy beams passing through dense tissue, resulting in the increase of the beam energy (*i.e.* hardening) due to the predominant absorption of low-energy photons. The hardened X-rays will pass through adjacent tissues more easily, resulting in an underestimation of the density of these tissues appearing as dark areas on the image [19,35,36]. In addition, the inclusion of metal objects in the scanned area can results in additional grey value inaccuracy in clinical practice. Metal artefacts are a prominent feature in all forms of CT imaging, causing dark and bright streaks in the vicinity of the metal object due to a variety of effects such as beam hardening, scatter, and photon starvation [35,36].

Another aspect of CBCT imaging that affects grey value distributions is the limited FOV size, which can be as small as a few cm^3. Although field limitation is an essential part of dose reduction for CBCT examinations, there are certain implications in terms of grey value accuracy, as previously shown by Katsumata *et al.* [14]. The presence of non-homogeneous and non-symmetrical tissues outside the FOV leads to variable projection data from different angles along the rotation arc. This is known as the local tomography effect and it can lead to grey value gradients or even artefacts depending on the mass and spatial distribution of materials or tissues outside the FOV [12,37]. In this study, the effect of local tomography was limited because the position of the insert columns was accurately reproduced when only the peripheral portion of the phantom could be scanned. Any shading or gradient due to the asymmetrical position of the phantom would have influenced all inserts equally. Previous studies have investigated the effect of the position of test objects on CBCT grey values, with

contradictory results for different scanners. Although the theory behind the local tomography effect is sound, the degree of this effect may vary between devices based on the interplay of exposure and reconstruction factors.

Three devices showed an r-value which was clearly lower (<0.8) than the others (>0.95). Apart from the local tomography effect which has been described above, the devices appear to have incorporated a 'histogram shift' in their reconstruction algorithm, implying that the grey values are distributed based on the contents of the scan. In this way, the contrast of each individual scan is optimised, but grey values differ between scans containing low- or high-density materials. The presence of high-density objects in the scan shifts the histogram leading to lower grey values throughout the image. This is illustrated in Figure 11.2 showing axial slices through the HA200 and aluminium inserts of the 3D Accuitomo XYZ, Veraviewepocs 3D and Kodak 9000 3D, as well as the grey value histograms for these images. All images are displayed using the same window/level setting. It can be seen that the aluminium rod leads to a shift of the histogram to the left, resulting in a relatively low grey value of aluminium compared to HA200. The grey value of the PMMA background illustrates the histogram shift clearly, as it appears much darker on the images containing aluminium. For these three devices, which showed the lowest r_{ALL} value for the full density range and excessive error values after recalibration, a clear increase for the r_{MED} value was seen, as the effect of the histogram shift was much less pronounced when only considering the four medium-density materials. This dynamic display range is an intentional choice by the manufacturer, renouncing on the quantitative use of grey values.

When comparing the current results to previous investigations on the use of CBCT grey values, it should be noted that findings and conclusions from past studies were often limited to a single CBCT device [11-18]. However, because of the wide range seen in CBCT image quality and radiation dose, it is not feasible to make statements regarding CBCT as a whole based on the results from particular CBCT devices. In this study, 30 exposure protocols from 13 CBCT devices were evaluated, which is still a sample from the large amount of devices that are currently on the market. It is therefore not possible to draw general conclusions regarding the use of CBCT for density estimations. The current study shows that exposure protocols from certain devices show stable grey values which could be related to Hounsfield Units and density. However, the correlation coefficients and error values were independent of the absolute grey values of the CBCT images. In practice, the actual grey scale will depend on the bit depth of the images and the calibration by the manufacturers. Even for MSCT devices, the relation between grey values and density is, to some extent, scanner type-

190

specific. It is doubtful if grey value ranges for bone quality, bone healing or differential diagnosis can be determined for CBCT. If this is not possible, the quantitative application of CBCT grey values will be limited, and the practitioner should use these with great care.
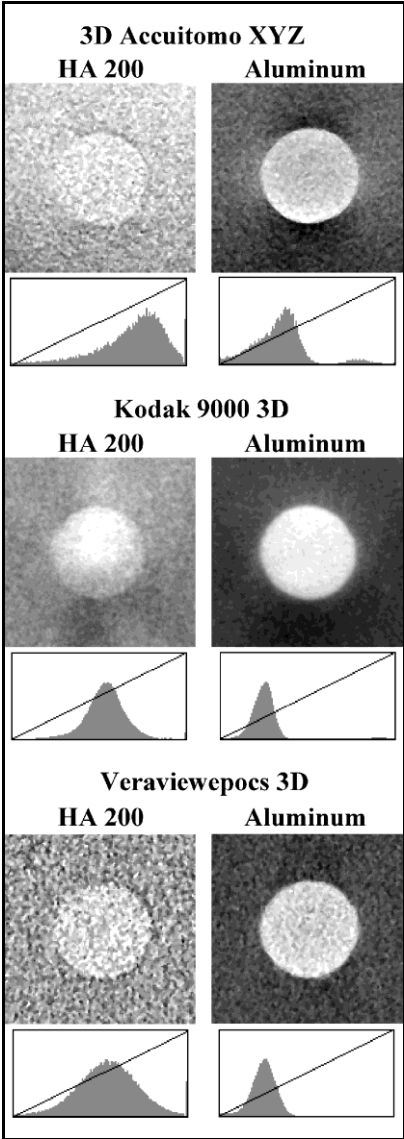

Figure 11.2 Slices from the HA 200 and aluminium inserts, showing the effect of histogram shifting. The presence of an aluminium rod results in a shift towards the left (*i.e.* lower grey values), resulting in similar mean grey values for HA 200 and aluminium. The histograms correspond to the entire axial slice rather than the illustrated ROI containing the rods.

Recently, alternative methods of bone quality analysis using CBCT images have been proposed. Fanuscu *et al.* have investigated the relation between morphometric parameters obtained from microCT images and bone density from CT and 2-D radiography [38]. While the study should be extended to larger sample sizes, there is an indication that morphometric parameters could be useful for application on CBCT datasets as well for the assessment of bone quality, providing that the image quality suffices in terms of spatial resolution, noise and

bone contrast. Alternatively, structural analysis using fractal dimension can provide an evaluation of bone density and structure. Torres *et al.* applied fractal dimension analysis on bisphosphonate-associated osteonecrosis patients [39]. Although fractal analysis needs to be further explored before implementation into clinical practice, it is certainly useful to apply it retrospectively, providing that large patient samples can be used. Hua *et al.* related fractal analysis and morphometric analysis on CBCT data with BMD from DXA scans [13]. They found a correlation between fractal dimension and morphometric bone area, but not for morphometric bone density. In two related studies by Hohlweg *et al.*, the applicability of two CBCT systems for the measurement of bone quantity and quality was assessed [10,11]. Although it was found that structural analysis of trabecular bone can only be performed using images of high spatial resolution, the small voxel sizes (<200 μm) of certain CBCT protocols point out that it should be possible to apply them for the assessment of bone density and architecture. Although improvements in CBCT imaging (*e.g.* reconstruction) could lead to more accurate grey value distributions which could be used as HU, the topic of bone quality analysis using fractal or morphometic analysis should be further explored *in vitro* or using patient data. Providing that large sample size are used, varying CBCT devices are included and a worthy gold standard is available, dedicated and validated bone quality parameters could be determined. Jiang *et al.* investigated the combination of BMD and structural analysis to predict mechanical properties of the bone, finding an improvement in the predictive value when combining multiple parameters [40]. Possibly, a prediction model for CBCT with multiple variables will offer the most accurate correlation with mechanical properties of the bone.

11.6 Conclusion

Even though most CBCT devices showed a good overall correlation with CT numbers, large errors can be seen when using the grey values in a quantitative way. The relatively large amount of noise in CBCT may lead to inaccurate grey values in the medium-density range, and the limited FOV diameter implies that the part of the scanned object which is outside the reconstructed volume can affect the grey values inside the FOV in a non-uniform way. Furthermore, it is possible that the grey values are distributed based on the densities within the FOV, leading to shifts in the grey value histogram. Although it could be possible to obtain pseudo-Hounsfield Units from certain CBCTs, the main focus in research should be the investigation and validation of alternative methods of assessing bone quality.

11.7 References

1. Bou Serhal C, Jacobs R, Quirynen M, van Steenberghe D. Imaging technique selection for the preoperative planning of oral implants: a review of the literature. Clin Implant Dent Relat Res 2002; 4: 156-172.

2. Guerrero ME, Jacobs R, Loubele M, Schutyser F, Suetens P, van Steenberghe D. State-of-the-art on cone beam CT imaging for preoperative planning of implant placement. Clin Oral Investig 2006; 10: 1-7.

3. Turkyilmaz I, Tumer C, Ozbek EN, Tözüm TF. Relations between the bone density values from computerized tomography, and implant stability parameters: a clinical study of 230 regular platform implants. J Clin Periodontol 2007; 34: 716-722.

4. Pauwels R, Beinsberger J, Collaert B, Theodorakou C, Rogers J, Walker A, Cockmartin L, Bosmans H, Jacobs R, Bogaerts R, Horner K, The SEDENTEXCT Project Consortium. Effective dose range for dental cone beam computed tomography scanners. Eur J Radiol 2012; 81: 267-271.

5. Hatcher DC, Dial C, Mayorga C. Cone beam CT for pre-surgical assessment of implant sites. J Calif Dent Assoc 2003; 31: 825-833.

6. Monsour PA, Dudhia R. Implant radiography and radiology. Aust Dent J 2008; 53: S11-25.

7. Van Assche N, van Steenberghe D, Guerrero ME, Hirsch E, Schutyser F, Quirynen M, Jacobs R. Accuracy of implant placement based on pre-surgical planning of three-dimensional cone-beam images: a pilot study. J Clin Periodontol 2007; 34: 816-821.

8. Veyre-Goulet S, Fortin T, Thierry A. Accuracy of linear measurement provided by cone beam computed tomography to assess bone quantity in the posterior maxilla: a human cadaver study. Clin Implant Dent Relat Res2008; 10: 226-230.

9. Moreira CR, Sales MA, Lopes PM, Cavalcanti MG. Assessment of linear and angular measurements on three-dimensional cone-beam computed tomographic images. Oral Surg Oral Med Oral Pathol Oral Radiol Endod 2009; 108: 430-436.

10. Hohlweg-Majert B, Pautke C, Deppe H, Metzger MC, Wagner K, Schulze D. Qualitative and quantitative evaluation of bony structures based on DICOM dataset. J Oral Maxillofac Surg 2011; 69: 2763-2770.

11. Hohlweg-Majert B, Metzger MC, Kummer T, Schulze D. Morphometric analysis - Cone beam computed tomography to predict bone quality and quantity. J Craniomaxillofac Surg 2011; 39: 330-334.

12. Bryant JA, Drage NA, Richmond S. Study of the scan uniformity from an i-CAT cone beam computed tomography dental imaging system. Dentomaxillofac Radiol 2008; 37: 365-374.

13. Hua Y, Nackaerts O, Duyck J, Maes F, Jacobs R. Bone quality assessment based on cone beam computed tomography imaging. Clin Oral Implants Res 2009; 20: 767-71.

14. Katsumata A, Hirukawa A, Okumura S, Naitoh M, Fujishita M, Ariji E, Langlais RP. Relationship between density variability and imaging volume size in cone-beam computerized tomographic scanning of the maxillofacial region: an in vitro study. Oral Surg Oral Med Oral Pathol Oral Radiol Endod 2009; 107: 420-425.

15. Lagravère MO, Carey J, Ben-Zvi M, Packota GV, Major PW. Effect of object location on the density measurement and Hounsfield conversion in a NewTom 3G cone beam computed tomography unit. Dentomaxillofac Radiol 2008; 37: 305-308.

16. Naitoh M, Hirukawa A, Katsumata A, Ariji E. Evaluation of voxel values in mandibular cancellous bone: relationship between cone-beam computed tomography and multislice helical computed tomography. Clin Oral Implants Res 2009;20:503-6.

17. Naitoh M, Hirukawa A, Katsumata A, Ariji E. Prospective study to estimate mandibular cancellous bone density using large-volume cone-beam computed tomography. Clin Oral Implants Res 2010; 21: 1309-1313.

18. Fuster-Torres MÁ, Peñarrocha-Diago M, Peñarrocha-Oltra D, Peñarrocha-Diago M. Relationships between bone density values from cone beam computed tomography, maximum insertion torque, and resonance frequency analysis at implant placement: a pilot study. Int J Oral Maxillofac Implants 2011; 26: 1051-1056.

19. Katsumata A, Hirukawa A, Okumura S, Naitoh M, Fujishita M, Ariji E, Langlais RP. Effects of image artefacts on gray-value density in limited-volume cone-beam computerized tomography. Oral Surg Oral Med Oral Pathol Oral Radiol Endod 2007; 104: 829-836.

20. Mah P, Reeves TE, McDavid WD. Deriving Hounsfield units using grey levels in cone beam computed tomography. Dentomaxillofac Radiol 2010; 39: 323-335.

21. Nackaerts O, Maes F, Yan H, Couto Souza P, Pauwels R, Jacobs R. Analysis of intensity variability in multislice and cone beam computed tomography. Clin Oral Implants Res 2011; 22: 873-879.

22. Pauwels R, Stamatakis H, Manousaridis G, Walker A, Michielsen K, Bosmans H, Bogaerts R, Jacobs R, Horner K, Tsiklakis K, The SEDENTEXCT Project

Consortium. Development and applicability of a quality control phantom for dental cone-beam CT. J Appl Clin Med Phys 2011; 12: 245-260.

23. Fuh LJ, Huang HL, Chen CS, Fu KL, Shen YW, Tu MG, Shen WC, Hsu JT. Variations in bone density at dental implant sites in different regions of the jawbone. J Oral Rehabil 2010; 37: 346-51.

24. Turkyilmaz I, Tözüm TF, Tumer C, Ozbek EN. Assessment of correlation between computerized tomography values of the bone, and maximum torque and resonance frequency values at dental implant placement. J Oral Rehabil 2006; 33: 881-888.

25. Sogo M, Ikebe K, Yang TC, Wada M, Maeda Y. Assessment of Bone Density in the Posterior Maxilla Based on Hounsfield Units to Enhance the Initial Stability of Implants. Clin Implant Dent Relat Res 2011. Epub ahead of print.

26. de Oliveira RC, Leles CR, Normanha LM, Lindh C, Ribeiro-Rotta RF. Assessments of trabecular bone density at implant sites on CT images. Oral Surg Oral Med Oral Pathol Oral Radiol Endod 2008; 105: 231-238.

27. Norton MR, Gamble C. Bone classification: an objective scale of bone density using the computerized tomography scan. Clin Oral Implants Res 2001; 12: 79-84.

28. Simon JH, Enciso R, Malfaz JM, Roges R, Bailey-Perry M, Patel A. Differential diagnosis of large periapical lesions using cone-beam computed tomography measurements and biopsy. J Endod 2006; 32: 833-837.

29. Kaya S, Yavuz I, Uysal I, Akkuş Z. Measuring bone density in healing periapical lesions by using cone beam computed tomography: a clinical investigation. J Endod 2012; 38: 28-31.

30. Rosenberg PA, Frisbie J, Lee J, Lee K, Frommer H, Kottal S, Phelan J, Lin L, Fisch G. Evaluation of pathologists (histopathology) and radiologists (cone beam computed tomography) differentiating radicular cysts from granulomas. J Endod 2010; 36: 423-428.

31. Cankaya AB, Erdem MA, Isler SC, Demircan S, Soluk M, Kasapoglu C, Oral CK. Use of cone-beam computerized tomography for evaluation of bisphosphonate-associated osteonecrosis of the jaws in an experimental rat model. Int J Med Sci 2011; 8: 667-672.

32. Ordinola-Zapata R, Bramante CM, Duarte MH, Ramos Fernandes LM, Camargo EJ, de Moraes IG, Bernardineli N, Vivan RR, Capelozza AL, Garcia RB. The influence of cone-beam computed tomography and periapical radiographic evaluation on the

assessment of periapical bone destruction in dog's teeth. Oral Surg Oral Med Oral Pathol Oral Radiol Endod 2011; 112: 272-9.

33. Patel S, Wilson R, Dawood A, Mannocci F. Detection of periapical pathology using intraoral radiography and cone beam computed tomography - a clinical study. Int Endod J 2011. Epub ahead of print.

34. Kumar V, Gossett L, Blattner A, Iwasaki LR, Williams K, Nickel JC. Comparison between cone-beam computed tomography and intraoral digital radiography for assessment of tooth root lesions. Am J Orthod Dentofacial Orthop 2011; 139: e533-541.

35. Schulze R, Heil U, Gross D, Bruellmann DD, Dranischnikow E, Schwanecke U, Schoemer E. Artefacts in CBCT: a review. Dentomaxillofac Radiol 2011; 40: 265-273.

36. Pauwels R, Stamatakis H, Bosmans H, Bogaerts R, Jacobs R, Horner K, Tsiklakis K, The SEDENTEXCT Project Consortium. Quantification of metal artifacts on cone beam computed tomography images. Clin Oral Implants Res 2011. Epub ahead of print.

37. Siltanen S, Kolehmainen V, Järvenpää S, Kaipio JP, Koistinen P, Lassas M, Pirttilä J, Somersalo E. Statistical inversion for medical x-ray tomography with few radiographs: I. General theory. Phys Med Biol 2003; 48: 1437-1463.

38. Fanuscu MI, Chang TL. Three-dimensional morphometric analysis of human cadaver bone: microstructural data from maxilla and mandible. Clin Oral Implants Res 2004; 15: 213-218.

39. Torres SR, Chen CS, Leroux BG, Lee PP, Hollender LG, Schubert MM. Fractal dimension evaluation of cone beam computed tomography in patients with bisphosphonate-associated osteonecrosis. Dentomaxillofac Radiol 2011; 40: 501-505.

40. Jiang C, Giger ML, Chinander MR, Martell JM, Kwak S, Favus MJ. Characterization of bone quality using computer-extracted radiographic features. Med Phys 1999; 26: 872-879.

Chapter 12: Technical versus diagnostic image quality in CBCT imaging

12.1 Abstract

Objectives: The aim of this study was to investigate image noise and diagnostic image quality at various exposure levels for different CBCT scanners, to determine the relationship between technical and clinical imaging parameters, and to define preliminary thresholds or reference levels for CBCT image quality.

Materials and methods: A homogeneous PMMA phantom and an anthropomorphic skull phantom containing a human skeleton embedded in polyurethane were used. The phantoms were scanned using four CBCT devices (3D Accuitomo 170, CRANEX 3D, Galileos Comfort, SCANORA 3D), including seven exposure protocols. For all protocols, the tube current-time product (mAs) was varied within the selectable range. Using the PMMA phantom, noise was measured as the standard deviation of grey values and corrected for voxel size. In parallel, an observer study was set up by selecting eight axial slices from the skull phantom. The slices were presented to five oral radiologists, providing scores for various anatomical and diagnostic parameters.

Results: A hyperbolic relation was seen between CNR and mAs. Similarly, a gradual reduction in diagnostic image quality was seen for reduced exposures. Depending on the diagnostic application, there is a possibility for a moderate or large mAs reduction while keeping the image quality at an acceptable level. The relation between mAs, CNR and observer scores was different for each CBCT device. Preliminary reference levels for CNR_{AIR} were between 7.7 and 12.6, depending on the criterion and clinical application.

Conclusion: A multi-predictor model including both spatial resolution and contrast resolution may provide objective criteria for image quality which are reproducible between devices. It could be possible to reduce exposure levels below the manufacturer's recommended setting for certain patient groups.

12.2 Introduction

The image quality of CBCT has been extensively studied in vitro and in vivo. Most authors have focused on certain diagnostic image quality aspects, such as the visibility of anatomical landmarks, the detection of caries, bone loss or bony lesions, and the segmentation accuracy of teeth and bone [1-6]. Different skull and jaw models are used which limits the standardization and intercomparison of quantitative image quality measurements, and findings from these studies are often limited to the investigated type(s) of scanner. Alternatively, geometrical phantoms have been used to investigate technical image quality parameters [7-9]. For straightforward image quality parameters such as contrast and noise, using these types of phantoms allows for a reproduction of the measurements on any type of scanner. Furthermore, the use of a geometrical image quality phantom in quality control could lead to a standardization of the quality assurance of CBCT devices, and to the possible implementation of reference levels for image quality which guide the user or medical physicist in the evaluation of a scanner's performance [10]. The limitation of using technical image quality parameters as reference levels for clinical practice is that there is no straightforward way of translating these parameters to diagnostic relevance. In practice, the choice of exposure protocols for different patient groups is left to the subjective interpretation of the operator (*i.e.* dentist, radiologist, X-ray technician), seeing that there are no guidance levels for radiation dose or image quality. Whether or not an image is acceptable for clinical purposes is determined by the observer of the image, adding another degree of subjectivity to the use of CBCT [11-14].

The aim of this study was to investigate image contrast, noise and diagnostic image quality at various exposure levels for different CBCT scanners, to determine the relationship between technical and clinical imaging parameters, and to define preliminary thresholds or reference levels for CBCT image quality.

12.3 Materials and methods

CBCT devices

Four CBCT devices were included in this study: 3D Accuitomo 170 (J. Morita, Kyoto, Japan), CRANEX 3D and SCANORA 3D (Soredex, Tuusula, Finland), and Galileos Comfort (Sirona, Bensheim, Germany). Exposure parameters are listed in Table 12.1. A total of seven imaging protocols, determined by the FOV size and voxel size, were selected. For the 3D

Accuitomo 170 and SCANORA 3D, a small and large FOV size with varying voxel size was selected. For the CRANEX 3D, a high- and low-resolution protocol was selected for the largest available FOV. For the Galileos Comfort, only the mAs was varied as the FOV and voxel size is fixed. The full available mAs range was included for each imaging protocol with the exception of the 3D Accuitomo 170, for which the highest mAs values were discarded for the observer study as they are up to 100% larger than clinically used mAs settings.

Table 12.1 Devices and exposure parameters

CBCT	FOV	Voxel size	kV	mAs
3D Accuitomo 170	14x10	0.25	90	18-123
	6x6	0.125	90	18-123
SCANORA 3D	13.5x14.5	0.35	90	11-17
	6x6	0.2	90	12-39
CRANEX 3D	6x8	0.2	90	56-139
	6x8	0.3	90	29-63
GALILEOS Comfort	15x15	0.29	85	10-42

Technical image quality

A head size PMMA phantom (16cm diameter) was used for the analysis of contrast and noise. The phantom is homogeneous with the exception of a central air hole of 10mm diameter at the bottom. As this air hole was needed for contrast analysis, the phantom was placed on a second PMMA phantom, allowing for the bottom part to be scanned without interference from supporting structures (*e.g.* metal platforms).

All datasets were exported as axial slices in DICOM format and evaluated with ImageJ software version 1.41o (National Institutes of Health, Bethesda, MD, USA). All measurements were performed by two researchers.

Contrast-to-noise ratio (CNR) was measured between the air hole and the PMMA by measuring the mean grey value and standard deviation for both materials, and using the following calculation:

$$CNR_{AIR} = \frac{MGV_{PMMA} - MGV_{AIR}}{\sqrt{(SD_{PMMA}.Voxel^{0.608})^2 + (SD_{AIR}.Voxel^{0.608})^2}}$$

with MGV the mean grey value, SD the standard deviation, and Voxel the voxel size of the image. The correction for voxel size is described in Chapter 10. It should be noted that no

grey value range correction is needed, as the CNR calculation itself takes the grey value range into account.

Diagnostic image quality

An anthropomorphic skull phantom (RANDO, The Phantom Laboratory, Salem, NY, USA) containing a human skeleton embedded in polyurethane was used (Figure 12.1). The phantom represents an adult male (175 cm tall; 73.5 kg), and consists of a human skull with full dentition, embedded a soft tissue-equivalent material (*i.e.* polyurethane) simulating muscle tissue with randomly distributed fat. The natural human skulls are adjusted to correct for a natural lack of symmetry. For each dataset, 8 axial slices and one coronal slice with relevant anatomical landmarks were selected and combined in a stack for the convenience of the observer.

Figure 12.1 RANDO phantom, head and neck portion

Six experienced oral radiologists were selected as observers. Using ImageJ, a total of 47 stacks each consisting of 9 selected slices was scored. The observers were allowed to adjust brightness and contrast, and instructed to fine-tune grey level display for optimal visualization of the different anatomical landmarks, rather than using a single window/level setting for the entire evaluation. The visualization of ten different anatomical landmarks was scored: mandibular symphysis, mental foramen, cortical bone, lamina dura, periodontal ligament (PDL) space, pulp canal, enamel, maxillary structure, incisive foramen and trabecular bone. For all landmarks which are present in both jaws (*e.g.* trabecular bone), a separate score for upper and lower jaw was provided. In addition, the observers provided a score expressing the usefulness of the image for three clinical applications: root pathology, sinus pathology and implant planning. For all evaluations, a 4-point rating scale was used,

summarized in Table 12.2. Inter-observer agreement was estimated using a weighted kappa, calculated with MedCalc (version 11.2, MedCalc Inc., Mariakerke, Belgium).

Table 12.2 Rating scale for observer study

Score	Anatomical landmarks	Usefulness for clinical application
1	Very poor visibility	Certainly not useful
2	Poor visibility	Probably not useful
3	Acceptable visibility	Probably useful
4	Excellent visibility	Certainly useful

The relation between mAs, noise, CNR and observer scores was evaluated. Based on the threshold score of 2.5, being the limit between acceptable and unacceptable image quality for the anatomical landmarks as well as the clinical applications, the corresponding CNR levels were determined.

12.4 Results

Scatter plots for CNR versus mAs are provided in Figure 12.2. For the 3D Accuitomo 170, a clear hyperbolic relation is seen as this device allows for the selection of a wide mA range, with a 10:1 ratio between the highest and lowest exposure. For the other devices, either a curved or linear section of a hyperbolic relation is shown as the mAs ratio between the highest and lowest exposure is smaller (SCANORA 3D: 3.1:1, CRANEX 3D: 2.2-2.5:1, GALILEOS Comfort: 4.2:1).

Selected axial slices for each exposure protocols at the level of the mental foramen and maxillary bone are shown in Figures 12.3 and 12.4, respectively. For each FOV/resolution protocol, the default mAs for dental clinical scanning was selected for these figures. Kappa values representing intra-observer agreement were between 0.336 and 0.677 with an average of 0.469 (Table 12.3).

Figure 12.5 demonstrates the relation between the CNR and the average observer score for all parameters. To calculate this average, values for mandible and maxilla (*e.g.* cortical bone) were first averaged before averaging with the other parameters. Considering a score of 2.5 as threshold value between an acceptable or unacceptable image (Table 12.2), most exposure protocols show an acceptable average score, even for the lowest mAs setting. Two exposure protocols dropped below this threshold for lower mAs values due to low scores for the mandibular symphysis, PDL space and lamina dura.

The highest score for all anatomical parameters was for the mental foramen, for which all scores were above the 2.5 mark. The maxillary lamina dura had the lowest score for all parameters (Figure 12.6). Difference between score for maxilla and mandible were highest for the cortical bone, for which the maxilla received a lower score (Figure 12.7). The difference between scores for maxilla and mandible were largest for the GALILEOS Comfort and lowest for the 3D Accuitomo 170, small volume (Table 12.4).
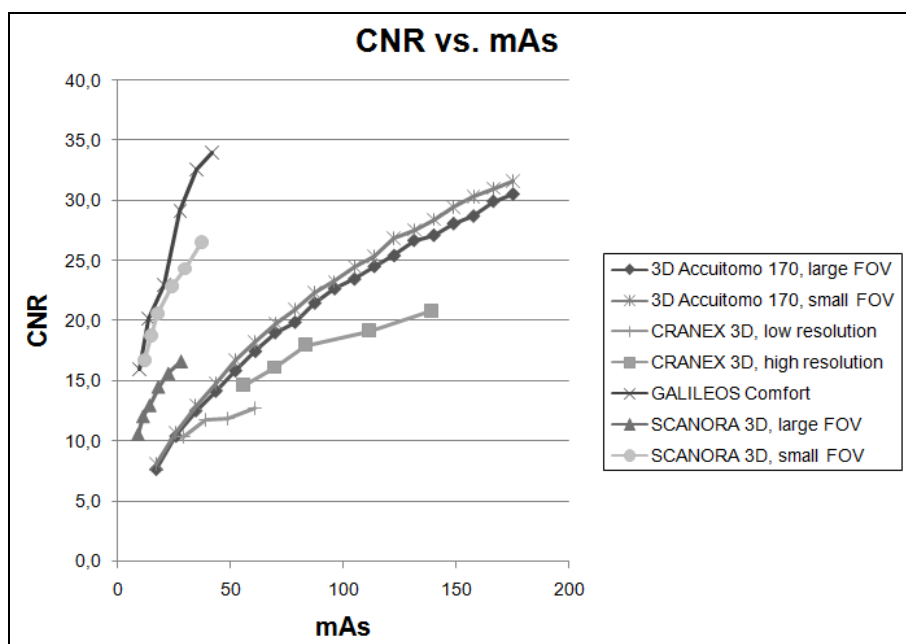
Figure 12.2 Contrast-to-noise ratio (CNR) versus tube current-time product (mAs)

Table 12.3 Intra-observer agreement, weighted kappa

	Observer 2	Observer 3	Observer 4	Observer 5	Observer 6
Observer 1	0.677	0.594	0.415	0.347	0.450
Observer 2		0.585	0.393	0.336	0.394
Observer 3			0.409	0.363	0.420
Observer 4				0.632	0.519
Observer 5					0.497

3D Accuitomo 170, small volume

3D Accuitomo 170, large volume

CRANEX 3D, high resolution

CRANEX 3D, low resolution

SCANORA 3D, small volume

SCANORA 3D, large volume

GALILEOS Comfort
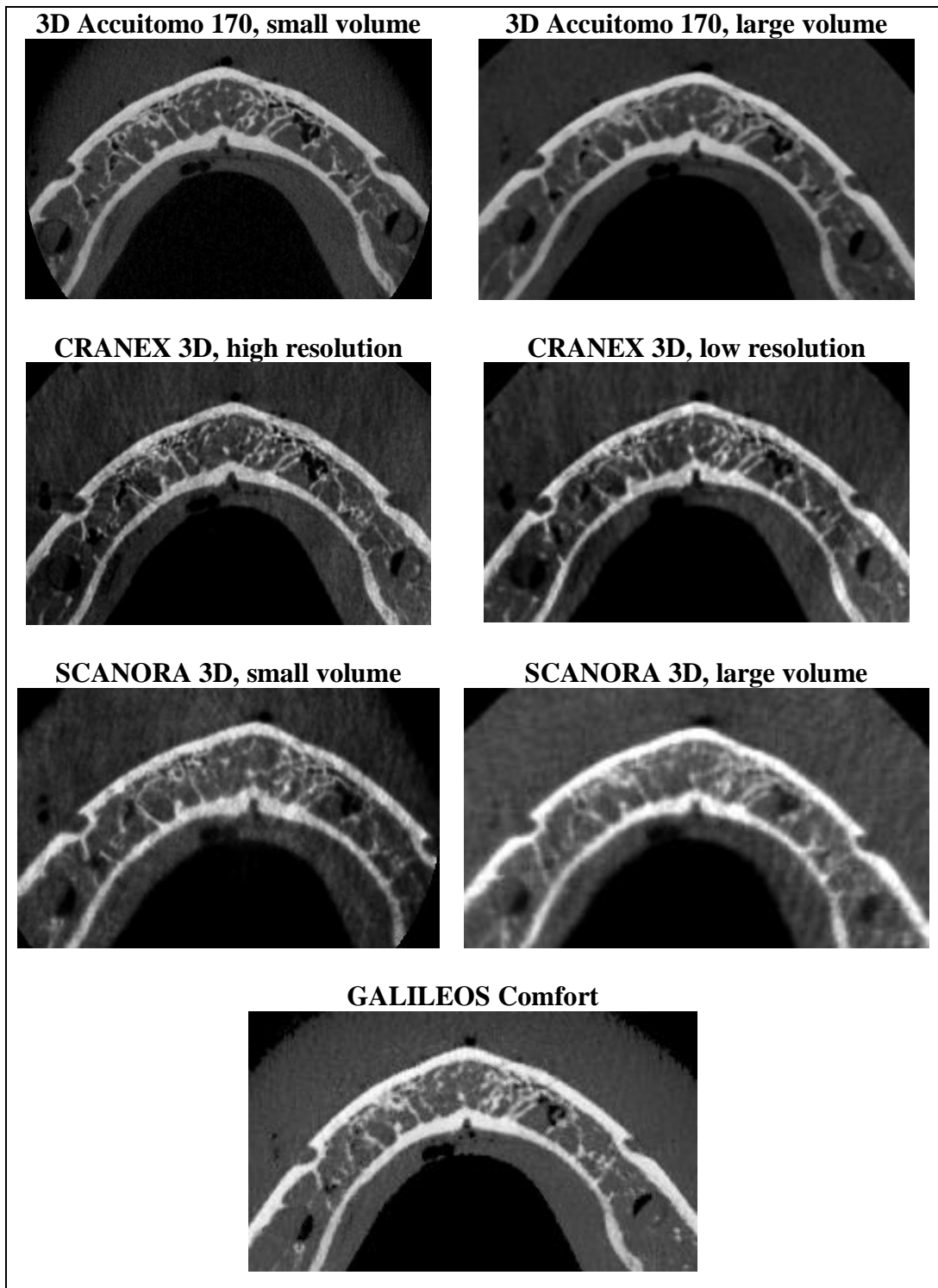
Figure 12.3 Axial slices at the level of the mental foramen, using the default mAs for each imaging protocol

3D Accuitomo 170, small volume   **3D Accuitomo 170, large volume**

CRANEX 3D, high resolution   **CRANEX 3D, low resolution**

SCANORA 3D, small volume   **SCANORA 3D, large volume**

GALILEOS Comfort
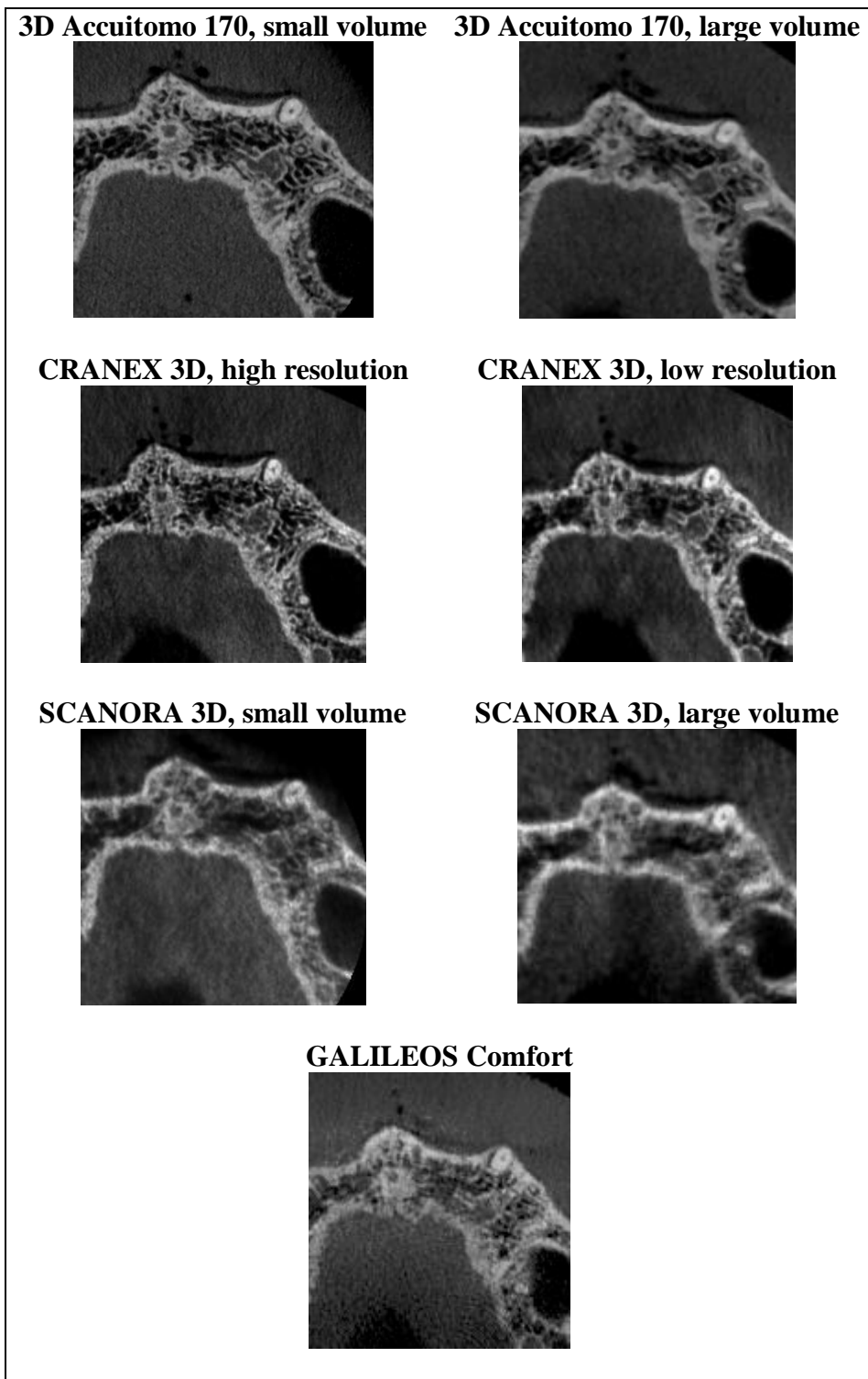
Figure 12.4 Axial slices at the level of the maxillary bone and sinus, using the default mAs for each imaging protocol
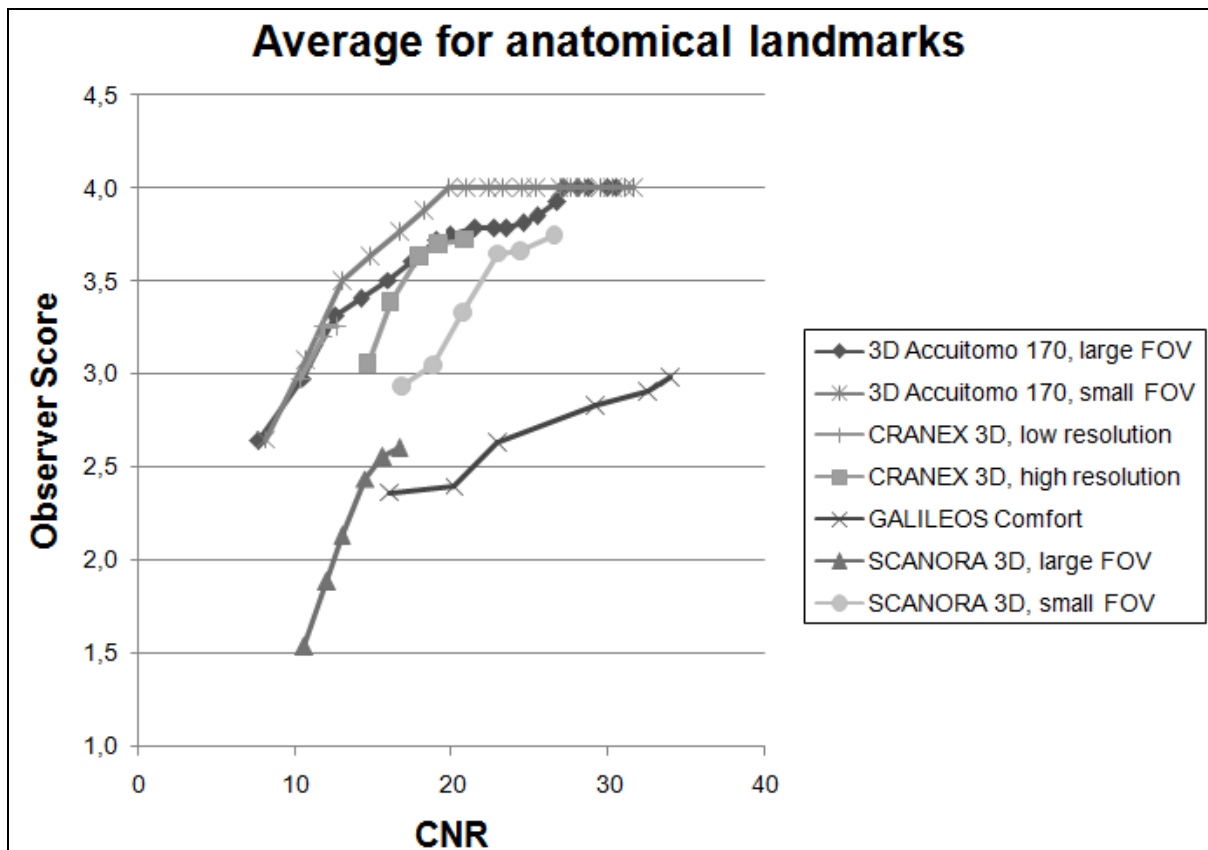
Figure 12.5 Relation between CNR and average score for all anatomical landmarks

Table 12.4 Difference between mandibular and maxillary scores. Positive values denote a higher score for mandible

CBCT device and protocol	Cortical bone	Trabecular bone	PDL space	Lamina dura	Pulp canal
3D Accuitomo 170, large FOV	0.27	-0.15	-0.01	0.07	0
3D Accuitomo 170, small FOV	0	0.04	0	0	0
CRANEX 3D, low resolution	0.05	0.05	0	0.03	0.01
CRANEX 3D, high resolution	0.15	0.03	0.00	0	0.09
GALILEOS Comfort	0.45	0.18	0.08	0.08	0
SCANORA 3D, large FOV	0.31	0.06	0.01	0.01	0
SCANORA 3D, small FOV	0.09	0.10	0.03	0.03	0
Average	0.19	0.04	0.02	0.03	0.01

PDL periodontal ligament
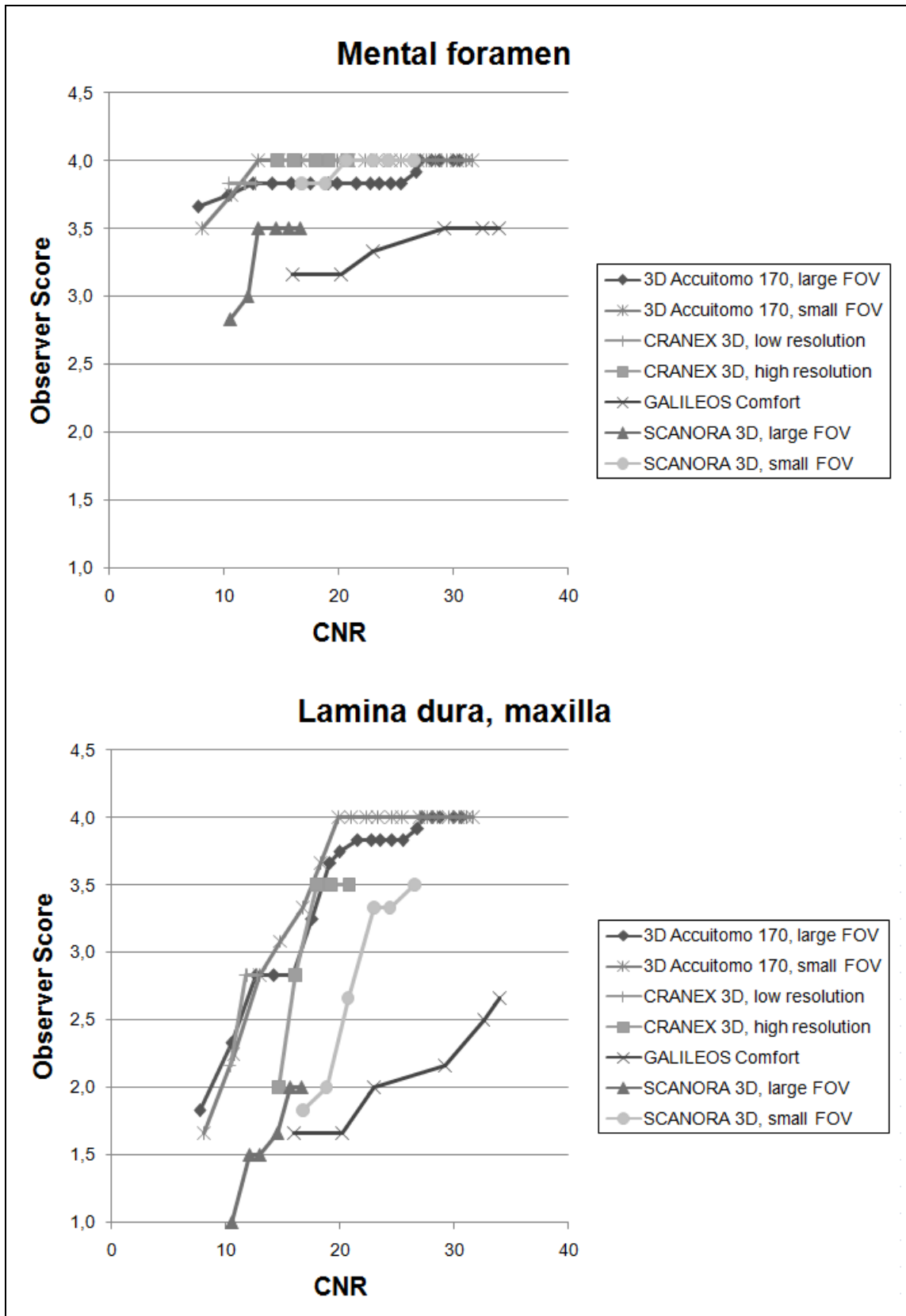
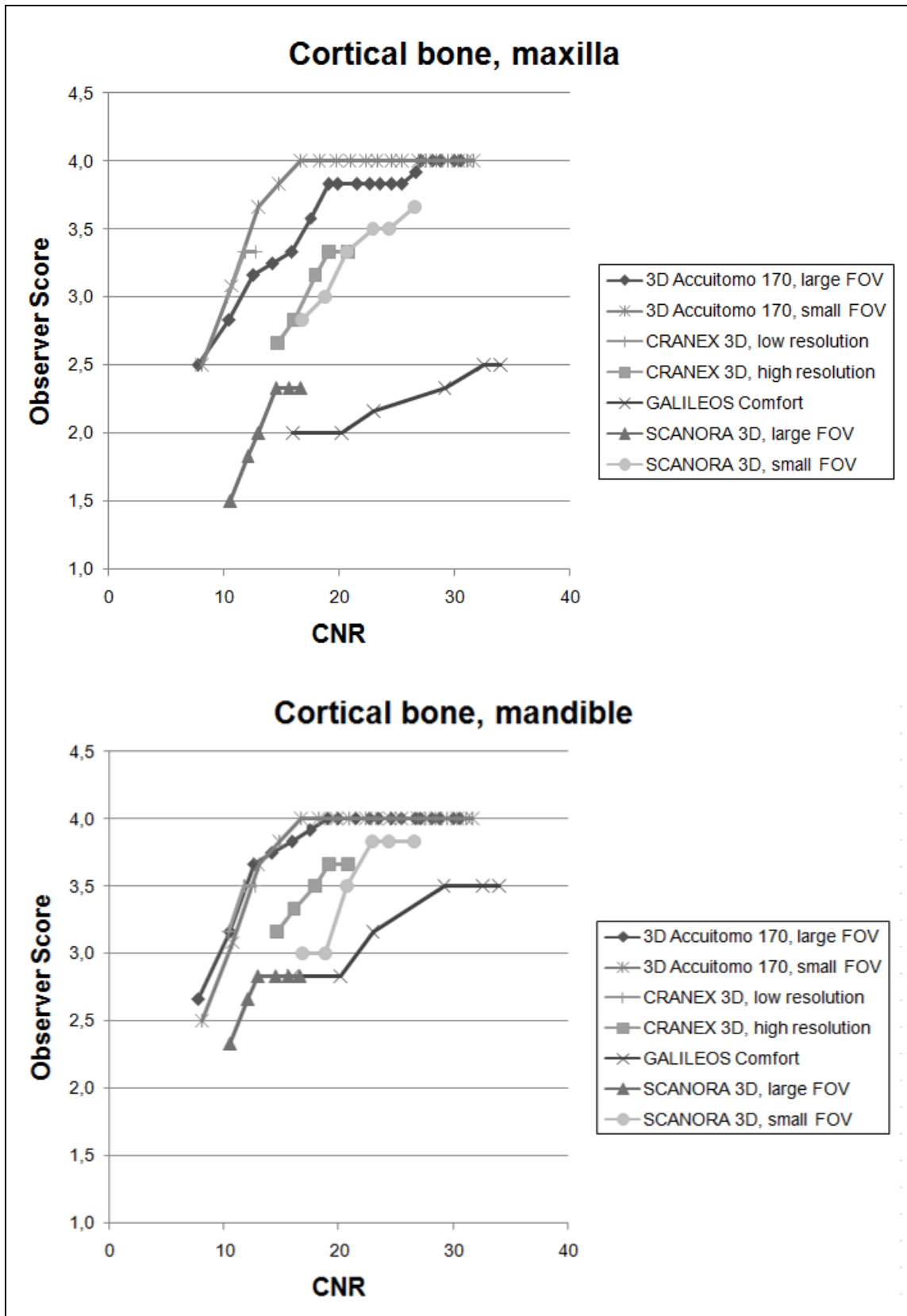**Figure 12.6** Relation between CNR and score for mental foramen and maxillary lamina dura

Figure 12.7 Relation between CNR and score for cortical bone, maxilla and mandible

Figure 12.8 shows the scores for the three clinical indications. Similar to the anatomical landmarks, a score of 2.5 corresponds to the threshold between an image that is suitable for the given clinical indication, and one that is not.
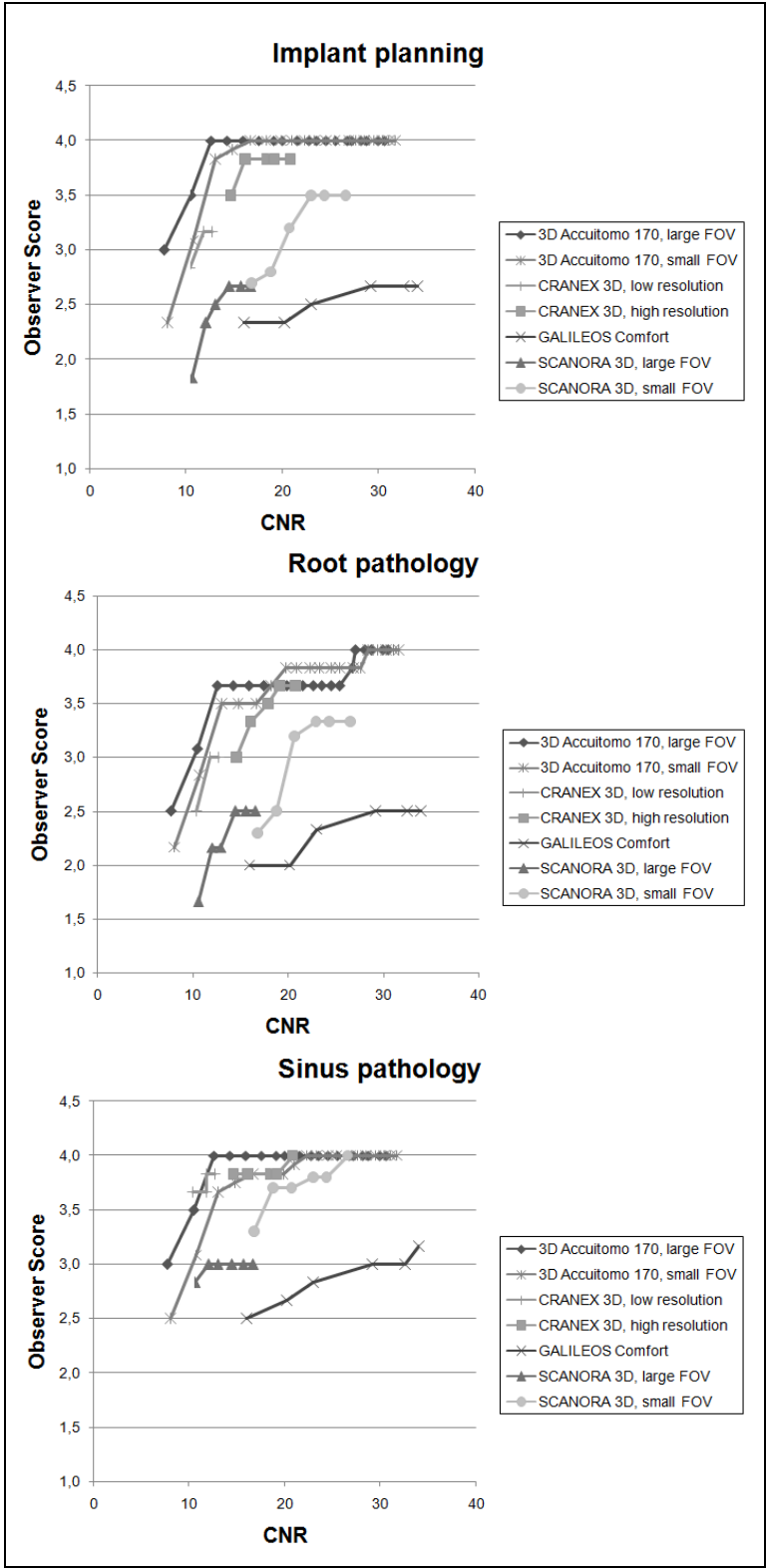

Figure 12.8 CNR versus observer scores for three clinical indications

Table 12.5 shows observer scores for all anatomical parameters. For all seven exposure protocols, the minimum and maximum score (*i.e.* scores for the lowest and highest mAs, respectively) for the fifteen anatomical landmarks is provided. Table 12.6 contains the minimal mAs level for which the scores for the three clinical indications was above the 2.5 threshold, as well as the corresponding CNR value. Also included in Table 12.6 is the minimal mAs value for which the score was 3 or more for each observer for the three clinical indications, and the corresponding CNR level. For three imaging protocols, there was no mAs for which all observers scored the images 3 or more for any of the clinical applications. For another protocol, this was the case for 'implant planning'. For the two acceptability criteria (*i.e.* average score >2.5 or all observers scoring minimum 3), a wide range is seen for the minimal mAs value, mainly due to the high mAs for CRANEX 3D high resolution protocol. For this protocol, amongst others, the lowest selectable mAs value was deemed acceptable for the 'average score' criterion and for the 'minimum score, sinus' criterion, indicating that it could be possible to reduce the exposure beyond the selectable range. A similar range is seen for the CNR values corresponding to these minimal mAs values. This is due to the disproportionally high CNR for the GALILEOS Comfort and SCANORA 3D large FOV, as demonstrated in the figures above.

12.5 Discussion

Translating technical image quality parameters to diagnostic image quality has been a long-time challenge for all medical imaging modalities. Given the wide exposure range in dental CBCT imaging and the interpretation of the patient scan by readers with varying academic backgrounds (general dentists, specialized dentists, oral and head and neck radiologists), it is pivotal that reference levels for image quality are proposed. Ideally, the image quality parameter or figure of merit used for this reference level can be routinely and reproducibly measured using tools that are available for manufacturers, medical physics experts and CBCT operators. In this pilot study, the relation between CNR and diagnostic image quality is investigated. CNR was selected as a technical image quality parameter as it can be measured in a straightforward fashion, shows a distinct relationship with tube output (mAs) and can be directly interpreted [15-16]. For the evaluation of diagnostic image quality at corresponding exposure levels, ten anatomical landmarks were included with varying relevance for the different dental CBCT applications. In addition, the applicability of the images for three dental applications with ranging image quality requirements was assessed.

Table 12.5 Observer scores for anatomical parameters

CBCT device and protocol	Mandibular symphisis		Mental foramen		Cortical bone M		Cortical bone m		Trabecular bone M		Trabecular bone m		Pulp canal M		Pulp canal m	
	Min	Max	Min	Max	Min	Max	Min	Max	Min	Max	Min	Max	Min	Max	Min	Max
3D Accuitomo 170, large FOV	2.8	3.8	3.7	3.8	2.5	3.8	2.7	4.0	2.5	4.0	2.5	3.8	2.5	3.8	2.5	3.8
3D Accuitomo 170, small FOV	3.2	4.0	3.5	4.0	2.5	4.0	2.5	4.0	1.8	4.0	2.2	4.0	2.5	4.0	2.5	4.0
CRANEX 3D, low resolution	2.2	2.5	3.8	3.8	3.0	3.3	3.2	3.5	3.0	3.2	3.2	3.3	3.0	3.2	3.2	3.2
CRANEX 3D, high resolution	3.2	3.7	4.0	4.0	2.7	3.3	3.2	3.7	3.0	3.8	3.2	3.8	3.2	3.5	3.3	3.7
GALILEOS Comfort	1.7	2.2	3.2	3.5	2.0	2.5	2.8	3.5	2.0	2.3	2.2	3.0	2.3	3.2	2.3	3.2
SCANORA 3D, large FOV	1.3	2.2	2.8	3.5	1.5	2.3	2.3	2.8	1.3	2.5	1.7	2.5	1.5	2.7	1.5	2.7
SCANORA 3D, small FOV	3.5	4.0	3.8	4.0	2.8	3.7	3.0	3.8	2.5	3.3	2.7	3.5	2.8	3.7	2.8	3.7

	Enamel		Maxillary suture		Incisive foramen		PDL space M		PDL space m		Lamina dura M		Lamina dura m	
	Min	Max	Min	Max	Min	Max	Min	Max	Min	Max	Min	Max	Min	Max
3D Accuitomo 170, large FOV	2.7	3.8	2.8	4.0	3.2	3.8	1.7	3.7	1.8	3.7	1.8	3.8	2.0	3.8
3D Accuitomo 170, small FOV	3.0	4.0	3.2	4.0	3.0	4.0	2.0	4.0	2.0	4.0	1.7	4.0	1.7	4.0
CRANEX 3D, low resolution	3.5	3.8	3.0	3.0	3.5	3.7	2.3	3.0	2.3	3.0	2.2	2.8	2.2	3.0
CRANEX 3D, high resolution	2.5	3.3	3.8	4.0	3.8	4.0	2.0	3.8	2.0	3.8	2.0	3.5	2.0	3.5
GALILEOS Comfort	2.5	2.8	3.0	3.7	2.8	3.5	1.8	2.5	2.0	2.7	1.7	2.7	1.8	2.8
SCANORA 3D, large FOV	1.2	2.7	1.0	3.0	1.8	2.8	1.2	2.2	1.3	2.2	1.0	2.0	1.2	2.0
SCANORA 3D, small FOV	2.5	3.8	3.7	4.0	3.7	4.0	1.8	3.3	2.0	3.3	1.8	3.5	2.0	3.5

M maxilla, *m* mandible, *PDL* periodontal ligament

Table 12.6 Minimal mAs & CNR values for which average or minimum scores were above acceptable threshold

CBCT	Average scores greater than 2.5						All observers scored 3 or more					
	Implant		Root		Sinus		Implant		Root		Sinus	
	mAs	CNR	mAs	CNR	mAs	CNR	mAs	CNR	mAs	CNR	mAs	CNR
3D Accuitomo 170 large FOV	18*	7.7	18*	7.7	18*	7.7	35	12.6	35	12.6	35	12.6
3D Accuitomo 170 small FOV	18*	7.7	26	10.7	18*	7.7	35	13.0	35	13.0	35	13.0
CRANEX 3D low resolution	29*	10.4	29*	10.4	29*	10.4	/	/	39	11.8	29*	10.4
CRANEX 3D high resolution	56*	14.6	56*	14.6	56*	14.6	70	16.1	69	16.1	56*	14.6
GALILEOS Comfort	21	23.0	28	29.2	10	16.0	/	/	/	/	/	/
SCANORA 3D large FOV	14	13.0	18	14.5	9*	10.6	/	/	/	/	/	/
SCANORA 3D small FOV	12*	16.8	15	18.8	12*	16.8	24	23.0	19	20.7	12*	16.8
Average	24	13.3	27	15.1	22	12.0	41	16.2	39	14.8	34	13.5
Standard deviation	15	5.5	14	7.2	16	3.8	20	4.8	18	3.7	16	2.4

*Lowest selectable mAs value for this protocol

A variety of anatomical parameters with ranging requirements in terms of image quality was selected. Furthermore, the suitability of the images for three clinical indications was evaluated. The investigated anatomical and clinical parameters provide a cross-section of the varying criteria for image quality for the different potential applications of CBCT in dentistry.

The main objective of this study was to investigate the relationship between technical and anatomical parameters; a secondary objective was to provide preliminary reference values for diagnostic use of CBCT. It was seen that the CNR, although clearly related to the observer scores, cannot provide a stable quantitative relation with the diagnostic suitability of an image. Figure 12.2 shows that the relationship between CNR and mAs, the latter being a fundamental exposure parameter, varies between devices. Although the peak voltage (kVp) was similar for all devices, variety in the ratio CNR/mAs can be caused by an interplay of other exposure factors (*e.g.* filtration, FOV size) and reconstruction. The relatively high CNR values for the SCANORA 3D may be caused by the use of an iterative reconstruction technique, although this was certainly not reflected in the observer scores. The GALILEOS Comfort's high CNR/mAs values will be primarily caused by processing during

reconstruction, as this device used an image intensifier as detector which is associated with higher noise levels than flat panel detectors [17].

The relationship between CNR and observer scores was reasonably consistent between the 3D Accuitomo 170 and CRANEX 3D. For the SCANORA 3D and GALILEOS Comfort, observer scores were lower than predicted by the CNR. The most important factor which caused this discrepancy is the spatial resolution. As revealed in a post-hoc discussion with the observers, lower scores for these devices were primarily caused by an inferior sharpness compared to the other image series. In addition, GALILEOS Comfort images were disturbed by artefactual streaks and dots, as seen in the lingual soft tissue in Figure 12.4. The CNR calculation did take the spatial resolution into account to some extent, by correcting the noise values in function of the voxel size. However, this correction did not properly represent the effect of the spatial resolution. Furthermore, as seen in Chapter 9, the voxel size does not always reflect the actual spatial resolution of an image. This is confirmed in the current study, as the two FOV protocols of the 3D Accuitomo 170 received similar scores despite a two-fold difference in voxel size. A similar finding was seen for the CRANEX 3D.

Due to the variety of hardware and software factors that influence image quality in CBCT, the ideal way of relating technical and diagnostic image quality may be to use a multi-predictor model which is tailored to each diagnostic application. The interplay between spatial resolution, contrast resolution, noise and even artefacts will affect the suitability of the image for different applications. To define this model, two challenges need to be addressed. A first one is to determine suitable technical parameters. The CNR used in this study, corrected for voxel size, provides an appropriate estimation of contrast resolution versus image homogeneity, although the exact correction factor for noise could be further investigated. For spatial resolution, PSF and line spread function (LSF) are suitable candidates, from which the full width at half maximum (FWHM) value could be derived, or a transformation to the modulation transfer function (MTF) could be calculated.

The remaining challenge is then to investigate to what extent each technical parameter influences diagnostic image quality for varying applications. This step, as seen in this study, always contains a degree of subjectivity because of the involvement of observers. Although the current (pilot) study used a sound approach for the observation, we believe that the currently investigated topic should be addressed on a much wider scale. Six experienced oral radiologists were included in this study, and the scoring system was more or less straightforward. Still, kappa values for inter-observer agreement were clearly lower than those for the visual analysis of line pair and rod patterns in Chapter 9, although higher than those in

certain studies on diagnostic image quality in CBCT [11-14]. Naturally, each radiologist has their own point of view on the constitution of an acceptable image. The only way to solve this is to include a much larger group of observers. Current literature on observer studies shows that in many cases a few observers are used, which could be acceptable for studies involving measurements. However, in order to determine definitive thresholds between acceptable and unacceptable image quality, a large enough sample of observers taken from the entire population of CBCT users is needed. Thresholds can then be determined in different ways, as demonstrated in Table 12.6. It can be defined as the dose level for which the average observer score is above a predetermined threshold value or as the level for which there was a (100%, 90% …) consensus between observers regarding acceptability, with the latter criterion being stricter. The resulting dose levels can then be correlated to the technical image quality, allowing for the predictive model to be fine-tuned as more and more CBCT devices are included.

The current results allow for the definition of preliminary threshold values for CNR which can be used as a starting point for future investigations. Similarly, it could be possible to suggest reference values for mAs, but it should be considered that this type of reference value may vary considerably if the X-ray spectrum is different from the CBCT devices in this study. Still, the minimal mAs values from Table 12.6 are generally well below the default clinical setting, indicating that it may be possible to reduce doses considerably for certain patient groups, taking into account that the image quality for actual patients can depend on the patient (*e.g.* patient size, presence of metals, patient motion). The CNR threshold values in Table 12.6 depended on the clinical indication, although they did not always differ between implant planning, sinus pathology and root pathology. Furthermore, values depended on the criterion, as the value corresponding to an observer score of 3 or more was usually, but not always, higher than the value corresponding to an average score above 2.5. For all CBCT devices, the lowest CNR values corresponding to an acceptable image quality for implant/root/sinus were 7.7 for the first criterion and 12.6/11.8/10.4 for the second. When comparing these values to the CNR_{AIR} measurements in Chapter 10 (Table 10.1), out of 30 investigated CBCT protocols, 8 were below the 7.7 threshold and 10 below the 12.6/11.8/10.4 threshold, indicating that their performance in terms of contrast is below the preliminary reference level found in this study. From another point of view, it can be seen that many exposure protocols resulted in a CNR_{AIR} well above these reference values, with 10 protocols having a CNR of 20 or more. As seen from the GALILEOS Comfort and SCANORA 3D results in the current study, this does not necessarily imply that the exposure levels for these

protocols from Chapter 10 can be lowered considerably; as it was shown that the CNR can overestimate the diagnostic image quality, the reference values proposed above can only be considered as 'preliminary minimally achievable values'; it is not yet feasible to determine (maximal) values or ranges for CNR above which the exposure should be lowered.

In current clinical practice, the choice of exposure levels is still partly manufacturer-driven and partly determined by the personal experience of the CBCT user. The manufacturer always provides the user with one or more default exposure protocols. In addition, as the user gathers experience with the different selectable exposure levels, he can fine-tune exposures for different patient groups. In both cases, the adherence to the ALARA principle of dose optimisation is left to the expertise and benevolence of two parties that are generally not overly concerned with dose reduction. The current study is a first step in changing this practice; the definition of standardized objective image quality criteria for CBCT can guide all parties involved in CBCT imaging (*i.e.* users, manufacturers, medical physicist) to achieve minimal exposure levels in all circumstances.

12.6 Conclusion

The relationship between technical image quality, measured as the CNR_{AIR} corrected for voxel size, and the diagnostic image quality, measured as observer scores for anatomical landmarks and three clinical indications, was investigated. Although the mAs showed a fair correlation with the observer scores, the relation with the CNR was specific for each device. A multi-predictor model including both spatial resolution and contrast resolution may provide objective criteria for image quality which are reproducible between devices.

The current results indicate that it could be possible to reduce exposure levels below the manufacturer's recommended setting for certain patient groups.

12.7 References

1. Liang X, Jacobs R, Hassan B, Li L, Pauwels R, Corpas L, Souza PC, Martens W, Shahbazian M, Alonso A, Lambrichts I. A comparative evaluation of Cone Beam Computed Tomography (CBCT) and Multi-Slice CT (MSCT) Part I. On subjective image quality. Eur J Radiol 2010; 75: 265-269.

2. Park YS, Ahn JS, Kwon HB, Lee SP. Current status of dental caries diagnosis using cone beam computed tomography. Imaging Sci Dent 2011; 41: 43-51.

3. Vandenberghe B, Jacobs R, Yang J. Detection of periodontal bone loss using digital intraoral and cone beam computed tomography images: an in vitro assessment of bony and/or infrabony defects. Dentomaxillofac Radiol 2008; 37: 252-260.

4. Esposito S, Cardaropoli M, Cotti E. A suggested technique for the application of the cone beam computed tomography periapical index. Dentomaxillofac Radiol 2011; 40: 506-512.

5. Liang X, Lambrichts I, Sun Y, Denis K, Hassan B, Li L, Pauwels R, Jacobs R. A comparative evaluation of Cone Beam Computed Tomography (CBCT) and Multi-Slice CT (MSCT). Part II: On 3D model accuracy. Eur J Radiol 2010; 75: 270-274.

6. Loubele M, Maes F, Schutyser F, Marchal G, Jacobs R, Suetens P. Assessment of bone segmentation quality of cone-beam CT versus multislice spiral CT: a pilot study. Oral Surg Oral Med Oral Pathol Oral Radiol Endod 2006; 102: 225-234.

7. Watanabe H, Honda E, Kurabayashi T. Modulation transfer function evaluation of cone beam computed tomography for dental use with the oversampling method. Dentomaxillofac Radiol 2010; 39: 28-32.

8. Vassileva J, Stoyanov D. Quality control and patient dosimetry in dental cone beam CT. Radiat Prot Dosimetry 2010; 139: 310-312.

9. Bryant JA, Drage NA, Richmond S. Study of the scan uniformity from an i-CAT cone beam computed tomography dental imaging system. Dentomaxillofac Radiol 2008; 37: 365-374.

10. Jessen KA. The quality criteria concept: an introduction and overview. Radiat Prot Dosimetry 2001; 94: 29-32.

11. Alqerban A, Jacobs R, Fieuws S, Willems G. Comparison of two cone beam computed tomographic systems versus panoramic imaging for localization of impacted maxillary canines and detection of root resorption. Eur J Orthod 2011; 33: 93-102.

12. Hashimoto K, Kawashima S, Kameoka S, Akiyama Y, Honjoya T, Ejima K, *et al*. Comparison of image validity between cone beam computed tomography for dental use and multidetector row helical computed tomography. Dentomaxillofac Radiol 2007; 36: 465-471.

13. Soğur E, Baksi BG, Gröndahl HG. Imaging of root canal fillings: a comparison of subjective image quality between limited cone-beam CT, storage phosphor and film radiography. Int Endod J 2007; 40: 179-185.

14. Hashimoto K, Arai Y, Iwai K, Araki M, Kawashima S, Terakado M. A comparison of a new limited cone beam computed tomography machine for dental use with a multidetector row helical CT machine. Oral Surg Oral Med Oral Pathol Oral Radiol Endod 2003; 95: 371-377.

15. Funama Y, Sugaya Y, Miyazaki O, Utsunomiya D, Yamashita Y, Awai K. Automatic exposure control at MDCT based on the contrast-to-noise ratio: Theoretical background and phantom study. Phys Med 2011. Epub ahead of print.

16. Muhogora WE, Devetti A, Padovani R, Msaki P, Bonutti F. Application of European protocol in the evaluation of contrast-to-noise ratio and mean glandular dose for two digital mammography systems. Radiat Prot Dosimetry 2008; 129: 231-236.

17. Baba R, Ueda K, Okabe M. Using a flat-panel detector in high resolution cone beam CT for dental imaging. Dentomaxillofac Radiol 2004; 33: 285-290.

General discussion and conclusions

The present thesis addresses the optimisation of CBCT in dentistry using different approaches. Optimisation of an X-ray imaging modality implies that there is an optimal balance between image quality and radiation dose. Apart from the first principle of justification, one of the key principles in radiation protection is ALARA, stating that the radiation exposure should be "As Low As Reasonably Achievable", balancing the benefit of the exposure with its detrimental effects. In radiography, this benefit is reflected as an improvement in diagnosis and/or treatment planning of the patient, owing to the additional information obtained from the radiological examination.

As is the case for other medical (and non-medical) procedures, a cost-benefit analysis can be applied to medical imaging to determine the current performance level and different approaches for optimisation. In X-ray imaging, the cost is represented as the stochastic risk for radiation-induced effects, although deterministic effects (*e.g.* eye lens) cannot be completely ignored for certain medical exposures. The benefit to the patient is reflected as an improvement in diagnosis and treatment planning, the detection of potential medical risks for a fraction of preselected patient subsets (*i.e.* screening), and the short- or long-term follow-up of treatment. Others potential patient benefits are improvements in patient comfort (*e.g.* shorter visit time, reducing invasiveness of diagnosis and treatment) and reduction of total cost. It can be seen that a risk-benefit analysis is typically performed on the population level, enabling justification and optimisation of patient doses on an individual level.

Applying the ALARA principle to dental CBCT imaging is not straightforward. The main issue is that CBCT is applied to a wide range of patient subsets. Different age groups undergo CBCT imaging, ranging from young children to adolescents and adults. Furthermore, certain clinical indications comprise different requirements in terms of field size and image quality than others. Before the start of the SEDENTEXCT project, which encompasses the work in this thesis, there were no guidelines on the appropriate use of CBCT in dental practice. Furthermore, there were no standardized tools available for quality control of CBCT devices, making it difficult to evaluate and inter-compare existing studies on CBCT image quality and dose. In this doctoral project, a wide-scale assessment of CBCT devices was worked out to evaluate the range in performance in terms of image quality and radiation dose,

and to enable the development of tools for practical image quality and radiation dose assessment.

In this general discussion, an extensive summary is given of the various chapters in this thesis. The different hypotheses which were proposed in the Introduction & Hypotheses section are discussed. Finally, the impact of the current results on CBCT optimisation on various levels, including current clinical practice, is described.

Overview of thesis contributions

Patient radiation dose in CBCT

Various topics regarding patient exposure were addressed in this thesis. The organ and effective dose was estimated in *Chapters 1-3* using anthropomorphic phantoms, involving a variety of CBCT devices and protocols. A thorough evaluation was performed using a large number of TLDs distributed in the head and neck, in order to accurately estimate the total absorbed dose to each organ of interest. The effective dose range in CBCT for an average adult was evaluated in *Chapter 1*. The general effect of FOV sizes was highlighted by grouping the exposure protocols by FOV size. In addition, the relative contribution of the various radiosensitive organs to the effective dose was studied, providing insights on the potential for dose reduction. Apart from FOV reduction, which has been further investigated in *Chapter 3*, *Chapter 1* also shows the importance of FOV positioning, as lower jaw exposures resulted in an increased dose compared with identical exposures at the level of the upper jaw due to an increase in thyroid dose. It should be noted that higher exposures are achievable in clinical practice, as seen in literature. Furthermore, very low doses have been reported in various studies, and it is indeed possible to reach doses as low as dose for panoramic radiography using small-FOV CBCT.

Chapter 2 focuses on the paediatric applications of CBCT by estimating organ and effective doses for two paediatric phantoms. Anthropomorphic phantoms representing a 10 year old and female were used, the latter representing an adolescent as its size is similar to an average 15 year old. Doses for various CBCT systems were investigated and compared to dose of panoramic and cephalometric radiography and MSCT. There are various factors involved in the comparison between adult and paediatric doses:

- For identical exposures, the total radiation energy which is deposited will be higher for patients with large size and mass as they will absorb a larger fraction of the beam. This

implies that larger patients should be imaged with an increased tube output to obtain an identical detector signal compared with small patients.

- The relative dose for identical beams, however, will be higher for children than for adults, as a proportionally larger portion of the head will be exposed.
- The risk for stochastic effects from radiation is age-dependent. Although *Chapter 2* contains pure dose measurements, the effect of this age-dependent risk factor is demonstrated in *Chapter 6.*

From the organ and effective doses in *Chapter 2,* it can be seen that for most devices, effective dose levels as estimated from paediatric phantoms can be kept at the same level as that of adult phantoms, as it is typically possible to manually reduce the exposure or apply preset paediatric exposure protocols. Still, dose reduction in CBCT remains pivotal for paediatric patients in particular, because of their higher sensitivity to radiation combined with a larger time window for expressing stochastic effects.

A final anthropomorphic phantom study was reported in *Chapter 3*, focusing on a single CBCT device which allows for the selection of FOV sizes between 4x4 cm and 17x12 cm, as well as the possibility of a 180° rotation with reduced acquisition and exposure time. Using a selection of clinically relevant exposure protocols, the effect of FOV reduction and 180 scanning could be singled out. The effect of FOV size on effective dose was confirmed and quantified, showing that the relation between them is not so straightforward. As the FOV height in CBCT affects the effective dose more than the FOV diameter, there is no straightforward correlation between the actual volume size (*i.e.* volume of the reconstructed cylinder) and the effective dose; a volumetric parameter expressed as $\log(\text{diameter x height}^2)$ showed a linear correlation with the effective dose. Regarding the dose of a 180° rotation protocol compared to a full rotation, it was seen that an average effective dose reduction of 36% could be achieved when the tube moves at the posterior side of the phantom. This would imply that an even higher dose reduction could be possible when the tube would move at the anterior side (Figure D.1). This warrants further investigation, although the difference in image quality for anterior or posterior rotation arcs should also be taken into account.
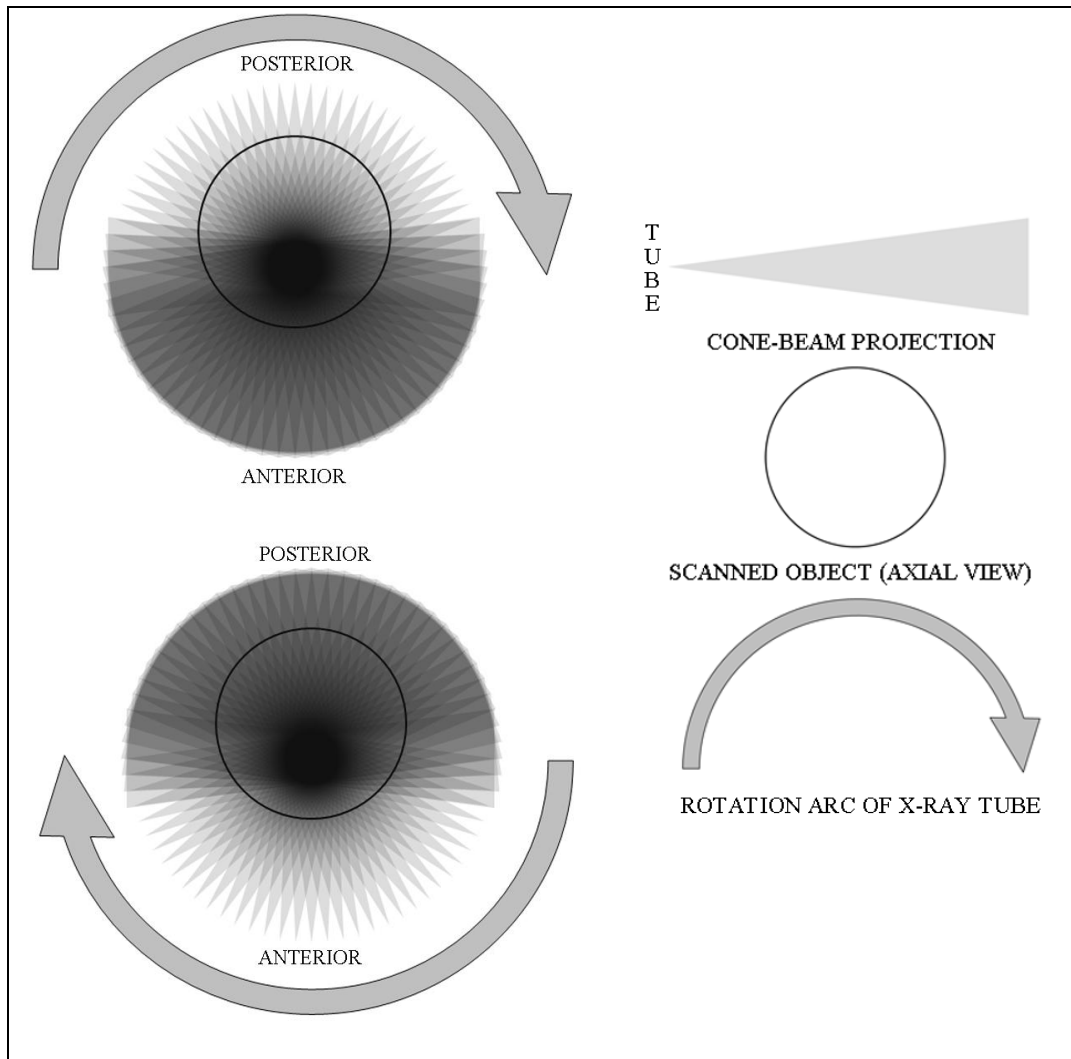
Figure D.1 Area exposed by primary beam during 180° scanning. Left: tube passes at posterior side. Right: tube passes at anterior side. FOV is positioned at the anterior side of the object (dark circle). Although this illustration does not take beam attenuation or beam hardening into account, it shows that the anterior portion of the human head (containing the largest fraction of radiosensitive tissues) is inside the primary beam for a larger portion of the rotation arc when the tube moves posterior. This effect, together with beam hardening, partly compensates the higher attenuation at the 'tube side' of the object.

An additional advantage of a 180° scan is the reduction in acquisition time. Most CBCT are reconstructed at a high spatial resolution, any slight movement (*i.e.* translation or rotation of the head or parts thereof, tremor) during the acquisition will result in motion blur or motion artefacts. In addition, most CBCT devices use seated or standing positioning with limited head fixation, and scan times are generally long, averaging at ~20 s. For young children, old patients, patient with mental handicap or severe discomfort, a reduction in scan time to 10 s or less would be of particular interest, reducing the risk for a retake due to patient motion.

The results of the anthropomorphic doses provided input for *Chapter 4*, in which an *in vivo* dosimetric experiment was set up. 269 patients were recruited, covering a wide range in age, size, mass, and a variety of clinical indications. Skin dose was measured during CBCT scanning using TLDs attached at various locations throughout the face and neck. Using the organ and effective dose measurements from *Chapters 1 and 3*, conversion factors from skin to organ dose were calculated. In addition, the BEIR VII model for dose-risk estimation in function of age at exposure was applied. This allowed for the calculation of an individual lifetime attributable cancer risk for each patient. It can be seen that the risk values can be very low for older patients, as they are less sensitive to radiation-induced stochastic effects. The risk increases exponentially at young ages, with a 36-fold risk ratio between the highest and lowest patient risk found in our study. The risk estimations in *Chapter 4*, alongside the paediatric phantom measurements in *Chapter 2*, fill in an important gap in CBCT literature, as the increased need for dose reduction for children was severely underreported. As CBCT is generally reported by manufacturers and researchers as a 'low dose' modality, it is now routinely applied to a variety of paediatric patients instead of (or in addition to) 2-D radiographs, leading to an important increase in radiation dose for the paediatric population. The present results indicate that the age of the patient should always be taken into account by both the referrer and the operator, with a need for careful justification and maximal optimisation for young children.

A final dosimetric topic which was addressed was the use of a suitable dose index for dental CBCT. A two-part study was set up to determine the dose distribution for various CBCT exposure geometries (*Chapter 5*), and to define and validate a dose index (*Chapter 6*). Although previous studies have brought up the issue of using a dose index in dental CBCT, there had been no wide scale evaluation of the influence of the different exposure factors on the dose distribution: FOV diameter and height, position, rotation arc … Measurements in homogeneous cylindrical water and PMMA phantoms provided valuable insights regarding scatter tails and axial dose gradients with important implications regarding the proposal of a suitable dose index for CBCT:

- Due to the varying beam heights in dental CBCT, it is inappropriate to use a 100 mm pencil ion chamber as a dosimetric tool. Because of increasing beam heights in MSCT, the $CTDI_{100}$ measured with a pencil chamber has been disputed (Dixon 2006). The use of an extended 300 mm ion chamber is not feasible for head phantoms; a dose index

based on phantom measurements should be performed with a small-volume ion chamber.

- Because of the sharp scatter tails and quasi-homogeneous dose distribution along the height of the primary beam, we have proposed to measure at strategic locations in the midaxial plane and apply a correction for beam height similar to the calculation of the Dose Length Product (DLP) in MSCT.

- The dose distribution in the axial plane can show sharp dose gradients because of small FOV diameter, off-axis FOV positioning or partial rotation. Next to this, we have observed that there is a general symmetry in dose distribution at both sides of the axis connecting isocentre and phantom centre.

Using this information, two candidate dose indices were defined, both measured in a homogeneous 16cm PMMA phantom with a small-volume ion chamber (*Chapter 6*). A first index was measured along the diameter of the phantom; the second index was a slightly adapted version of the $CTDI_w$. The indices were verified using a variety of exposure geometries, and preliminary conversion factors to effective dose were calculated using the measurements from *Chapter 3* as gold standard. It was found that both indices are suitable and can be converted to effective dose after applying correction factors for beam height, beam diameter and rotation arc. Even though Index 1, measured along the diameter of the phantom with the FOV being positioned according to the clinical situation, appears more sensible and relevant for dental CBCT, its values were similar to those of Index 2, which is measured like the $CTDI_w$ but using a ½ weighting for central and peripheral measurements instead of a one-third vs. two-thirds weighting used in MSCT. Although both indices are useful to measure CBCT exposures routinely, the added value of Index 1 is yet to be demonstrated.

The different dosimetric studies contributed, each in their own way, to the topic of optimisation which is discussed further below.

Image quality of CBCT

A vast amount of image quality evaluations of CBCT had been reported in literature. Although there have been many useful studies covering various image quality aspects, most of them contain important limitations, some of which were addressed in the present thesis project. First of all, many studies included only one or two CBCT device; any measurements or conclusions are therefore only applicable to the device in question. Many statements have been made regarding different image quality aspects of CBCT which are either under- or

overestimating the performance in CBCT, depending on the evaluated device in each particular study. In addition, comparisons with 2-D radiography and MSCT had been made which are limited in relevance because of the wide image quality range which can be expected in CBCT imaging, resembling the exposure range. In addition, many image quality studies used a suboptimal phantom set-up. Whether an anatomical (*e.g.* skull, jaw, teeth models) or a geometric (*e.g.* cylindrical) phantom is used, it is important that it represents the total attenuation of the human head, in order to obtain similar levels in detector flux and scatter compared to clinical scans. A final limitation seen in literature was the gap between diagnostic image quality studies, which are clinically relevant but always involve some degree of subjectivity, and technical image quality studies which may provide actual image quality quantification but are often difficult to translate to clinical practice.

To overcome these limitations, a three-part image quality evaluation was set up. First, a phantom with inserts for the analysis of different image quality parameters was developed. A preliminary evaluation was performed to verify the suitability of the phantom for dental CBCT (*Chapter 7*). Based on the initial findings, a series of improvements were implemented into the phantom and insert design. Using the second prototype phantom, a wide scale evaluation of CBCT image quality was performed, focusing on different image quality aspects (*Chapters 8-11*). The purpose of this evaluation was multifold:

- To evaluate of the suitability of the phantom and its inserts, and further improve its design.
- To determine the most suitable measurement methodology for certain image quality parameters.
- To determine the image quality performance range in current CBCT imaging.
- To verify different specific hypotheses regarding CBCT image quality (*e.g.* use of grey values for density estimations, reduction of metal artefacts through adjustment of exposure …).
- To compare CBCT and MSCT image quality.
- To investigate the use of image quality parameters in acceptance testing and quality control.
- To relate technical and diagnostic image quality.

Chapter 7 describes the development and evaluation of the first prototype of the image quality phantom. The phantom consisted of a head size PMMA cylinder with central and peripheral holes, allowing for the placement of small inserts for various types of image quality evaluations. A series of inserts was developed for the evaluation of spatial resolution, contrast resolution, noise, metal artefacts and grey value accuracy and stability. The first prototype was evaluated using seven CBCT devices. Reproducibility of image quality measurements was assessed, and the performance of the selected CBCT exposure protocols was evaluated for varying parameters, such as contrast-to-noise ratio (CNR), CT number correlation, noise, uniformity, artefact added value (AAV) and full width at half maximum (FWHM) of the point spread function (PSF). Although the phantom proved to be useful for image quality evaluation, a series of improvements were implemented into the second prototype. In addition, for certain image quality parameters the measurement methodology was adapted:

- A homogeneous PMMA section was included at the bottom of the phantom, allowing for the analysis of noise and uniformity without the need for 'blank' PMMA inserts (*Chapter 10*).

- In addition to the metal artefact insert containing titanium rods, a second insert with lead rods was manufactured. The measurement of the metal artefact parameter was changed; the standard deviation was measured in the entire insert area excluding the rods, and normalised in two steps to a percentage (*Chapter 8*)(Figure D.2).

- Apart from using a correlation coefficient to evaluate the use of CBCT grey values for density estimations, a recalibration of the grey values was performed allowing for the calculation of the absolute grey value error in the medium density range (*Chapter 11*)

- Five additional inserts were included, containing the same materials as the five inserts used for CNR and CT number evaluation, but using pentagonal pattern with rods of varying diameters allowing for a visual check of contrast detail (*Chapter 9*).

- A line pair insert containing alternating aluminium and polymer sheets was included (*Chapter 9*).

The second prototype phantom was evaluated using 13 CBCT devices and 1 MSCT device, including a total of 32 exposure protocols. This allowed not only for a wide scale evaluation of the phantom, but served as a cross-sectional study describing the performance of current-generation CBCTs.
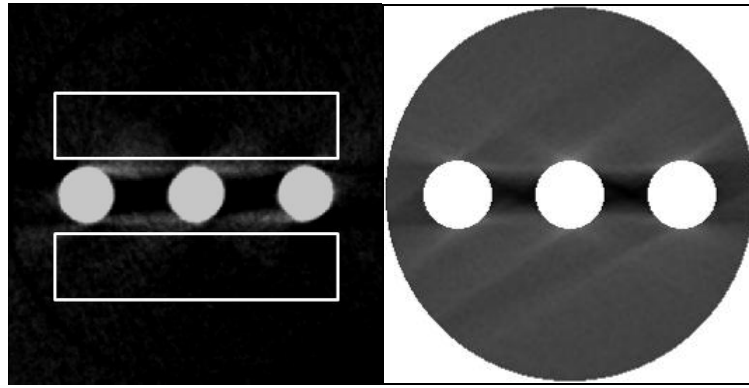
Figure D.2 Two measurement methodologies for the quantification of metal artefacts. Left: AAV measured after subtraction of PMMA grey value (*Chapter 7*). Right: ROI for SD measurement (*Chapter 8*). The right ROI (*i.e. a*ll non-white pixels) covers the entire insert region with the exception of the metal rods, whereas the ROI on the left is limited to two rectangular areas adjacent to the rods.

Chapter 8 focused on the quantification of metal artefacts on CBCT datasets. The evaluation method in *Chapter 7* had shown the net increase in grey values in the vicinity of the metal objects due to bright streaks, but had not provided a complete assessment of the entire region. A new figure of merit was introduced, measuring the standard deviation (SD) of voxel values in the entire insert region (exc. the metal rods). This provided a general estimate of the effect of the artefact, as the value is influenced by the severity of the white streaks, the darkened areas surrounding the inserts, and the black areas between the rods. To allow for a comparison between images with varying grey value ranges, the SD was normalised to a 12 bit value. A second conversion was performed to allow for a more straightforward interpretation of the artefact value, by expressing it as the percentage of the maximum SD for 12 bit images. The resulting parameter allowed for the comparison of artefacts from different CBCT and MSCT devices and exposure protocols, leading to valuable insights on artefact induction and reduction. It was seen that artefact values, while differing between devices and between FOV sizes from the same device, were relatively unaffected by the exposure level. Although an increased number of projection or a higher beam energy or tube output will certainly affect the artefact to some extent, it is not justified to increase the exposure for the sole purpose of reducing artefacts, as the increase in radiation dose is disproportional to the slight improvement in artefact quality.

Visual inspection of image quality using line pair and rod inserts is described in *Chapter 9*. Although the scores of the line pair insert were primary affected by spatial resolution and those of the rod insert by contrast resolution, images from both inserts were affected by a combination of spatial resolution, contrast resolution and noise. When ranking the included

devices by score, it could be seen that the MSCT protocols were at the bottom end for the line pair insert but at the top end for the rod insert, confirming the hypothesis that CBCT images are generally sharper, but poorer in contrast than MSCT images. All rods for air and aluminium could be detected for all included CBCT and MSCT protocols, and the only distinction between them was on the visibility of the hydroxyapatite rods. Furthermore, the line pair insert results revealed that the voxel size can be a bottleneck in CBCT imaging, as it was seen that voxel sizes in certain protocols do not correspond to the actual spatial resolution of the image. The manufacturer's choice of reducing reconstruction time and DICOM file size by increasing the voxel size does not adhere to the optimisation principle.

Chapter 10 included the measurement of CNR, noise and uniformity. An important limitation to the use of noise as a quantitative parameter is that it is affected by the reconstructed voxel size, which ranges between 0.08 mm and 0.5 mm in dental CBCT. The effect of image noise, expressed as the standard deviation of grey values within a homogeneous material, on general image quality is therefore difficult to quantify. Different strategies were explored to correct noise values based on the voxel size. Noise was simulated on a 2-D grey image, which was resampled using a wide range of pixel sizes. Next, CBCT images containing homogeneous PMMA were resampled at various voxel sizes. Finally, raw CBCT data was reconstructed at various voxel sizes. For all images, the relation between voxel (or pixel) size and noise was assessed, and the most appropriate noise correction factor for voxel size was determined.

CNR measurements confirmed the findings from *Chapter 7* on the wide range of included devices. A generally adequate high contrast resolution is seen for CBCT, but low contrast resolution can be poor and differs between devices. In addition, the issue of intra-scan uniformity (*i.e.* difference between central and peripheral ROIs within the same image, for large FOVs) and inter-scan uniformity (*i.e.* overall difference in grey values between central and peripheral FOV positioning, for small FOVs) was highlighted. Depending on the size and mass of the scanned object, the position and size of the FOV, and the grey value calibration of the unit, images can show a centre-to-periphery or a front-back grey value gradient due to effects like beam hardening.

A next study focused on the variability of CBCT grey values and their use for density estimations (*Chapter 11*). Six materials of varying density were selected: air, aluminium, PMMA, and hydroxyapatite (HA) of 50, 100 and 200 mg/cm^3). Reference grey values (CT numbers) were obtained from a MSCT device. Similar to the evaluation in *Chapter 7*, the correlation between CBCT grey values and CT numbers was calculated for the full density

and the medium density ranges. However, the value of these correlation coefficients is difficult to interpret and has often been evaluated too optimistically in literature. Therefore, the grey value 'error' was determined after recalibrating the CBCT grey values using the CT numbers for air and aluminium as reference points. The error values for the included CBCT protocols, even the best performing ones, pointed out that CBCT grey values for density estimations should be used with great care. Furthermore, the experimental set-up in this Chapter did not take the uniformity (*Chapters 7 and 10*) and effect of metals (*Chapter 8*) on grey values into account, both of which can further affect the variability of density estimations in clinical practice.

As a final study regarding image quality, the link between technical and diagnostic image quality was investigated (*Chapter 12*). The homogeneous section of the image quality phantom was scanned using 7 imaging protocols on 4 CBCT devices. For each protocol, the mAs was varied within the full available exposure range. CNR was measured for each exposure range. In parallel, scans were obtained from the RANDO phantom using identical exposures, and an observation study was set up by evaluating the visibility of anatomical parameters and the use of images for different diagnostic applications. The results indicated that, depending on the clinical indication, exposure levels well below standard clinical protocols could be achieved. Although a phantom image will always look better than a patient image because of the absence of motion and artefacts, the current results warrant further investigation on a clinical level. Although clinical and technical image quality parameters showed a clear relation with each other and with the mAs, it was difficult to find a numerical correlation between them because of the influence of spatial resolution. Although this correlation should be further explored, and the implementation of reference or suspension levels for technical image quality parameters for CBCT should be investigated, it can be concluded that a visual check of spatial and contrast resolution during QC or acceptance testing (*Chapter 9*) provides an added value for the medical physicist.

Hypotheses

A series of hypotheses were defined in the Introduction & Hypotheses section of this thesis. Our study allowed to confirm or refute them, or to formulate interesting tracks for future research.

Effective dose values for CBCT range between those of 2-D radiography and MSCT.

This hypothesis was addressed in *Chapters 1-3*, and was confirmed for adult and paediatric anthropomorphic phantoms. The CBCT dose range is situated very closely (and partly overlaps) to that of panoramic radiography but reaches MSCT for certain applications and specific devices. It must be stated that doses in MSCT have been substantially lowered over the past years and will be reduced even more owing to the more general availability of iterative reconstruction in the upcoming years.

Radiation risks are substantially higher for children than for adults due to the relatively larger exposes area, in combination with the increased radiation sensitivity at lower ages.

This topic was covered by *Chapters 2 and 4*. Although absorbed and effective doses as evaluated from anthropomorphic paediatric phantoms were not considerably higher than those of the adult phantom due to the presence of specific paediatric imaging protocols, the age-dependence of radiation risk leads to higher risk estimations, as confirmed *in vivo*.

Significant dose reduction can be achieved by reducing the FOV or by use of a partial rotation.

This hypothesis was confirmed in *Chapter 3*, using FOV sizes between 4x4cm and 17x12 as well as 360° and 180° rotation arcs.

Individual patient doses in CBCT depend on the size and mass of the patient.

No clear effect of size and mass on the absorbed dose at the skin level was found in the *in vivo* study in *Chapter 4*. Differences in individual radiation risk were primarily determined by age at exposure.

Dose distribution in CBCT is highly affected by the exposure geometry (FOV diameter and height, FOV position, rotation arc).

This statement, although theoretically sound, was experimentally confirmed by the dose distribution measurements in *Chapter 5*.

A dose index for CBCT, which takes the varying dose distribution into account, can be defined and converted to effective dose.

The two dose indices proposed in *Chapter 6* are both suitable to evaluate CBCT dose distribution, and can be converted to effective dose using appropriate correction factors.

An image quality phantom, which can be applied to all types of CBCT devices on the market, can be developed.

The image quality phantom developed in *Chapter 7* is applicable to all CBCT devices, and contains inserts which are suited and relevant for dental CBCT imaging

CBCT grey values can be used for (bone) density estimations, similar to the use of Hounsfield Units in MSCT.

Although generally high correlation coefficients were seen for the two density ranges included in *Chapter 11*, the error after recalibration of grey values revealed that deviations, even in this controlled experiment, are too high for actual density estimation but could be used for categorical bone classification.

Metal artefacts on CBCT or MSCT images can be quantified and compared.

Chapters 7 and   8 contained the measurement of metal artefacts from titanium and lead rods. A corrected standard deviation proved to be a suitable and practical figure of merit.

Image quality (spatial resolution, contrast detail) in CBCT can be evaluated visually by use of suitable test objects.

Chapter 9 addressed this hypothesis using a line pair and rod insert. Although the design of the line pair was improved in the final prototyping stage, both inserts were suitable and showed high observer agreement.

CBCT images generally have a good contrast resolution for high-contrast materials, a poor contrast resolution for low-contrast materials, and a high amount of noise. Furthermore, uniformity within or between scans can be poor.

The statement regarding contrast resolution was confirmed in *Chapters 7, 9 and 10*. Noise and uniformity were measured in *Chapters 7 and 10*. It was seen that contrast-to-noise levels varied considerably between CBCT scanners but were generally inferior to MSCT. Uniformity of grey values was device- and FOV-dependent.

Technical image quality can be linked to diagnostic image quality, and thresholds for acceptable image quality can be determined based on technical parameters

Chapter 12 investigated the image quality / dose relation for technical image quality parameters (CNR) and diagnostic image quality parameters (anatomical landmarks, clinical

applicability). Both types of parameters could be linked, although their relation was device-specific. Further study is needed to predict diagnostic image quality (and determine thresholds) using technical parameters.

Optimisation of CBCT

As demonstrated by the different topics which were addressed in this thesis, optimisation in CBCT can be achieved at various levels. Figure D.3 shows the connection between the 12 Chapters in this thesis and various optimisation topics discussed further below.
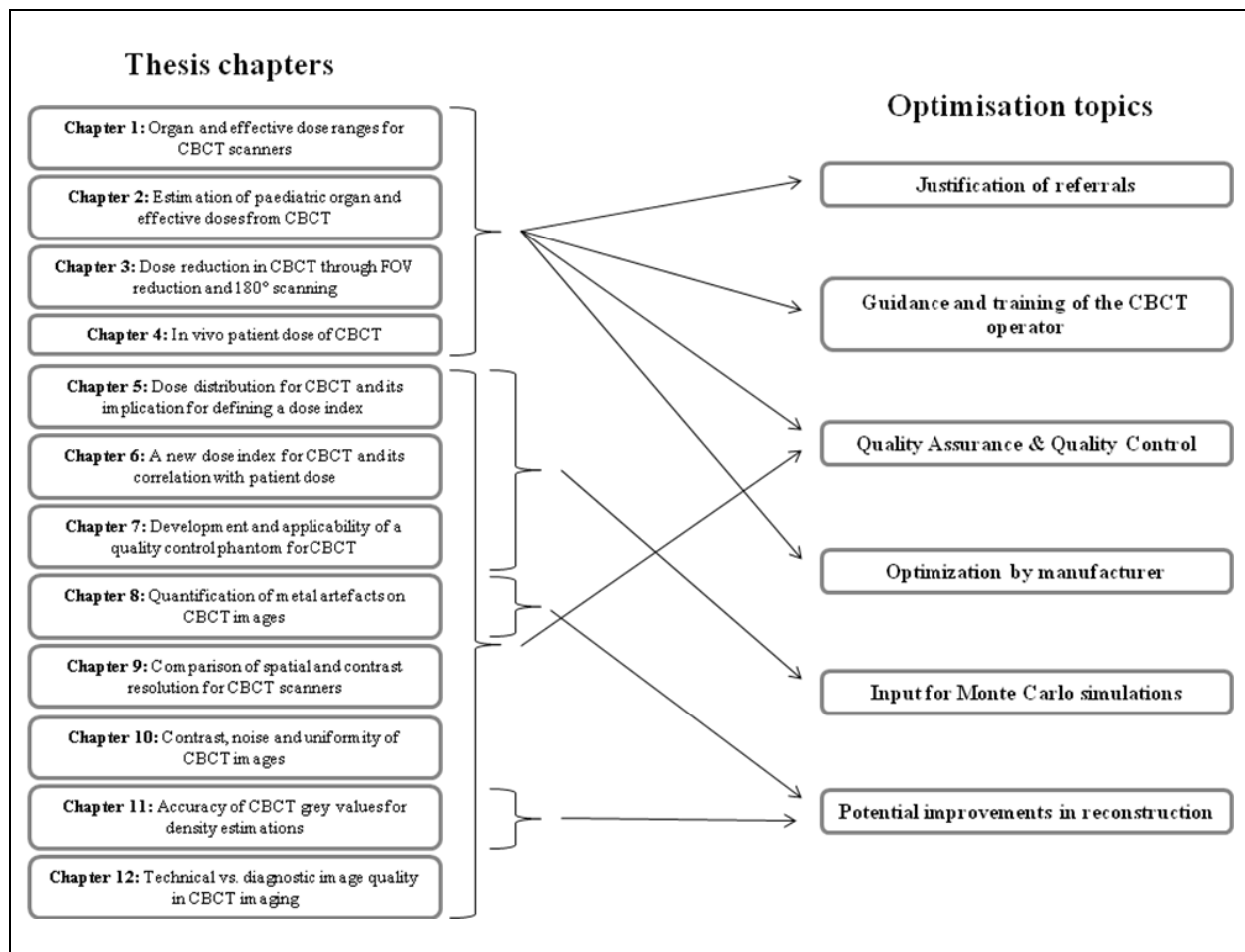
Figure D.3 Link between thesis chapters and CBCT optimisation

Optimisation by the referrer

The referrer is a key person in the 'justification' of an exposure. He plays an important part in dose reduction by making balanced decisions regarding the need for a CBCT scan, and (in case the referrer is not the operator of the device) by providing clear instructions regarding the desired exposure protocol (*e.g.* required region of interest, resolution), considering dose reduction whenever possible. Using the available clinical and radiographic information, he

should apply the justification principle to each individual case, rather than using routine decisions. When the CBCT examination is justified, the referrer should always precisely specify the desired scanning region, considering FOV limitation as much as possible. Furthermore, depending on his experience with the CBCT device which is referred to, he can either indicate the general requirements in terms of image quality, or provide the user with an exact exposure protocol with the lowest possible exposure parameters. Appropriate communication and feedback between referrer and operator is crucial for both parties.

Optimisation by the CBCT operator

The operator plays an important part in the optimisation process. Often, influence of the operator on the patient's exposure is limited, which can be for positive (*i.e.* clear instructions by the referrer) or negative (*i.e.* constrained exposure parameters on the device) reasons. When certain choices need to be made regarding exposure parameters, the operator should be knowledgeable to make these decisions, avoiding the routine use of certain exposure protocols for all patients. It can be assumed that none of the different CBCT operator groups (dentists, radiologists, radiation technicians, *etc.*) are adequately trained for the use of CBCT without receiving additional, specialized theoretical and practical training. Although parts of this training are applicable to the use of any radiographic modality (*e.g.* theoretical training on the basics of radiation physics and radiation protection, practical hardware and software operations for the specific device), the training can be tailored by implementing evidence provided in the current thesis as well as other studies. From the current findings, different topics can be emphasized in user training:

- Selecting the optimal FOV size and position for various types of clinical indications
- Avoiding the thyroid gland as much as possible through cranial FOV positioning
- Identifying patients for whom 180° scanning can be beneficial because of the reduction in scan time (*e.g.* small children)
- Dealing with metal objects in the scanned area: keeping metals outside (*i.e.* above or below) the FOV, not adjusting exposure factors to attempt metal artefact reduction
- Selecting the lowest possible exposure for each patient, taking its age, size and the clinical indication into account. Deciding on the threshold level of acceptable image quality will always be partly experience-based, and could be done by the operator himself if he is also the one interpreting the image (dentist, radiologist …), through

feedback with the referrer/reader after scanning and through communication with medical physicists.

- Performing regular quick quality checks or calibrations, guided by the medical physicist or manufacturer
- …

Optimisation by the medical physicist

As the medical physicist is, amongst others, responsible for acceptance testing and periodical quality control, many of the chapters in this thesis can be useful to optimise his approach on CBCT testing. The main contribution of the current thesis to the work of the medical physicist was the development of suitable tools, methodologies and parameters for the assessment of radiation dose and image quality. The dose indices proposed in *Chapter 6* could allow for a standardized routine measurement (and periodical follow-up) of exposure levels for all types of CBCT devices, relating those exposures to patient dose. Furthermore, using the evidence provided in *Chapters 1-4*, the medical physicist can guide the operator to ensure that exposure protocols are appropriately selected.

Parallel to the evaluation of radiation dose, the image quality phantom which was developed in Part II of this thesis can aid the medical physicist in the evaluation of the technical image quality. It allows for the assessment of image quality performance, by comparing quantitative results with any public (reference) performance levels that are available. These levels could be determined similarly to diagnostic reference levels (DRLs) used for radiation dose in diagnostic radiology and nuclear medicine. The concept of DRL was introduced by the ICRP in 1996 (Recommendation 73) and is defined in Council Directive 97/43 by Euratom as "Dose levels in medical radio diagnostic practices or, in the case of radiopharmaceuticals, levels of activity, for typical examinations for groups of standard-sized patients or standard phantoms for broadly defined types of equipment. These levels are expected not to be exceeded for standard procedures when good and normal practice regarding diagnostic and technical performance is applied". Different dose quantities are used to determine DRLs, and they are typically defined as the third quartile value of the range of doses obtained from a large sample of measurements. Values above this level can be interpreted as an opportunity for optimisation, although the DRL cannot be considered as a dose limit but as a guide for manufacturers and CBCT users, with the medical physicist being able to verify and compare dose levels from any radiological equipment to national and

international DRLs. Although the definition of a DRL refers to a dosimetric parameter, it could be useful to establish DRL values for image quality parameters as well.

Using the results from Chapters 8-10, DRLs could be tentatively proposed for different image quality parameters as they were measured on a wide range of CBCT devices, representing a reasonable sample of the variety of CBCT devices currently on the market. Depending on the nature of the parameter, which can be positively (*e.g.* CNR) or negatively (*e.g.* noise, metal artefacts) correlated with image quality, the DRL can be defined as the first or third quartile of the distribution of values for this parameter. Values below the first quartile or above the third quartile can then be considered as suboptimal. Figure D.4 shows the distribution for CNR_{AL} for the 30 CBCT exposure protocols included in Chapter 10. The first quartile value corresponds to the DRL, with 75% of protocols showing a higher CNR_{AL}. Table D.1 shows other potential DRL values from the image quality parameters investigated in Chapters 8-10. Certain parameters were not considered for DRL calculation: the line pair scores from Chapter 9 as they were determined subjectively, the CNR values for hydroxyapatite 50 (mg/cm^3) and 100 as there is in general no strict requirement in low-contrast resolution in dental imaging, the uniformity measurements as the distinction between intra- and inter-scan uniformity reduced the acquired sample of exposure protocols in half, and the grey value correlation and error values from Chapter 11 as the use of absolute grey values cannot be considered as a quality requirement in dental CBCT imaging. As more CBCT devices and exposure protocols are tested, preferably using the same phantom and methodology as in the current study, the reference sample would increase and the validity of the DRL value would increase. Furthermore, further investigations regarding the relation between technical and diagnostic image quality could lead to a diagnostically relevant figure of merit, taking all image quality aspects such as contrast and spatial resolution into account, for which DRLs could be determined for various clinical applications.
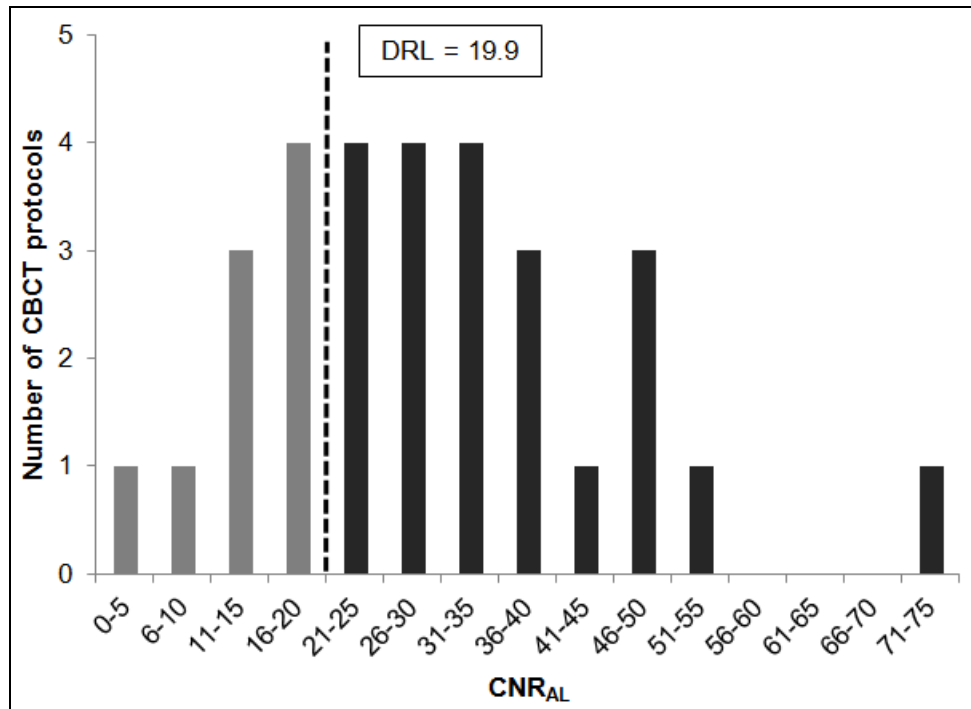
Figure D.4 Distribution for aluminium contrast-to-noise ratio (CNR$_{AL}$) with diagnostic reference level (DRL) based on first quartile value

Table D.1 Provisional diagnostic reference levels for metal artefacts and contrast resolution, based on 30 CBCT exposure protocols from 13 devices

Image quality parameter	DRL
Ti	18.5[a]
Pb	31.1[a]
Rod score	1.5[b]
CNR$_{AL}$	19.9[b]
CNR$_{200}$	3.5[b]
CNR$_{AIR}$	9.0[b]

[a]Third quartile values, higher values are suboptimal
[b]First quartile values, lower values are suboptimal
Ti titanium artefact, *Pb* lead artefact, *CNR* contrast-to-noise ratio

In parallel, the phantom enables the investigation of dose reduction at acceptable image quality levels, as it was seen in *Chapter 12* that the clinical acceptance of an image can be related to its noise or contrast level. However, as it is still too early to propose definite reference or suspensions levels for any image quality parameter, it can be expected that inserts may still have to be refined, especially if attempts are made to calculate measures such as MTF or noise power. Other examples relate to the evaluation of metal artefacts. It remains to be seen whether any calculated measure can replace visual assessment. In the ideal case, in

the following years a consensus will be reached, allowing for standardization of QA protocols for both radiation dose and image quality evaluation in CBCT.

Optimisation by manufacturers

Many optimisation schemes are useless if the manufacturer does not allow for their implementation. Ideally, any CBCT device should allow for the selection of a wide range for every exposure parameters, allowing for the choice of the most optimal exposure settings for each individual patient. A wide range of FOV options should be provided, to enable the selection of the minimal FOV size that covers the ROI, assuming that the operator is properly trained to position this minimally sized FOV correctly. The tube current and/or exposure time (*i.e.* number of projections) should be selectable as a function of patient size and diagnostic image quality requirements. Also, it should be possible to reduce the kVp within a certain range, although the optimal kVp for dental CBCT scanning is yet to be determined. When the choice of kVp is enabled, its selection is currently left to the operator's experience. Finally, a quick scan option (<10 s) should be included for patient groups with risk of motion.

In dental practice, however, it is seen that certain devices are purchased for use on a specific subgroup of patients (*e.g.* implant practice). In this case, it would be acceptable that the device enables the choice of a few exposure protocols which are relevant to that specific patient group. However, a small FOV option should always be implemented, as it can be suitable for any clinical indication if the region of interest is limited to one or two teeth (or other structures with similar volume size).

The manufacturer, in parallel with (or in collaboration with) the research community, should also focus on the further development of all parts of the CBCT imaging chain. As there is continuous innovation in MSCT, CBCT development should follow suit to ensure that it can be truly considered as a low-dose alternative to MSCT. Although certain hardware improvements (*e.g.* X-ray tube, detector) can always be expected, the highest potential for optimisation is currently found at the software level. A first possible optimisation strategy by the manufacturer would be the introduction of automatic exposure control (AEC). There are two levels of AEC. In its basic form, it implies that the mAs (possibly in combination with the kVp) is automatically determined based on the grey level ('density') histogram of the scout image, leading to an automatic reduction of exposure levels for smaller (*i.e.* size and mass) patients (Figure D.5). This technique has been implemented by one CBCT manufacturer for many years but has not been adapted by others, to our knowledge. However, most CBCT devices include either preset protocols for different patient size, or the manual selection of the

exposure within certain ranges. It is difficult to determine which method (automatic, preset or manual exposure control) would generally lead to the lowest patient exposures, although future development strategies should certainly focus on the further sophistication of the basic AEC. Additionally, a dynamic AEC could be considered, by adapting the exposure during the acquisition. As the primary beam encounters varying depths and densities of attenuating tissues during the rotation (Figure D.6), a dynamic adapted exposure would ensure an adequate detector flux during the entire acquisition, avoiding over- or underexposure for certain projection angles. For any type of AEC, the ranging image quality criteria for different dental indications need to be taken into account, seeing that a single reference level for AEC would not be suitable for dental imaging.

Another area of development in CBCT imaging can be found in the beam collimation. As of now, all CBCT devices allow for one or more discrete options in terms of FOV size. Although certain devices allow for a variety of volume sizes, the user is always limited by the available options. Even for those devices with an array of FOV options, additional dose reduction could still be achieved if the FOV size could be any value within an available range (with an upper limit determined by the detector size). Seeing that the operator can exactly determine the ROI size based on a frontal and lateral scout image, the use of a dynamic FOV size which is drawn by the operator on the scout images warrants further investigation.

At the other end of the imaging chain, there is also much room left for innovation. The basic algorithm for CBCT reconstruction is a modified filtered backprojection (FBP) technique developed by Feldkamp. However, with the increase in computational power, the use of iterative reconstruction has gotten increasingly popular in MSCT imaging and has been applied in nuclear imaging (PET, SPECT) and MRI as well. The main advantage of iterative reconstruction algorithms is their versatility. A conventional example of iterative reconstruction is the algebraic reconstruction technique, which expresses the projectional information as a large number of mathematical equations, and tries to find the most optimal solution. Further development of iterative reconstruction, and the incorporation of *a priori* (*e.g.* X-ray spectrum, anatomical patient model) and *a posteriori* (*e.g.* metal objects, patient motion) information into the algorithm will lead to significant improvements in image quality, which can be used as a possibility for further dose reduction. However, the computational power needed for iterative reconstruction techniques is holding back its clinical introduction. As of now, there is only one CBCT device to our knowledge which is using the algebraic reconstruction technique in its most basic format.
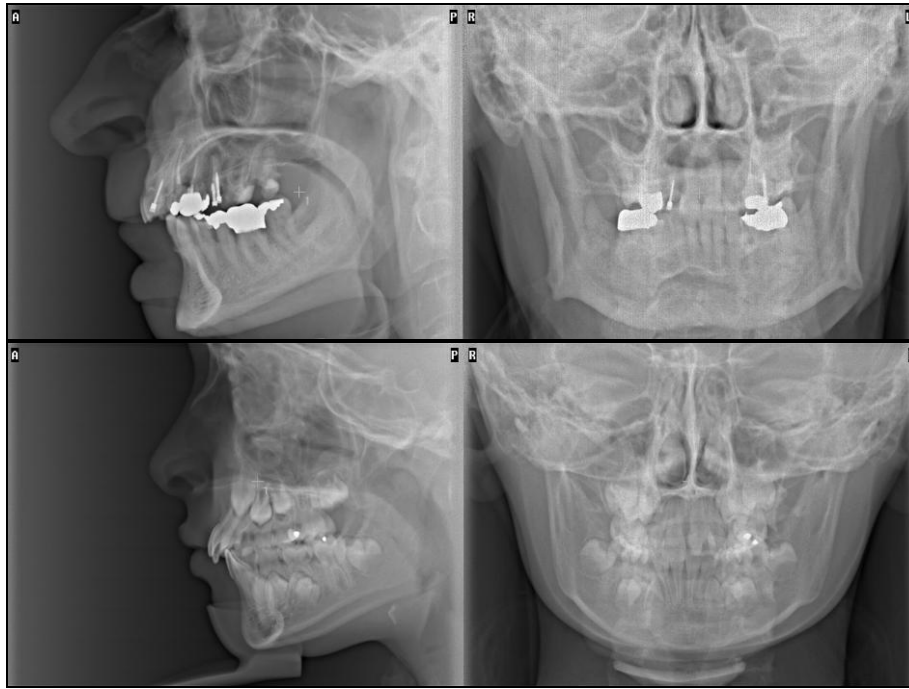
Figure D.5 Lateral and frontal scout images of the 3D Accuitomo 170, illustrating the possibility of basic AEC. Top: male patient, 73 years old. Bottom: female patient, 8 years old. AEC based on the density distribution of these scout images would lead to considerable dose reduction for the bottom patient.
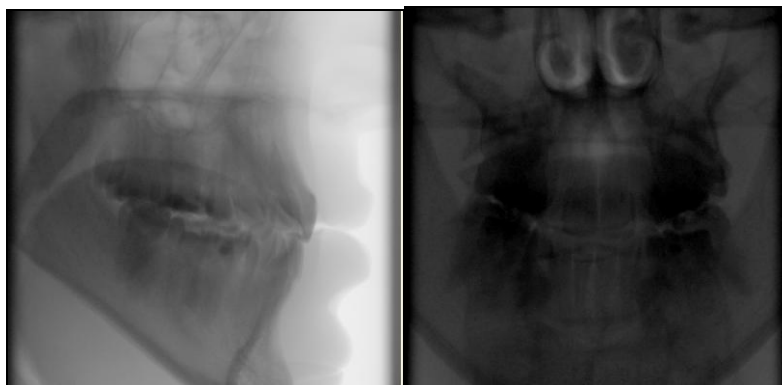

Figure D.6 Variability of detector flux during CBCT exposure. Grey values are directly related to detector signal. Left: lateral projection angle with high detector signal. Right: frontal projection angle with lower detector signal.

Two other potential improvements at the level of reconstruction, which are gradually being introduced into practice, is the use of metal artefact reduction (MAR) algorithms and motion correction. MAR is being applied by certain manufacturers, but when it is used in combination with FBP the clinical improvement in image quality is limited, as it typically involves an adjustment of the projection data and an interpolation to reduce the artefacts. Therefore, improvements in the appearance of the metal artefacts are often artificial or

balanced with a general loss in image quality. To a large extent, MAR can be easily incorporated into iterative reconstruction (Figure D.7), as it allows for the modelling of the polychromatic beam spectrum which would take the large amount of scatter, absorption and beam hardening by metal objects into account. However, as mentioned above, the computational power of current-generation reconstruction units can be considered as a bottleneck for the clinical use of advanced iterative reconstruction in dental CBCT.
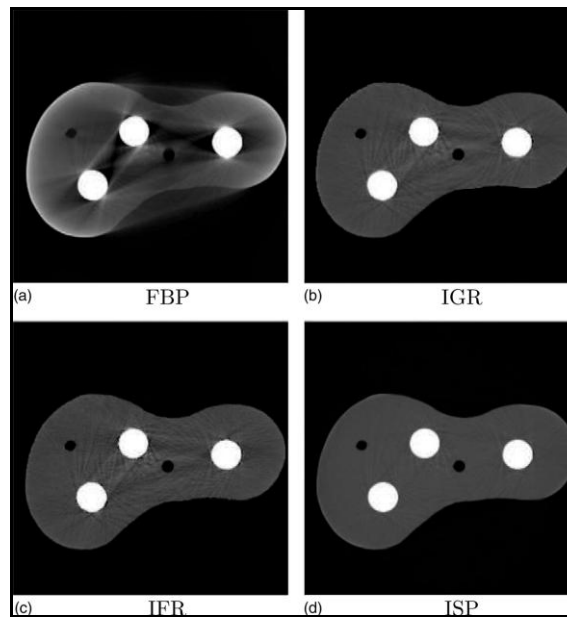

Figure D.7 Reduction of beam hardening artefacts through iterative reconstruction in CT. FBP: filtered backprojection. IGR: FBP-based optimisation. IFR: Gradient based optimisation. ISP: Sinogram pre-processing method. From Van Gompel *et al* 2011.

Next to MAR, motion reduction is also explored these days. One manufacturer has implemented a very basic method for motion correction, by allowing the user to discard projections from one of the four 90° quadrants if excessive motion has occurred at some point of the acquisition. Ideally, motion detection and correction should be done at the level of the raw data, comparing consecutive projection images or comparing the first and last projection, providing that they are taken from the same angle. Although excessive movement can only be compensated by removing the projections in which the movement has occurred, small movements or tremor could be resolved through matching of the projections, leading to an increased image sharpness.

A final potential improvement in reconstruction, which needs to be carefully considered by manufacturers, is the calibration of grey values for density estimations. Although the current results have shown that different factors affect the variability of absolute grey values in CBCT, future improvement in reconstruction techniques (*e.g.* artefact

reduction) may lead to acceptable grey value accuracy, at least for bony tissues. Although certain CBCT manufacturers claim to be using Hounsfield Units, there is still room for improvement in terms of grey value calibration, ensuring the stability of grey values within and between images. The use of a reference object with known density in the scanned volume during clinical scanning has been proposed in *Chapter 11*, as it may provide a partial solution to this problem (Figure D.8). The use of anti-scatter grids could be of value as well, although this does not seem to under consideration in current CBCT practice, as its use would require a greater radiation exposure to the patient due to the partial absorption of primary X-rays.
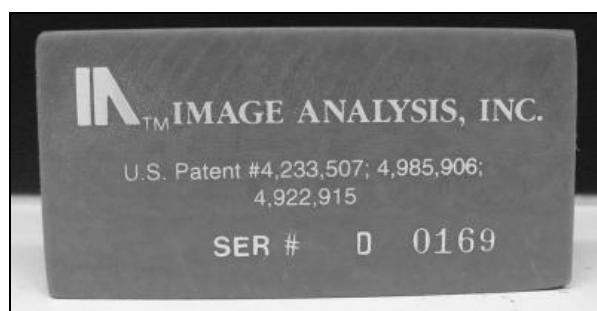

Figure D.8 QCT–Bone Mineral Phantom (Image Analysis Inc., Columbia, KY, USA) containing three materials of known density (Nackaerts *et al.* 2011). Similar, smaller, density phantoms could be applied in dental CBCT for grey value calibration.

Optimisation by the research community and academic associations

In terms of development and innovation, much of the work that can be done in academic research is similar to that of manufacturers, although the latter are evidently more involved in hardware-based improvements in the imaging chain. The improvement in general image reconstruction, metal artefact and motion reduction have been or will be hot topics in research. Although a joining of forces between the academic and corporate worlds could benefit both parties and speed up the introduction of new innovations in dental CBCT, it is important to avoid any conflict of interest when collaborating. As the research community is also responsible for the dissemination of all types of information to the public, there must always be a clear distinction between the interests of researchers and those of manufacturers.

In addition to this parallel work, the research community typically focuses on additional optimisation aspects, more closely related to the actual clinical image interpretation. A prime example is the ongoing research on bone quality analysis in CBCT, exploring different types of methods to evaluate bone density and architecture. The use of morphometric parameters and structural analysis using fractal dimension has been investigated for CBCT (Fanuscu *et al.*, Torres *et al.* 2004, Hua *et al.* 2009). Nowadays, these

topics are further explored *in vitro* or *in vivo*, in an attempt to find dedicated and validated bone quality parameters for CBCT. Possibly, a prediction model for CBCT with multiple variables (calibrated grey values in combination with morphometric and structural parameters) will offer the most accurate correlation with the actual mechanical properties of the bone (Jiang *et al.* 1999).

Another topic which is currently being addressed in academic research is the simulation of CBCT exposures using Monte Carlo methods (Zhang *et al.* 2011). Although simulations can never fully replace experimental measurements, they can be used to provide complimentary information and to explore dosimetry and image quality beyond practical limitations. Using Monte Carlo (MC) methods, all components of the imaging chain can be simulated. Existing CBCT devices can be mimicked by simulating the different components of the X-ray tube as well as the rotational geometry. Different kinds of voxel models, based on geometrical phantoms, anthropomorphic phantoms or patient data can be put into the MC framework, and the radiation distribution can be visualized. In addition, the detector could be modelled allowing for image reconstruction based on simulated projections (Figure D.9). In principle, every CBCT system could be modelled inside a MC framework, providing that all required parameters are known. However, the main added value of MC simulations over experimental measurements is their versatility, as it possible to adjust and evaluate exposure parameters beyond the limitations of existing systems. Possible applications are multifold, and most chapters in the current thesis could be linked to MC simulations to provide an added value:

- Estimating organ doses using standard phantoms or patient data. Any type of segmented human model could be simulated, allowing for the determination of effective dose (*Chapters 1-3*) or individual patient doses (*Chapter 4*).
- Investigating possible dose indices and conversion/correction factors for any CBCT exposure geometry (*Chapters 5-6*).
- Evaluating the suitability of specific materials or patterns for image quality analysis before manufacturing (*Chapter 7*).
- Singling out the effect of exposure parameters (kVp, filtration, mAs …) on image quality, finding optimum values for the balance between image quality and dose.
- …

It can be expected that validated MC frameworks will lead to considerable optimisation possibilities in the near future, and the results in the current thesis provide a solid basis for future simulation work.
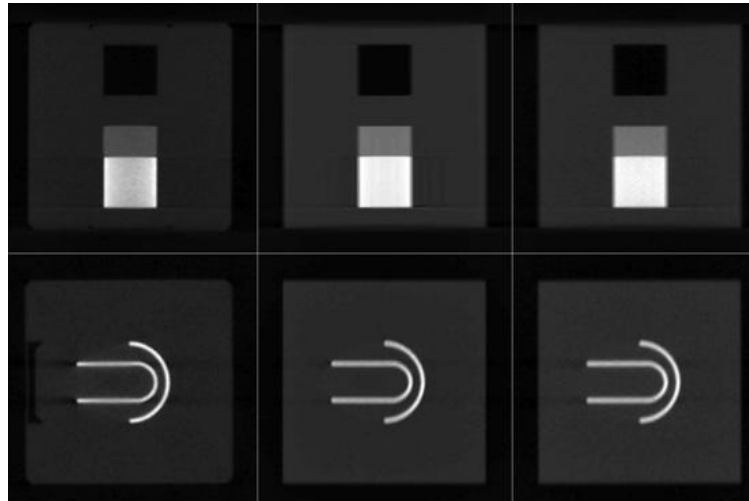

Figure D.9 Monte Carlo simulation of two geometric phantoms. Left: reconstructed central slices of the actual CBCT image. Middle and right: simulated images with ideal and realistic detector performance. Taken with permission from Zhang *et al* 2011.

Finally, the research community actively participates in the standardization process applied to different aspects of CBCT use, by contributing to evidence-based guidelines on the use of CBCT as well as developing training tools and approaches for theoretical and practical instruction on the use of CBCT. Typically, international academic associations are involved in this process. Within the SEDENTEXCT project, which encompassed the studies in this thesis, the European Academy of DentoMaxilloFacial Radiology (EADMFR, http://www.eadmfr.info/) was involved as a major stakeholder, providing input in the work package on guideline development as well as enabling dissemination of the guidelines and training tools. This collaboration allows for these guidelines to be implemented into recommendations by international commissions or governing bodies (see below). The current work (*i.e.* wide-scale quantitative evaluation of radiation dose and image quality, definition of potential dose indices, development of a dosimetry and image quality phantom) provided input for the SEDENTEXCT Guidelines document, which covers the justification of referrals, the optimisation of exposures and the development of a quality assurance protocol for CBCT. Although this type of guidelines is generally directed towards the CBCT user and medical physicist, it is also picked up by the manufacturers who may consider adapting their device to suit certain guidelines.

Optimisation by international commissions and governing bodies

Strictly speaking, international commissions, committees and associations have none or limited jurisdictional authority and primarily serve an advisory role; however, they are responsible for providing standards, recommendations and guidance on different levels. Regional, national and international legislation regarding radioprotection are based on their recommendations and guidelines. Their work is often based on a critical review of the available scientific literature. The most important commissions related to the use of CBCT equipment and radiation exposure are the International Commission on Radiological Protection (ICRP), the International Commission on Radiation Units and Measurements (ICRU), the International Electrotechnical Commission (IEC) and the United Nations Scientific Committee on the Effects of Atomic Radiation (UNSCEAR). All of these organizations cover a wide scope, and provide documents that can be applied to all use of medical radiation, all types of radiation, all types of electronic devices, *etc*. The impact of this thesis on this level is of course limited, but not negligible, as the results are disseminated through journal publications and additional sources, and any question for more detailed information is welcomed. It is therefore plausible that certain results and ideas provided by the current thesis can reach these commissions. The SEDENTEXCT Guidelines, to which this thesis has provided input, have been published by the European Atomic Energy Community (EAEC or Euratom) as "Radiation Protection 172. Evidence Based Guidelines on Cone Beam CT for Dental and Maxillofacial Radiology.", which strengthens its impact on a European and international level.

Different governing bodies are involved in the use of CBCT in dental practice. It should be noted that even though they can have certain jurisdiction in radiation protection, they can also provide reports similar to the guideline documents by the commissions mentioned above. Some bodies are internationally spread, like the International Atomic Energy Agency (IAEA), but most are nationally oriented. Examples are the Federal Agency for Nuclear Control (FANC, Belgium), the Radiation and Nuclear Safety Authority (STUK, Finland) and the Health Protection Agency (HPA, UK). For the development of regulations on the use of medical radiation, these agencies liaise with researchers, clinical users and other stakeholders. A concrete example can be found in the HPA recommendations for the design of X-ray facilities and QA of dental CBCT (Holroyd *et al*. 2010). The findings of this thesis, mainly with respects to the patient dose range and QC-related aspects, may provide input to future regulations and recommendations.

Conclusions and future prospects

In this thesis, a variety of topics regarding dosimetry and image quality in dental CBCT were addressed. Apart from serving as a wide-scale performance evaluation of current-generation CBCT devices, the main objectives were to provide evidence-based strategies for optimisation of CBCT in dentistry, and to develop tools which may enable standardized assessments of exposure and image quality.

The findings in this thesis provide valuable input for optimisation schemes at various levels, most notably the referrer, the operator, the medical physicist and the manufacturer. In addition, certain Chapters provide interesting prospects for future research. Specific topics which could be (further) addressed in the nearby future are:

- Age- and gender-dependency of radiation effects at low doses (*Chapters 2 and 4*), evaluating the current risk models using a combination of *in vivo* and *in vitro* dosimetry, dose simulations, radiobiology and epidemiology.
- Further investigation of a CBCT dose index and determination of general conversion and correction factors using MC simulation (*Chapters 5 and 6*).
- Dose and image quality optimisation using MC. Going beyond the limitations of exposure parameters from existing devices, to find the optimal balance between image quality and dose for each exposure parameter (*e.g.* kVp).
- Long-term (>5 years) follow-up of image quality deterioration on CBCT devices.
- Establishing suitable thresholds for technical image quality parameters, either as reference levels or suspension levels (*Chapter 12*).
- Bone quality analysis using CBCT images (*Chapter 11*).
- Improvement of CBCT reconstruction, implementation of advanced iterative reconstruction for general image quality improvement, metal artefact reduction (*Chapter 8*), grey value calibration (*Chapter 11*), …

As CBCT is becoming increasingly popular in clinical practice and research, it can be expected that most of these future prospects will be achieved in the near future. However, the topic of dose optimisation will always be relevant. The ALARA principle should not be adhered to passively but actively, exploring all possibilities for dose reduction.

Summary

In recent years, cone beam computed tomography (CBCT) has become a widely accepted radiographic tool for diagnosis, treatment planning and follow-up in dentistry. However, current use of CBCT can be considered as suboptimal in terms of justification of exposures as well as optimisation of patient radiation dose.

This thesis covers different dose- and image quality-related aspects of dental CBCT imaging. The various chapters each cover a particular topic related to CBCT dosimetry or image quality. The aim was to aid in all processes related to optimisation, standardization and guidelines for CBCT as part as the multicentre project SEDENTEXCT (www.sedentexct.eu).

In a first dosimetric evaluation, adult and paediatric anthropomorphic phantoms were used to estimate absorbed organ dose and effective dose from CBCT examinations using thermoluminescent dosimeters (TLDs) distributed throughout the head and neck of the phantoms (*Chapters 1-3*). The range of effective dose was assessed for a variety of CBCT equipment using phantoms representing an average adult (*Chapter 1*), a 10-year old child and an adolescent (*Chapter 2*). In addition, the absolute effect of field of view (FOV) reduction and 180° vs. 360° scanning was evaluated (*Chapter 3*). The results showed the importance of FOV limitation, as many radiosensitive tissues in the head can be left outside the primary beam during (part of) the exposure, leading to significant reduction in patient dose. In addition, the results showed that the thyroid dose can be reduced considerably by positioning the FOV as cranially as possible.

A second dosimetric study focused on *in vivo* dosimetry by measuring skin doses from patients undergoing CBCT examinations (*Chapter 4*). 269 patients were included. TLDs were attached to the skin at eight locations, and the measured skin doses were converted to organ doses using conversion factors obtained from the measurements in *Chapters 1 and 3*. Finally, an age-dependent risk estimation was performed. The results showed that, although the dose uptake can differ between patients because of varying patient size and exposure factors, the actual risk for the patient is mainly determined by the age at exposure.

A final dosimetric topic involved the definition of a suitable dose index for CBCT (*Chapters 5 and 6*). First, the dose distribution for a wide range of exposure geometries was assessed in cylindrical water and polymethyl methacrylate (PMMA) phantoms, using different dosimetric tools (*Chapter 5*). Based on our findings, two candidate dose indices were

proposed and evaluated (*Chapter 6*). Both indices were found to be suitable for CBCT, and a conversion to effective dose was investigated using correction factors for beam height, diameter and rotation arc.

The second part of this thesis focuses on image quality, with a particular focus on the development of tools and methodologies for quality control (QC). A prototype phantom for the evaluation of technical image quality parameters in CBCT was developed (*Chapter 7*). It consists of a head-size PMMA cylinder containing central and peripheral holes for the placement of inserts. A variety of inserts was developed allowing for the analysis of spatial resolution, contrast resolution, noise, grey value accuracy and stability, and metal artefacts. A first evaluation was performed to check the suitability of the phantom and inserts for CBCT, and to investigate the reproducibility of the obtained measurements. A number of improvements were implemented into the phantom's design, and a second prototype was manufactured allowing for a wide-scale evaluation of different image quality characteristics (*Chapters 8-11*).

Chapter 8 investigated the quantification of metal artefacts. The effect of titanium and lead rods on the surrounding grey values was investigated. A suitable parameter was determined by measuring the standard deviation of voxel values of the PMMA area around the rods, and normalising this value using the bit depth. The main conclusion from this evaluation is that, for a given CBCT device, the appearance of metal artefacts is relatively unaffected by varying mAs settings. The only valid approach for metal artefact reduction is the use of specific algorithms rather than increasing the tube output or projection number.

Visual analysis of spatial and contrast resolution was performed in *Chapter 9* using line pair and rod (*i.e.* contrast-detail) inserts. The suitability of a visual check for quality control and acceptance testing was assessed, and the influence of imaging parameters such as mAs and voxel size was evaluated.

Chapter 10 evaluated contrast, noise and uniformity was assessed using materials of ranging densities as well as homogeneous PMMA. The performance range in terms of contrast and noise of CBCT was determined and compared with MSCT and the intra- and inter-scan uniformity and its influence on the variability of grey values was calculated. Results showed an acceptable high-contrast resolution but poor low-contrast resolution for CBCT. Non-uniformity of grey values can affect their use for quantitative density estimations. This topic was further addressed in *Chapter 11*, which focused on the variability of CBCT grey values. Using MSCT as a reference, the correlation and calibration of grey values for

density estimations was assessed. Although certain devices showed reasonable potential for grey value calibration, quantitative use should always be done with great care.

Finally, the relationship between technical and diagnostic image quality for CBCT was investigated in *Chapter 12*. Contrast and noise measurements were obtained from air and homogeneous PMMA and an observer study was performed by scoring anatomical and diagnostic parameters on an anthropomorphic phantom, using a step-wise reduction in exposure for different CBCT devices. An additional aim was to determine thresholds for diagnostic image quality, and correlating them to technical image quality parameters. Although there was a clear relation between CNR, mAs and observer scores, it was clear that the scores were highly affected by the spatial resolution. A multi-predictor model of technical image quality parameters should be able to provide a reasonable estimation of diagnostic image quality, enabling the definition of ranges of threshold values for varying clinical applications.

The chapters in this thesis have various contributions to the optimisation of CBCT at different levels. The dosimetric and image quality evaluations provided input for the development of guidelines, justification criteria and training within the SEDENTEXCT project. In addition, tools and methodologies were developed which can be applied by the medical physicist in quality control and quality assurance.

References

Alqerban A, Jacobs R, Fieuws S, Nackaerts O, The SEDENTEXCT Project Consortium, Willems G. Comparison of 6 cone-beam computed tomography systems for image quality and detection of simulated canine impaction-induced external root resorption in maxillary lateral incisors. Am J Orthod Dentofacial Orthop 2011; 140: e129-139.

Council Directive 97/43 Euratom of 30 June 1997 on health protection of individuals against the dangers of ionizing radiation in relation to medical exposure, and repealing Directive 84/466/Euratom. Official Journal of the European Communities, 1997.

Dawood A, Patel S, Brown J. Cone beam CT in dental practice. Br Dent J 2009; 207: 23-28.

Dixon RL. Restructuring CT dosimetry - a realistic strategy for the future. Requiem for the pencil chamber. Med Phys 2006; 33: 3973-3976.

Fanuscu MI, Chang TL. Three-dimensional morphometric analysis of human cadaver bone: microstructural data from maxilla and mandible. Clin Oral Implants Res 2004; 15: 213-218.

Feldkamp LA, Davis LC, Kress JW. Practical cone-beam algorithm. J Opt Soc Am 1984; 1: 612–619.

Garcia Silva MA, Wolf U, Heinicke F, Gründler K, Visser H, Hirsch E. Effective dosages for recording Veraviewepocs dental panoramic images: analog film, digital, and panoramic scout for CBCT. Oral Surg Oral Med Oral Pathol Oral Radiol Endod 2008; 106: 571-577.

Gavala S, Donta C, Tsiklakis K, Boziari A, Kamenopoulou V, Stamatakis HC. Radiation dose reduction in direct digital panoramic radiography. Eur J Radiol 2009; 71: 42-48.

Holroyd JR, Walker A. Recommendations for the Design of X-ray Facilities and the Quality Assurance of Dental Cone Beam CT (Computed Tomography) Systems – A report of the HPA Working Party on Dental Cone Beam CT. HPA-RPD-065. Health Protection Agency, March 2010.

Hua Y, Nackaerts O, Duyck J, Maes F, Jacobs R. Bone quality assessment based on cone beam computed tomography imaging. Clin Oral Implants Res 2009; 20: 767-71.

International Commission on Radiological Protection. Recommendations of the International Commission on Radiological Protection. ICRP Publication 26. Ann ICRP. Oxford, UK: Pergamon Press, 1977.

International Commission on Radiological Protection. 1990 Recommendations of the International Commission on Radiological Protection. ICRP Publication 60. Ann ICRP. Oxford, UK: Pergamon Press, 1991.

International Commission on Radiological Protection. Radiological Protection and Safety in Medicine. ICRP Publication 73. Ann ICRP. Oxford, UK: Pergamon Press, 1996.

International Commission on Radiological Protection. ICRP Publication 89: Basic Anatomical and Physiological Data for Use in Radiological Protection: Reference Values. Ann ICRP. Oxford, UK: Pergamon Press, 2003.

International Commission on Radiological Protection. Recommendations of the International Commission on Radiological Protection. ICRP Publication 103. Ann ICRP. Oxford, UK: Pergamon Press, 2007.

Jiang C, Giger ML, Chinander MR, Martell JM, Kwak S, Favus MJ. Characterization of bone quality using computer-extracted radiographic features. Med Phys 1999; 26: 872-879.

Kamburoğlu K, Murat S, Kolsuz E, Kurt H, Yüksel S, Paksoy C. Comparative assessment of subjective image quality of cross-sectional cone-beam computed tomography scans. J Oral Sci 2011; 53: 501-508.

Liang X, Jacobs R, Hassan B, Li L, Pauwels R, Corpas L, Souza PC, Martens W, Shahbazian M, Alonso A, Lambrichts I. A comparative evaluation of Cone Beam Computed Tomography (CBCT) and Multi-Slice CT (MSCT) Part I. On subjective image quality. Eur J Radiol 2010; 75: 265-269.

Lofthag-Hansen S, Thilander-Klang A, Gröndahl K. Evaluation of subjective image quality in relation to diagnostic task for cone beam computed tomography with different fields of view. Eur J Radiol 2011; 80: 483-488.

Loubele M, Jacobs R, Maes F, Schutyser F, Debaveye D, Bogaerts R, Coudyzer W, Vandermeulen D, van Cleynenbreugel J, Marchal G, Suetens P. Radiation dose vs. image quality for low-dose CT protocols of the head for maxillofacial surgery and oral implant planning. Radiat Prot Dosimetry 2005; 117: 211-216.

Loubele M, Jacobs R, Maes F, Denis K, White S, Coudyzer W, Lambrichts I, van Steenberghe D, Suetens P. Image quality vs radiation dose of four cone beam computed tomography scanners. Dentomaxillofac Radiol 2008; 37: 309-318.

Loubele M, Bogaerts R, Van Dijck E, Pauwels R, Vanheusden S, Suetens P, Marchal G, Sanderink G, Jacobs R. Comparison between effective radiation dose of CBCT and MSCT scanners for dentomaxillofacial applications. Eur J Radiol 2009; 71: 461-468.

Ludlow JB, Davies-Ludlow LE, Brooks SL, Howerton WB. Dosimetry of 3 CBCT devices for oral and maxillofacial radiology: CB Mercuray, NewTom 3G and i-CAT. Dentomaxillofac Radiol 2006; 35: 219-226.

Ludlow JB, Ivanovic M. Comparative dosimetry of dental CBCT devices and 64-slice CT for oral and maxillofacial radiology. Oral Surg Oral Med Oral Pathol Oral Radiol Endod 2008; 106: 106-114.

Ludlow JB, Davies-Ludlow LE, White SC. Patient risk related to common dental radiographic examinations: the impact of 2007 International Commission on Radiological Protection recommendations regarding dose calculation. J Am Dent Assoc 2008; 139: 1237-1243.

Miracle AC, Mukherji SK. Conebeam CT of the head and neck, part 1: physical principles. Am J Neuroradiol 2009; 30: 1088-1095.

Nackaerts O, Maes F, Yan H, Couto Souza P, Pauwels R, Jacobs R. Analysis of intensity variability in multislice and cone beam computed tomography. Clin Oral Implants Res 2011; 22: 873-879.

Scarfe WC, Li Z, Aboelmaaty W, Scott SA, Farman AG. Maxillofacial cone beam computed tomography: essence, elements and steps to interpretation. Aust Dent J 2012; 57: 46-60.

Suomalainen A, Kiljunen T, Käser Y, Peltola J, Kortesniemi M. Dosimetry and image quality of four dental cone beam computed tomography scanners compared with multislice computed tomography scanners. Dentomaxillofac Radiol 2009; 38: 367-378.

Thorne MC. Background radiation: natural and man-made. J Radiol Prot 2003; 23: 29-42.

Torres SR, Chen CS, Leroux BG, Lee PP, Hollender LG, Schubert MM. Fractal dimension evaluation of cone beam computed tomography in patients with bisphosphonate-associated osteonecrosis. Dentomaxillofac Radiol 2011; 40: 501-505.

Van Gompel G, Van Slambrouck K, Defrise M, Batenburg KJ, de Mey J, Sijbers J, Nuyts J. Iterative correction of beam hardening artifacts in CT. Med Phys 2011; 38: S36.

Zhang G, Pauwels R, Marshall N, Shaheen E, Nuyts J, Jacobs R, Bosmans H. Development and validation of a hybrid simulation technique for cone beam CT: application to an oral imaging system. Phys Med Biol 2011; 56: 5823-5843.

Curriculum vitae

Ruben Pauwels was born on August 23rd 1985 in Herk-de-Stad, Belgium. He graduated as a biomedical scientist in 2007 and as master in medical imaging in 2008. His PhD programme started in January 2008, simultaneous with the start of the SEDENTEXCT project (www.sedentexct.eu), a European collaborative project which encompassed this PhD thesis.

Articles in internationally reviewed academic journals

Pittayapat P, Galati D, Huang Y, Dreesen K, Schreurs M, Couto Souza P, Rubira-Bullen I, Westphalen F, Pauwels R, Kalema G, Willems G, Jacobs R. An in-vitro comparison of subjective image quality of panoramic views acquired via 2D or 3D imaging. Clinical Oral Investigations 2012. Epub ahead of print.

Theodorakou C, Walker A, Horner K, Pauwels R, Bogaerts R, Jacobs R, The SEDENTEXCT Project Consortium. Estimation of paediatric organ and effective doses from dental cone beam CT using anthropomorphic phantoms. The British Journal of Radiology 2012; 85: 153-160.

Pauwels R, Theodorakou C, Walker A, Bosmans H, Jacobs R, Bogaerts R, Horner K, The SEDENTEXCT Project Consortium. Dose distribution for dental cone beam CT and its implication for defining a dose index. Dentomaxillofacial Radiology 2012. *In press.*

Pauwels R, Beinsberger J, Stamatakis H, Bosmans H, Bogaerts R, Jacobs R, Horner K, Tsiklakis K, The SEDENTEXCT Project Consortium. Comparison of spatial and contrast resolution for cone beam computed tomography scanners. Oral Surgery, Oral Medicine, Oral Pathology, Oral Radiology, and Endodontology 2012. *In press.*

Pauwels R, Stamatakis H, Bosmans H, Bogaerts R, Jacobs R, Horner K, Tsiklakis K, The SEDENTEXCT Project Consortium. Quantification of metal artifacts on cone beam computed tomography images. Clinical Oral Implants Research 2011. Epub ahead of print.

Stamatakis H, Tsiklakis K, Pauwels R, Jacobs R, Horner K, The SEDENTEXCT Project Consortium. Development of a universal quality control phantom specifically designed for dental CBCT. Digital Dental News 2011; 5: 6-11.

Pauwels R, Stamatakis H, Manousaridis G, Walker A, Michielsen K, Bosmans H, Bogaerts R, Jacobs R, Horner K, Tsiklakis K, The SEDENTEXCT Project Consortium. Development and applicability of a quality control phantom for dental cone-beam CT. Journal of Applied Clinical Medical Physics 2011; 12: 245-260.

Zhang G, Pauwels R, Marshall N, Shaheen E, Nuyts J, Jacobs R, Bosmans H. Development and validation of a hybrid simulation technique for cone beam CT: application to an oral imaging system. Physics in Medicine and Biology 2011; 56: 5823-5843.

Nackaerts O, Maes F, Yan H, Couto Souza P, Pauwels R, Jacobs R. Analysis of intensity variability in multislice and cone beam computed tomography. Clinical Oral Implants Research 2011; 22: 873-879.

Pauwels R, Beinsberger J, Collaert B, Theodorakou C, Rogers J, Walker A, Cockmartin L, Bosmans H, Jacobs R, Bogaerts R, Horner K, The SEDENTEXCT Project Consortium. Effective dose range for dental cone beam computed tomography scanners. European Journal of Radiology 2012; 81: 267-271.

Liang X, Lambrichts I, Sun Y, Denis K, Hassan B, Li L, Pauwels R, Jacobs R. A comparative evaluation of Cone Beam Computed Tomography (CBCT) and Multi-Slice CT (MSCT). Part II: On 3D model accuracy. European Journal of Radiology 2010; 75: 270-274.

Liang X, Jacobs R, Hassan B, Li L, Pauwels R, Corpas L, Souza P, Martens W, Shahbazian M, Alonso A, Lambrichts I. A comparative evaluation of Cone Beam Computed Tomography (CBCT) and Multi-Slice CT (MSCT). Part I. On subjective image quality. European Journal of Radiology 2010; 75: 265-269.

Loubele M, Bogaerts R, Van Dijck E, Pauwels R, Vanheusden S, Suetens P, Marchal G, Sanderink G, Jacobs R. Comparison between effective radiation dose of CBCT and MSCT scanners for dentomaxillofacial applications. European Journal of Radiology 2009; 71: 461-468.

Presentations at international scientific conferences

Pauwels R, Nackaerts O, Stamatakis H, Tsiklakis K, Walker A, Bosmans H, Bogaerts R, Jacobs R, Horner K, The SEDENTEXCT Project Consortium. Accuracy of CBCT grey values for density estimations.13th European Congress of Dentomaxillofacial Radiology, 2012, Leipzig, Germany.

Pauwels R. Dosimetry and image quality of CBCT in dentistry. Jornada Brasileira de Radiologia Odontológica, 2011, Praia do Forte, Bahia, Brazil.

Pauwels R, Theodorakou C, Walker A, Bosmans H, Jacobs R, Bogaerts R, Horner K, The SEDENTEXCT Project Consortium. Dose distribution for CBCT and its implication for defining a dose index. 18th International Congress of Dentomaxillofacial Radiology, 2011, Hiroshima, Japan.

Pauwels R, Beinsberger J, Theodorakou C, Walker A, Cockmartin L, Bosmans H, Jacobs R, Bogaerts R, Horner K, The SEDENTEXCT Project Consortium. Effective dose range for cone beam computed tomography scanners. 12th European Congress of Dentomaxillofacial Radiology, 2010, Istanbul, Turkey.

Pauwels R, Stamatakis C, Manousarides G, Walker A, Michielsen K, Bosmans H, Jacobs R, Horner K, Tsiklakis K, The SEDENTEXCT Project Consortium. Image analysis of a quality assurance phantom for cone beam CT. 17th International Congress of Dentomaxillofacial Radiology, 2009, Amsterdam, The Netherlands.

Pauwels R, Loubele M, Liang X, Lucas V, Van Bever P, Van Hevele J, Jacobs R. Assessment of metal artefacts on Cone Beam CT images. 11th European Congress of Dentomaxillofacial Radiology 2008, Budapest, Hungary.

Presentations at other scientific conferences and symposia

Pauwels R, Theodorakou C, Walker A, Bosmans H, Jacobs R, Horner K, Bogaerts R, The SEDENTEXCT Project Consortium. Dose distribution for dental cone beam CT and its implication for defining a dose index. 27th BHPA symposium, 2012, Brussels.